Unified Framework to Design Efficient Membrane Distillation for Brine Concentration

by

Jaichander Swaminathan

S.M., Massachusetts Institute of Technology (2014)
B.Tech., Indian Institute of Technology Madras (2012)

Submitted to the Department of Mechanical Engineering
in partial fulfillment of the requirements for the degree of

Doctor of Philosophy in Mechanical Engineering

at the

MASSACHUSETTS INSTITUTE OF TECHNOLOGY

June 2017

Author .....
Department of Mechanical Engineering
May 12, 2017

Certified by .....
John H. Lienhard V
Abdul Latif Jameel Professor of Water
Thesis Supervisor

Accepted by .....
Rohan Abeyaratne
Graduate Officer, Department of Mechanical Engineering

Unified Framework to Design Efficient Membrane Distillation for Brine Concentration

by

Jaichander Swaminathan

Submitted to the Department of Mechanical Engineering
on May 12, 2017, in partial fulfillment of the
requirements for the degree of
Doctor of Philosophy in Mechanical Engineering

Abstract

Increasing regulations requiring industrial zero-liquid discharge necessitate the development of efficient desalination technologies for treating high salinity brine. Membrane distillation (MD) is promising for such applications since it is a scalable process that that can be coupled with a low temperature heat source to concentrate water up to saturation. More than five configurations of MD, based on different condensation and heat recovery approaches, have simultaneously been under development in the literature. In this thesis, we establish a common framework to characterize the thermodynamic performance of MD systems and to rank these configurations in terms of a combination of their energy efficiency (represented as GOR) and pure water productivity (flux).

A simplified heat exchanger (HX) analogy model is developed for single-stage balanced counterflow MD, based on the effectiveness-NTU method for heat exchanger analysis. This model can predict GOR and flux as a function of inlet temperatures, system size and flow rates, without using iterative finite difference solvers. A hydrophobic microporous membrane establishes the interface for evaporation in MD. In contrast to a simple heat exchanger, both heat conduction and vapor transfer occur through this membrane. While vapor transport results in pure water production, heat conduction is a loss mechanism. To account for these additional effects, two new dimensionless parameters are defined. These parameters together with NTU and feed salinity can completely characterize a general MD system's energy efficiency.

Contrary to some prior design suggestions, we show that low conductivity is preferable only between the evaporation and condensation interfaces, to limit heat conduction losses. In all other regions, a high conductance is ideal, and results in improvements in both GOR and flux. Based on the above findings, a conductive gap MD (CGMD) configuration is proposed. CGMD approaches the upper-limit performance of direct contact MD and permeate gap MD, for a given membrane and channel heat transfer characteristics.

Another widely used MD configuration is air gap MD (AGMD) which includes a region of stagnant air between the membrane and condensation surface. AGMD

performance can also be predicted using the proposed analytical framework by considering the membrane and the air region together as the effective membrane. Since this effective membrane is thicker, less conductive and has a higher permeability coefficient, AGMD is best suited for high salinity applications. However, if the air gap region gets flooded with pure water during operation, performance can deteriorate towards the lower limit of permeate gap MD performance. CGMD and DCMD can also be resilient to high feed salinity by using a thicker membrane. A framework is proposed for choosing the cost-optimal membrane thickness along with optimal membrane size, as a function of the relative cost of membrane area compared to thermal energy.

At small system size, increasing area per unit feed flow rate (specific area) leads to better GOR at the expense of lower flux. Beyond a critical specific area, both flux and GOR start to decline. At high feed salinity, this critical area is small enough to be practically relevant. A closed form expression for this critical specific area is derived using the HX analogy equations, as a function of feed salinity, top temperature and the two dimensionless parameters defined previously.

Finally, two methods of achieving high overall pure water recovery using membrane distillation, namely batch recirculation and multi-effect MD (MEMD) are analyzed. A batch design outperforms other brine recirculation alternatives such as semi-batch and continuous recirculation. The number of effects is an additional degree of freedom in MEMD system design. The number of effects is analogous to the specific area of single stage MD and plays the major role in determining GOR and flux, whereas the total specific area of MEMD determines its overall recovery ratio. For a given brine concentration application, it is shown that MEMD with feed preheating energetically outperforms batch MD.

Thesis Supervisor: John H. Lienhard V
Title: Abdul Latif Jameel Professor of Water

Acknowledgments

First, I would like to thank Professor John Lienhard V for his guidance, for reposing great trust in my abilities and providing me with several avenues for professional growth. He has created and maintained a lab group environment that encourages exploration and development of new interesting ideas.

I would like to thank Prof. Rohit Karnik and Prof. Evelyn Wang who provided important comments and suggestions to improve the quality of this work. I also want to extend this acknowledgment to all my guru-s, for providing the impetus towards my quest for knowledge.

My lab mates in the Lienhard Research Group have been a constant source of knowledge and inspiration. With them, I have had the opportunity to learn about and work on several projects in addition to what is presented in this thesis. I would like to thank Hyung Won for his contributions and discussions regarding the content in several chapters of this thesis. David has provided practical perspectives and has been an important partner in experimental evaluations of membrane distillation. Urmi not only shared her knowledge and insights regarding nanofiltration, but also gave important feedback about communicating my results effectively to a general audience. Kishor was a collaborator on MVC-MD hybrid systems analysis and I appreciate his attention to detail. Discussions with Karim have helped me appreciate entropy generation analysis much better. Emily was very helpful in discussions regarding numerical modeling of batch RO process. I would like to thank Omar, Quantum, Yvana and Andrew for interesting discussions and feedback. I am grateful to Ed Summers for sharing his MD system modeling and analysis. I would also like to thank several lab alumni: Prakash for providing friendly tips and guidance throughout the PhD, Rónán for being an 'entrepreneurship in residence' from whom I could learn a lot, Leo Banchik for the discussions and encouragement, Greg for his Pitzer model implementation and explanations, and Karan for his work on the effect of solute composition on desalination energy consumption.

Several experimental results presented in this study were made possible through

the contributions of MIT undergraduate students. I would like to thank Bailey Montano, Elizabeth Vasquez, Luke Roberto, and Mallory Whalen for their help with experimentally testing conductive gap MD performance, and Tiffany Tao and Elizabeth Vasquez for running the nanofiltration experimental system.

I would like to thank all my friends for their support and for making this PhD even more memorable. In particular, I would like to thank Deepak for sharing this experience start-to-finish, Rohit for additionally entertaining me with interesting problems from his research and classes, and also Ranga, Yashovardhan, Krithika, Rajesh, Divya, and Suhrid for hanging out at various avenues. I would like to thank my friend and music teacher, Srini for opening me to a new art form as an additional worthy pursuit. Through the MIT Samskritam club, I have taught spoken samskritam to several students and I am thankful for all their kind words of encouragement and acknowledgment. I would like to thank Vidya for inspiring me on this path.

I would like to thank Tata Center for Technology and Design at MIT for awarding me a fellowship. This enabled me to visit textile dyeing units in India and to try to develop practically relevant technology solutions for this industry. Portions of this work were funded by the Cooperative Agreement Between the Masdar Institute of Science and Technology (Masdar Institute), Abu Dhabi, UAE and the Massachusetts Institute of Technology (MIT), Cambridge, MA, USA, Reference No. 02/MI/MI/CP/11/07633/GEN/G/00, and facilitated by the MIT Deshpande Center for Technological Innovation and the Masdar Institute Center for Innovation and Entrepreneurship (iInnovation). I am grateful for this support.

Finally, to my family: ammA jAnaki, appA swAminAthan, pATTi umAmaNi, thAtthA kriShNamUrtthi uTpaDa anaivarukkum enathu namaskArangaL pala. avargaLin AtharavinRi ethaiyum ennAl sAthitthirukka muDiayAthu. nALthOrum varum innalgaLaiyum magizhccigaLaiyum avargaLuDan pagirnthE ithai kaDanthuLLEn.

Contents

List of Figures

List of Tables

Nomenclature

Acronyms

AGMD	Air gap membrane distillation
BPE	Boiling point elevation, °C
BRO	Batch reverse osmosis
CapEx	Capital expenditure
CGMD	Conductive gap membrane distillation
DCMD	Direct contact membrane distillation
GOR	Gained output ratio
HCR	Heat capacity ratio
HDH	Humidification dehumidification
HX	Heat exchanger
LMH	L/m^2-hr
MD	Membrane distillation
MEE	Multi-effect evaporation
MEMD	Multi-effect membrane distillation
MVC	Mechanical vapor compression
MW	Molar mass, kg/mol
MR	Mass flow ratio
NF	Nanofiltration
NTU	Number of transfer units
OpEx	Operating expenditure
PGMD	Permeate gap membrane distillation

RO	Reverse osmosis
RR	Recovery ratio
SW	Seawater
TTD	Terminal temperature difference, °C
VMD	Vacuum membrane distillation
ZLD	Zero-liquid discharge

Roman Symbols

A	Area, m^2
a_w	Activity of water
B	Membrane permeability, $kg/m^2 \cdot s \cdot Pa$
B_0	Membrane permeability coefficient, s
c	Specific cost
C	Cost factor
c_p	Specific heat capacity, $J/kg \cdot K$
d	Depth or thickness, m
D	Diffusivity, m^2/s
$f_{ch:m}$	Non-dimensional resistance ratio
$f_{c:v}$	Non-dimensional resistance ratio
h	Heat transfer coefficient, $W/m^2 \cdot K$
h_{fg}	Enthalpy of vaporization, J/kg
J	Permeate flux, $L/m^2 \cdot hr$
k	Thermal conductivity, $W/m \cdot K$
L	Length of module, m
m	Molality, mol/kg-solvent
$\dot{m}$	Mass flow rate, kg/s
M	Mass, kg
N	Number of effects/stages
$\dot{Q}$	Heat transfer rate, W
$\dot{q}$	Heat flux, W/m^2

P	Pressure, Pa
p^{vap}	Vapor Pressure, Pa
R	Thermal resistance, K/W
s	Salinity, g/kg
t	Time, s
T	Temperature, °C
T_0	Ambient temperature, , °C
U	Overall heat transfer coefficient, W/m^2·K
v	Velocity, m/s
w	Width, m

Greek Symbols

δ_{m}	Membrane thickness, m
ε	Exchanger effectiveness
η	Thermal efficiency
ϕ	Porosity
τ	Time

Subscripts, Superscripts

amb	Ambient
b	Bulk
br	Brine
∞, limit	Upper limit performance of DCMD (large HX), CGMD (high h_{gap})
c	Cold channel
ch	Feed/cold channel
cond	Conduction
crit	Critical value
d	Distillate
eff	Effective

f	Feed channel
gap	Gap between membrane and condensing surface
in	Inlet
m	Membrane
max	Maximum
min	Minimum
out	Outlet
p	Permeate
sat	Saturated state
vap	Vapor
w	Wall

Chapter 1

Introduction

A separation process that has gained significant importance over the last half century is desalination, or the separation of fresh water from a saline feed source. Most commonly, desalination technologies have been used to treat seawater for satisfying human needs for potable water, in areas with insufficient natural renewable supply.

The separation of pure water is achieved either by the application of mechanical work, in the form of pressure in the case of reverse osmosis, or electricity in the case of electrodialysis, or by the use of thermal energy through phase change as in multi-effect distillation, multi-stage flash distillation, freeze desalination, etc. Even when carefully optimized, desalination is an energy-intensive process and hence many investigators have looked towards offsetting the energy requirement through renewable energy resources. Solar thermal energy or geothermal energy can be used for thermal desalination. Similarly, renewable electricity production has been used to reduce the carbon-footprint of reverse osmosis or electrodialysis systems.

Initially, the most common method of extracting pure water from salt solution was phase change. Large-scale thermal-energy driven multi-stage flash and multi-effect distillation processes were the dominant processes for desalination. Today, pressure-driven reverse osmosis (RO) is the fastest technology for seawater desalination.

Desalination processes are also being used for inland brackish groundwater purification. Some industries that require additional purity of process water, such as food and beverage, pharmaceutical, and semiconductor industries also employ desalination

processes. Desalination has also played a role in industrial pollution management, for effluent cleaning and reuse.

1.1 Desalination at high feed salinity

A more salty brine solution is produced as a byproduct in desalination processes. In the case of seawater desalination, this brine stream is disposed back into the ocean. In doing so, it is important to ensure good mixing at the point of disposal in order to not adversely affect the local salinity.

There are several situations where such disposal may not not be a vaible option. For example, the flowback and produced waters from hydraulic fracturing can be several times more concentrated that seawater, and would also differ in terms of composition. Industrial effluents can also have dissolved impurities that can be toxic. Regulations by environmental protection agencies governing such solutions may require deep-well injection, or zero-liquid-discharge.

For such applications, desalination processes can be used to concentrate solutions up to saturation, before salts can be precipitated out in a crystallizer. Membrane based separation processes would require much higher than the current-standard 70 bar of applied pressure to effect desalination of such concentrated solutions. Thermal phase-change based processes like MED and MSF on the other hand can concentrate water up to high salinity, while operating at reasonable top temperatures, and are the current standard for such applications.

One disadvantage of these thermal desalination processes is their large size and use of vacuum pressures, necessitating significant materials cost. This is in contrast to RO, which is modular and scalable down to very small-sizes- such as a kitchen cabinet top system producing 15 L per hour. As a result, there is an active interest in identifying scalable alternatives such as RO, that can desalinate water up to very high feed concentrations.

1.2 Membrane distillation

Membrane distillation (MD) is a thermal desalination technology that has received increased attention for small scale, renewable-energy-driven desalination applications as well as for treating high salinity brines. Scalability, the ability to handle high salinity feed streams, and relatively high fouling resistance are some of the advantages of the MD process. Several MD configurations with relative advantages and disadvantages have been proposed in the literature. The four common MD configurations include air gap (AGMD), direct contact (DCMD), vacuum (VMD) and sweeping gas membrane distillation (SGMD) [8]. In addition, other configurations have been suggested recently, including the permeate (liquid or water) gap MD (PGMD), and material gap membrane distillation (MGMD) [37]. Several multi-staged configurations based on the above designs have also been proposed in literature and commercially implemented [134].

MD is particularly interesting for renewable energy applications because it can use low temperature, low grade heat sources. The process is very simple, requiring no high-pressure or vacuum pumps leading to a modular scalable system. Ghaffour et al. [42] recently investigated membrane distillation and adsorption desalination as innovative energy efficient desalination options for combining with renewable energy sources. Sarbatly and Chiam [88] evaluated MD powered by geothermal energy and found that while cost of water from a vacuum MD system powered from conventional sources is about US\$1.29/m^3, with geothermal energy use, the cost drops to about US\$0.5/m^3 making it competitive with other desalination technologies.

Suarez et al. [96] investigated low-temperature direct contact membrane distillation in combination with a solar thermal gradient salt pond. About 70% of the total energy collected was used within the MD module, but sensible heat conduction losses through the membrane made up 50% of this energy. The authors of this study identified the need to reduce heat losses and improve the thermal efficiency of the process in order to make solar-powered renewable desalination viable.

Another relevant question associated with renewable MD systems is the choice of

MD configuration. Zaragoza et al. [133] investigated this by experimentally comparing five commercial MD modules in air gap, permeate gap, and multi-effect vacuum configurations for desalination coupled with solar thermal energy. Although the recovery ratio, defined as pure water production divided by feed flow rate, of the multi-effect system can be an order of magnitude higher than for single stage configurations, the energy efficiency of single stage spiral wound permeate gap systems was the maximum. Electrical energy consumption for maintaining the vacuum was also significant in the case of the multi-effect vacuum configuration.

The recurring challenges in the above studies are the low energy efficiency of membrane distillation preventing MD's widespread use for renewable desalination and the various MD configurations being pursued without a clear hierarchy in terms of their energetic performance. In this article, multiple membrane distillation configurations are investigated under similar conditions to compare their energy efficiency and capital cost. In any given single stage MD configuration, there is a trade-off between energy efficiency and capital costs, with energy costs decreasing and capital expenditure increasing with larger module length. In the present work, a clear trend is established in terms of overall performance and cost among different MD configurations. The similarity between MD and heat exchangers is recognized and used to develop a simple theory to explain MD performance metrics. In addition, numerical models are developed for direct contact, permeate and conductive gap MD systems based on this theory. These can be utilized without large computational or experimental expenditure. These results will hasten the development of optimized MD systems for renewable desalination applications.

1.2.1 Membrane distillation configurations

Most studies on MD start by listing four different configurations of membrane distillation in the introduction, before choosing to focus on one of these configurations. The fundamental principle of operation of all these configurations is the same. Separation is achieved through evaporation of the more volatile component of a mixture. When used for desalination, pure vapor preferentially passes through the pores of a

hydrophobic membrane that prevents liquid feed from passing through. The different configurations of MD vary based on how this vapor is captured and condensed to obtain pure water, and how this condensation energy is recovered. In the case of DCMD, cooler pure water flows on the other side of the membrane, countercurrent to the feed, and the vapor condenses into this stream and warms it up. The warm pure water stream would then be passed through a heat exchanger to preheat incoming salt water [64, 98]. DCMD is the oldest MD configuration proposed [56]. In AGMD, the vapor condenses on a condensing plate that is cooled by the incoming feed. The feed thereby gets preheated within the module by the condensing vapor, hence recovering some of the energy input. The air gap between the membrane and the condensing surface is meant to reduce the sensible heat loss from the hot to the cold side [121].

Direct contact membrane distillation (DCMD) is the oldest configuration [52], with cold pure water receiving and immediately condensing the vapor on the other side of the membrane. The vapor is carried out of the module and condensed externally in the vacuum and sweeping gas configurations. In the air gap membrane distillation configuration (AGMD), condensation occurs inside the module, within an air gap between the membrane and the condensing surface. The feed water acts as the coolant enabling direct heat recovery within the module [118, 121]. This eliminates the external heat exchanger that needs to be used in the case of DCMD to transfer the energy from the pure water leaving the MD module to the incoming feed.

The energy efficiency of a single stage vacuum MD system is low, necessitating multi-staging for performance improvement [20, 48, 98, 99]. A single stage sweeping gas MD is thermodynamically similar to a humidification dehumidification desalination system and so is restricted to low energy efficiency values without staging or extraction [107]. AGMD and DCMD on the other hand, can potentially achieve higher energy efficiency in a single stage system [98] and hence will be considered in this study.

More recently, several novel MD configurations with modified gaps have been proposed in the literature, including permeate gap membrane distillation (PGMD) [21, 127] where the gap region is filled with pure condensate, material gap membrane

distillation with additional substances such as sand added to the gap [37] as well as conductive gap membrane distillation (CGMD) with high rather than low overall conductance of the gap region [65, 103]. Swaminathan et al. [103] showed that CGMD outperforms PGMD by about two times in terms of GOR, and that PGMD itself can have about 10% higher GOR than AGMD.

In the case of SGMD and VMD, the condensation happens outside the MD module. The sweeping air gets heated and humidified before leaving the module in SGMD, and in VMD, the vacuum pump would draw out relatively pure vapor in the case of VMD. This is passed through a condenser or vapor trap to recover pure liquid water [107]. Recently, a system using an aspirator was proposed to more efficiently recover the product water in VMD systems [48], eliminating the vacuum pump and concerns associated with incomplete condensation.

1.2.2 Energy Efficiency

Energy is supplied to MD systems both in the form of heat and work. Work transfer is usually used to achieve fluid flow through the channels. Heat is required to increase the temperature of the feed liquid and thereby enabling evaporation of water. Heat energy consumption by far exceeds pumping power requirements under normal operating conditions. Energy consumption in MD has been relatively higher than that of other desalination technologies as illustrated by Mistry et al. [74]. As a result, MD companies have focused on applications with available waste heat energy, from power plants or other sources [119, 134]. MD is also readily coupled with renewable and waste heat sources due to its ability to operate at low temperatures and still achieve desalination.

Energy efficiency is analyzed as gained output ratio (GOR) (Eq. 1.1):

$$\mathrm{GOR} = \frac{\dot{m}_\mathrm{p} h_\mathrm{fg}}{\dot{Q}_\mathrm{h}} \tag{1.1}$$

Most MD systems until recently have been restricted to GORs of less than about 4-6 [133, 134]. In contrast, large scale thermal desalination systems such as multi-stage

flash and multi-effect distillation, which may have significantly more complicated designs often have GOR higher than about 7-10 [44]. Increasing the GOR of MD close to these values would make MD more competitive with these conventional technologies.

The GOR of single stage MD configurations has been previously analyzed and compared by Summers et al. [98]. While single stage VMD systems are restricted to GOR below 1, single stage SGMD also does not achieve GOR beyond about 4 [107]. In contrast, DCMD and AGMD are relatively simple systems, and were shown to be capable of achieving higher GORs [40, 43, 57, 98].

1.2.3 System design parameters

The focus of this study is large scale MD systems with condensation energy recovery for feed preheating to achieve high GOR. Within each MD configuration, there are several independent design and operating parameters that affect overall MD performance. The temperatures of the feed and coolant streams play an important role in the MD process. Since vapor pressure various approximately exponentially with temperature, a higher feed temperature results in a larger vapor driving force and improved MD performance. Temperatures in MD are usually limited below 100 °C. In this study, we aspire to identify an optimal MD configuration and set of design parameters. The top feed temperature is held constant at 85 °C and the coldest temperature is set at 25 °C, except where stated otherwise.

The hydrophobic micro-porous membrane is at the heart of the MD process, and its properties have a direct effect on MD performance. Usually the membrane is made of polymers such as PVDF, PTFE or PP based on phase inversion, or electrospinning processes. Sometimes the membrane may include multiple layers, an active layer that is hydrophobic and establishes the liquid-vapor interfaces for evaporation and condensation, as well as a support layer. In this study, the active layer will be referred to as the membrane.

In addition to the material, other parameters considered when characterizing a membrane for MD are its porosity, tortuosity, pore-radius, fabrication method, etc. The overall objective of membrane design is to allow vapor transport from the hot

evaporating fluid interface to the condensing side without significant resistance, while inhibiting heat conduction losses. A high porosity and pore size, along with low tortuosity and low overall thermal conductivity of the membrane are preferred. The other important design choice is the membrane's thickness. A thicker membrane is preferred for high salinity desalination, whereas a thinner membrane is advantageous at low salinity. The question of optimal membrane thickness, for a given set of other properties is considered in Chapter 6.

The membrane's permeability coefficient to vapor (B_0) and overall thermal conductivity ($k_{\text{eff,m}}$) are defined independent of thickness. The thermal conductivity is obtained as a weighted average of the conductivities of the membrane material and air/vapor. Several models have been used to evaluate the membrane's permeability coefficient based on combining the molecular diffusion, Knudsen and viscous mechanisms of vapor transport across the membrane [59]. In this study, the permeability coefficient is set at 60% of the molecular diffusion limiting value. For the chosen top and bottom temperatures, this corresponds to an average value of $B_0 = 1.5 \times 10^{-10}$ s. In multi-effect MD, a different value of B_0 is used for each effect, based on the feed and cold side temperatures, whereas everywhere else, this permeability coefficient value is used. Membrane permeability can be adjusted by changing the membrane thickness δ_{m}. The membrane permeability is given by $B = B_0/\delta_{\text{m}}$.

The feed and cold channels constitute additional thermal resistances resulting in temperature polarization. The width and depth of these channels, together influence flow velocity, and can affect the channel heat transfer coefficients. The use of spacers in these channels can also influence the thermal resistance of these flow channels.

In the case of DCMD, an external heat exchanger is used for energy recovery to preheat the incoming feed stream. The area and overall heat transfer coefficient of this heat exchanger will affect the energy efficiency of the DCMD process. In the case of gap MD systems, the choice of gap thickness can play a similar role. Finally, membrane area, and the feed flow rate affect the overall performance of large-scale MD modules.

1.3 Thesis overview

In Chapters 2 and 3, specific aspects of DCMD and gap MD system operation to maximize energy efficiency are considered. In the case of DCMD, a simple method for ensuring close-to-balanced operation is proposed based on adjusting the pure water inlet flow-rate by measuring the brine exit flow rate and salinity. For PGMD, the importance of the flow-direction in the gap between the membrane and the condensing surface is highlighted. Additionally, the effect of the gap conductance is investigated to conclude that contrary to some claims in the literature, a high gap heat conductance is favorable compared to a low gap heat conductance not only in terms of flux, but also GOR.

In Chapter 4, the four simple single stage MD configurations are compared in terms of GOR and flux simultaneously, at seawater salinity. It is shown that CGMD can outperform AGMD and PGMD by up to 2 times. The relative performance of DCMD is a function of the external heat exchanger. If the heat exchanger is the same size as the membrane and condensing surface of gap MD, GOR of DCMD is lower than that of CGMD. A simplified heat-exchanger analogy of MD systems is introduced for predicting flux and GOR without using a full discretized model. This method is based on extending the $\varepsilon-\mathrm{NTU}$ method for heat exchangers to MD systems. The simplified HX method predicts performance within about 10% of the discretized model and has better accuracy for larger system size. In Chapter 5, a lab-bench scale system is used to compare and validate the better overall energy efficiency of CGMD compared to AGMD and PGMD at low salinity, due to its better energy recovery.

In Chapter 6, the performance of MD configurations is compared at high feed salinity. At low salinity, GOR rises with an increase in system specific area. There exists a practically relevant critical specific area for high salinity MD, beyond which GOR and flux both decrease. A closed-form analytical expression is derived to predict this critical system size as a function of top temperature, salinity, and two newly introduced non-dimensional thermal resistance ratios. At high salinity and low flux, GOR of AGMD is significantly better than that of CGMD. The relative advantage

of AGMD at high salinity is related to its larger effective membrane thickness (which includes the air gap), and its higher vapor permeability to conductivity ratio. Using a thick membrane in CGMD can help improve CGMD performance under these conditions. A method is proposed to choose cost-optimal membrane thickness at the design stage, along with the choice of system size, based on the specific cost of system area and thermal energy.

Chapters 7 and 8 deal with methods to obtain a high overall recovery ratio with MD. In Chapter 7 techniques based on brine recirculation are considered. Batch process outperforms semi-batch and continuous recirculation designs. A batch system spends more time at lower feed salinity, for the same overall recovery ratio. The importance of real-time feed flow rate control in batch, for preventing operation above the critical specific system size is illustrated. An optimal membrane thickness can be identified as a function of operating flux, similar to the case of single stage MD. Chapter 8 deals with the multi-effect design of gap MD (MEMD) systems that enables high per-pass recovery ratio by recovering condensation energy from one effect into the feed stream of a subsequent effect. The number of effects is the main design variable that affects GOR and flux, whereas specific area can be used to set the overall recovery ratio. With feed-preheating using both brine and permeate streams in the interstage heat exchangers, MEMD can outperform batch MD for the same concentration application.

In Chapter A, the case of replacing a heat exchanger with an MD system to not only transfer heat but simultaneously produce additional pure water is considered. An MVC-MD hybrid system is considered as a case study. Compared to conventional MD, both the thermal energy and part of the capital cost are 'free' leading to potentially favorable economics.

Finally, Appendices B and C deal with methods to improve the energy consumption of membrane desalination. In Appendix B the case of textile dyeing effluent recycling is considered and a method to change the effluent chemistry to reduce cost of desalination is considered. In Appendix C, the practical aspects of system design of a batch RO system are considered in the context of reducing the energy consumption

of desalination up to 70 g/kg compared o single stage RO. In particular, it is found that the volume of external piping needs to be minimized, and the cycle reset time has to be much smaller than the productive time for batch RO to provide net savings compared to single stage continuous RO.

Chapter 2

Simple Method for Balancing Direct Contact Membrane Distillation

Abstract

A simple theoretical method for maximizing efficiency via real-time balancing of direct contact membrane distillation (DCMD) systems is presented. The method is applicable under variable operating conditions. Balancing involves measuring only the flow rates of feed stream out of the module and the cold water flow into the module, as well as the salinity of the feed. A valve or variable frequency drive is used to set the condensate water flow into the module so that the heat capacity rates of the hot and cold streams are equal. This method is much simpler and more general than what is proposed in the literature, which generally requires more measurements and a complicated expression. Balancing leads to 20-50% improvement in efficiency (GOR) compared to equal inflow of both feed and pure water streams, which is the common practice. Real-time balancing is particularly useful for variations in feed salinity, whereas the improvement by real-time balancing is low for changes in system top or bottom temperatures.

The contents of this chapter are adapted from [105].

2.1 Introduction

DCMD is the oldest configuration of MD and the most commonly studied configuration due to its relatively simple design [52]. Optimizing DCMD operation to improve energy efficiency is the focus of this work. In DCMD, hot saline water flows across

one side of a microporous hydrophobic membrane. Cooler pure water is passed on the other side of the membrane. Due to the vapor pressure difference established by the temperature difference between the two streams, water vapor passes from the hot side to the cold side and condenses into the pure water stream. In addition, heat is also transferred from the hot side to the cold side in the form of conduction, which is a loss mechanism in MD. As a result of these two processes, the temperature of the hot stream decreases as it flows through the system and the temperature of the cold stream increases. In order to reuse energy and achieve gained output ratio (GOR) greater than 1, the energy in the warm distillate stream would have to be recovered. To do this, a counterflow external heat exchanger is used as shown in Fig. 2-1a that preheats the feed water before further heat is added in the feed top heater [10].

The pure water stream is recirculated after the fresh water produced within the MD module is removed. The feed may also be recirculated in a closed loop to increase the overall recovery ratio. Additional external cooling is necessary if both streams are recirculated, to prevent temperature rise of the feed and cold water loops. Heat recovery from the permeate stream can be achieved only when $T_{\mathrm{c,out}} > T_{\mathrm{f,out}}$ if the feed is recirculated. This condition may not be satisfied for very short length systems.

Some studies use an optional additional heat exchanger to reduce the pure water inflow temperature down to ambient temperature [45, 64]. This increases the temperature difference for desalination within the MD module, leading to higher flux. Figure 2-1b shows the difference in performance between using an additional heat exchanger and not using the additional heat exchanger based on numerical modeling. The system with an additional heat exchanger performs better especially when the MD area is small, and hence overall energy efficiency is low. For systems with larger membrane area, the difference in performance between the two systems is smaller. This computation was performed using the model described by Summers et al. [98], by setting $T_{\mathrm{c,in}} = T_{\mathrm{c,HX,out}}$ (for the case of no additional heat exchanger) or $T_{\mathrm{c,in}} = T_{\mathrm{amb}}$ (for the case of using a large additional HX). This study will focus on a system with no additional heat exchanger because of its relative simplicity and lower cost.

The hot and cold water streams are usually set up in counterflow configuration in

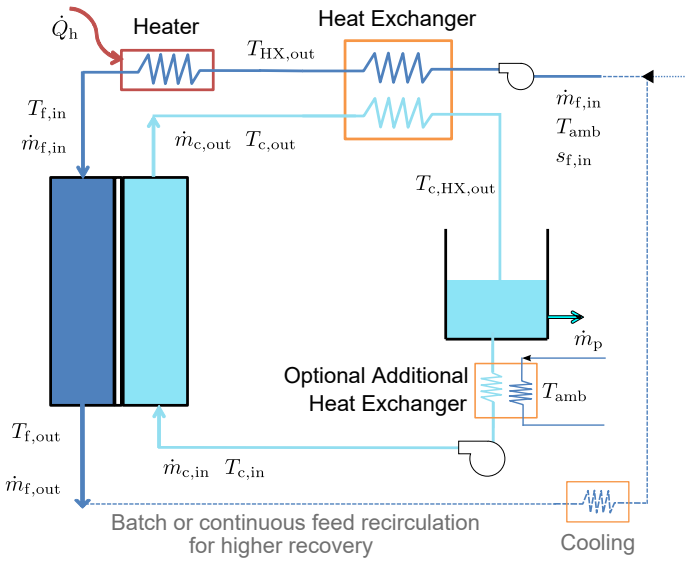

(a) Direct Contact Membrane Distillation process with a closed loop pure product.

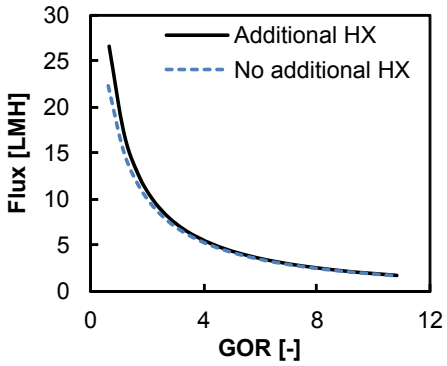

(b) Effect of additional cooling of condensate. Length is varied from 0.5 to 12 m. Other parameters are set at baseline values mentioned in Table 1.

Figure 2-1: DCMD system schematic diagram and effect of additional HX.

order to distribute the flux uniformly within the system and achieve higher energy efficiency.

Swaminathan et al. [103] showed that the energy efficiency of permeate gap (PGMD) and conductive gap (CGMD) MD systems was maximized when the pure water in the gap flows countercurrent to the cold water stream, as opposed to parallel or crossflow conditions. When the pure water flows in the same direction as the hot stream and countercurrent to the cool stream, at any local position along the MD module, the total flow in either direction is equal. This leads to a more uniform driving temperature difference across the module length and higher energy efficiency by about 40% compared to a case with pure water flow co-current to the cold stream. Thermodynamically, this increased efficiency is attributed to lower specific entropy generation within the module.

Unlike in the case of AGMD and other configurations, in DCMD, the flow rate of the cold water stream can be varied independently of the warm water flow rate. Several studies in the past used an equal input flow rate of hot and cold water into the module. Guan et al. [45] performed DCMD simulations and found that the GOR

was maximized when the feed and cold water inlet flow rates are approximately equal. Winter [126] experimentally showed that flux and GOR are both maximized under a symmetric operating condition where the mass flow rates of the hot and cold streams are equal at the hot end of the module.

Lin et al. [64] showed through numerical modeling of a coupled DCMD-Heat Exchanger (DCMD-HX) system, that the optimal value of cold pure water mass flow rate is not equal to that of the hot inflow, but about 90–92% of this value. They developed an analytical expression for this critical mass flow ratio, $\mathrm{MR}_{\mathrm{Lin}}$ as a function of T_{top}, T_{bottom}, $\mathrm{BPE}_{\mathrm{f,in}}$, $\mathrm{BPE}_{\mathrm{f,out}}$, $c_{\mathrm{p}}^{\mathrm{f}}$ and $c_{\mathrm{p}}^{\mathrm{c}}$ (Eq. 2.3) where mass flow rate ratio MR is defined as $\mathrm{MR} \equiv \frac{\dot{m}_{\mathrm{c,in}}}{\dot{m}_{\mathrm{f,in}}}$. Temperature and salinity are combined in the form of T^*, defined as:

$$T_{\mathrm{f,in}}^* = T_{\mathrm{sat}}\left(P_{\mathrm{vap}}\left(T_{\mathrm{f,in}}, s_{\mathrm{f}}\right)\right) \tag{2.1}$$

$$T_{\mathrm{c,in}}^* = T_{\mathrm{sat}}\left(P_{\mathrm{vap}}\left(T_{\mathrm{c,in}}, s_{\mathrm{f}}\right)\right) \tag{2.2}$$

where P_{vap} is the vapor pressure of salt water and is a function of temperature and salinity (s_{f}). A higher salinity results in a lower T^* through an increase in boiling point elevation (BPE), since $T^* \approx T - \mathrm{BPE}$.

The value of critical MR is then evaluated by considering the conditions for permeate limiting or feed limiting regime:

$$\mathrm{MR}_{\mathrm{Lin}} = \left(\frac{T_{\mathrm{f,in}} - T_{\mathrm{c,in}}^*}{T_{\mathrm{f,in}}^* - T_{\mathrm{c,in}}}\right) \cdot \left(\frac{\left(\frac{h_{\mathrm{fg}}}{c_{\mathrm{p}}^{\mathrm{c}}}\right) - \frac{T_{\mathrm{f,in}}^* - T_{\mathrm{c,in}}}{2}}{\left(\frac{h_{\mathrm{fg}}}{c_{\mathrm{p}}^{\mathrm{f}}}\right) + \left(\frac{c_{\mathrm{p}}^{\mathrm{c}}}{c_{\mathrm{p}}^{\mathrm{f}}}\right) \cdot \left(\frac{T_{\mathrm{f,in}} + T_{\mathrm{c,in}}^*}{2}\right) - T_{\mathrm{c,in}}^*}\right) \tag{2.3}$$

2.2 DCMD balancing theory

The balancing framework presented here is based on the analogy between MD systems and heat exchangers presented by Swaminathan et al. [106]. For a counter-flow heat exchanger, the balanced condition corresponds to a case of equal heat capacity rates ($\dot{m}c_{\mathrm{p}}$) of the two streams.

In the case of the MD system, the mass flow rates of the two streams also vary along the length of the channel. For a counterflow MD system though, there is an

interesting property that if the feed flow rates of the two streams are equal at any point along the length of the module, they would remain equal at all points along the module.

In countercurrent configuration, the feed flow rate reduces from $x = 0 \rightarrow L$, whereas the pure water flow increases from $x = L \rightarrow 0$ where $x = 0$ and $x = L$ correspond to feed inlet and outlet, respectively. Since any mass that leaves the feed enters the pure water stream, if the cold water input flow rate is set equal to the flow rate of the feed exit, at every point along the module length, the two flow rates would remain equal. For example, if the feed flow rate and the distillate flow rate are equal at the cold end of the module:

$$\dot{m}_{\mathrm{f,out}} = \dot{m}_{\mathrm{c,in}} \tag{2.4}$$

The flow rates of the two streams at the other end of the module can be expressed as a function of the pure water produced within the module as:

$$\dot{m}_{\mathrm{f,out}} = \dot{m}_{\mathrm{f,in}} - \dot{m}_{\mathrm{p}} \tag{2.5}$$

$$\dot{m}_{\mathrm{c,in}} = \dot{m}_{\mathrm{c,out}} - \dot{m}_{\mathrm{p}} \tag{2.6}$$

and hence $\dot{m}_{\mathrm{f,in}} = \dot{m}_{\mathrm{c,out}}$.

In the case of pure water as the feed, the balanced condition for DCMD systems is particularly simple; the flow rates of the hot and cold streams are equal because the specific heat capacities are identical. Since the flow rate of each stream varies along the length direction, we would set the flow rates at one end of the modules to be equal and hence they remain equal at every point along the length of the module. In addition, in this balanced condition, the flow rates through the external HX are also equal and so the HX is also balanced at the same condition.

2.2.1 Effect of solutes

For desalination, we are interested in salt water which has different a specific heat capacity compared to that of pure water. As a result, balanced condition for salt water corresponds to a more general case where heat capacity rates (i.e., $\dot{m}c_{\mathrm{p}}$) of the two streams at one end of the system are equal rather than the flow rates. The control system proposed in this study would set the product of the mass flow rate and the specific heat capacity of the cold stream at its inlet to be equal to the product of the mass flow rate and specific heat capacity of the salt water exiting the module:

$$\dot{m}_{\mathrm{c,in}} = \dot{m}_{\mathrm{f,out}} \times \frac{c_{\mathrm{p}}^{\mathrm{f}}}{c_{\mathrm{p}}^{\mathrm{p}}} \tag{2.7}$$

This can be achieved by using a simple control system that measures the two flow rates and the feed exit salinity as shown in Fig. 2-2a. If mass flow rate is directly measured, this measurement may be used directly. If instead, a volumetric flow measurement is implemented, the density of the stream as a function of the measured salinity can be used to evaluate the mass flow rate.

This criterion is general and holds true, irrespective of the membrane permeability, area, or heat transfer coefficients within the channels. This method equates the heat capacity rate ratio (or HCR) of the system to unity at the cold inlet, and we refer to this condition as "Balanced" in Fig. 2-4,2-5 and 2-6. Since the recovery in a single pass of DCMD is only about 6-7% usually, salinity of the brine is close to that of the feed and so $c_{\mathrm{p}}^{\mathrm{f}}$ is approximately equal at both ends of the module.

Note that unlike in the case of pure water, where setting this HCR to 1 at one end of the module results in a value of unity throughout the system, in the case of salt water, since $c_{\mathrm{p}}^{\mathrm{f}}$ is not equal to $c_{\mathrm{p}}^{\mathrm{p}}$, along the module the heat capacity rates of the two streams would not be identically equal. More specifically, the mass flow rate at any location is subtracted or added but HCR involves a ratio (i.e., division). Therefore, it is algebraically not possible to maintain HCR of unity when the c_{p} values of the two streams are different. Then there exists an optimal heat capacity ratio (HCR) value (defined at the cold inlet) that corresponds to a maximum GOR. This condition is

referred to as "Max GOR" in Fig. 2-4,2-5 and 2-6. The HCR value corresponding to maximum GOR is determined by numerical optimization in Engineering Equation Solver using a Golden Section search [53] as:

$$\text{Max GOR} = \max_{\text{MR}\in[0.6,1.4]} \text{GOR} \tag{2.8}$$

Although the HCR corresponding to this optimal condition is not necessarily unity, we show that "Balanced" condition with HCR = 1 is almost identical to the "Max GOR" case. We will compare the two control systems (Fig. 2-2) as well as the alternative of setting MR=1.

The comparisons in the subsequent sections are carried out based on the numerical modeling framework described in detail in Summers et al. [98]. The effect of salt concentration polarization is included [103]. The feed stream is assumed to be a sodium chloride solution. The effect of dissolved salt on the vapor pressure of the feed stream is given by:

$$p_{\text{vap}}^{\text{f,m}} = P_{\text{sat}}\left(T_{\text{f,m}}\right) \times a_{\text{w}}\left(T_{\text{f,m}}, s_{\text{f,m}}\right) \tag{2.9}$$

where a_{w} is the activity of water evaluated using the Pitzer equations as described by Thiel et al. [114].

The effect of salinity on the specific heat capacity of the feed stream is evaluated as a curve fit from the more detailed Pitzer model, at $T = 60\,^{\circ}\text{C}$:

$$c_{\text{p}} = 15.556\,m^2 - 241.78\,m + 4161.9 \tag{2.10}$$

where c_{p} is the specific heat capacity of the stream in J/kg-K and m is the molality of NaCl.

The baseline parameters for the simulations are given in Table 2.1.

2.3 Comparison of various control systems

Figure 2-2 shows two possible control systems for optimizing the performance of DCMD systems. Note that the balancing method presented in this study, does not

Table 2.1: Baseline values for validation test cases

S No	Variable	Value	Units
1	$T_{\mathrm{f,in}}$	85	°C
2	T_{amb}	25	°C
3	$\dot{m}_{\mathrm{f,in}}$	1	kg/s
4	sl_{in}	35	g/kg
5	L	6	m
6	w	12	m
7	$d_{\mathrm{f}}, d_{\mathrm{p}}$	0.001	m
8	B	1.0×10^{-6}	kg/m^2 s Pa
9	$k_{\mathrm{m,material}}$	0.2	W/m K
10	ϕ_{m}	0.8	-
11	δ_{m}	1.5×10^{-4}	m

involve measuring the top and bottom temperatures reducing the number of measurements required relative to earlier methods. Both these control systems as well as the simple method of setting MR=1 are compared to the numerically evaluated optimal operating condition.

Figure 2-3 shows that despite not measuring the system top and bottom temperatures, the current balancing method can account for variations in these two parameters. Changes in temperature lead to a change in flux and hence brine mass flow rate which is measured directly. Since mass flow rates are measured, changes in system top temperature can be handled by the proposed control system.

Compared to setting MR=1, GOR is improved significantly by using either of the two control systems (30–60%) (Fig. 2-4b). At very large lengths, the system based on Eq. 2.3 deviates from the maximum possible GOR, whereas the balancing of the heat capacity rates achieves almost exactly the same result as the numerical optimization.

The reason for the deviation of Lin et al. from the absolute maximum is the fact that heat conduction through the membrane is not accounted for when deriving Eq. 2.3. At larger module lengths, thermal efficiency (η, which is defined as the fraction of energy transfer across the membrane in the form of mass transfer) is lower since the temperature difference across the membrane is closer to the BPE of the feed

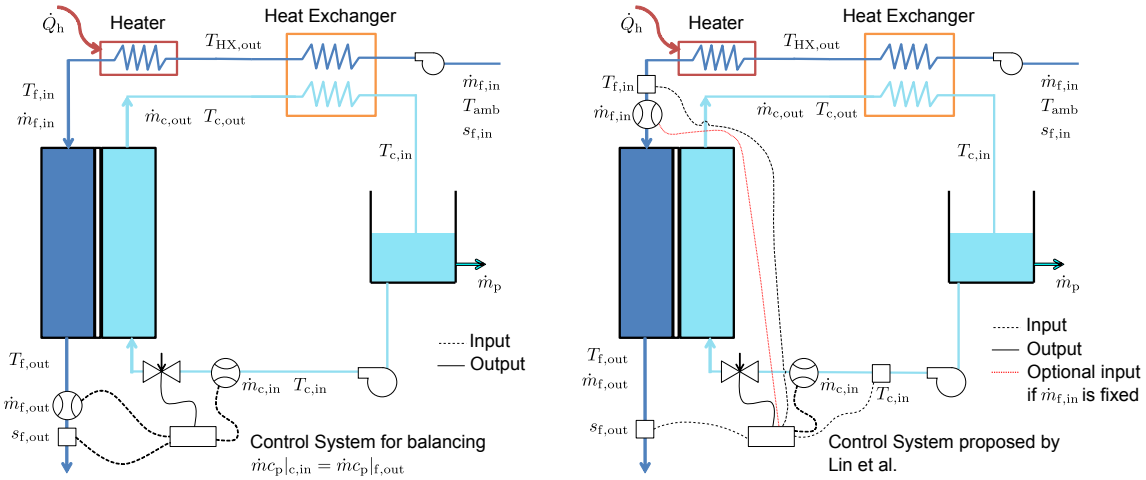

(a) Proposed control system to achieve HCR=1.

(b) Control system proposed in Lin et al. (Eq. 2.3).

Figure 2-2: Control systems proposed for DCMD GOR balancing.

stream.

The efficiency η can be expressed as a function of various system parameters [106] as:

$$\eta = \left(1 + \frac{k_m}{\delta_m B h_{fg}} \frac{1}{bAe^{bT_{avg}}\left(1 - \frac{BPE}{\Delta T_m}\right)}\right)^{-1} \tag{2.11}$$

where $A = 1054.8$ Pa and $b = 0.0479$ °C^{-1} are fitting parameters based on an exponential curve fit of vapor pressure as a function of temperature ($p_{vap} = Ae^{bT}$ between 25 °C and 85 °C), T_{avg} is an average temperature within the MD module, BPE is the boiling point elevation at the feed salinity and top temperature, ΔT_m is the temperature difference across the membrane, k_m is the thermal conductivity of the membrane, and B is the membrane permeability.

In order to illustrate that the present control system performs better at lower values of η, the systems are compared at different values of membrane material conductivity. At larger membrane material conductivity, the thermal efficiency (η) drops. Figure 2-5 shows that Eq. 2.3 deviates more from the maximum possible GOR at higher thermal conductivity of the membrane material and lower η.

Figure 2-6 shows the effect of various control systems over a range of feed salinities.

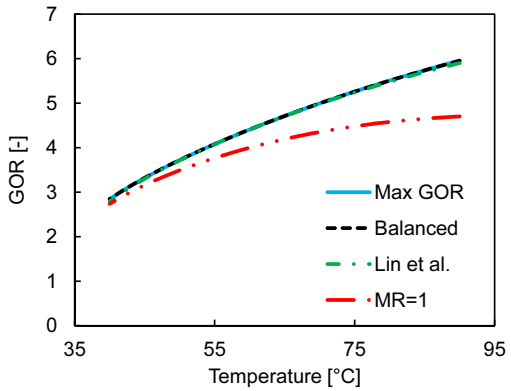

(a) Effect of balancing method on GOR. The curves for “Max GOR", “Balanced" and “Lin et al." coincide.

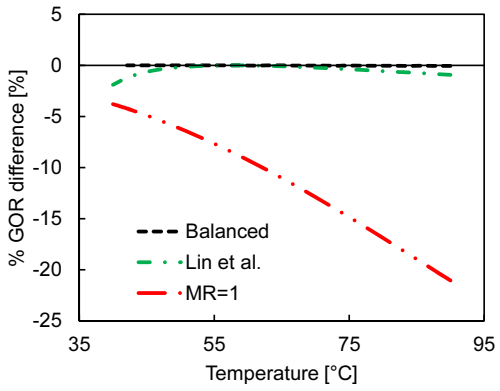

(b) Comparison of GOR from various balancing techniques with maximum GOR possible.

Figure 2-3: Comparison of balancing techniques at different system top temperature .

Here as well, at higher inlet salinity and correspondingly higher BPE and lower η, a system operating in accordance to , Eq. 2.3 deviates by up to 15% from the maximum GOR possible. The balancing method proposed in this work does not deviate from the maximum possible GOR until high salinities, and then only by 5%. This deviation is due to the large difference between the specific heat capacities of the two streams.

2.4 Real-time balancing

Using the proposed control system, dynamic balancing of DCMD can be achieved. This is similar to the dynamic optimization proposed for a humidification dehumidification (HDH) system with changes in operating conditions such as system top and bottom temperatures [16, 18]. The effect of dynamic balancing with changes in system top or bottom temperature is shown in Fig. 2-7a. Dynamic balancing refers to continuously measuring the flow rates of interest and maintaining a HCR value of 1. This is compared to the case of one-time or initial balancing at $T_{\mathrm{f,in}} = 85$ °C, $T_{\mathrm{c,in}} = 25$ °C and $s_{\mathrm{f,in}} = 35$ g/kg, where the HCR is equated to 1 under these operating conditions and the cold stream input flow rate is held constant at this value in spite of changes in system top and bottom temperatures or feed inlet salinity. In

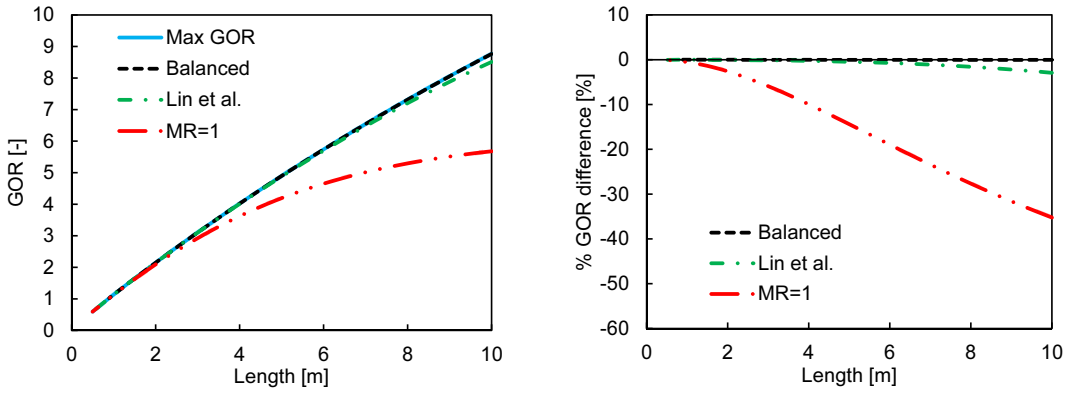

(a) Effect of balancing method on GOR. The curves for "Max GOR" and "Balanced" coincide.

(b) Comparison of GOR from various balancing techniques with maximum GOR possible.

Figure 2-4: Comparison of balancing techniques for systems of different sizes.

HDH, the effective specific heat capacity of the air stream is a non-linear function of temperature due to the exponential dependence of saturation vapor pressure on temperature. As a result, real-time balancing with changing system top or bottom temperature leads to up to 50–150% improvement in GOR.

In MD, real-time balancing has little benefit for changes in system bottom temperature and leads to about 5% increase in GOR for a 40 °C change in system top temperature, compared to initial balancing at the baseline conditions. This difference can be attributed to the higher effect of top temperature on MD performance compared to the bottom temperature due to the exponential nature of vapor pressure dependence on temperature. Since MD performance changes more significantly with top temperature, the effect of balancing is also more for a varying top temperature.

The bottom temperature is varied at a fixed top temperature of 85 °C in this analysis. In real systems, the heat input may be fixed allowing the top temperature to vary with changes in bottom temperature. Under this scenario, the overall effect of changes in bottom temperature could be more significant and real-time balancing may be more useful.

If the incoming feed water salinity was to vary over a wide range ($s_{f,in}$ = 35–200 g/kg), for example in a batch MD process with feed recirculation for achieving higher overall recovery ratio, real-time balancing leads to about 10–15% higher GOR than

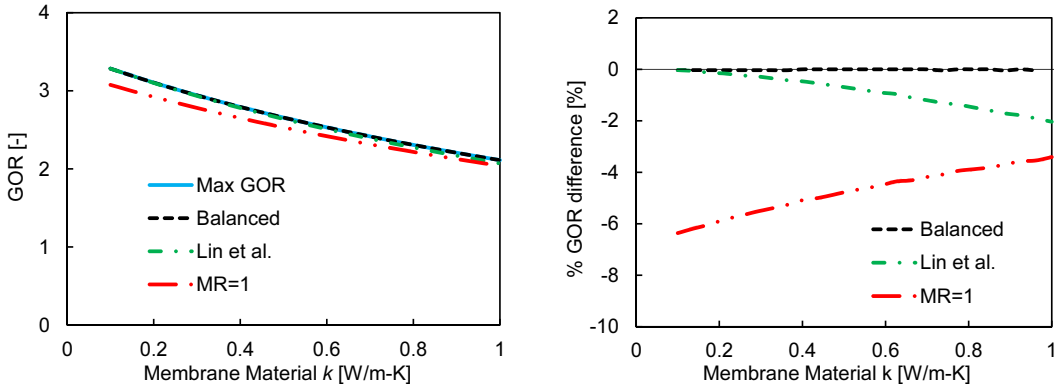

(a) Effect of balancing method on GOR. The curves for "Max GOR" and "Balanced" coincide.

(b) Comparison of GOR from various balancing techniques with maximum GOR possible.

Figure 2-5: Comparison of balancing techniques at various values of membrane material conductivity.

fixed MR or initial balancing (Fig. 2-7b), due to the more significant variation in specific heat capacity of water with salinity.

The results presented here do not account for any lag, measurement errors, or other dynamics of the control system. These factors should be considered in more detail when a control system is practically implemented.

2.5 Conclusions

1. Direct contact membrane distillation can be balanced by setting the heat capacity rate ratio to 1 at one end of the module. Optimization in real-time can be achieved using a simple control system that sets the cold stream inlet flow rate as a function of the feed exit flow rate and salinity as: $\dot{m}_{\mathrm{c,in}} = \dot{m}_{\mathrm{f,out}} \times \frac{c_{\mathrm{p}}^{\mathrm{f}}}{c_{\mathrm{p}}^{\mathrm{p}}}$.

2. Balancing leads to 20-50% higher GOR than a case with equal inlet flow rates.

3. The proposed balancing method results in a GOR very close to that of the absolute maximum GOR achievable, evaluated using numerical optimization. The GOR achieved by the proposed balancing method deviates from the absolute maximum GOR by about 5% at higher feed salinities due to larger difference

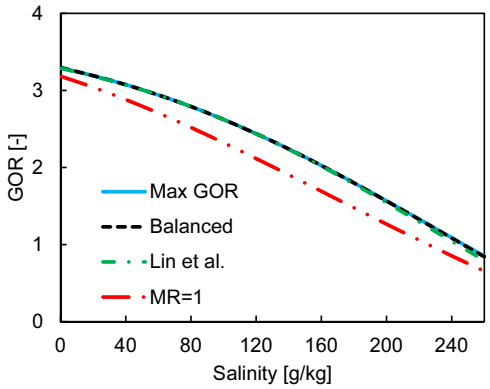

(a) Effect of balancing method on GOR.

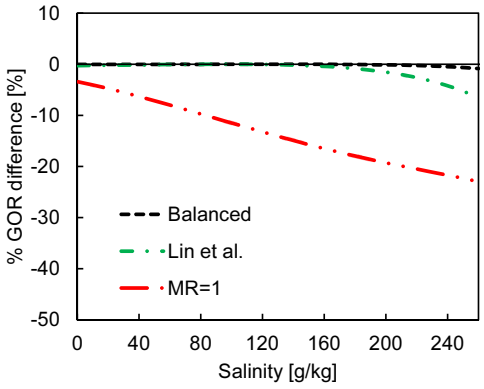

(b) Comparison of GOR from various balancing techniques with maximum GOR possible.

Figure 2-6: Comparison of balancing techniques with changes in feed salinity.

between $c_{\mathrm{p}}^{\mathrm{f}}$ and $c_{\mathrm{p}}^{\mathrm{c}}$.

4. Over a wide range of operating conditions, the ideal MR evaluated using the permeate limiting formula proposed by Lin et al. [64] results in a performance close to the absolute maximum value. Using their control system, GOR deviates from the maximum possible GOR for systems with low thermal efficiency. That condition occurs at large module length, higher membrane material thermal conductivity or lower permeability, or higher feed salinity.

5. Real-time balancing is most useful compared to one-time or initial balancing, when there are large variations in the feed salinity such as in the case of a batch recirculation system. It may be useful with large changes in system top temperature but will be relatively unimportant for changes in bottom temperature at fixed top temperature.

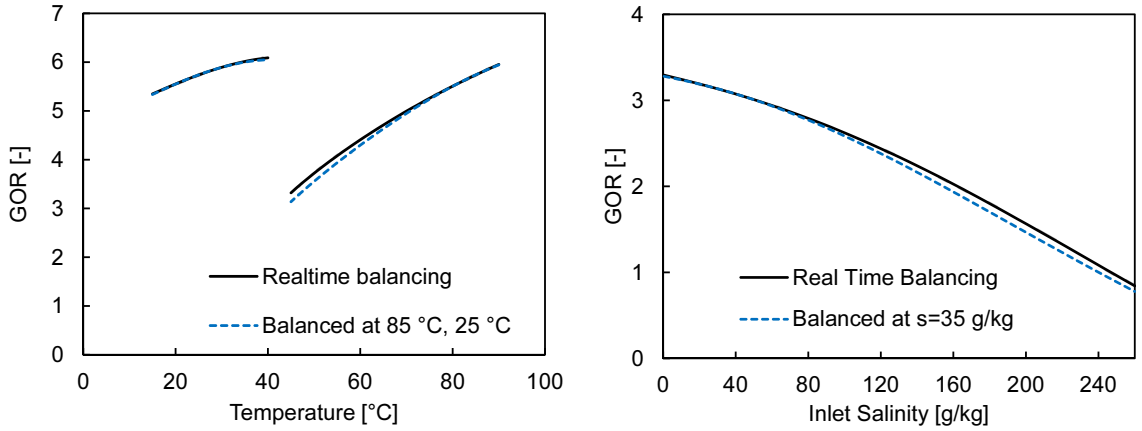

(a) Effect of real-time balancing with changes in system top and bottom temperatures.

(b) Effect of real-time balancing on GOR with changes in inlet salinity.

Figure 2-7: Effect of dynamic balancing with changes in inlet salinity, top and bottom temperatures.

Chapter 3

Energy Efficiency of Permeate Gap and Novel Conductive Gap Membrane Distillation

Abstract

This work presents numerical modeling results and flux experiments for a novel membrane distillation configuration called conductive gap membrane distillation (CGMD), as well as permeate gap membrane distillation (PGMD). CGMD has a conductive spacer in the gap between the membrane and condensing surface rather than more commonly used insulating materials. Flux measurements with two experimental systems are used to validate the numerical models for PGMD and CGMD. PGMD has 20% higher GOR (energy efficiency) than an air gap membrane distillation (AGMD) system of the same size, whereas CGMD can have two times higher GOR than even PGMD. Increasing gap effective thermal conductivity in CGMD has negligible benefits beyond $k_{\text{gap}} \approx 10$ W/m·K under the conditions of this study. The direction of pure water flow in the gap has a significant influence on overall system energy efficiency, especially in the case of CGMD. Using a countercurrent configuration for the pure water flow in the gap relative to the cold stream leads to 40% higher GOR than flow cocurrent with the cold water stream.

The contents of this chapter are adapted from [103].

3.1 Introduction

3.1.1 Permeate Gap Membrane Distillation

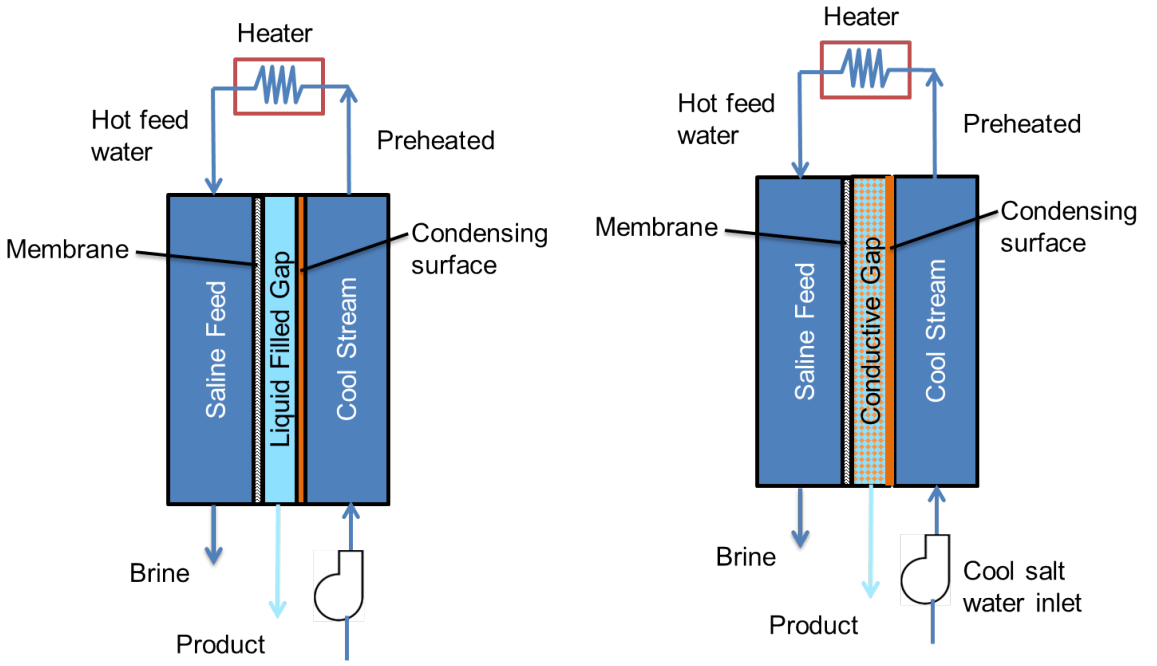

(a) Permeate Gap Membrane Distillation

(b) Conductive Gap Membrane Distillation proposed as a modification of PGMD

Figure 3-1: MD configurations analyzed in this study

Permeate Gap MD is also referred to as Water Gap and Liquid Gap MD. Simply, it can be understood as a modification of AGMD where the gap between the membrane and the condensing surface is filled with permeate water (Fig. 3-1a). PGMD has shown improved fluxes compared to AGMD [21, 118, 121] as have other modifications such as material gap MD systems with sand added to the gap [37]. A clear comparison of GOR between AGMD and PGMD has not been established, though commercial spiral wound PGMD modules have achieved higher GOR . Winter et al. [127] suggested PGMD as a modification of DCMD with internal heat recovery by separation of the distillate from the coolant. Therefore the coolant can be any other liquid, such as incoming feed water. They note that "The presence of the distillate channel reduces sensible heat losses due to an additional heat transfer resistance. An additional effect is the reduction of the effective temperature difference across

the membrane, which slightly lowers the permeation rate." PGMD can therefore be intuitively placed between AGMD and DCMD with intermediate thermal resistance of the gap, thereby having lower sensible heat transfer to the permeate as compared to DCMD, but perhaps more heat loss than AGMD. A hollow fiber MD system in PGMD configuration was experimentally analyzed by Singh et al. [93], where the condensate from one AGMD module was passed into another module. Singh et al. note that the second module would perform between AGMD and DCMD when the gaps are filled with condensate. Hollow fiber systems with high packing density may also lead to much lower effective gap sizes [19] and sections of the module may have pure water extending across the narrow gaps between membrane and non-porous fibers. While the focus of the present work is on modeling flat sheet and similar spiral-wound MD systems, the overall trends are applicable to hollow fiber MD systems as well.

3.1.2 Conductive Gap Membrane Distillation

Conductive gap MD (CGMD) is suggested as a novel MD configuration (Fig. 3-1b). In CGMD, the overall thermal conductance of the gap is increased. One way of achieving this is to insert a high conductivity material (such as a metal mesh) into the gap of a PGMD system. Increasing the conductivity of the gap in hollow fiber MD systems by inserting high conductivity materials was suggested by Ma et al. [65] in 2010. This is in contrast to other systems proposed in the literature such as material gap MD where low conductivity materials such as sand were added to the gap region [37]. This also contradicts the conventional wisdom and the historical development in the field towards developing MD configurations with lower sensible heat loss than DCMD [12], such as the the evolution from DCMD to AGMD or PGMD. Possible implementations involve using a metal spacer instead of a plastic spacer, or implementing fins on the conductive surface extending up to the membrane to increase the net conductivity of the gap. The gap is filled with pure water, similar to the PGMD system. Vapor would condense immediately as it leaves the membrane. The energy is conducted through the gap into the cold stream, preheating it. While this configuration may have a higher sensible heat loss than even PGMD, perhaps close to that of a DCMD

system, for a given membrane area and feed flow rate, it rejects brine at a lower temperature and correspondingly achieves higher preheating of the cold stream. This could therefore result in a higher overall GOR.

In this study, we use numerical modeling to investigate the energy efficiency of PGMD and CGMD systems. The results are compared to previously published results for other conventional MD configurations under the same operating conditions. The effect of pure water flow direction in the gap is evaluated. The effect of gap conductivity and membrane material conductivity on GOR is studied.

3.2 Numerical Modeling

3.2.1 Review

Several MD models with varying degrees of complexity have been developed to understand the effect of system parameters on flux [2, 25]. Fewer, however, have analyzed energy efficiency [15, 64, 135]. The modeling approach followed in this paper is very similar to that found in Summers et al. [98]. As a result, only the new features of the modeling are discussed in detail.

A one-dimensional model of the MD modules is studied, where properties vary along the length of the module, but are constant along the width (direction into the page). In the depth direction, property variations due to transport processes are evaluated by considering the temperature and concentration boundary layers. The bulk properties of the fluids are assumed equal to the value at the fluid interior; the boundary layers are assumed to be thin, but not negligible. Mass, and energy conservation equations are solved for each computational cell coupled with property evaluations performed using built-in functions on Engineering Equation Solver (EES) [53].

The overall computational cell is shown in Fig. 3-2.

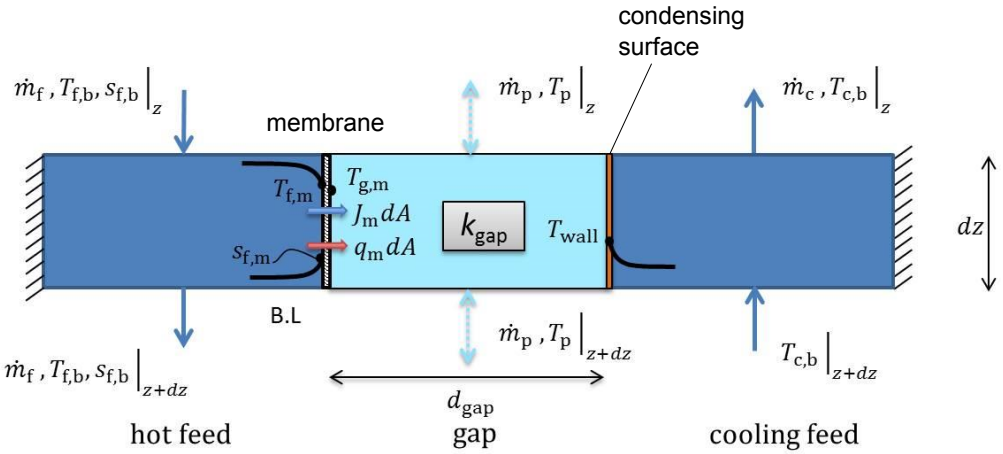

Figure 3-2: PGMD computational cell

3.2.2 Feed Channel

Modeling of the feed channel is common to both configurations. A concentration boundary layer is incorporated into the feed channel model to account for desalination of salt water and capture second order effects associated with salinity of the feed. The film model of concentration polarization (Eq. 3.1) is used to relate the salt concentrations at the membrane interface ($c_{f,m}$) to the bulk concentration ($c_{f,b}$), effective mass transfer coefficient (k) in the channel and vapor flux thorough the membrane (J):

$$\frac{c_{f,m}}{c_{f,b}} = \exp\left(\frac{J}{\rho_f k_{mass}}\right) \tag{3.1}$$

The effect of dissolved salt on the vapor pressure of water is captured using Raoult's law (Eq. 3.2):

$$p_{f,m}^{vap} = P_{sat}\left(T_{f,m}\right) \times \left(1 - \frac{\frac{2c_{f,m}}{MW_{solute}}}{\frac{2c_{f,m}}{MW_{solute}} + \frac{1000 - c_{f,m}}{MW_{water}}}\right) \tag{3.2}$$

The difference in vapor pressure across the membrane is the driving force for water vapor transfer as shown in Fig. 3-2. The effect of salt content on the enthalpy of the

feed solution is not modeled in detail since we are focusing on low salinity conditions where these secondary effects are negligible. The effect of salt on other thermophysical properties of the streams is not modeled. At close to seawater salinities considered in this study, the reduction in vapor pressure is the only thermally significant effect.

The flux through the membrane is calculated locally from the vapor pressure difference and the membrane permeability coefficient, B:

$$J = B \times \left(p_{\mathrm{f,m}}^{\mathrm{vap}} - p_{\mathrm{g,m}}^{\mathrm{vap}}\right) \tag{3.3}$$

3.2.3 Gap

The region between the membrane and the condensing surface will be referred to as the gap. For air gap Summers et al. [98] presented a vapor diffusion with air counter diffusion model. For PGMD and CGMD, similar to the case of DCMD, vapor condenses immediately upon exiting the membrane pores into a stream of pure water. From here, the heat is convected across the gap into the condensing surface. In this study, the water flow rate is assumed to be relatively low and hence energy transfer across the gap is approximated by conduction across the gap (3.4):

$$\dot{q}_{\mathrm{gap}} = \frac{k_{\mathrm{gap}}}{d_{\mathrm{gap}}} \times \left(T_{\mathrm{g,m}} - T_{\mathrm{w}}\right) \tag{3.4}$$

Depending on the direction of water flow in the gap, $\dot{q}_{\mathrm{gap}}$ would be different. In the case of crossflow configuration, the water produced at any given location along the length would flow perpendicularly out of the module (in this case, into or out of the plane of the paper, as shown in Fig. 3-4). On the other hand, the flow can also be countercurrent to the cold stream or parallel to the flow stream. The corresponding equations for cell number n are given below (cell number 1 at the hot side):

$$\begin{aligned}
\dot{q}_{\mathrm{gap,cross}}^{n} &= J^{n} h_v\left(T_{\mathrm{f,m}}^{n}\right) + q_{\mathrm{m}}^{n} - J^{n} h_l\left(T_{\mathrm{p}}^{n}\right) \\
\dot{q}_{\mathrm{gap,countercurrent}}^{n} &= J^{n} h_v\left(T_{\mathrm{f,m}}^{n}\right) + q_{\mathrm{m}}^{n} + \left[\dot{m}_{\mathrm{p}}^{n-1} h_l\left(T_{\mathrm{p}}^{n-1}\right) - \dot{m}_{\mathrm{p}}^{n} h_l\left(T_{\mathrm{p}}^{n}\right)\right]/dA \\
\dot{q}_{\mathrm{gap,parallel}}^{n} &= J^{n} h_v\left(T_{\mathrm{f,m}}^{n}\right) + q_{\mathrm{m}}^{n} + \left[\dot{m}_{\mathrm{p}}^{n+1} h_l\left(T_{\mathrm{p}}^{n+1}\right) - \dot{m}_{\mathrm{p}}^{n} h_l\left(T_{\mathrm{p}}^{n}\right)\right]/dA
\end{aligned} \tag{3.5}$$

In the case of PGMD, the gap is filled with water with some plastic spacers often used to support the membrane. On the other hand, in the case of conductive gap MD, conductive materials are used to enhance the conductivity of the region. The effective thermal conductivity of this gap (k_{gap}) would therefore be a function of the conductivities of water and additional material in the gap as well porosity and geometry of the region. In this study, $k_{\text{gap}} = 0.6$ W/m-K is used for PGMD and $k_{\text{gap}} = 10$ W/m-K is used for reporting CGMD results.

The baseline conditions for the numerical model are shown in Table 3.1.

Table 3.1: Baseline values of parameters

No.	Variable	Value	Units
1	$T_{\text{f,in}}$	85	°C
2	$T_{\text{c,in}}$	25	°C
3	$\dot{m}_{\text{f,in}}$	1	kg/s
4	$c_{\text{f,in}}$	35	ppt
5	L	6	m
6	w	12	m
7	$d_{\text{f}}, d_{\text{c}}$	0.001	m
8	d_{gap}	0.001	m
9	k_{gap}(PGMD)	0.6	W/m-K
10	k_{gap}(CGMD)	10	W/m-K
11	B	16×10^{-7}	kg/m^2 s Pa
12	δ_{m}	93.75	μm

3.3 Validation

The numerical modeling framework presented above has been validated for AGMD and DCMD in the past [98]. PGMD experiments were carried out using the AGMD apparatus described in detail elsewhere [102]. The apparatus was used to study PGMD by collecting water from the top, hydrostatically forcing the gap region to be flooded with pure water. Experiments were conducted at different values of $T_{\text{f,in}}(40, 50, 60, 70\,^{\circ}\text{C})$ and $T_{\text{c,in}}(17, 20, 25\,^{\circ}\text{C})$. For the numerical model predictions,

an effective gap conductivity of $k_{\text{gap}} = 0.6$ W/m-K and effective gap thickness of 1 mm were used. Under similar conditions compared to PGMD, the flux for AGMD is about 20% lower at higher $T_{\text{f,in}}$ and more than 50% lower at lower temperatures. This result is comparable to results in the literature that show that flux for liquid gap MD is higher than that of AGMD. The magnitude of improvement in this study may be smaller since a smaller gap thickness is used, resulting in lower resistance in the case of AGMD.

The results comparing the numerical modeling predictions against the experimental results are shown in Fig. 3-3a. Each set of three data points corresponds to one value of hot side temperature.

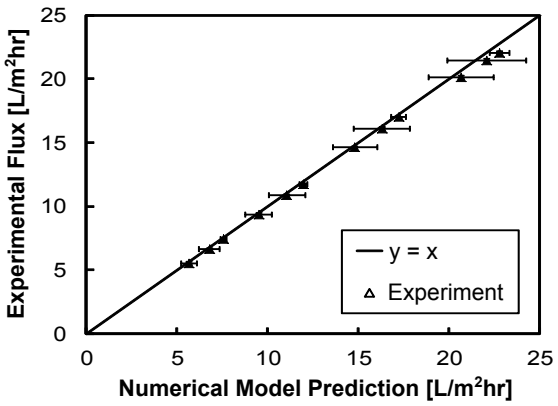

(a) Experimental flux compared with numerical modeling results. $T_{\text{f,in}} = 40, 50, 60, 70\,^{\circ}\text{C}$, $T_{\text{c,in}} = 17, 20, 25\,^{\circ}\text{C}$

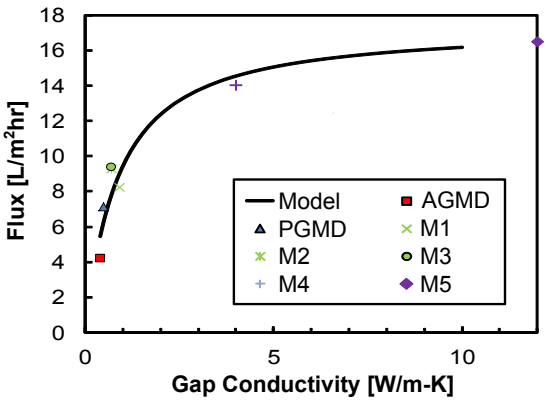

(b) Experimental flux measurements at different values of gap conductivity

Figure 3-3: Model validation with experimental flux measurements

Further validation of the model for the effect of gap conductivity in CGMD configuration was carried out using a modified Sterlitech apparatus described in [3] and the results are shown in Fig. 3-3b. In the figure, M1 to M5 correspond to different types of metal meshes used in the gap which is about 2-4 mm thick. M1 to M3 are woven aluminum mesh spacers (McMaster-Carr part numbers 9227T53, 9227T56, 9227T57). M4 is a porous Duocel Aluminum material (ERGAerospace part number 6101-T6) hammered down to half its thickness and covered by a thin brass mesh to protect the membrane. M5 is a specially manufactured copper plate with fins. The

gap conductivity in the case of M5 is likely to be much higher, but since the increase in flux is negligible at higher conductivities, the point is plotted at the edge of the plot.

These results are also in overall agreement with flux results presented by Francis et al. [37] on material gap MD configurations. With the introduction of sand that has lower thermal conductivity than water, the flux was found to be lower than with only water in the gap. The opposite effect is observed in terms of flux for CGMD.

In order to validate the model for a larger system with energy recovery, data from spiral wound module analysis reported in [127] is used. The current model was run at the following conditions to compare with reported results: ($B = 16 \times 10^{-7}\,\mathrm{kg/m^2 \cdot s \cdot Pa}$, $k_\mathrm{m} = 0.25\,\mathrm{W/m \cdot K}$, $\delta_\mathrm{m} = 70\,\mu\mathrm{m}$, $L = 7\,\mathrm{m}$, $w = 0.7\,\mathrm{m}$, $d_\mathrm{ch} = 3.2\,\mathrm{mm}$, feed flow inlet rate = 0.04166 kg/s, permeate flow in counterflow direction, $k_\mathrm{gap} = 0.5\,\mathrm{W/m \cdot K}$ (for water and a plastic spacer), $d_\mathrm{gap} = 1\,\mathrm{mm}$, $T_\mathrm{f,in} = 80\,^\circ\mathrm{C}$, $T_\mathrm{c,in} = 25\,^\circ\mathrm{C}$). The predicted specific thermal energy consumption is 158 $\mathrm{kWh/m^3}$, and the flux is 1.76 LMH. The values reported in [127] for the same operating conditions are specific thermal energy consumption of 150–160 $\mathrm{kWh/m^3}$ and a flux of about 1.5–1.6 LMH. The membrane permeability value, as well as the gap conditions were not available and were assumed. Also, the model does not account for heat loss to the environment.

3.4 Results and Discussion

3.4.1 GOR comparison, Effect of gap flow

The configuration of pure water flow in the gap can affect the performance of a PGMD or CGMD system. Figure 3-4 shows the different options for pure water flow in the gap. On the left, pure water in the gap flows countercurrent to the coolant fluid across the condensing plate. The opposite gap configuration is to have the pure water flow parallel to the coolant stream, as seen on the right. An intermediate design (middle) may be that of perpendicular or crossflow, where water flows in a direction

perpendicular to that of cold water flow and leaves the module at several positions along the length of the module.

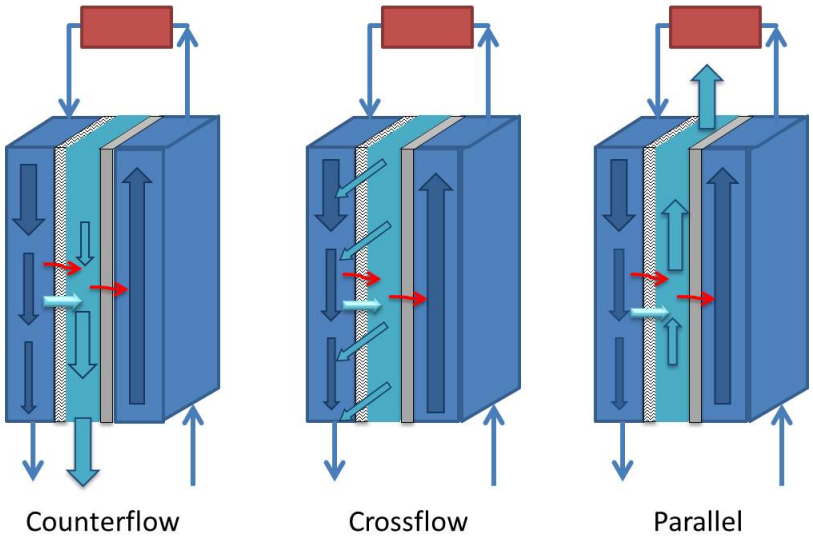

Figure 3-4: Illustration of various flow configurations in the gap region

The system with gap flow countercurrent to the cold stream (left) is likely to have the highest energy efficiency since the pure water would leave the system close to the cold stream inlet temperature; this is similar to the well-known behavior of a counterflow heat exchanger. On the other hand, the parallel configuration (right) would be rejecting a warm pure water stream close to the top temperature. Even though the amount of water released is less than 8% of the feed stream, it can still have a detrimental effect on energy efficiency. The perpendicular configuration is likely to lie in between, since water is released both at warmer temperatures and cooler temperatures, and hence on average the stream is going to be of intermediate temperature.

The effect of length on GOR is shown for all three flow orientations in Fig. 3-5. The GOR trend is as expected. At $L = 5$ m, the GOR differs by about 1 between parallel and perpendicular and between perpendicular and countercurrent for CGMD systems (Fig. 3-5a). The trend is similar for PGMD systems, but the difference in magnitude of GOR differences is much smaller at about 0.2. The flux at $L = 5$ m, is 5.8 L/m^2-hr for PGMD and 6.6 L/m^2-hr for CGMD in countercurrent configuration.

The higher GOR observed at larger membrane areas is accompanied by a lower flux, which is similar to the trade-off observed for DCMD systems by Gilron et al. [43]. As a result, operating at very high GOR may not be optimal.

Comparing the graphs with data from [98] for AGMD, DCMD and VMD systems over the same operating conditions, GOR of PGMD is about 20% higher than that of AGMD across the range of lengths. The GOR of CGMD in turn is about two times higher than that of PGMD.

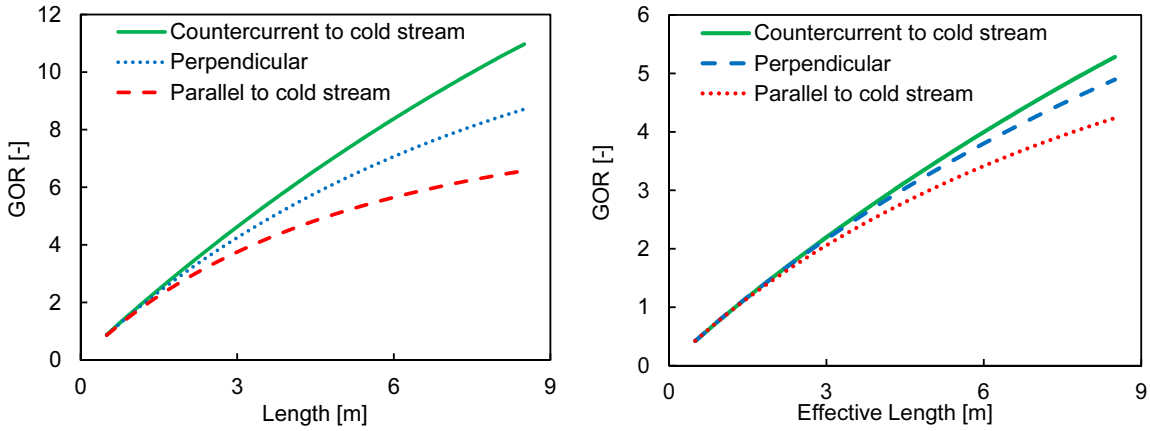

(a) Effect of gap flow direction on CGMD (b) Effect of gap flow direction on PGMD

Figure 3-5: Effect of gap flow direction and system length. Other parameters set at baseline values (Table 3.1).

Figure 3-6a shows the bulk stream temperature profiles within the module for the three different flow orientations when $L = 5$ m. The temperature profiles are more straight for the counterflow case than the crossflow and parallel arrangements. The cold stream leaves at a higher temperature in the case of the counterflow configuration. This means that better preheating is achieved and hence less heat will be added from the heater, contributing to a higher GOR. Figure 3-6b shows the driving temperature difference between the hot and cold stream bulk temperatures along the length of the module. Interestingly, in counterflow design, the pinch point temperature difference occurs at the hot side, leading to lower external heat input, whereas in both the other configurations, the pinch point occurs at the cold end. The driving force is also relatively more constant in the counterflow design, contributing to lower entropy generation within the module and better overall energy efficiency [113].

All subsequent results and discussions will focus on the counterflow configuration. The trends will be relatively similar for other flow configurations as well.

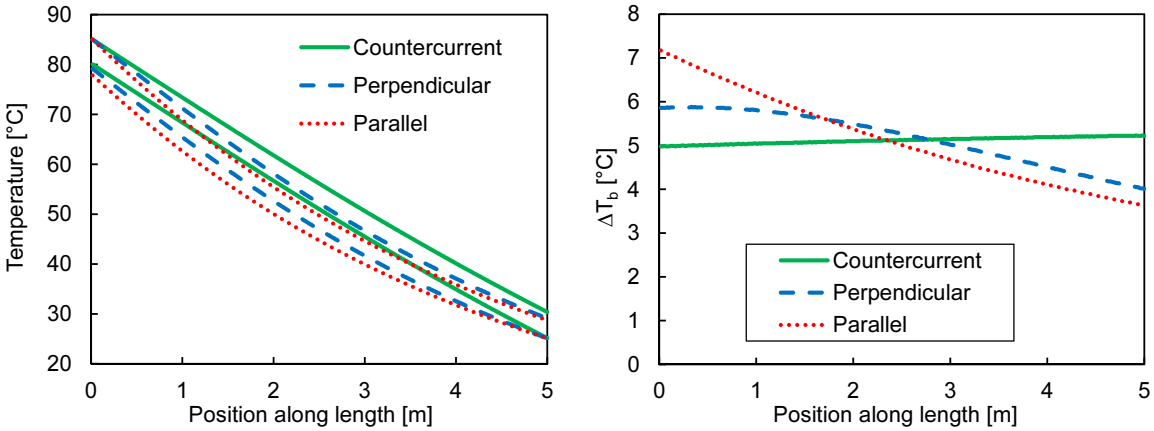

(a) Hot and cold side bulk temperature profiles for different flow configurations

(b) Temperature difference between the streams along the module

Figure 3-6: Effect of gap flow direction on temperature profile in CGMD. Other parameters set at baseline values (Table 3.1).

3.4.2 Effect of Gap Thermal Conductivity

Figure 3-7 shows the effect of gap conductivity on GOR. k_{gap} is varied over a range of 0.5 W/m-K to more than 30 W/m-K. At lower k_{gap}, an increase in the conductivity leads to significant improvements in GOR (Fig. 3-7) whereas beyond about $k_{\text{gap}} = 10$ W/m-K, increase in conductivity doesn't result in much further improvement.

The results shown in Fig. 3-7 are also applicable for analyzing PGMD with smaller gap as can be easily achieved by using a thinner spacer or packing the fibers more densely in the case of hollow fiber system. The effect of reducing the gap thickness is similar to that of increasing the conductivity of the gap. From Eq. 3.4, we see that the parameter of interest is the gap conductance given by $k_{\text{gap}}/\delta_{\text{gap}}$. At higher gap conductivity or lower gap thickness the system would start behaving closer to CGMD. The value of gap conductance corresponding to a $k_{\text{gap}} = 10$ W/m-K as used in this study is 10000 W/m^2-K. To achieve a similar conductance with a permeate gap system, the gap thickness would have to be 60 μm.

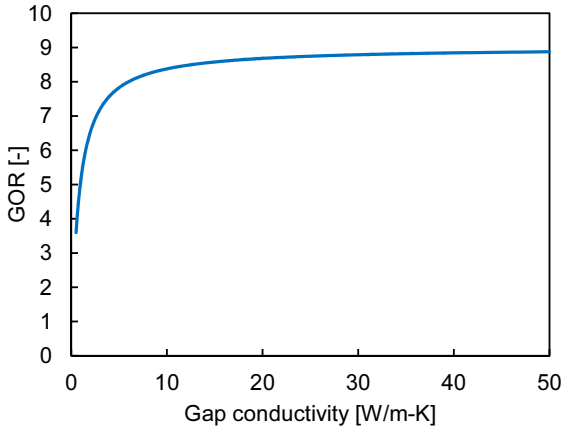

Figure 3-7: Energy efficiency as a function of gap conductivity = 0.5–30 W/m·K. Other parameters set at baseline values (Table 3.1).

Figure 3-8 illustrates the effect of k_{gap} on $\dot{m}_{\text{p}}$ and $\dot{Q}_{\text{h}}$. $\dot{m}_{\text{p}}$ increases and $\dot{Q}_{\text{h}}$ decreases, both leading to an improvement in GOR. Among the two, the increase in $\dot{m}_{\text{p}}$ is about 15% whereas the decrease in $\dot{Q}_{\text{h}}$ is around 60%. Together, both of these effects result in the nearly 100% higher GOR for CGMD compared to PGMD, as k_{gap} increases from about 0.6 to 10 W/m-K.

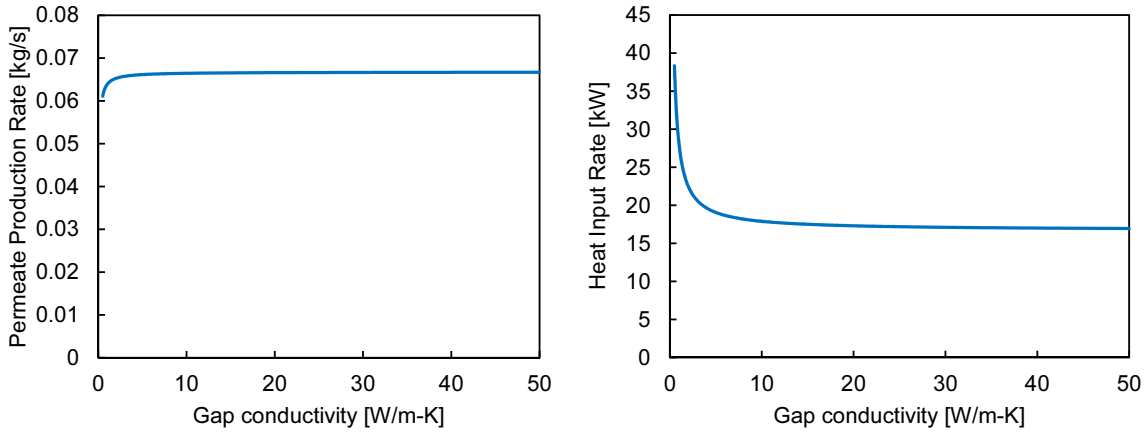

(a) Water production

(b) Heat input

Figure 3-8: Effect of gap conductivity on permeate production and heat input rate. Other parameters set at baseline values (Table 3.1).

The temperature profiles within the modules are illustrated in Fig. 3-9 and help explain the results physically. For PGMD, a relatively large difference in temperature is observed between the membrane surface and the condensation plate. As a result,

there is a smaller temperature difference across the membrane leading to lesser pure water production, even though the overall pinch point temperature difference between the bulk streams is much larger compared to the profile for CGMD. On the other hand, since the pinch point temperature difference is smaller in CGMD, lesser external energy supply was required too.

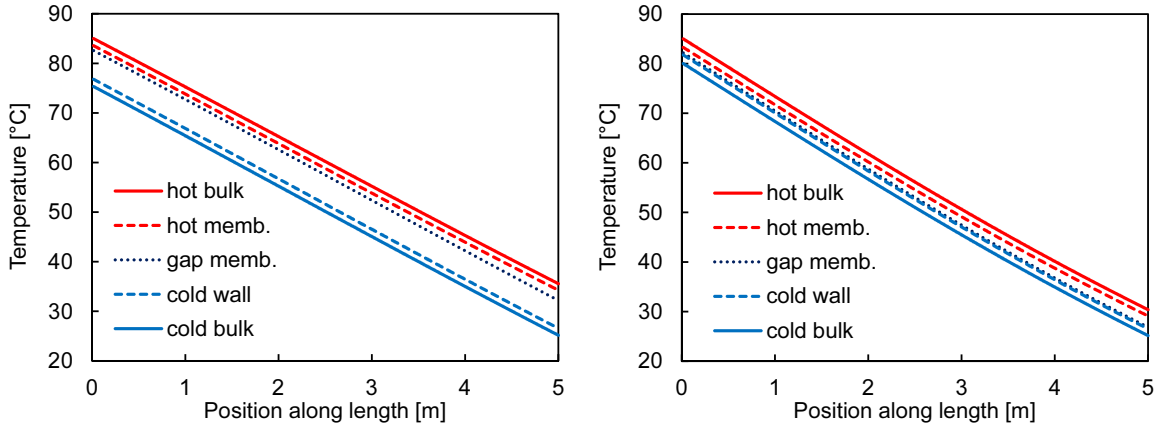

(a) PGMD (b) CGMD

Figure 3-9: Temperature profiles in PGMD and CGMD systems. Simulation parameters set at baseline values (Table 3.1).

3.5 Conclusions

1. Numerical modeling shows that PGMD systems have higher GOR than AGMD. The proposed CGMD configuration with a high thermal conductivity gap has two times higher GOR than even PGMD.

2. Pure water flow in the gap countercurrent to the cold stream leads to highest energy efficiency followed in order of efficiency by crossflow and parallel configurations.

3. An increase in gap conductivity improves permeate production and GOR, with diminishing returns beyond $k \approx 10$ W/m-K in the cases considered here.

4. The main reason for improved GOR of CGMD is better energy recovery into the cold stream within the MD module.

Acknowledgments

The authors would like to thank MIT undergraduate students Ann M. Huston and Grace Connors for their help in preparing the manuscript and setting up the experiments.

Chapter 4

Membrane distillation model based on heat exchanger theory and configuration comparison

Abstract

Improving the energy efficiency of membrane distillation (MD) is essential for its widespread adoption for renewable energy driven desalination systems. Here, an energy efficiency framework for membrane distillation modules is developed based on heat exchanger theory, and with this an accurate but vastly simplified numerical model for MD efficiency and flux is derived. This heat exchanger analogy shows that membrane distillation systems may be characterized using non-dimensional parameters from counter-flow heat exchanger (HX) theory such as effectiveness (ε) and number of transfer units (NTU). Along with the commonly used MD thermal efficiency (η), "MD effectiveness" ε should be used to understand the energy efficiency (measured as gained output ratio, GOR) and water vapor flux of single stage membrane distillation systems. GOR increases linearly with η (due to decreasing conduction losses), but increases more rapidly with an increase in ε (better heat recovery). Using the proposed theoretical framework, the performance of different single stage MD configurations is compared for seawater desalination. The gap between the membrane and the condensing surface constitutes the major resistance in both air gap (AGMD) and permeate gap (PGMD) systems (75% of the total in AGMD and 50% in PGMD). Reducing the gap resistance by increasing gap conductance (conductive gap MD (CGMD)), leads to an increase in ε through an increase in NTU, and only a small decrease in η, resulting in about two times higher overall GOR. GOR of direct contact MD (DCMD) is limited by the size of the external heat exchanger, and can be as high as that of CGMD only if the heat exchanger area is about 7 times larger

than the membrane. While MD membrane design should focus on increasing the membrane's permeability and reducing its conductance to achieve higher η, module design for seawater desalination should focus on increasing ε by reducing the major resistance to heat transfer. A simplified model to predict system GOR and water vapor flux of PGMD, CGMD and DCMD, without employing finite difference discretization, is presented. Computationally, the simplified HX model is several orders of magnitude faster than full numerical models and the results from the simplified model are within 11% of the results from more detailed simulations over a wide range of operating conditions.

The contents of this chapter are adapted from [106].

4.1 Introduction

4.1.1 Chapter outline

In Section 4.1, existing membrane distillation efficiency parameters such as energy efficiency or gained output ratio (GOR), η (MD thermal efficiency), and flux (J) are reviewed. The finite difference numerical model used in this study is reviewed.

Effectiveness (ε) is introduced in Section 4.2 as an additional useful parameter to understand MD energetic performance. The energy efficiency of single stage MD systems with internal heat recovery is derived in terms of η and ε. Using this expression, an upper limit for MD's GOR is evaluated and compared to the thermodynamic limit for a generic thermal desalination system.

The literature has mostly focused on the importance of reducing conduction losses through the membrane (increasing η). In Section 4.3, the relatively higher importance of achieving better heat recovery within the module (or higher effectiveness ε) is illustrated. The theory developed in the previous sections is used to understand the trend of increasing GOR observed in PGMD and CGMD with improving gap conductance, for desalination of seawater.

In Section 4.4, the GOR of DCMD is derived in terms of η and ε and the properties of the external heat exchanger, to enable comparison with other configurations with internal heat regeneration. The inherent disadvantage of using an additional external heat exchanger in DCMD is quantified through the $\mathrm{TTD}_{\mathrm{factor}}$. This parameter is

a function of the terminal temperature difference (TTD) of the MD and the heat exchanger (HX). The GOR of DCMD is lower than that of CGMD when the external heat exchanger area is equal to the membrane area. If the relative size of the heat exchanger is increased, DCMD performance approaches and eventually marginally exceeds that of CGMD.

In Section 4.5, the magnitude of the various internal heat transfer resistances are compared for the various configurations. The gap between the membrane and the condensing surface constitutes the major resistance in AGMD and PGMD, whereas the flow channel and the membrane resistances are important in the case of DCMD and CGMD. Using this framework, the effects of increasing membrane permeability and flow channel heat transfer coefficients are analyzed.

Finally, in Section 4.6, a simplified model for evaluating the performance of PGMD and CGMD systems without employing finite-difference or other discretization techniques is presented. The model is inspired by the ε-NTU (number of transfer units) method for heat exchangers, recognizing the similarity between a well-designed MD system and a counter-flow heat exchanger. ε and η are rewritten in terms of the effective transport resistances within the MD module, and so the GOR and flux of an MD system can be evaluated given the geometrical parameters of the system and the input conditions such as feed flow rate and heater outlet temperature. This simplified model is intuitive and computationally orders of magnitude faster than discretization based methods, while producing results within 10% of the more complicated models over a wide range of operating conditions.

4.1.2 MD efficiency parameters

MD thermal energy efficiency is expressed as a gained output ratio (GOR). A higher GOR indicates lower thermal energy consumption. While thermal energy constitutes the major part of the cost of water from MD, capital costs may also be significant. The performance parameter relevant to capital cost is the flux of water through the membrane, which quantifies the membrane productivity. Higher flux results in lower capital cost of the MD process. Some of these existing efficiency metrics for MD are

reviewed in this section.

Gained output ratio

The overall system energy efficiency is measured as a non-dimensional parameter, gained output ratio (GOR):

$$\mathrm{GOR} = \frac{\dot{m}_\mathrm{p} h_\mathrm{fg}}{\dot{Q}_\mathrm{h}} \tag{4.1}$$

where $\dot{m}_\mathrm{p}$ is the rate of permeate production, h_fg is the enthalpy of evaporation and $\dot{Q}_\mathrm{h}$ is the power input in the heater. GOR is the inverse of specific thermal energy consumption times the enthalpy of vaporization of water. A higher value of GOR corresponds to a lower thermal energy consumption per unit mass of distillate. A value of 1 corresponds to a system with no losses and no condensation energy recovery. In practice, multiple energy losses occur, such as the disposal of hot brine or heat conduction through the walls of the system, and so a system without condensation energy recovery would have GOR much lower than 1. In contrast, large scale thermal desalination plants such as multi-stage flash and multi-effect distillation systems may have GOR of about 10.

A large majority of membrane distillation studies have been performed on a small scale without energy recovery, and hence do not discuss GOR. Summers and Lienhard [100] performed a detailed analysis to scale AGMD performance as a function of system size. Summers et al. [98] reported GOR of AGMD and DCMD systems of about 5-6 based on numerical modeling. They showed that GOR increases with an increase in channel heat transfer coefficient, membrane area, top temperature or bottom temperature. At larger specific membrane area $\left(= \frac{A}{\dot{m}_\mathrm{f}}\right)$, Summers et al. found that AGMD achieves the highest GOR, whereas at lower areas, DCMD achieves higher GOR. This result was based on a fixed external heat exchanger TTD=3 °C for the DCMD module. The feed and cold stream input flow rates were also set to be equal in this study, and hence there is scope for improvement by balancing the DCMD operation.

Zuo et al. [135] analyzed the GOR and cost of a cross-flow hollow fiber DCMD

module. Gilron et al. [43] analyzed a cascade of cross-flow DCMD modules, where increasing the number of stages is similar to increasing the length of a flat sheet countercurrent MD system. A GOR of about 9.5 was reported for an 11-stage system with a top temperature of 95 °C. Lin et al. [64] report the specific thermal energy consumption of DCMD as a function of MR (ratio of distillate and feed input mass flow rates) and membrane permeability. Over the range of membrane permeability considered, they found that the maximum GOR varies from about 1.5–10.

He et al. [49] and Geng et al. [40] have reported high experimental values for GOR for hollow fiber AGMD. The maximum GOR reported in [40] is 8.8 at hot and cold temperatures of 90 and 40 °C and feed NaCl salinity of 35 g/kg.

Zaragoza et al. [133] compared the performance of several commercial MD modules in permeate gap, air gap and multi-effect vacuum configurations. While multi-effect vacuum MD achieved much higher recovery ratio, spiral wound single stage systems achieved the highest energy efficiency and similar permeate flux as the multi-effect system.

Flux

Pure water flux J, often measured in L/m^2 h or LMH is the subject of significant investigation in the membrane distillation literature. Flux can be expressed as:

$$J = \frac{\dot{m}_{\mathrm{p}}}{A} \times 3600 \left[\frac{\mathrm{s}}{\mathrm{hr}}\right] \times \frac{1}{\rho \left[\frac{kg}{L}\right]} \tag{4.2}$$

where A is the area of membrane in m^2 and ρ is the density of the feed stream in kg/L.

DCMD has the highest flux, and AGMD has much lower flux, for coupon scale experiments. A coupon sized experiment is where the hot and cold stream temperatures do not change significantly along the flow direction between the entrance and exit of the module. As a result, lower mass transfer resistance in DCMD directly corresponds to a higher flux.

While the flux in coupon sized experiments can be higher than 100 LMH, in a real MD system with heat regeneration, the driving temperature difference across the

membrane is lower and hence fluxes are more modest at about 5 LMH.

The trade-off between flux and GOR was recognized for hollow fiber DCMD in [43], with GOR increasing with stages, but flux decreasing. Several other researchers have recognized this trade-off and some have used flux vs. GOR plots to visualize the same [45, 49].

Under coupon scale systems, the flux with PGMD has been shown to be higher than that of AGMD [21, 37]. Recently, CGMD was shown to have four times higher flux than AGMD for a gap thickness of about 3 mm [103]. Tian et al. [115] also performed coupon-sized experiments under CGMD conditions by allowing partial contact between the membrane and the condensing surface and achieved better mixing of the feed stream. The flux under this condition was 120 LMH with $T_{\mathrm{f}} = 77\,^{\circ}\mathrm{C}$ and $T_{\mathrm{c}} = 12\,^{\circ}\mathrm{C}$. In a larger system with energy recovery, it is shown that the flux of PGMD and CGMD are likely to of similar magnitude [103] or even lower than that of AGMD for the same membrane area (Fig. 4-8b).

Wu et al. [128] recently developed a heat-exchanger (ε-NTU) model to evaluate the flux of DCMD. The model is applicable for both parallel and counterflow configurations at low feed salinity and operates at small computational cost compared to finite difference methods. Since an overall heat transfer coefficient defined between the feed and cold bulk streams is used, a correction factor was additionally used to enhance the accuracy of the model by increasing the relative importance of the heat transfer coefficient on the hot side over the cold side.

Thermal efficiency

Thermal efficiency (η) of membrane distillation is defined as the fraction of the energy transferred from the hot side by mass transfer. For a system with little or no condensation energy recovery, η is the most important efficiency parameter of interest. In the ideal scenario, all the heat supplied to the MD process should be used for evaporation and should not be leaked from the hot side to the cold side as heat conduction losses. This ideal case would correspond to a thermal efficiency of 1. However, even with a membrane material that is perfectly insulating, η cannot reach 1 due heat

conduction through the vapor [64]. Nevertheless, $\eta = 1$ is a useful upper limit to consider. Formally, η may be defined as follows:

$$\eta = \frac{\dot{Q}_{\text{mass}}}{\dot{Q}_{\text{tot}}} = \frac{\dot{Q}_{\text{mass}}}{\dot{Q}_{\text{mass}} + \dot{Q}_{\text{cond}}} \tag{4.3}$$

where, $\dot{Q}_{\text{mass}}$ is the heat transfer rate associated with vapor transport through the membrane, which can be evaluated as the area weighted sum of the heat flux ($\dot{q}$) as:

$$\dot{Q} = \int_A \dot{q}\, dA \tag{4.4}$$

where the integral is evaluated over the total area of the membrane. The heat flux at any local section along the length of the module is a function of the membrane permeability (B) and vapor pressure difference across the membrane (Δp_{vap}), given by:

$$\dot{q}_{\text{mass}} = B \cdot \Delta p_{\text{vap}} h_{\text{fg}}(T_{\text{g,m}}) \tag{4.5}$$

Similarly, $\dot{Q}_{\text{cond}}$ refers to the conduction heat transfer rate through the membrane and is based on the local heat conduction flux given by

$$\dot{q}_{\text{cond}} = \frac{k_{\text{m}}}{\delta_{\text{m}}} (T_{\text{f,m}} - T_{\text{g,m}}) \tag{4.6}$$

where k_{m} is the effective conductivity of the membrane, δ_{m} is the thickness of the membrane and $T_{\text{f,m}}$ and $T_{\text{g,m}}$ are the temperatures at the feed-membrane and gap-membrane surfaces.

Membrane design should focus on increasing porosity and reducing membrane material conductivity to achieve high η [26]. There are clear differences in η between various MD configurations. DCMD has the lowest η among MD configurations. The presence of the additional air layer, with a much lower conductivity, leads to a larger η in the case of AGMD. Although the overall effective permeability and hence flux is lower in the case of AGMD, the fraction of heat transferred through conduction is also lower, leading to higher η. Ali et al. [7] analyzed the effect of various membrane properties on the cost of water production from a small-scale MD system and found that

while DCMD costs were affected by membrane conductivity and thickness, AGMD was relatively unaffected. This can be explained based on the trends in η discussed previously.

The value of η for MD systems has often been measured in coupon sized systems with relatively high flux. A wide of range of values have been reported for η, ranging from 0.2 to 0.95. In AGMD, the presence of the air gap ensures that $\eta > 0.85$ [11]. For DCMD, in contrast, η can vary over the wide range as a function of membrane properties and operating conditions. For low permeability membranes [131], or at high feed salinity [60], η can be quite low [82] . On average, η is greater than about 50–60% [4, 45, 62, 80, 111], and for well-designed membranes η can be quite high at about 0.75–0.85 [12, 34, 57, 67]. The discussion in Section 4.6 can help explain this wide range in the observed values.

For larger systems with significant energy recovery, GOR is directly affected by η. Fane et al. [36] expressed the GOR of DCMD as:

$$\mathrm{GOR_{DCMD}} = \eta \times \frac{\Delta T_{\mathrm{MD}}}{\mathrm{TTD_{MD}} + \mathrm{TTD_{HX}}} \tag{4.7}$$

where ΔT_{MD} is the axial temperature change of the feed as it flows through the MD module. This expression has been used subsequently by several other investigators [43, 135].

Koschikowski et al. [55] expressed GOR of a system with internal heat regeneration, such as PGMD, AGMD, and CGMD, as a function of η in the form:

$$\mathrm{GOR} = \eta \times \frac{T_{\mathrm{c,out}} - T_{\mathrm{c,in}}}{T_{\mathrm{f,in}} - T_{\mathrm{c,out}}} \tag{4.8}$$

Guan et al. [45] proposed an implicit expression linking GOR and η based on measured permeate and feed flow rates.

4.1.3 Modeling

The modeling results presented in this study are based on the one-dimensional finite difference numerical modeling framework presented in [98, 103]. The variations in

parameters such as flow rate, temperature and salinity along the module length are modeled along with the effect of heat and mass transfer boundary layers. All the results are presented for 'balanced' system conditions with highest efficiency. Balancing is achieved based on the principle of thermodynamic equipartition presented in Thiel et al. [113]. In the case of PGMD, CGMD and AGMD, balance refers to the condition where the pure water in the gap flows in the same direction as the feed water [103]. In the case of DCMD, balance refers to the condition where the heat capacity rates of the two streams are equal [64, 105]. The validation of the model against experimental data from large-scale MD systems is presented in 4.8.1.

4.2 MD energy efficiency theory

4.2.1 GOR as a function of MD effectiveness, ε

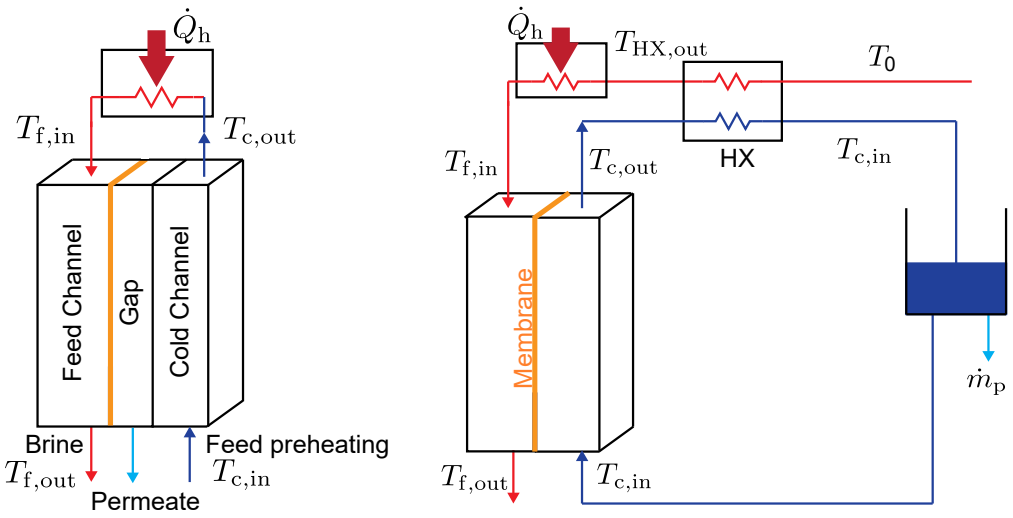

(a) AGMD, PGMD or CGMD. (b) DCMD system.

Figure 4-1: Schametic diagrams of MD systems.

Figure 4-1 shows schematic diagrams of the MD configurations considered in this study and the various temperatures are labeled. The flux of CGMD is higher than that of PGMD for coupon-sized systems. For a larger scale system designed for high GOR, Swaminathan et al. [103] showed that the higher GOR of CGMD compared to PGMD is not because of improved flux, but rather an effect of better energy recovery

within the module [103]. Better energy recovery within the module leads to a higher temperature of the preheated stream, leading to lower external heat input and hence higher GOR. In this context, another parameter, the MD system effectiveness, ε is defined here. Adapted from two-stream heat exchanger theory, ε compares the actual change in enthalpy of the cold stream to the maximum possible change in enthalpy of the cold stream. The specific heat capacity is relatively constant over the range of temperatures considered, so the equation may be reduced to a ratio of temperature differences:

$$\varepsilon = \frac{h_{\mathrm{c,out}} - h_{\mathrm{c,in}}}{h_{\mathrm{f,in}} - h_{\mathrm{c,in}}} = \frac{T_{\mathrm{c,out}} - T_{\mathrm{c,in}}}{T_{\mathrm{f,in}} - T_{\mathrm{c,in}}} \tag{4.9}$$

The cold stream is an ideal choice for defining ε since the mass flow rate and salinity of the cold stream are constant along the length of the module (for PGMD, CGMD, and AGMD).

ε is therefore a measure of energy transfer between the hot and cold streams scaled by the total possible energy transfer, and a value of $\varepsilon = 1$ corresponds to an infinite area MD heat exchanger where the cold stream leaves at the hot inlet temperature and vice versa.

The GOR of AGMD, PGMD and CGMD can be expressed in terms of η and ε as follows:

$$\begin{aligned}
\mathrm{GOR} &= \frac{\dot{m}_{\mathrm{p}} h_{\mathrm{fg}}}{\dot{Q}_{\mathrm{h}}} \\
&\approx \frac{\dot{Q}_{\mathrm{mass}}}{\dot{Q}_{\mathrm{h}}} \\
&= \eta \times \frac{\dot{Q}_{\mathrm{total}}}{\dot{Q}_{\mathrm{h}}} \\
&= \eta \times \frac{T_{\mathrm{c,out}} - T_{\mathrm{c,in}}}{T_{\mathrm{f,in}} - T_{\mathrm{c,out}}} \\
&= \eta \times \frac{\varepsilon}{1 - \varepsilon}
\end{aligned} \tag{4.10}$$

where $\dot{Q}_{\mathrm{total}}$ is the total heat transferred from the hot stream to the cold stream and $\dot{Q}_{\mathrm{mass}}$ is the heat transfer associated with vapor transfer across the membrane. The numerical values of GOR evaluated using Eqs. 4.1 and 4.10 may differ slightly based

on the temperature at which h_{fg} is evaluated in Eq. 4.1, since in Eq. 4.10 an average value of h_{fg} within the module is used.

From Eq. 4.10, GOR increases non-linearly with an increase in ε, whereas the dependence on η is linear. This expression will be used to understand the effect of increasing the gap conductivity in next section.

4.2.2 Deriving an expression for the upper limit of MD GOR

The maximum possible efficiency for MD systems can be derived from the new expression for MD GOR with ε, Eq. 4.10, and using the limitation of boiling point elevation.

Mistry et al. [75] analyzed the maximum performance limit for a general thermal desalination system with heat supply from a source at T_h and environment temperature T_0 by setting entropy generation equal to zero as:

$$\begin{aligned} \mathrm{GOR}^{\mathrm{limit}}_{\mathrm{thermodynamic}} &= \frac{h_{fg}}{\frac{\dot{Q}_{h,least}}{\dot{m}_p}} \\ &= \frac{h_{fg}\left(1-\frac{T_0}{T_h}\right)}{g_p + \left(\frac{1}{RR}-1\right) g_{br} - \frac{1}{RR} g_f} \end{aligned} \tag{4.11}$$

where g is the Gibbs energy, RR is the recovery ratio or ratio of pure product production to feed input, T_{amb} is the ambient temperature and T_h is the temperature of the heat source in the heater.

The least heat of separation for pure water is zero [73], corresponding to a maximum achievable GOR approaching ∞. At higher input salinities, the denominator increases and hence the maximum achievable GOR is lower.

For a single stage MD system, the GOR predicted by Eq. 4.10 should be lower than this thermodynamic limit. For an infinite area MD system, $\varepsilon \to 1$ so that GOR $\to \infty$ if $\eta > 0$. This is possible when the feed is pure water; with real solutions, boiling point elevation makes approaching ε of one impossible. When the feed is salt water of salinity s_f, in order to sustain positive fluxes within the module, the feed and cooling fluid temperature difference at the membrane surface ($T_{f,m} - T_{c,m}$, at any local position

within the module) should be greater than the local value of boiling point elevation ($BPE\left(T_{\mathrm{f,m}}, s_{\mathrm{f,m}}\right)$) [20]. At infinite area, flux is very close to zero, leading to near zero temperature and concentration polarization ($T_{\mathrm{f,m}} \approx T_{\mathrm{f,b}}$, $T_{\mathrm{c,m}} \approx T_{\mathrm{c,b}}$), and hence only the membrane offers resistance to transport. The minimum temperature difference between the bulk streams in MD and heat exchangers occurs at one end of the system and can be defined as the terminal temperature difference (TTD). TTD would have to be at least greater than or equal to the maximum BPE within the module to sustain positive vapor flux within the system (i.e., $\mathrm{TTD}_{\mathrm{min}} = \mathrm{BPE}_{\mathrm{f,in}}$). To understand the upper bound for GOR, an effective membrane thermal conductivity of 0 W/m-K is assumed by setting $\eta = 1$. In reality, even if the membrane is extremely porous, the lower limit for effective thermal conductivity is $k_{\mathrm{air}} \approx 0.02$ W/m-K, leading to $\eta < 1$.

ε can be expressed as a function of module TTD $= T_{\mathrm{f,in}} - T_{\mathrm{c,out}}$, using Eq. 4.9 as

$$\varepsilon = 1 - \frac{\mathrm{TTD}}{T_{\mathrm{f,in}} - T_{\mathrm{c,in}}} \tag{4.12}$$

Equation 4.10 can then be rearranged as

$$\mathrm{GOR} = \eta \left(\frac{T_{\mathrm{f,in}} - T_{\mathrm{c,in}}}{\mathrm{TTD}} - 1 \right) \tag{4.13}$$

The upper bound for GOR can therefore be expressed by substituting $\mathrm{TTD}_{\mathrm{min}} = \mathrm{BPE}_{\mathrm{f,in}}$ and $\eta = 1$ as

$$\mathrm{GOR}_{\mathrm{limit,MD}} = \frac{T_{\mathrm{f,in}} - T_{\mathrm{c,in}}}{\mathrm{BPE}_{\mathrm{f,in}}} - 1 \tag{4.14}$$

The two functions (Eqs. 4.11, 4.14) are plotted as a function of input salinity in Fig. 4-2. A recovery ratio (RR) of 10.11% is used for evaluating the thermodynamic limit since that is the average recovery ratio with an infinite area MD system with zero heat conduction across the membrane over the range of input salinities considered. The seawater property package of Sharqawy et al. and Nayar et al. [92, 79] is used to evaluate the Gibbs energy and boiling point elevation of seawater at various salinities and temperatures.

As seen in Fig. 4-2, $\mathrm{GOR}_{\mathrm{max,MD}}$ is bounded by $\mathrm{GOR}_{\mathrm{max,thermodynamic}}$. One reason for lower $\mathrm{GOR}_{\mathrm{max,MD}}$ is that the boiling point elevation varies along the module

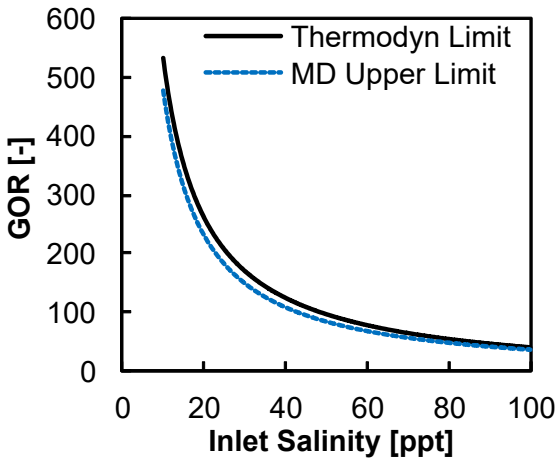

Figure 4-2: Limits of MD system energy efficiency

length. As a result, vapor flux is driven by a non-zero driving force, generating entropy elsewhere. Both η and ε are lower for real MD systems since the membrane is not a perfect insulator and the area of the system is finite. As a result, real GOR values are at least an order of magnitude lower than the maximum possible GOR, leading to a second law efficiency of less than 10% as observed by Mistry et al. [74].

4.3 MD configuration comparison

Results are presented based on a membrane with an average pore size of 0.2 μm, porosity of 80% and permeability coefficient of $B_0 = 1.5 \times 10^{-10}$ s. The baseline membrane thickness is set at $\delta_m = 150$ μm, resulting in $B = 10^{-6}$ kg/m^2-s-Pa. The channel thickness as well and the gap thickness are set at 1 mm. The feed inlet velocity is about 8.3 cm/s and the heat transfer coefficient within the channel is $h_\mathrm{f} = h_\mathrm{c} \approx 2400$ W/m^2·K. The channel width is 12 m, and channel length is 6 m, wherever not explicitly stated.

Figure 4-3 shows the comparison between various MD configurations. All the configurations show a trade-off between permeate flux and GOR, as previously observed for DCMD [45]. Assuming similar capital cost per unit area, a configuration whose performance curve lies towards the top-right is strictly better since it has both higher

energy efficiency and flux. At a constant flux, the GOR of CGMD is two times higher than that of PGMD. The energy efficiency of DCMD lies between those of PGMD and CGMD. Similarly, at constant GOR, flux of CGMD is about two times higher than that of PGMD. The reason for this trend in terms of the values of thermal efficiency and effectiveness is shown in Fig. 4-3b. η decreases with length for all the configurations. The η of AGMD is higher than 0.9 over the entire range of system lengths. The η for PGMD, DCMD and CGMD are lower and decrease more significantly with area. The value of η for these three systems is relatively similar.

One of the important results is that a low thermal conductivity of the gap region, when the gap is filled with water, is not particularly useful in maintaining a higher value of η. This was the motivation behind maintaining low thermal conductivity in the case of PGMD [127] and material gap MD [37]. On the contrary, with a highly conductive gap, as in the case of CGMD, η is only slightly lower. The reason is that η is only a function of the membrane properties and conditions at the boundary of the membrane (Eq. 4.23). Changes in other parts of the system, can influence η only through changing the boundary conditions across the membrane. An air gap does lead to a higher η at the expense of lower ε. With an increase in length, GOR increases from about 1 to about 15, in spite of the small decrease in η with length. This is a result of the significant increase in ε. DCMD has the largest ε, followed by CGMD, PGMD and AGMD. The higher ε leads to higher overall energy efficiency in the case of CGMD, compared to AGMD and PGMD.

Figure 4-4 shows the same comparison for a membrane with lower permeability ($B = 5 \times 10^{-7}$kg/m^2-s-Pa). As a consequence of the lower permeability, the η values for all the configurations are lower, although the effect is much more pronounced for CGMD, PGMD and DCMD, where the thermal efficiency drops by 0.1 (Fig. 4-4b). As a result of this, the trends in terms of GOR are also affected. The energy efficiency of CGMD is only 80% higher, compared to 100% higher in the previous case. Also, PGMD which was slightly better than AGMD, becomes worse than AGMD under these conditions. The effect of B on the flux of the various configurations at fixed channel length is shown in Fig. 4-6b. In AGMD, since the air-gap dominates the

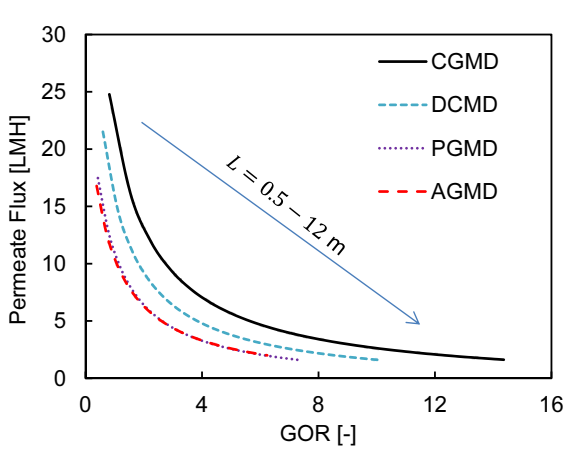

(a) Comparison of flux and GOR.

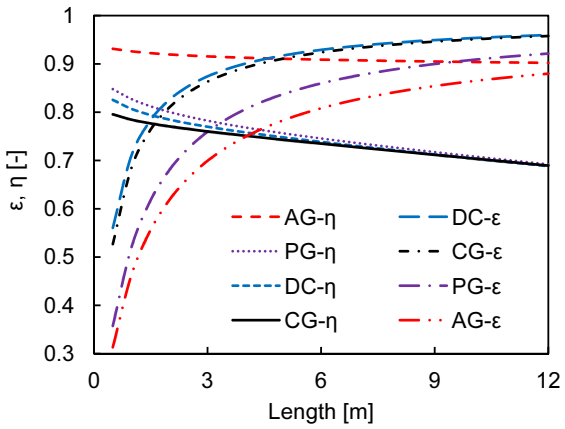

(b) ε and η variation for various configurations.

Figure 4-3: Module comparison. $w = 12$ m, $\dot{m}_{\mathrm{f,in}} = 1$ kg/s, $T_{\mathrm{f,in}} = 85\,^{\circ}$C, $T_{\mathrm{c,in}} = 25\,^{\circ}$C, $B = 10 \times 10^{-7}$ kg/m^2-s-Pa, $d_{\mathrm{gap}} = 1$ mm.

resistance to both heat transfer and vapor flux, a change in B does not lead to significant variation in flux or η. Conceptually, Eq. 4.23 can be used to understand the high η of AGMD by considering the membrane and the air-gap together as a thick “membrane" separating the salt water and pure water interfaces. The overall resistance to heat transfer is largest in AGMD, leading to a low ε and correspondingly higher value of $\mathrm{TTD_{MD}}$. A major portion of this temperature drop happens across the membrane and air gap, occuring between the feed water interface and the condensing film interface at the condensing surface. The overall thermal conductivity of this region is also lower than the effective thermal conductivity of the membrane, leading to a higher value of η.

The relative performance of the various configurations is also affected by the gap thickness. All results are reported for an effective gap thickness of 1 mm. The effective gap thickness is often lower than the thickness of the gap spacer since the membrane gets pressed into the gaps in the spacer and the spacer disrupts the condensation film in AGMD. At very low gap thicknesses, the performance of PGMD overlaps with CGMD. The performance of AGMD improves with decreasing gap thickness, although practically, pure water bridging and flooding can start becoming significant under those conditions pushing AGMD performance closer to that of PGMD at smaller gap

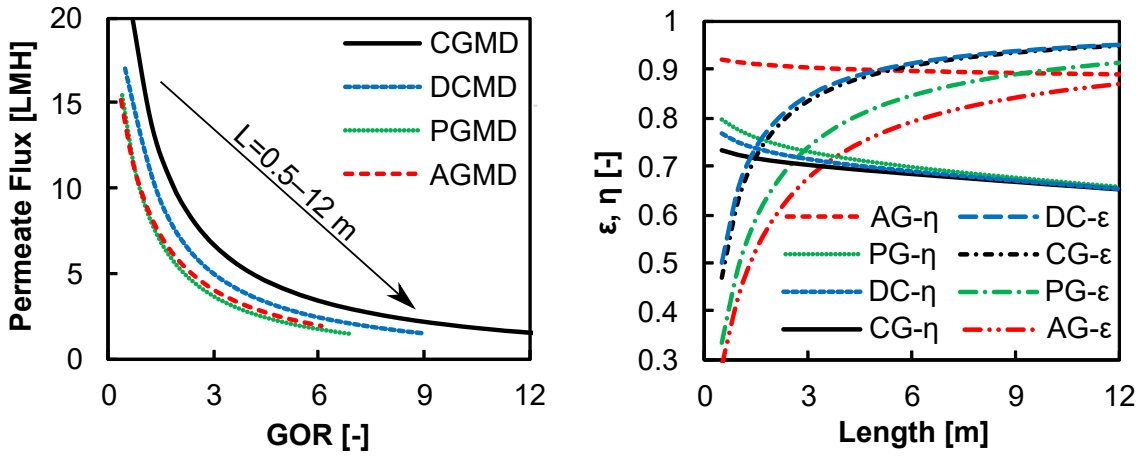

(a) Comparison of MD configurations.

(b) ε and η variation.

Figure 4-4: Module comparison for lower permeability coefficent of the membrane: $B_0 = 1 \times 10^{-10}$ s, $\delta_m = 200$ μm $\rightarrow$ $B = 5 \times 10^{-7}$ kg/m^2-s-Pa. $w = 12$ m, $\dot{m}_{f,in} = 1$ kg/s, $T_{f,in} = 85\,^\circ$C, $T_{c,in} = 25\,^\circ$C, $d_{gap} = 1$ mm.

thickness.

4.4 Effect of DCMD external heat exchanger area

Figures 4-3 and 4-4 show that the GOR of DCMD is lower than that of CGMD in spite of having both a slightly higher η and ε than CGMD. The reason for the lower overall GOR is the presence of the external heat exchanger (HX) in DCMD for energy recovery.

Equation 4.7 can be rewritten as follows to enable the comparison with CGMD:

$$\begin{aligned} \mathrm{GOR_{DCMD}} &= \eta \times \frac{\Delta T_{MD}}{\mathrm{TTD_{MD}} + \mathrm{TTD_{HX}}} \\ &= \eta \times \frac{\Delta T_{MD}}{\mathrm{TTD_{MD}}} \times \frac{\mathrm{TTD_{MD}}}{\mathrm{TTD_{MD}} + \mathrm{TTD_{HX}}} \\ &= \eta \times \frac{\varepsilon}{1-\varepsilon} \times \frac{\mathrm{TTD_{MD}}}{\mathrm{TTD_{MD}} + \mathrm{TTD_{HX}}} \end{aligned} \tag{4.15}$$

Note that the mass flow rate of the cold stream varies along the length in DCMD, but ε is still defined as in Eq. 4.9.

Under similar operating conditions, ε and η are slightly higher for DCMD compared to CGMD (Figs. 4-3b, 4-4b) because:

1. DCMD has a lower overall resistance since the gap resistance is eliminated

2. For the same feed inlet flow rate as CGMD, the average flow rate in balanced DCMD is lower. In CGMD the total mass flow rate of the feed and the product in the gap is a constant, whereas the feed flow and pure water flow rates are both maximum at the hot end of the module in DCMD and reduce along the length. For a recovery ratio of 10%, the average feed water flow rate and heat capacity rate are therefore around 5% lower in DCMD. This leads to a larger NTU, and hence a larger ε.

3. $T_{c,in}$ is greater than T_0 (ambient temperature, at which feed enters the desalination system (Fig. 4-1b)) for the DCMD systems considered in this study. This is because the external heat exchanger has a finite TTD and no additional cooling system is used [105]. Flux decreases and energy efficiency increases and with an increase in $T_{c,in}$.

For an infinite area external HX, $\mathrm{TTD_{HX}} = 0\,^{\circ}\mathrm{C}$, and therefore the GOR of DCMD with an infinite external HX ($\mathrm{GOR_{DCMD}^{\infty HX}}$) can be written as:

$$\mathrm{GOR_{DCMD}^{\infty HX}} = \eta \times \frac{\varepsilon}{1-\varepsilon} \tag{4.16}$$

and due to the higher value of ε and η for DCMD compared to a CGMD of the same size, $\mathrm{GOR_{DCMD}^{\infty HX}}$ is approximately 5-10% higher than $\mathrm{GOR_{CGMD}}$.

4.4.1 Quantifying the loss due to HX: $\mathrm{TTD_{factor}}$

A new variable, $\mathrm{TTD_{factor}}$ is introduced to understand the loss associated with using an external HX to recover energy. $\mathrm{TTD_{factor}} \equiv \frac{\mathrm{TTD_{MD}}}{\mathrm{TTD_{MD}+TTD_{HX}}}$ is defined as a function of the terminal temperature difference in the two balanced exchangers, the MD module and external HX. Equation 4.15 can then be rewritten as:

$$\mathrm{GOR_{DCMD}} \approx \mathrm{GOR_{DCMD}^{\infty HX}} \times \mathrm{TTD_{factor}} \tag{4.17}$$

For a DCMD system with additional cooling (Fig. 4-1b), where the cold water enters the MD module at ambient temperature ($T_{c,in} = T_0$), the equality in Eq. 4.17 is exact. For a DCMD system as shown in Fig. 4-1b, where the cold pure water inlet temperature $T_{c,in} = T_0 + \mathrm{TTD_{HX}}$, $\eta \times \frac{\varepsilon}{1-\varepsilon}$ is around 3% higher than $\mathrm{GOR}_{\mathrm{DCMD}}^{\infty \mathrm{HX}}$ when the area of the HX is half that of the membrane, and the deviation decreases as the HX area increases and $T_{c,in} \to T_0$.

$\mathrm{TTD_{factor}}$ represents the loss in DCMD associated with having an additional heat exchanger(HX) for energy recovery. If the external HX is as effective as the MD exchanger, and achieves similar TTD as the MD exchanger, $\mathrm{TTD_{factor}} = 0.5$, leading to DCMD system's GOR being half of $\mathrm{GOR}_{\mathrm{DCMD}}^{\infty \mathrm{HX}}$ and little over half that of a similarly sized CGMD system. If the goal is to transfer heat from fluid A to fluid B, using one HX is always better than using two HXs with an intermediate fluid C that flows between these two HXs (Here fluid C is DCMD's pure water flow loop). The introduction of the intermediate fluid means that the overall heating of fluid B is lower. Only if the second HX is made much larger, the relative loss associated with adding the extra HX and intermediate fluid can be reduced. The idea in the case of DCMD is similar. All the previous results are reported for the case where the area of the external heat exchanger is equal to the area of the membrane, in order to have a fair comparison between systems, since the condenser surface area would be equal to the membrane area in AGMD and PGMD. If CGMD is implemented by adding fins, the effective condenser area would be higher, but if it is implemented by having a very small gap thickness, the condenser area would be equal to the membrane area. The overall heat transfer coefficient for the HX was set at a representative value of $U_{\mathrm{HX}} = 1300$ W/m^2-K, e.g., for a liquid-liquid heat exchanger with copper tubing. Under these conditions, $\mathrm{TTD_{factor}} = 0.65$, leading to DCMD system's GOR being about 30% lower than that of similarly sized CGMD.

The effect of the external heat exchanger area on $\mathrm{TTD_{HX}}$ and thereby on $\mathrm{TTD_{factor}}$ and $\mathrm{GOR_{DCMD}}$ are shown in Fig. 4-5. The GOR of DCMD becomes equal to that of similarly sized CGMD system only when the external HX area is seven times that of the membrane area within the MD module. Beyond this area ratio, the GOR of

DCMD slightly exceeds that of CGMD. However, an external HX that is seven times larger than the MD module will entail significant increase in the capital expenditure, counterbalancing the energetic improvement.

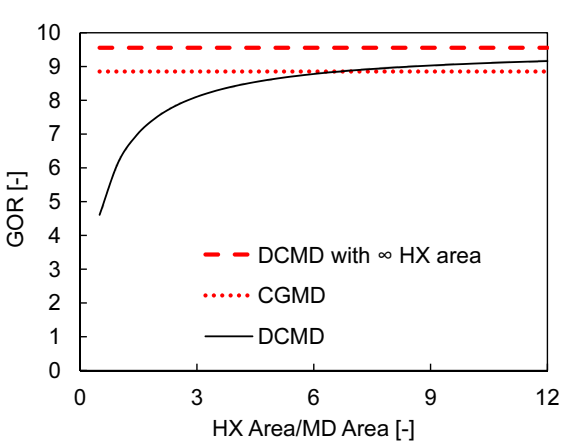

(a) Energy efficiency.

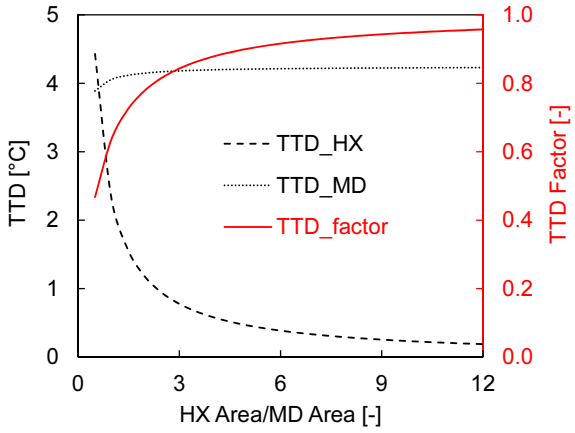

(b) Terminal temperature differences and $\mathrm{TTD}_{\mathrm{factor}}$.

Figure 4-5: Effect of HX to membrane area ratio on the performance of DCMD. Other parameters are fixed at baseline values specified in Sec. 4.3.

4.5 Effect of transport resistances

4.5.1 Effect of membrane permeability

The influence of membrane permeability (B) on system GOR for various MD configurations is shown in Fig. 4-6a. By making the active layer thinner to increase B, keeping $B_0 = B \cdot \delta_{\mathrm{m}}$ constant, CGMD and DCMD gain the most, with greater than two times improvement in GOR associated with an order of magnitude increase in B. The improvement in the case of PGMD is less significant and in the case of AGMD, the improvement with increase in B is even lower. Similar trends can be observed with increase in vapor peremability coefficient B_0. The reason for this is that the membrane constitutes the major resistance in the series of resistances within the MD module, in the case of CGMD and DCMD. On the other hand, in the case of PGMD and AGMD, the gap constitutes the major resistance (Fig. 4-7), leading to lower im-

provements with a more permeable membrane. Figure 4-6b shows the variation in flux with changes in membrane permeability. Since the thickness of the membrane is reduced to increase B, this is associated with an increase in heat conduction loses. As a result, flux starts to decline, beyond a ceratin reduction in membrane thickness. On the other hand, the air gap consitutes the major resistance to heat conduction and hence AGMD flux is not adversely affected.

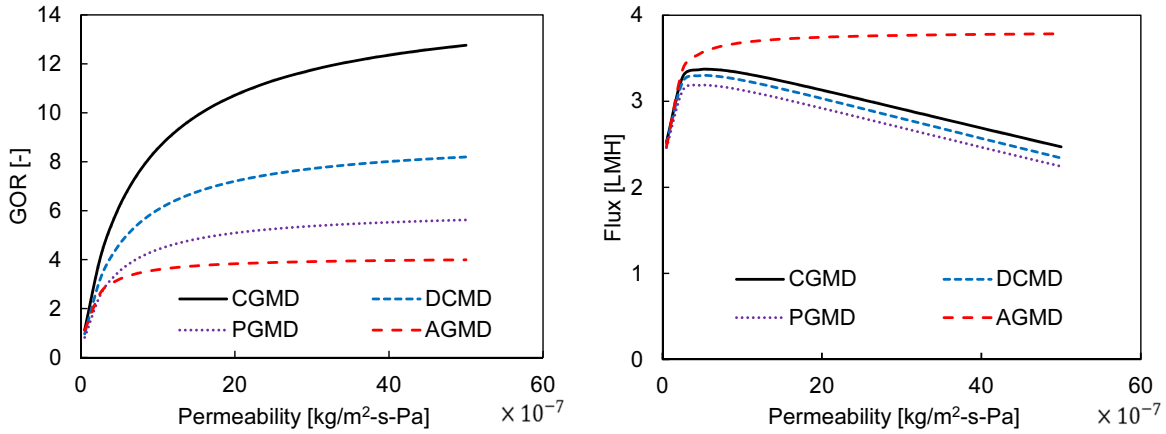

(a) Effect of membrane permability (B) on GOR.

(b) Effect of membrane permability (B) on flux.

Figure 4-6: Effect of membrane permability (B). Other parameters are fixed at baseline values specified in Sec. 4.3.

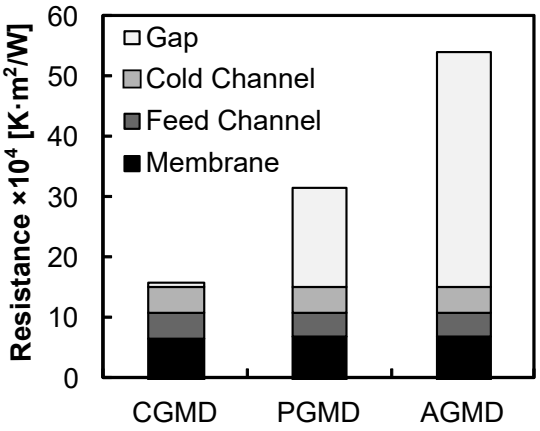

Figure 4-7: MD module heat transfer resistances. Comparison between modules at baseline conditions specified in Sec. 4.3.

4.5.2 Effect of channel heat transfer coefficients

Channel heat transfer is varied by changing the channel depth in the range of 1.5 to 0.5 mm, with higher h at lower channel depth. In CGMD and DCMD, the heat transfer coefficients of the channels contribute significantly to overall resistance (Fig. 4-7), since the gap resistance itself is negligible. As a result, increasing the feed and cold channel heat transfer coefficient leads to significant improvements in GOR. Since the gap constitutes the major resistance, improvements are once again more modest for AGMD and PGMD, as shown in Fig. 4-8a. The flux for the various MD configurations is plotted in Fig. 4-8b. Flux is slightly higher for AGMD over the entire range, due to the higher η in the case of AGMD.

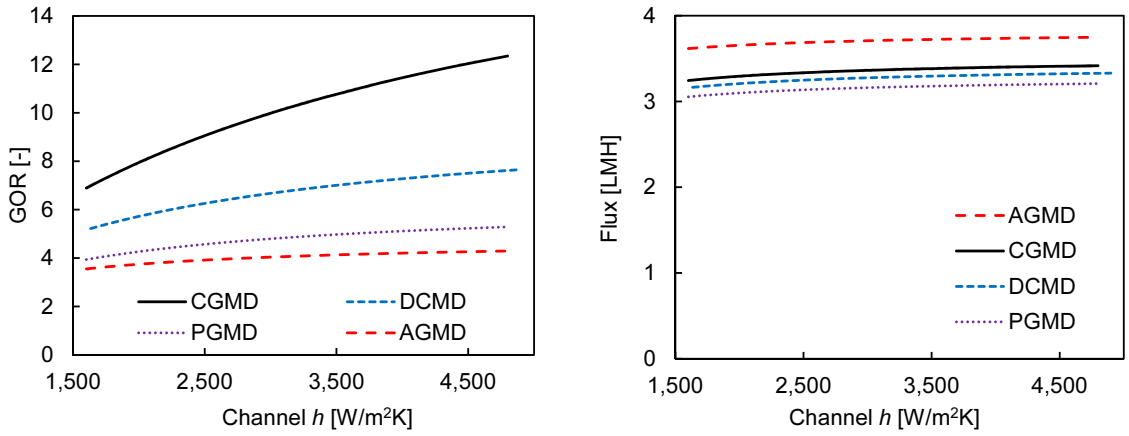

(a) Effect of channel heat transfer coefficients on GOR.

(b) Effect of channel heat transfer coefficients on flux.

Figure 4-8: Effect of channel heat transfer coefficients $h_f = h_c$. h is varied by changing d_{ch} between 0.5–1.5 mm. The feed velocity changes from 4.15 – 12.45 cm/s. Other parameters are fixed at baseline values specified in Sec. 4.3.

4.6 Heat exchanger based simplified model of CGMD, PGMD and DCMD

In this section, a simplified heat-exchanger-based mathematical model of MD is developed. Usually MD is modeled by discretization of the module area and solving

the transport equations within each computational cell and ensuring mass, momentum and energy balance between the cells [64, 98, 103, 135]. This is computationally expensive and complicated. The ε-NTU method for heat exchangers [63] enables evaluation of total heat transfer in a heat exchanger given only the input stream parameters, without discretization of the heat exchanger area.

Inspired by the ε-NTU method, η and ε are rewritten in terms of the transport resistances within the MD system. A single stage membrane distillation module resembles a counter-flow heat exchanger with hot brine and pure product transferring energy into the cooler feed, thereby preheating it (Fig. 4-1). Similar analogies with heat exchangers have been used to develop simplified effectiveness-MTU (mass transfer units) models for reverse osmosis [14] and pressure retarded osmosis systems [91].

ε of the system can be related to the number of transfer units (NTU) of the module, where NTU is defined as:

$$\mathrm{NTU} = \frac{UA}{\dot{m}c_{\mathrm{p}}} \tag{4.18}$$

Here, U is the overall heat transfer coefficient of the system in W/m^2-K. The overall heat transfer coefficient has been introduced and used to evaluate DCMD flux multiple times in the literature [4]. Other investigators [64] have used a parameter similar to NTU such as the specific membrane area times a transfer coefficient.

The resistances in permeate and conductive gap MD include boundary layer resistance in the cold and hot streams, the effective resistance of the membrane and the heat conduction resistance of the gap. As a result, the overal heat transfer coefficient U can be expressed as:

$$\frac{1}{U} = \frac{1}{h_{\mathrm{f}}} + \frac{1}{h_{\mathrm{eff,m}}} + \frac{d_{\mathrm{gap}}}{k_{\mathrm{gap}}} + \frac{1}{h_{\mathrm{c}}} \tag{4.19}$$

where h_{f} is the heat transfer coefficient in the feed, h_{c} is the heat transfer coefficient in the cold channel and $h_{\mathrm{eff,m}}$ is the effective heat transfer coefficient of the membrane.

Across the membrane, both heat and mass transfer occur. The transfer of water vapor through the membrane, which is the fundamental separation step in MD, is driven by a vapor pressure difference. While the other transport resistances are

relatively constant along the module length, the heat transfer associated with vapor transport is higher at the higher temperature end due to the exponential nature of vapor pressure dependence on temperature. The total resistance across the membrane $\left(\frac{1}{h_{\mathrm{eff,m}}}\right)$ can be expressed as two resistances in parallel, corresponding to heat conduction $\left(\frac{\delta_{\mathrm{m}}}{k_{\mathrm{m}}}\right)$ and mass transfer $\left(\frac{1}{h_{\mathrm{m}}^{\mathrm{mass}}}\right)$, and so the conductances may be added:

$$h_{\mathrm{eff,m}} = \frac{k_{\mathrm{m}}}{\delta_{\mathrm{m}}} + h_{\mathrm{m}}^{\mathrm{mass}} \tag{4.20}$$

where k_{m} is the effective thermal conductivity of the membrane and is the weighted average of the conductivities of the membrane material (such as PVDF) ($k_{\mathrm{s}} = 0.2$ W/m-K) and the vapor filling the pores ($k_{\mathrm{v}} = 0.02$ W/m-K). This expression is plugged into Eq. 4.19 to evaluate the overall heat transfer coefficient.

The resistance to mass transfer needs to be rewritten in terms of the temperature difference so that it can be combined with other resistances. A heat transfer coefficient corresponding to vapor transfer across the membrane ($h_{\mathrm{m}}^{\mathrm{mass}}$) is defined such that the following relation between the average vapor pressure difference and average temperature difference across the membrane holds: $Bh_{\mathrm{fg}}\Delta p_{\mathrm{m}} = h_{\mathrm{m}}^{\mathrm{mass}}\Delta T_{\mathrm{m}}$.

The vapor pressure of pure water can be approximately given by $P_{\mathrm{sat}}(T) = A\mathrm{e}^{bT}$ ($A = 1054.8$ Pa, $b = 0.0479$ °C^{-1}. R^2=0.9978 for $T \in [25\,^{\circ}\mathrm{C}, 85\,^{\circ}\mathrm{C}]$). On the feed side, water also contains salt, and hence the vapor pressure is given as $p_{\mathrm{f,m}} = P_{\mathrm{sat}}(T_{\mathrm{f,m}}) \times a_{\mathrm{w}}(T_{\mathrm{f,m}}, x_{\mathrm{f,m}}) \approx P_{\mathrm{sat}}(T_{\mathrm{f,m}} - \mathrm{BPE}(T_{\mathrm{f,m}}, x_{\mathrm{f,m}}))$. At any local position in the module:

$$\begin{aligned} h_{\mathrm{m}}^{\mathrm{mass}} &= Bh_{\mathrm{fg}}\frac{\Delta p_{\mathrm{m}}}{\Delta T_{\mathrm{m}}} \\ &= Bh_{\mathrm{fg}}\frac{\left(A\mathrm{e}^{b\left(T_{\mathrm{p,m}}+\Delta T_{\mathrm{m}}-\mathrm{BPE}_{\mathrm{f,m}}\right)} - A\mathrm{e}^{bT_{\mathrm{p,m}}}\right)}{\Delta T_{\mathrm{m}}} \\ &= Bh_{\mathrm{fg}}bA\mathrm{e}^{bT_{\mathrm{p,m}}}\left(1 - \frac{\mathrm{BPE}}{\Delta T_{\mathrm{m}}}\right)\left(\frac{\mathrm{e}^{b(\Delta T_{\mathrm{m}}-\mathrm{BPE})} - 1}{b\left(\Delta T_{\mathrm{m}} - \mathrm{BPE}\right)}\right) \end{aligned} \tag{4.21}$$

Note that this equation is not applicable to AGMD since pure water is not in contact with the cold side of the membrane in AGMD.

Equation 4.21 shows that the resistance of the membrane to mass transfer is

lower at higher temperatures. This is a direct result of the exponential nature of the vapor pressure dependence on temperature. In addition to this, B itself is in reality temperature dependent, and is higher at higher temperatures, further reducing mass transfer resistance at the hot end of the module. These effects are simplified by defining an average mass transfer resistance of the membrane as a function of some average value of $T_{\mathrm{p,m}}$, denoted by T_{avg} and by defining an average value of BPE at the feed membrane interface within the module.

ε can then be evaluated [63] assuming a perfect counter-flow heat exchanger as

$$\varepsilon = \frac{\mathrm{NTU}}{1 + \mathrm{NTU}} \tag{4.22}$$

η can be evaluated as the fraction of the heat transferred through the mass transfer resistance (Eq. 4.20) as

$$\begin{aligned} \eta &= \frac{B h_{\mathrm{fg}} \Delta p_{\mathrm{m}}}{B h_{\mathrm{fg}} \Delta p_{\mathrm{m}} + \frac{k_{\mathrm{m}} \Delta T_{\mathrm{m}}}{\delta_{\mathrm{m}}}} \\ &= \frac{1}{1 + \frac{k_{\mathrm{m}}}{\delta_{\mathrm{m}} B h_{\mathrm{fg}}} \frac{\Delta T_{\mathrm{m}}}{\Delta p_{\mathrm{m}}}} \\ &= \frac{1}{1 + \frac{k_{\mathrm{m}}}{\delta_{\mathrm{m}}} \frac{1}{h_{\mathrm{m}}^{\mathrm{mass}}}} \end{aligned} \tag{4.23}$$

The ratio of heat to mass conductance $\left(\frac{k_{\mathrm{m}}}{\delta_{\mathrm{m}} B}\right)$ is important [67]. A lower value of this fraction leads to a higher η. Therefore, the thermal efficiency is very sensitive to this parameter. Additionally, a higher temperature on the hot or cold side would lead to a higher η as has been reported by most researchers in the past. Finally, a larger feed salinity leading to higher BPE results in a lower value of η. Under this condition, it is important to keep ΔT_{m} much larger than BPE. This is the reason why Eykens et al. [34] found that at higher feed salinities in the DCMD configuration, thicker membranes with lower transfer coefficient have better thermal performance.

The average temperature difference across the membrane, ΔT_{m}, is an unknown in Eqs. 4.23, 4.21. It can be related to the TTD of the MD system, as a function of the heat transfer resistance offered by the membrane $\left(\frac{1}{h_{\mathrm{eff,m}}}\right)$ and the overall resistance

$\left(\frac{1}{U}\right)$ as:

$$\frac{\text{TTD}}{((1/U))} = \frac{\Delta T_{\text{m}}}{1/h_{\text{eff,m}}} \tag{4.24}$$

where, TTD itself is a function of ε and the exchanger top and bottom temperatures:

$$\text{TTD} = (1 - \varepsilon) \cdot (T_{\text{f,in}} - T_{\text{c,in}}) \tag{4.25}$$

and hence, these equations are solved iteratively.

Equations 4.22 and 4.23 can be substituted into Eq. 4.10 to evaluate GOR. Additionally, heat transfer rate into the system can be expressed as a function of the system top and bottom temperatures and ε:

$$\dot{Q}_{\text{h}} = \dot{m}_{\text{f,in}} c_{\text{p}} \times (1 - \varepsilon)\,(T_{\text{f,in}} - T_{\text{c,in}}) \tag{4.26}$$

and flux can be evaluated by substituting values of $\dot{Q}_{\text{h}}$ and GOR into Eqs. 4.1 and 4.2.

A fit for T_{avg} as a function of top temperature is obtained from the detailed finite difference numerical model as $T_{\text{avg}} = (0.3586 \times T_{\text{f,in}} + 21.922)$. The average BPE at the membrane interface for the case of seawater salinity considered in this study is set at 0.4 °C. The entire set of 33 equations that were solved with Engineering Equation Solver [53] for the simplified HX based model of PGMD and CGMD is provided in 6.5.6.

A comparison of the simplified HX model of DCMD with an external heat exchanger (based on additional equations discussed in Section 4.4) is provided in Section 4.8.2.

4.6.1 Validation of the proposed simplified model

The proposed heat-exchanger-based energy efficiency evaluation model is compared against the more detailed finite difference numerical model over a range of top temperatures ($T_{\text{f,in}}$ = 40–85°C) and module areas (L = 0.5–12 m). Additionally comparisons are carried out at fixed L = 6 m and $T_{\text{f,in}}$ = 85 °C, by varying the mem-

brane permeability ($B = 5$–50×10^{-7} kg/m^2-s-Pa), channel heat transfer coefficients ($h_f = h_c = 1600$–4800 W/m^2-K) and gap conductivity ($k_m = 0.6$–30 W/m-K). h_{fg} is evaluated at $T = 25\,^\circ$C. The differences in the simplified model results compared to the discretized model, as a percent deviation in flux and GOR are plotted in Fig. 4-9. The deviation tends to increase at lower feed inlet temperature and shorter module length, and the maximum deviation is about 11%. The deviations in the case of DCMD are shown in Fig. 4-12, and are also lower than 10%.

The finite difference model with 100 computational cells has over 2000 equations and takes about 6 seconds for each computation, whereas the heat exchanger based model is evaluated in about 1 μs.

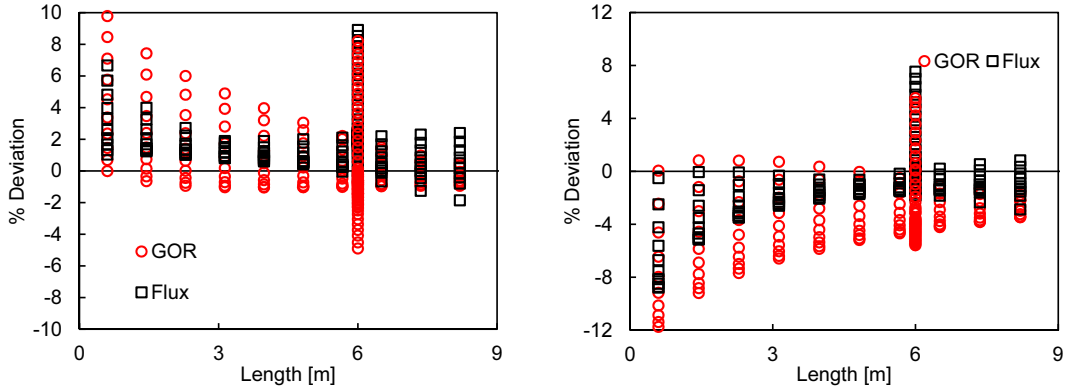

(a) Comparison of simplified HX based model and finite difference model of CGMD. $L = 0.6$–8.2m and $T_{f,in} = 40$–$85\,^\circ$C. $B = 5\times10^{-7}$–50×10^{7} kg/m^2-s-Pa. $h_f = 1600$–4800 W/m^2-K. $k_{gap} = 0.6$–30 W/m-K. Other parameters are held constant at baseline values specified in Sec. 4.3.

(b) Comparison of simplified HX based model and finite difference model of PGMD. $k_{gap} = 0.6$ W/m·K. $L = 0.6$–8.2m and $T_{f,in} = 40$–$85\,^\circ$C. $B = 5 \times 10^{-7}$–50×10^{7} kg/m^2-s-Pa. $h_f = 1600$–4800 W/m^2-K. Other parameters are held constant at baseline values specified in Sec. 4.3.

Figure 4-9: Percentage deviation in GOR and flux evaluated by heat exchanger based model compared to finite difference 1-D model over a wide range of operating conditions.

4.7 Conclusions

Balanced single-stage MD systems can be approximated and analyzed as counter-flow heat exchangers. The exchanger effectiveness ε and NTU are key parameters along with η to understand the energetic performance of these systems. Using this framework, insights on the relative performance of various MD configurations as well as a simplified model are developed.

1. Energy efficiency of MD systems with internal heat regeneration is expressed in terms of thermal efficiency (η) and exchanger effectiveness (ε) as GOR $= \eta\frac{\varepsilon}{1-\varepsilon}$. This expression is useful to understand the higher effect of the heat energy recovery (ε) compared to reducing heat conduction losses (η). Design of MD module should focus on increasing overall U, while the design of the membranes should focus on maximizing η.

2. An expression for the theoretical maximum GOR for single-stage MD is derived as a function of temperatures and feed salinity or boiling point elevation (BPE) as: $\mathrm{GOR}_{\mathrm{limit,MD}} = \frac{T_{\mathrm{f,in}}-T_{\mathrm{c,in}}}{\mathrm{BPE}_{\mathrm{f,in}}}-1$, for an ideal perfectly insulating membrane using the proposed model. This expression is validated against the thermodynamic limit for GOR evaluated for a generic thermal desalination system with no entropy generation.

3. The GOR of DCMD can be expressed as $\mathrm{GOR}_{\mathrm{DCMD}}^{\infty\mathrm{HX}} \times \mathrm{TTD}_{\mathrm{factor}}$, where $\mathrm{GOR}_{\mathrm{DCMD}}^{\infty\mathrm{HX}}$ corresponds to the energy efficiency when the external heat exchanger area is infinite, and $\mathrm{TTD}_{\mathrm{factor}}$ quantifies the loss associated with having finite external HX area. While $\mathrm{GOR}_{\mathrm{DCMD}}^{\infty\mathrm{HX}}$ is around 5–10% higher than that of a similarly sized CGMD system, the actual GOR of DCMD is equal to that of that of a similar size CGMD system only when the external heat exchanger area is about 7 times higher than the membrane area.

4. At a constant value of flux (J) and area of condensing surface, GOR of CGMD is higher than that of DCMD and PGMD. CGMD represents the practical upper limit performance of both PGMD and DCMD. A PGMD system with very low

gap thickness and a DCMD system with large external HX area compared to membrane area approach this limit. Membrane and flow channel heat transfer resistances are significant in the case of DCMD and CGMD, whereas the gap constitutes the major heat transfer resistance in the case of AGMD and PGMD. At seawater salinity, and for the membrane properties and conditions considered in this study, the GOR of AGMD is approximately equal to that of PGMD.

5. ε is expressed as a function of NTU through an analogy with counter-flow heat exchangers. GOR can therefore be expressed as $\eta \times$ NTU for AGMD, PGMD and DCMD. η is also approximated as a function of the membrane properties and temperatures across the membrane for PG, CG and DCMD. A simplified model for predicting the performance of these MD systems without detailed modeling is presented.

6. The percent deviation associated with using the simplified heat-exchanger parameter model for predicting GOR and flux of CGMD, PGMD and DCMD is below 11% over a wide range of operating conditions.

Acknowledgments

This work was funded by the Cooperative Agreement Between the Masdar Institute of Science and Technology (Masdar Institute), Abu Dhabi, UAE and the Massachusetts Institute of Technology (MIT), Cambridge, MA, USA, Reference No. 02/MI/MI/CP/11/07633/GEN/G/00, and facilitated by the MIT Deshpande Center for Technological Innovation and the Masdar Institute Center for Innovation and Entrepreneurship (iInnovation).

The authors acknowledge Tamanna Urmi for help with proofreading the manuscript.

4.8 Chapter Appendix

4.8.1 Model validation

The MD system is discretized along the length direction and in each computational cell, the water flux and total heat flux across the membrane are evaluated. The transport model across the membrane was validated using experimental results from a bench-top apparatus [103, 101]. Using the mass and heat flux evaluated, properties at subsequent cells are evaluated by applying conservation of mass, species and energy. Experimental and numerical modeling results are provided in Winter [126] for systems with larger membrane area of around 10 m^2.

Figure 4-10 compares the current model predictions with Winter's model (which was validated against experimental data) for AGMD, PGMD and DCMD systems with variation of feed inlet temperature and feed inlet flow rate. The following inputs were used in the present model for comparison: $T_{f,in} = 80\,°C$, $T_{c,in} = 25\,°C$, $s_{f,in} = 0.2$ g/kg, $\delta_m = 70$ μm, $k_m = 0.25$ W/m-K, $L \approx 10$ m (around 70% of the design value since membrane exists on both sides of the channel in this design, leading to inefficient use of some portions of the membrane), $w = 0.7$ m, $d_{ch} = 1.6$ mm (1 mm for the AGMD module, corresponding to half of the reported channel height). The effective gap thickness was set at around 65% of the design value for AGMD ($d_{gap} = 1.3$ mm) based on experience with bench-scale apparatus experiments where the membrane gets pushed into the gaps in the spacer. The gap thickness for PGMD is 0.5 mm and the effective thermal conductivity of the gap is set as 0.5 W/m-K. The membrane permeability was set at a constant value of $B = 9 \times 10^{-7}$ kg/m^2-s-Pa for all the simulations. The DCMD system is balanced.

The correct trends are captured by the present model for all three configurations. The effects of spiral wound module geometry, spacer design and other details have not been incorporated in detail in the model, and would be necessary to make more accurate predictions for specific systems. This work focuses on comparing various MD configurations that employ the same membrane and have similar geometry. In this context, it is noteworthy that the present model predicts similar trends as those ob-

served by Winter, for the cross-over in performance between the PGMD and DCMD. For DCMD systems, an external heat exchanger with fixed TTD of 2 °C was used to model the HX, and additional permeate cooling was assumed so that the pure water inlet temperature into the MD module is equal to 25 °C. At low feed inlet temperature and feed flow rate, PGMD outperforms DCMD. The TTD of the MD module decreases under these conditions, whereas the external HX TTD is fixed, thereby limiting the energy efficiency of the overall system. The effect of the external HX area and TTD on DCMD GOR is discussed in Section 4.4.

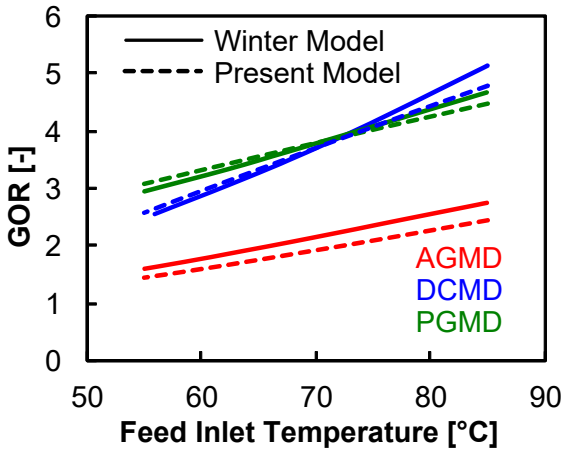

(a) GOR of AGMD, PGMD and DCMD as a function of feed inlet temperature. $\dot{m}_f = 300$ kg/hr.

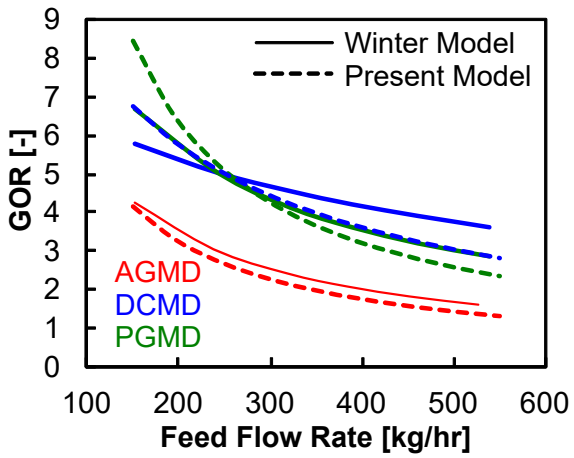

(b) GOR of AGMD, PGMD and DCMD as a function of feed flow rate.

Figure 4-10: Comparison of present model with results from Winter [126] for large spiral-wound MD modules.

Figure 4-11 shows that the present model predicts similar trends in terms of the effect of the gap thickness in PGMD as the discretization model and experimental results reported by Winter. A PGMD system with a vanishingly small gap is one realization of CGMD, and hence the performance prediction for CGMD is also similar between the two models.

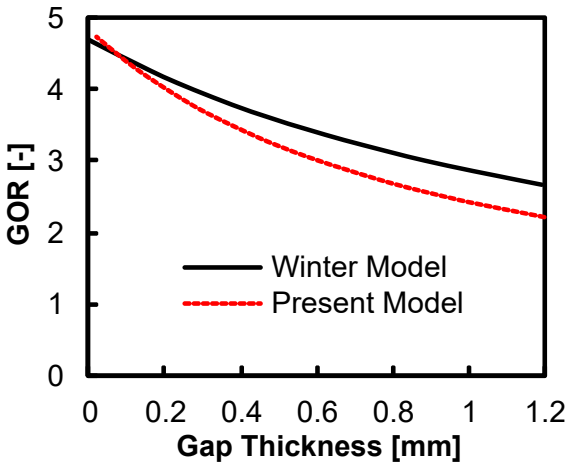

Figure 4-11: Comparison of present model with results from Winter [126] on the effect of gap thickness in PGMD. $\dot{m}_{\mathrm{f}}$ =400 kg/hr.

4.8.2 Comparison of simplified HX model of DCMD

The difference between the HX based model and the finite difference model for DCMD are shown in Fig. 4-12. The maximum deviation between the two models is lesser than 10% in this case as well.

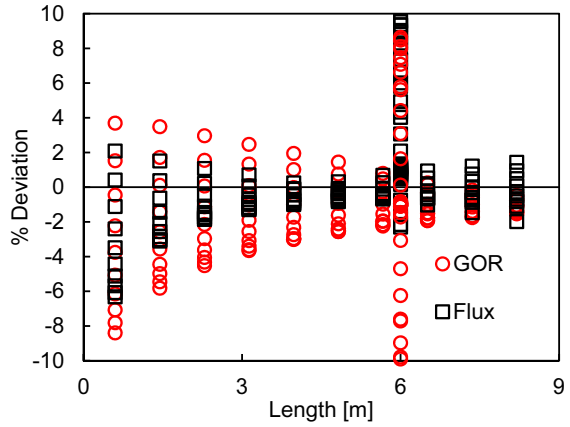

Figure 4-12: Comparison of simplified HX based model and finite difference model of DCMD over a wide range of operating conditions. $L = 0.6$–8.2m and $T_{\mathrm{f,in}} = 40$–$85\,^{\circ}$C. $B = 5 \times 10^{-7}$–50×10^{7} kg/m^2-s-Pa. $h_{\mathrm{f}} = 1600$–4800 W/m^2-K. Other parameters are held constant at baseline values specified in Sec. 4.3.

Chapter 5

Experimental investigation of single-stage membrane distillation energy efficiency

Abstract

A novel single-stage membrane distillation (MD) configuration, known as conductive gap membrane distillation (CGMD), has been suggested by numerical modeling results to achieve up to two times higher energy efficiencies than conventional air gap MD systems. CGMD consists of an MD module with a high thermal conductivity material in the gap region between the membrane and condensing plate, increasing the effective thermal conductivity of the gap. Such systems, if realized practically, could make MD competitive as a large scale thermal desalination technology that is not restricted only to specialized waste heat applications and could also make a stronger case for MD's use in waste-heat applications. In this study, an experimental comparison of different MD configurations is carried out on a bench scale system keeping membrane area constant, and results are compared to model predictions. The role of energy recovery within the module on improving CGMD efficiency is illustrated. A system with a simple copper woven mesh introduced in the gap in the place of plastic spacers is found to have 40% to 60% higher GOR than AGMD. The potential for further improvements in GOR and issues associated with studying MD efficiency at a laboratory bench scale are also discussed.

The contents of this chapter are adapted from [104].

5.1 Introduction

Swaminathan et al. [103] extended the numerical models developed by Summers et al. [98] to study PGMD system performance. Based on these results, they also proposed a novel MD configuration, conductive gap membrane distillation (CGMD), for improved energy efficiency. In CGMD, the goal is to increase the conductivity of the gap region rather than to reduce heat conduction through the gap as in the case of AGMD. While increasing the gap conductivity would lead to an increase in undesirable heat conduction losses from the hot feed to the coolant, the overall effect is positive in terms of system level energy efficiency, expressed as a gained output ratio (GOR).

The gap conductivity can be increased by allowing the gap to be filled with water, as in the case of PGMD. In CGMD, in addition to filling the gap with water, it is proposed that conductive materials be used in the region between the membrane and the plate to increase the overall thermal conductivity. Several methods of doing this, including the use of fins on the condensing surface extending up to the membrane, have been proposed.

This paper experimentally compares major single stage MD configurations including air gap (AGMD), permeate gap (PGMD), and conductive gap (CGMD) systems having the same total membrane area under similar operating conditions such as feed flow rate, external heat input and channel geometries. Various simple woven mesh spacers are used to change the thermal conductivity of the gap region to simulate CGMD conditions. These results are compared with numerical modeling results and major trends are verified. Finally the reasons for the variation between absolute magnitudes of GOR observed in the experiments and those predicted by the model are discussed.

5.2 Theory

A configuration of MD could have a higher GOR, either by producing more water under similar operating conditions or by consuming lesser thermal energy to produce a similar quantity of water. In the case of PGMD and CGMD as compared to AGMD, since the thermal resistance of the gap is reduced, the overall heat transfer coefficient between the hot side and the cold side is increased. As a result, for the same total heat exchange area (NTU), the effectiveness of heat transfer is improved and hence more heat is recovered in the preheating process within the module. This results in significant reduction in $\dot{Q}_{\text{in}}$, while retaining a relatively constant value of $\dot{m}_{\text{p}}$, resulting in improved GOR.

In order to increase the thermal conductivity of the gap, simple mesh spacers made of copper were used. The AGMD and PGMD experiments were also conducted with spacers, made of plastic, to support the membrane and prevent tearing of the membrane. Summers et al. [97] previously investigated several geometries of spacer material and found that the woven mesh spacer provided good support to the membrane. Woven mesh spacers were therefore adopted for this study as well. By choosing copper and polypropylene spacers of similar thickness, it was possible to analyze the effect of conductivity of the spacer on GOR.

The conductance of the gap (h_{gap}) ultimately affects the MD process in PGMD and CGMD and can be expressed as

$$h_{\text{gap}} = k_{\text{gap}}/\delta_{\text{gap}} \tag{5.1}$$

where k_{gap} is the effective thermal conductivity of the gap and δ_{gap} is the thickness of the gap. The effective thermal conductivity of wire meshes in the direction perpendicular to the plane has been found to vary over a wide range of values ranging from close to 0.02 W/mK to above 100 W/mK for copper mesh in air, depending on the type of contact between the mesh elements, the geometry of the mesh, and the volumetric ratio of metal to air [61].

For the single layer copper and plastic woven meshes used in this study, without

good contact (as the filaments not sintered together) between the wires, the thermal conductivity change from that of the fluid (water) is expected to be small. Rayleigh's analytical expression [84] (Eq. 5.2) is commonly used to estimate the effective conductivity of a single layer wire mesh in terms of the porosity (ϕ) and the conductivities of the solid (k_s) and fluid (k_f). The volumetric porosity of the mesh used is about 0.8. Under these conditions, Rayleigh's formula predicts $k_{\text{eff,Cu,water}} = 0.89$ W/mK and $k_{\text{eff,PP,water}} = 0.5$ W/mK for copper and polypropylene spacers, respectively. Thermal conductivity of water was assumed to remain constant at 0.6 W/mK.

$$k_{\text{eff,Rayleigh}} = \frac{k_f \left[k_{rmf} + k_s - (1-\phi)(k_f - k_s)\right]}{k_f + k_s + (1-\phi)(k_f - k_s} \tag{5.2}$$

5.3 Experimental Procedure

A schematic diagram of the experimental apparatus is shown in Fig. 2a. The feed water (0.1% NaCl solution to enable leak detection) is passed through the cold side to cool the condensing surface before being passed through a heater. The heat supply from the heater is controlled using a variable voltage controller. This heated water is then passed on the other side of the module over the MD membrane, counter-flow to the cold flow. The water is then passed back into the feed tank which is cooled to maintain it at a constant temperature. The apparatus is described in detail in Summers and Lienhard [100], with the only significant changes being reducing the channel depth to increase velocity, and adding insulation. For testing permeate gap and conductive gap configurations, further modifications were made.

In the above apparatus, the gap between the MD membrane and the condensing surface was modified to conduct experiments on AGMD, PGMD, and CGMD configurations. For AGMD, a plastic woven mesh is used. For PGMD, the same plastic woven mesh is used to support the mesh while water is now collected from the top with the bottom sealed so that the gap gets filled with liquid water (Fig. 5-1b). In the case of CGMD, in addition to collecting water from the top, the plastic mesh is replaced by a metal mesh.

During operation, fiberglass insulation was used on the inlets and exits to the

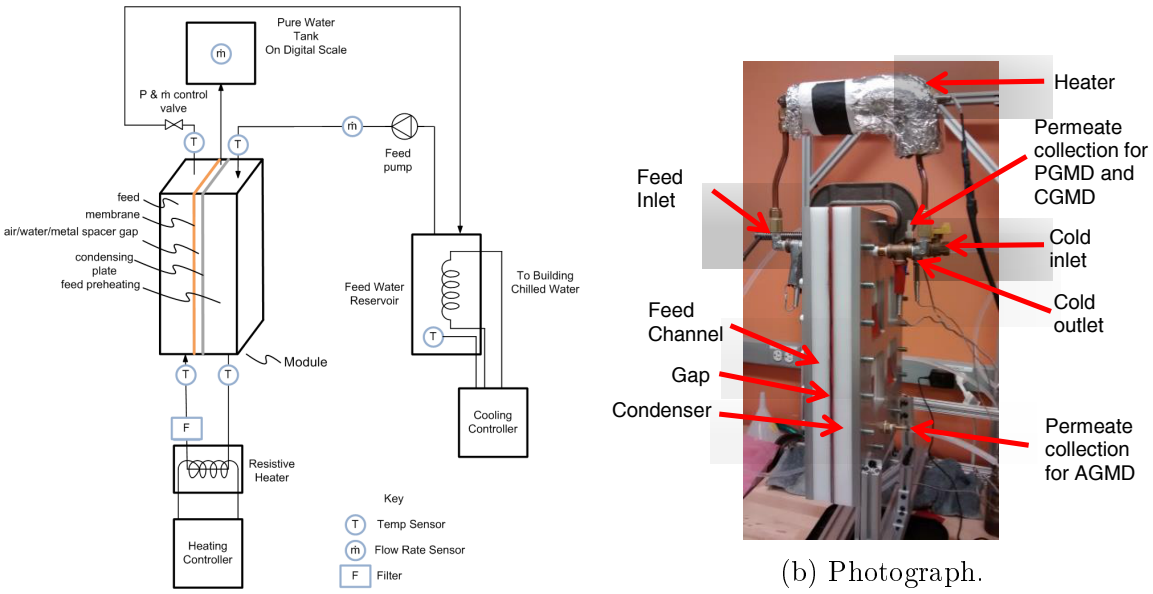

(a) Schematic diagram.

(b) Photograph.

Figure 5-1: Experimental apparatus.

heater, and foam insulation was applied on the outer surface to reduce the heat loss to the environment. The feed stream is circulated using a magnetic drive pump with no metallic parts exposed to the fluid. Low mass flow rate was achieved using the needle valve at the outlet of the module just before the flow returns to the tank. Therefore most of the pressure drop occurs after the feed stream leaves the MD module. This keeps the static pressure inside the module high enough to maintain a flat membrane. Feed flow rate was measured by collecting the feed for a known time interval (e.g., 50 sec.) and measuring its weight using a scale with 0.01 g accuracy. Permeate flow rate was calculated in a similar manner. Temperatures were measured using type T thermocouples with 1 °C accuracy. A cloth filter was used following the heater before flow entered the hot side of the MD module to prevent rust particulates from the heater depositing on the membranes and leading to membrane wetting.

Experiments were carried out under the same heater energy input conditions while varying the feed mass flow rate for each configuration, with different mesh sizes in the gap.

5.4 Results

The total length of the channel is 0.85 m, the width is 0.05 m, and the channel depth is 0.035 m. The channels are arranged such that the hot and cold fluid streams are in a counterflow orientation. The simulations were conducted at a constant power input of 90 W. The effective conductivity of the permeate gap is set as 0.6 W/mK, whereas for the conductive gap case, an effective conductivity of 10 W/mK is used. These would refer to the best case scenario values for k_{gap}. As highlighted earlier, with the simple woven meshes, the conductivity in the permeate gap experiments is likely to be approximately 0.5 W/mK, and about 0.9 W/mK rather than 10 W/mK in the copper mesh CGMD experiments. These results are then compared with the best-case scenarios to determine the trends and evaluate how much further improvement is possible.

Figure 5-2a shows the numerical modeling prediction on the effect of gap thermal conductivity on GOR. At lower values of k_{gap}, up to about 4 W/mK, a steep increase in GOR is predicted, followed by diminishing returns beyond this point. The exact number is a function of the relative dominance of the gap resistance among other thermal resistances between the hot and cold fluids. One can observe that an ideal CGMD process should have about twice as much GOR as that of AGMD, when all other parameters are held constant.

Figure 5-2b shows experimental results on the effect of gap configuration on GOR at two values of feed flow rate. Under both flow rate conditions, an increasing trend of GOR is observed between the AGMD, PGMD, and CGMD configurations. The magnitude of increase in GOR between AGMD and CGMD is between 40 to 60%, whereas between AGMD and PGMD it is about 20%. The flux at a GOR of 0.3 is 2.43 LMH. The heat supply rate was held constant at 174 W in all the experiments and so the GOR is a linear function of the flux.

As noted in Section 5.3, another method to affect the process performance by changing gap conductance is to change dgap. Figure 4a shows that lower dgap leads to a higher GOR for all configurations. In the case of CGMD, the improvement is less

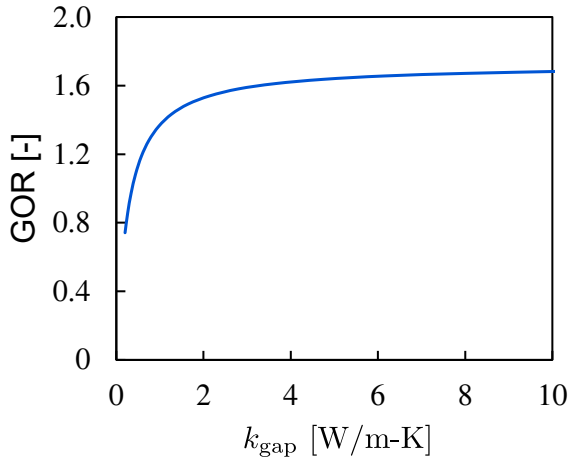

(a) Numerical model results on effect of k_{gap} on GOR ($\dot{m}_f = 1$ g/s,$d_{gap} = 1.24$ mm).

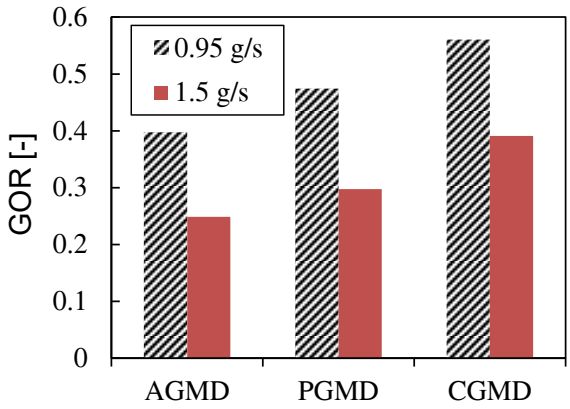

(b) Experimental GOR at $d_{gap} = 1.24$ mm for different MD configurations and two feed flow rates.

Figure 5-2: Effect of gap conductivity.

pronounced as the increase in hgap does not affect the total resistance much because of the aforementioned diminishing returns, as the gap is no longer a major resistance. It should be noted that this figure indicates that while AGMD and PGMD perform worse at higher dgap, at lower gap thicknesses their performance approaches that of CGMD. Practical constraints such as the pressure drop for the permeate flow will set the lower limit on dgap in these cases.

Experimentally, mesh thickness effectively sets the gap thickness. Energy efficiency using a mesh thickness of 1.12 mm was found to be higher than using a 1.24 mm thick mesh. As predicted by the model, the improvement in GOR is higher for AGMD than for PGMD, 23% compared to 12%, while the magnitudes of GOR in the PGMD case are higher.

Figure 5-4a shows numerical modeling results on the effect of feed flow rate on GOR. In all three configurations, a smaller feed flow rate leads to a higher GOR due to better energy regeneration in the MD module (larger NTU for the same area and transfer coefficient). Also the GOR increases exponentially as we get to very small flow rates, and is limited only by the increase in flow boundary layer resistances to heat and mass transfer.

Experimentally, a similar trend is observed in terms of the effect of feed flow rate

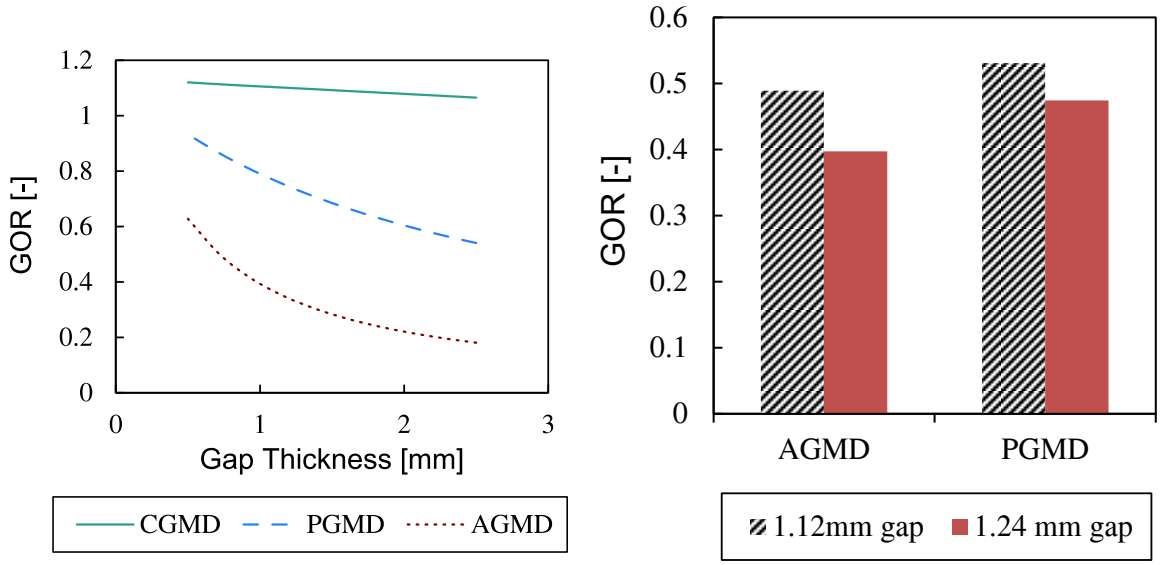

(a) Numerical modeling predictions on the effect of gap thickness on GOR ($\dot{m}_f = 1.5$ g/s).

(b) Experimental results on the effect of gap thickness on AGMD, PGMD performance at $\dot{m}_f = 1.5$ g/s.

Figure 5-3: Effect of gap thickness.

(Fig. 5-4b). At lower feed mass flow rates, for the same external heat input, the feed stream is heated more as it leaves the cold channel leading to higher top temperature and higher water permeate production rate. The reason why CGMD performs better at any given flow rate is also similar. For the same set of inlet conditions and heat input, the CGMD system has better internal heat transfer coefficients, enabling more heat transfer in the module leading to better preheating of the cold stream. As a result, the cold outlet stream temperature is higher in CGMD compared to PGMD which in turn is higher than AGMD. Since the heat input is constant, this leads to a higher top temperature in CGMD and therefore higher flux and pure water production rates. This experimentally observed mechanism is also numerically verified.

5.5 Discussion

While the results in Section IV are consistent with those from the numerical model, on average the absolute magnitude of the numerically predicted GORs is about twice that of the experimentally observed GORs. This section discusses some of the rea-

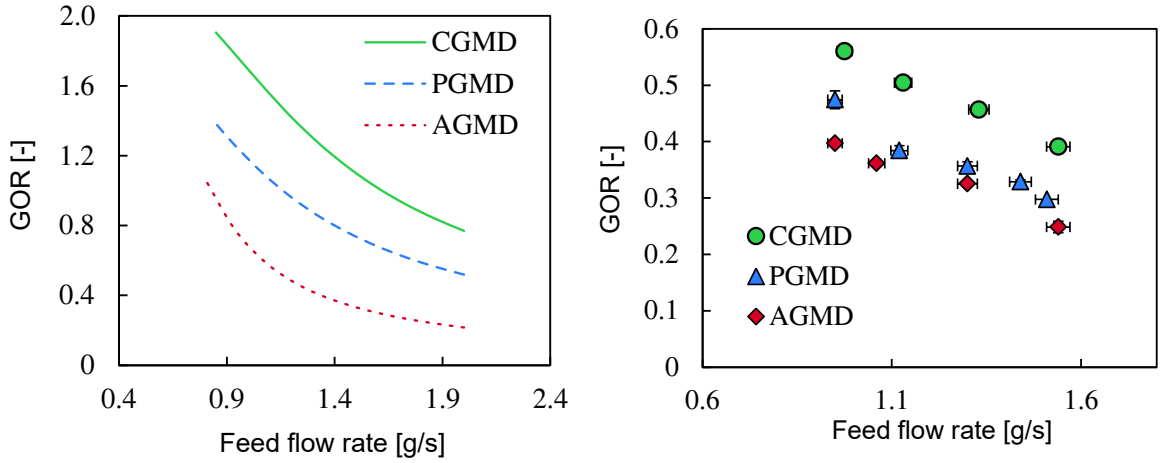

(a) Numerical model predictions on GOR as a function of feed flow rate.

(b) Experimental GOR as a function of flow rate, $d_{\text{gap}} = 1.24$ mm.

Figure 5-4: Effect of gap thickness.

sons for this mismatch and suggestions for future bench scale MD energy efficiency experiments.

The two major reasons for the mismatch between experiments and the model are heat losses to the environment, which are neglected in the model, and cross-conductance in the condensing plate due to compact module design. In addition to these, the reason for the relative improvement in CGMD performance in the experiment being lower than that predicted numerically has been explained briefly in terms of the actual effective thermal conductivity of the mesh spacer used for CGMD being much below the value of 10 W/mK assumed in the model.

5.5.1 Compact MD modules and cross-conductance

For MD installations of small membrane area, the feed flow rate needs to be low. This can be understood based on the fact that MD flux is likely to be about 2-4 L/m^2-hr for a well-designed system with energy recovery. As a result, for smaller membrane area systems, the feed flow rate needs to be scaled down in order to achieve a good recovery ratio in the module.

Lower feed and coolant flow rates lead to higher temperature and concentration polarization in these channels. In order to accommodate a longer channel within the

feed and cold side plates, circuitous flow geometry was used, as shown in Fig. 5-5. This leads to cross conduction in the copper condensing plate leading to the MD module's departure from counter-flow behavior thereby degrading heat recovery substantially.

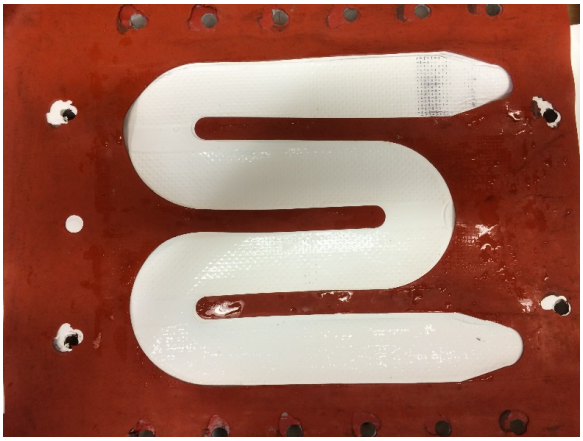

Figure 5-5: Flowchannel geometry.

5.5.2 Heat loss

In the numerical model, heat loss to the environment was neglected. The channel was machined out of Delrin plates of 2.54 mm thickness to provide insulation. In addition, insulation was used, but couldn't cover the module uniformly. The heat loss to the environment scales as $\dot{Q}_{\text{loss}} = h_{\text{eff}} A \Delta T_{\text{eff}}$ where h_{eff} and ΔT_{eff} are effective heat transfer coefficient and temperature difference associated with the heat loss. The effective heat transfer coefficient is the effective conductance of a series network of forced convection, conduction through module housing and natural convection resistances. In most cases, natural convection resistance is the dominant resistance. For the range of experimental conditions, natural convection heat transfer coefficient is proportional to ΔT_{eff} to a power less than one (e.g., 1/6). Therefore, h_{eff} can be considered to be approximately constant. In the current experiments, same amount of heat input was used. The feed stream is heated up to a higher temperature when the mass flow rate is lower. So at lower mass flow rate, ΔT_{eff} is higher, resulting in an increased heat loss. In this experimental setup, heat loss was significant, accounting

for roughly 20% of the heater power. Again, for lower mass flow rates, the heater power as an absolute magnitude is lower. While $\dot{Q}_{\text{loss}}$ is a function of only the surface area and ΔT_{eff}, and is not directly affected by changes in flow rate, for a constant top temperature system for example, the magnitude of heat input would still be lower for the lower mass flow rate system, leading to a higher percentage heat loss. This large heat loss is the second reason why GOR was low for this experimental setup. While the numerical model ignores heat loss and predicts an exponential increase in GOR, at lower flow rates the experiment shows a leveling off of GOR. This too is a result of higher heat losses at the lower flow rate cases due to higher top temperature in the module, as shown in Fig. 7. The heat loss is calculated by applying the energy balance on the MD module as shown in Eq. 5.3.

$$\dot{Q}_{\text{loss}} = \dot{m}_{\text{f}} c_{\text{p}} T_{\text{f}} - \dot{m}_{\text{b}} c_{\text{p}} T_{\text{b}} - \dot{m}_{\text{p}} c_{\text{p}} T_{\text{p}} + \dot{m}_{\text{f}} c_{\text{p}} (T_{\text{c,in}} - T_{\text{c,out}}) \tag{5.3}$$

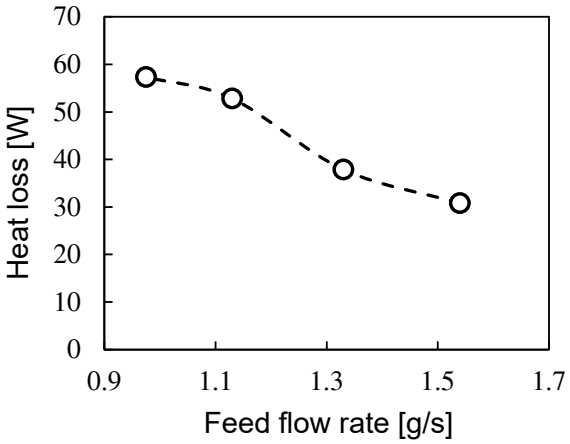

Figure 5-6: Heat loss as an effect of flowrate.

5.6 Conclusions

Numerical models predict that the GOR of a well-designed CGMD configuration with high k_{gap} can be more than two times higher than that of an AGMD system of the same membrane area. Experimentally, using woven mesh spacers of relatively low

k_{eff}, the predicted trends in GOR were verified. The CGMD system GOR was up to 60% higher than that of AGMD, and PGMD outperforms AGMD by about 20%. The higher GORs of PGMD and CGMD are due to lower transport resistances within the module leading to better preheating of the feed. The effect on reducing flux of heat loss and cross-conductance in MD modules machined compactly with common condensation surface is explained, which may facilitate better design of future bench-scale conductive-gap MD experiments for studying GOR.

Chapter 6

Membrane distillation at high salinity: evaluating critical system size and cost-optimal membrane thickness

Abstract

This study provides a comprehensive framework to analyze and design single stage membrane distillation (MD) systems for desalination up to high feed salinity. MD performance is measured in terms of energy efficiency (GOR) and water flux, which together affect specific cost. For small systems, GOR rises with size. A critical system size (membrane area relative to feed flow rate, expressed non-dimensionally as NTU^{crit}) exists beyond which GOR plateaus and starts declining. Using the heat exchanger analogy for MD, an analytical expression for the critical system size is derived as a function of salinity and two non-dimensional ratios of heat transfer resistances within sections of the MD module. At higher salinity, this critical size is small enough to be practically relevant and hence care should be taken to avoid exceeding this size. An unified understanding and ranking of various single stage MD systems' performances is developed based on the non-dimensional ratios of thermal resistances. Air gap MD (AGMD) is affected least by salinity since the air gap results in a thick 'effective membrane'. Conductive gap MD (CGMD) and direct contact MD (DCMD) employing a thick membrane are also resilient to high salinity, while eliminating the danger of performance decline due to gap-flooding. The GOR and flux of CGMD and DCMD are similar when the heat transfer resistance of the gap (in CGMD) and that of the external heat exchanger (in DCMD) are identical. Finally, we

propose a method to identify a cost optimal membrane thickness in combination with the choice of ideal system size. For each value of water flux, at a given feed salinity there exists a membrane thickness that maximizes GOR; correspondingly an upper limit GOR-flux curve can be obtained. The operating point along this curve, and correspondingly system size and membrane thickness, can be identified to minimize specific cost of water, based on the ratio of specific cost of heat energy to amortized specific cost of module area.

6.1 Introduction

The salinity of incoming feed water and the desired recovery ratio impact not only the energy consumption of desalination, but also the ideal choice of technology. Desalination of more saline feed streams is required for industrial effluent recycling for zero-liquid-discharge [110], inland desalination brine management, concentration of produced water from hydraulic fracturing [112], etc. Conventional spiral wound RO is typically operated below 70 bar [39], and is therefore unsuitable for these applications where the feed osmotic pressure can be as high as 300 bar [114]. In contrast, thermal distillation processes are routinely used to desalinate water up to high concentrations. Humidification dehumidification [70, 78] is a simple technology that has recently been successfully applied towards treating ultra-saline produced waters [17].

Membrane distillation (MD) has been identified as a candidate technology for implementing modular desalination of high salinity brines [66, 116]. MD has been experimentally and numerically investigated for high salinity applications, mostly with small scale systems. A unified perspective on the future of MD system design for high salinity is lacking. In this study we develop theories concerning three key aspects of MD system design for wide range of inlet salinities:

1. Choice of MD configuration: Popular single stage MD configurations (air gap, direct contact, permeate gap and conductive gap - AGMD, DCMD, PGMD and CGMD) are compared and ranked in terms of their energy efficiency and flux so as to guide future research and development efforts.

2. System design and operation: An expression for critical specific system size

is derived in terms of feed salinity, top and bottom temperatures and heat transfer resistances within the MD module. This expression can be used at both design and operation stages to avoid unproductive operating conditions with low energy efficiency and flux.

3. Choice of cost-optimal membrane thickness: A method is presented for choosing the cost-optimal membrane thickness for a specific application based on the feed salinity and the relative cost of system capital and thermal energy.

6.1.1 Membrane distillation studies at high salinity

Small systems: flux, thermal efficiency

Most studies have focused on small membrane area systems because of their ease of fabrication at a lab-scale. The impact of high salinity on water flux has been widely reported [1, 86, 132]. Guan et al. [46], Li et al. [60], and Alkhudhiri et al. [9] tested MD with various electrolyte solutions up to high salinity and found that water activity is a good predictor of the pure water flux. Vapor pressure at the solution-vapor interface is proportional to the activity of water, which reduces differently for each electrolyte solution, with an increase in feed salinity.

In addition to water flux, the effect of high salinity on MD thermal efficiency (η) has also been investigated, through experimental [4, 34] and numerical [38] techniques. Thermal efficiency is the fractional contribution of vapor transport to the overall heat transfer across the membrane. η is also diminished at higher feed salinity.

Another interesting application of high salinity MD is the MD crystallizer system in which pure water is extracted from a saturated solution using MD with the brine recirculated into a tank where salt is precipitated out of solution [30, 83].

Larger area systems: energy efficiency

With the availability of commercial larger size MD modules, studies on energy efficiency (represented as a gained output ratio, GOR) have also increased. Chung et al. [20] studied GOR as a function of feed salinity for wide range of salinities focusing

on the multistage vacuum membrane distillation configuration. Winter et al. [127] measured flux and specific thermal energy consumption (inversely proportional to GOR) for spiral-wound PGMD modules up to 105 g/kg. At higher salinity levels, a peak GOR was observed with changes in feed flow rate. Similarly, Thiel et al. [114] used numerical models of PGMD to illustrate the existence of an optimal system size (represented through a terminal temperature difference) at which GOR is maximized.

These studies indicate the existence of a critical feed flow rate (for fixed system size), or critical system size (for a specific feed flow rate) at which GOR is maximized. Below the critical feed flow rate or above critical system size, both flux and GOR decrease. This may be referred to as a counterproductive operating condition. Since both performance metrics decrease, no argument favors operating under these conditions, irrespective of the relative cost of thermal energy and system area. In Section 6.3.3 we evaluate an expression for this critical system size relative to feed flow rate as a function of salinity and heat transfer coefficients within the module. This expression will be useful in avoiding counterproductive operating conditions.

6.1.2 Choice of MD configuration

Figure 6-1 shows various single stage MD systems. The relative performance of various MD configurations needs to be understood in order to choose the right configuration for a given application. Eykens et al. [35] experimentally demonstrate that the sensitivity of flux to various process conditions (such as temperature, feed velocity, salinity etc.) is configuration dependent. Winter [126] reported results from pilot-scale modules of AGMD, PGMD and DCMD. It was found that the GOR and flux of PGMD and DCMD are close, and higher than that of AGMD. At high salinity, just as at small sizes, large-scale AGMD was more resilient to increases in feed salinity, whereas the performance of DCMD and PGMD drops faster.

Swaminathan et al. [106] used performance curves in the energy efficiency-flux space to compare 'balanced' [105, 103] single stage MD configurations at seawater salinity. We use the same framework in this study, as we extend the analysis to higher salinities. The rationale behind this choice is that the cost of pure water production

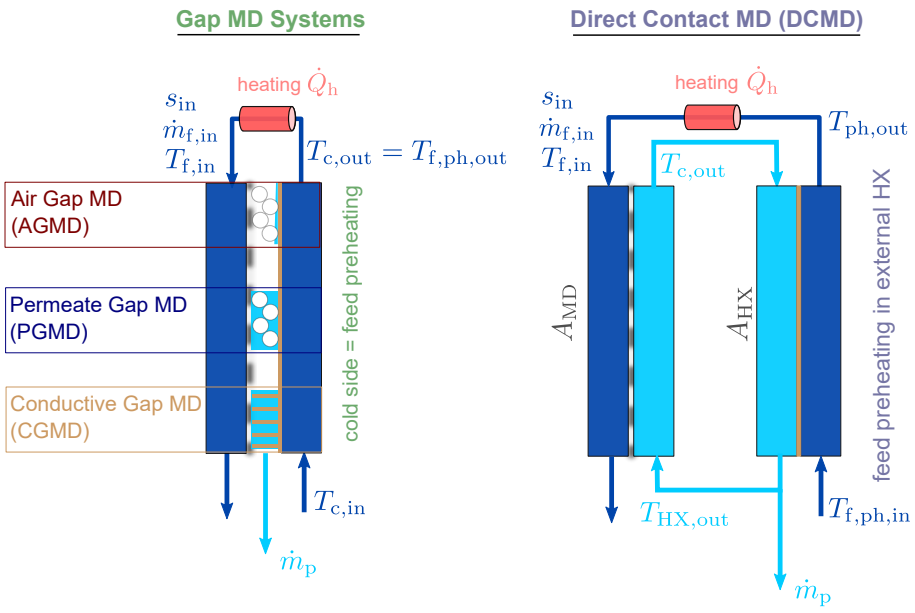

Figure 6-1: A schematic representation of single stage MD configurations considered in this study. AGMD, PGMD and CGMD differ based on the gap conditions. DCMD requires an external HX for feed preheating.

or brine concentration is always affected both by capital expenditure (CapEx) and operating expenses (OpEx). The cost of water can be expressed as a function of GOR and flux in as (see 6.5.1):

$$c_{sp,water} = \frac{C_{GOR}}{GOR} + \frac{C_{flux}}{J} \tag{6.1}$$

where C_{GOR} is the scaled specific cost of thermal energy and and C_{flux} is the scaled amortized specific cost of system area. GOR is a non-dimensional measure of energy efficiency, equal to h_{fg} times the inverse of specific thermal energy consumption (see Eq. 6.3), and J is the pure water flux in L/m^2·hr (or LMH). For a specific application, C_{GOR} and C_{flux} are considered to be relatively constant across various MD configurations, and hence a configuration whose performance curve lies in the top-right of a GOR-versus-flux graph is strictly better.

Some studies evaluating MD's specific cost of water production neglect the cost of thermal energy assuming that a free source of low-grade "waste" heat may be available [7]. Many membrane tests on the small scale have also focused exclusively on flux. In reality, the cost of thermal energy is usually quite significant [87]. Even

if a waste-heat source is available, the cost of equipment such as heat exchangers to access the waste heat should to be included in the economic analysis, in the form of an equivalent CapEx that is affected by system energy efficiency.

Another metric of MD's efficiency that is more readily measured with lab-scale systems is its thermal efficiency η [52] :

$$\eta = \frac{\dot{Q}_{\text{vap}}}{\dot{Q}_{\text{vap}} + \dot{Q}_{\text{cond}}} \tag{6.2}$$

η is the fraction of heat transfer across the membrane that is mediated by evaporation and condensation ($\dot{Q}_{\text{vap}}$), as opposed to by heat conduction ($\dot{Q}_{\text{cond}}$). A low value of η indicates significant heat conduction loss through the membrane.

For a simple MD system that does not recover energy from the condensing vapor GOR is restricted to values much smaller than 1. This is because heater heat input $\dot{Q}_{\text{h}} \geq \dot{Q}_{\text{vap}} + \dot{Q}_{\text{cond}}$ (with equality only if there are no losses), $\dot{Q}_{\text{vap}} = \dot{m}_{\text{p}} h_{\text{fg}}$, and from Eqs. 6.3 and 6.2, GOR $\leq \eta$, which is always less than 1. A low value of GOR corresponds to high specific thermal energy consumption and high OpEx.

On the other hand, GOR for practically relevant larger systems which include condensation energy recovery can be expressed as [106]:

$$\text{GOR} = \frac{\dot{m}_{\text{p}} h_{\text{fg}}}{\dot{Q}_{\text{h}}} = \eta \frac{\varepsilon}{1-\varepsilon} \tag{6.3}$$

While GOR is proportional to η, it is also affected by the extent of feed preheating, and this effect is captured by the exchanger effectiveness, $\varepsilon = (T_{\text{c,out}} - T_{\text{c,in}})/(T_{\text{c,in}} - T_{\text{c,in}})$. Feed preheating can happen within the module (gap MD systems) where the feed acts as a coolant in contact with the condensation surface, or in an external heat exchanger (HX) as in the case of DCMD, where warm pure water stream leaving the module transfers energy to the incoming feed in a HX. The interplay between η and GOR is important to understand the effect of salinity on MD performance.

In Section 6.3.1 we compare MD configurations to derive a general result comparing PGMD, CGMD and DCMD performance. The parameters of the gap and external HX decide the relative performance of these systems irrespective of feed

salinity, temperatures, membrane or channel geometry. Further comparisons in this study are therefore restricted to CGMD and AGMD. Later, in Section 6.3.4, we show that the uniqueness of AGMD performance (compared to the other three systems) is a result of its thicker 'effective membrane' which includes the air-gap. CGMD and DCMD with thick membranes would perform similar to AGMD. The gap in real AGMD systems can get flooded (especially for small gap thickness), unwittingly resulting in PGMD type operation. As a result, a CGMD or DCMD system with a thicker membrane could be more robust approach to achieving similar performance as AGMD. An important implication of this result is that the focus is shifted away from 'choice of optimal MD configuration' towards 'choice of system properties, including membrane thickness', which will be addressed in the final part of the study.

Choice of membrane thickness

Pure water flux is driven by a difference in vapor pressure between the evaporating and condensing liquid-vapor interfaces and is proportional to the membrane permeability (B). The difference in vapor pressure is influenced by the temperature difference between these two interfaces (ΔT_{m}) and feed salinity ($s_{\mathrm{f,m}}$). Heat conduction loss across the membrane is only a function of ΔT_{m}. Membrane permeability is inversely proportional to membrane thickness (δ_{m}). As thickness is decreased, flux when desalinating salty water initially increases (due to higher permeability), but starts declining as a result of conduction losses when thickness goes below an optimal value. Below this optimal thickness, ΔT_{m} across the module is low relative to the feed boiling point elevation (BPE). As a result, mass transfer is inhibited and heat conduction losses become dominant. For distillation of very low salinity water, the membrane has to be as thin as possible. The optimal membrane thickness is larger for higher salinity feed water.

Several authors have considered the question of optimal membrane thickness, especially in the context of maximizing flux in DCMD. For a small DCMD module, at fixed hot and cold side temperatures and feed salinity, an ideal value of membrane thickness can be determined to maximizes flux [34, 68].

Ali et al. [5] evaluated the optimal membrane thickness for multiple values of system size at a fixed salinity. They show that, for smaller system size, a thin membrane maximizes flux, whereas as the system size increases, the driving temperature difference (ΔT_{m}) decreases, thereby making the optimal membrane thickness larger.

Winter [126] evaluated the optimal thickness for large scale spiral wound modules under two operating conditions: high recovery and high flux. A numerical model was used to infer optimal membrane thicknesses for a given system size and feed inlet flow rate over a range of salinity levels. Two kinds of optima were identified - one that maximizes GOR and another which maximizes flux.

Identifying an optimal membrane thickness is an inherent part of MD system design. It should therefore be considered together with the choice of optimal system size, rather than independently. In Section 6.3.5 we expand on the above studies by proposing a method to identify the cost-optimal membrane thickness. The effect of membrane thickness on the GOR-flux performance curve at a given salinity is used to identify an optimal membrane thickness as a function $C_{\mathrm{GOR}}/C_{\mathrm{flux}}$.

6.2 Methodology

6.2.1 Numerical model

A length-wise discretized finite difference modeling framework is used, which has been described and validated previously [53, 98, 106, ?]. Model features that are particularly relevant to high salinity are discussed here. Pure sodium chloride solution up to 260 g/kg is considered as the feed. To account for the nonlinear effect of high feed salinity on vapor pressure, Pitzer's equations [81] describing the properties of aqueous NaCl solution were used to evaluate water activity and thereby water vapor pressure on the feed side:

$$p_{\mathrm{vap}}^{\mathrm{f,m}} = P_{\mathrm{sat}}\left(T_{\mathrm{f,m}}\right) \times a_{\mathrm{w}}\left(s_{\mathrm{f,m}}, T_{\mathrm{f,m}}\right) \tag{6.4}$$

The specific heat capacity of water changes significantly with salinity and so this

effect is also included. Enthalpy of sodium chloride solution is obtained as a polynomial fit from Pitzer's equations over $T \in [20, 90]\,^{\circ}\text{C}$ and $s \in [0, 260]$ g/kg. Similarly, the effect of increased salinity on feed thermal conductivity is included.

Since the goal of this analysis is to provide system level insights and compare various configurations, other effects of high salinity such as on viscosity are not considered. The membrane is characterized by an average permeability coefficient (B_0), thickness (δ_m), porosity (ϕ) and membrane material conductivity (k_m). Permeability to vapor (B) can be expressed as B_0/δ_m. The baseline values of system properties are listed in Table 6.2.

Validation

Experiments are conducted to evaluate the effect of feed salt concentration on MD flux. The module design is detailed elsewhere [124], and is chosen to achieve constant temperature, salinity and flowrate over the active membrane area. Figure 6-2a plots the measured flux as a function of feed inlet NaCl salinity, along with the model prediction. We can conclude that including the vapor pressure depression due to salt content is sufficient to account for the increased salinity of feed water in MD. The following parameters were used in the model (consistent with previous fitting of model performance at low salinity): $T_{\text{f,in}} = 70.4\,^{\circ}\text{C}$, $T_{\text{c,in}} = 19.5\,^{\circ}\text{C}$, $\dot{Q}_\text{f} = 15.1$ L/min, $\dot{Q}_\text{c} = 13.9$ L/min, $B = 16 \times 10^{-7}$ kg/m^2·s·Pa, $k_\text{m} = 0.2$ W/m·K, $\delta_\text{m} = 200$ μm, $\phi_\text{m} = 0.8$.

Figure 6-2b shows comparisons of present model predictions to reported data [126] on the effect of feed salinity on overall energy efficiency of larger spiral wound MD modules. The model conditions are the same as those used in [106] for comparing the effect of feed inlet temperature and flow rate. The model captures the trends observed experimentally: GOR of PGMD and DCMD are close, start higher than AGMD at low salinity, but also decline fast with increasing salinity. In contrast, AGMD GOR remains relatively constant over the entire salinity range.

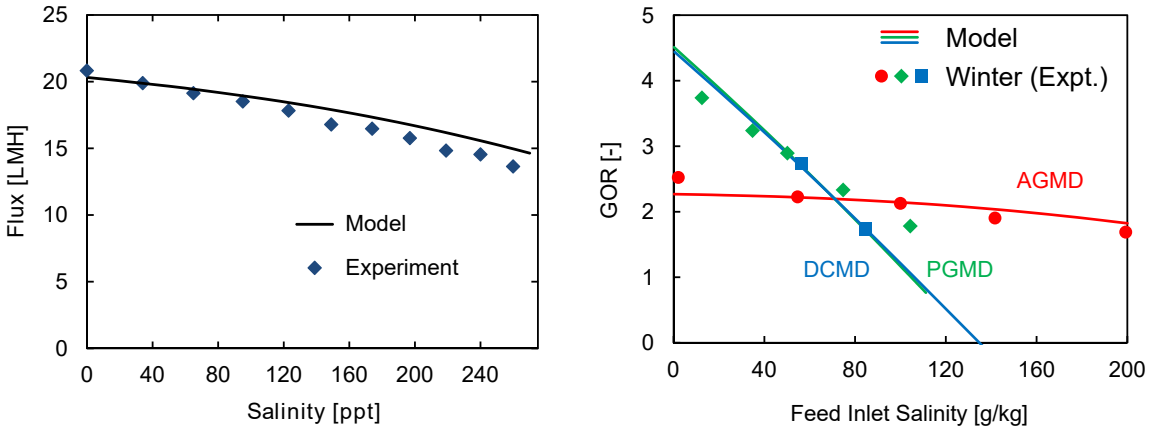

(a) Effect of high salinity on AGMD flux - comparison of experimental AGMD results with numerical model predictions.

(b) Comparison of present numerical model with experimental results from large modules reported in Winter [126].

Figure 6-2: Validation of the finite difference discretized numerical model by comparing against experimental data for flux and published data of energy efficiency with large scale modules.

6.2.2 Simplified heat exchanger (HX) analogy model adapted to high salinity

In addition to the full discretized numerical model, a much-simplified model based on a HX-analogy of MD systems was proposed in [106]. That model has a good predictive capability for the effect of system properties on GOR and flux. At seawater salinity, over a range of operating conditions, simplified model's0 predictions for GOR and flux compared to the discretized model were within 10% deviation. The model predictions are particularly good at larger system size (corresponding to higher GOR and lower flux).

This simplified HX model is also extended to higher salinities by including the effect of salt on vapor pressure and feed solution specific heat. In this model, the effect of feed salinity is included through the boiling point elevation (BPE). BPE is a function of salinity and temperature, and is evaluated at the mean temperature and at a salinity 4% higher than the inlet feed stream (to account for feed concentration change with length and concentration polarization. In reality, concentration polarization is a function of flux and channel mass transfer coefficient, which can be

implemented if better accuracy is desired at high flux). The full set of HX model equations along with the equations for finding the critical system size (as explained in Section 6.3.3) are provided in 6.5.6.

Comparison of the simplified HX model with the discretized model are provided in Fig. 6-8 before the HX model is used to derive an expression for critical system size.

6.3 Results and Discussion

In Section 6.3.1, the comparison between single stage MD configurations based on the heat exchanger analogy is generalized to be valid up to high salinity. Limiting case CGMD (with infinite gap conductance) and DCMD (with infinite HX area) are found to perform similarly irrespective of feed salinity. A real CGMD system always outperforms PGMD (since PGMD has a lower gap conductance), and CGMD or PGMD would outperform DCMD if the external HX area is smaller than $A_{\mathrm{MD}} \times \frac{h_{\mathrm{gap}}}{U_{\mathrm{HX}}}$. In subsequent subsections, comparisons are restricted to those between CGMD and AGMD.

The concept of critical MD membrane area for high salinity applications is discussed in Section 6.3.2. As system size is increased beyond this critical value, both GOR and flux start to deteriorate. In Section 6.3.3, a closed-form expression for this critical size is derived as function of feed salinity and two non-dimensional ratios of heat transfer resistances within the MD module.

In Section 6.3.4 air gap MD is brought into the HX analogy framework of MD by recognizing that AGMD performance is similar to that of CGMD system with a thicker less conductive membrane. This is because the air gap and membrane both occur between the evaporating and condensing liquid interfaces in AGMD, and these layers together constitute the 'effective membrane'. Some implications of this result for the choice of MD configuration are then discussed.

Finally, in Sec. 6.3.5, we discuss the role of membrane thickness. The optimal thickness that results in maximum GOR is not only a function of feed salinity but

also depends on flux. A framework for simultaneously choosing MD system size and membrane thickness to minimize overall cost of pure water production is described.

6.3.1 Single stage MD configurations comparison: Recap and generalized results applicable to high salinity

In a previous study [103], single stage MD configurations were compared in terms of both GOR and flux simultaneously. In order to make the comparisons fair, the membrane properties and feed/cold channel heat transfer coefficients were held constant across the different configurations.

The following parameters specific to each of the configurations were used:

- For AGMD, PGMD, CGMD: effective gap thickness $d_{\text{gap}} = 1$ mm. k_{gap} is 0.6 W/m-K for PGMD and 10 W/m-K for CGMD.
- For DCMD: $A_{\text{HX}} = A_{\text{membrane}}$, $U_{\text{HX}} = 1300$ W/m^2-K.

Under these conditions, for $s = 35$ g/kg, the previous study concluded that at the same flux, the GOR of CGMD is about 2 times higher than those of AGMD and PGMD, and about 40% higher than that of DCMD. In this section, we develop a general comparison between PGMD, CGMD and DCMD that is valid over a range of feed salinities, gap conductances and external HX designs.

To develop this general comparison, we use the simplified HX analogy model (based on the ε-NTU method) for CGMD, PGMD, and DCMD. The simplified HX modeling was restricted to these three configurations for which vapor transport across the membrane is directly influenced by the temperature difference between the two faces of the membrane. In AGMD, one side of the membrane faces air which may not be saturated with vapor. Hence, temperature and vapor pressure are not necessarily related as $T = T_{\text{sat,water}}(p_{\text{vap}})$. Also, in AGMD, the resistance of the air-gap to vapor diffusion must be considered. In Section 6.3.4, the limitation of the simplified HX model's applicability to AGMD is ameliorated.

Figure 6-4 illustrates the resistance network used to analyze PGMD, CGMD and DCMD. In DCMD, the heated pure water exiting the module transfers energy to

preheat the feed in a separate counterflow HX whose area can be adjusted independent of the MD membrane area (cf. Fig. 6-1). Note that for two balanced counterflow heat exchangers with an intermediate fluid, the overall thermal resistance is simply the sum of the thermal resistances of the two heat exchangers (Fig. 6-3). Therefore the pure stream nodes of the MD system and the HX can simply be connected as shown in Fig. 6-4.

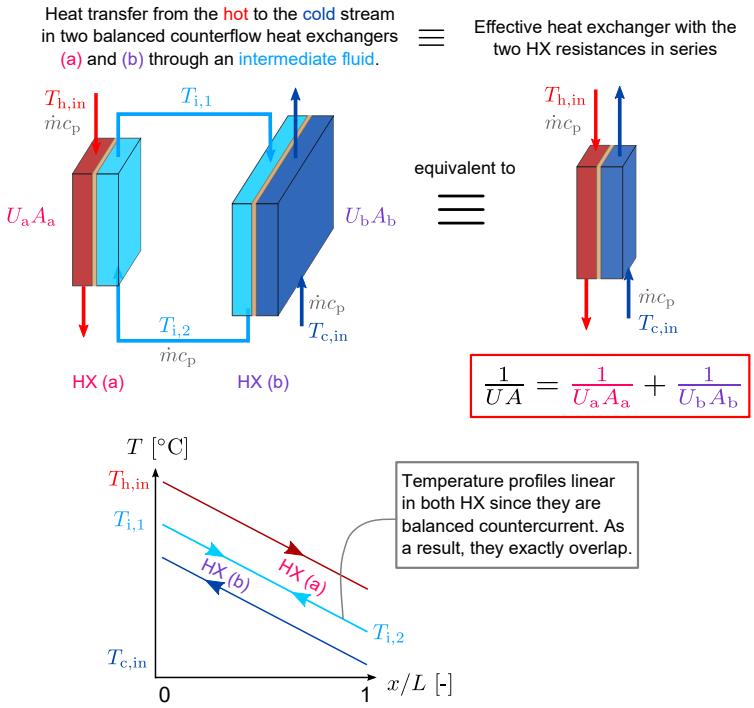

Figure 6-3: If heat is transfered from a hot fluid (feed stream in DCMD) to a cold stream (feed preheating stream) using two balanced counterflow heat exchangers (MD module and external HX), the overall resistance is simply the sum of the individual HX resistances. The intermediate fluid corresponds to the pure water stream in DCMD.

The goal of MD system design is to decrease the overall resistance between the feed stream (T_f) and the preheating feed stream ($T_{f,ph}$) such that maximum energy is recovered for a given system size leading to a reduction in external heating load. Simultaneously, high η must be ensured in order that heat conduction losses through the membrane are reduced. To do this, the resistance of the membrane to conduction has to be larger than its resistance to vapor transport.

Only the membrane mass transfer resistance, in this simplified model, is a function

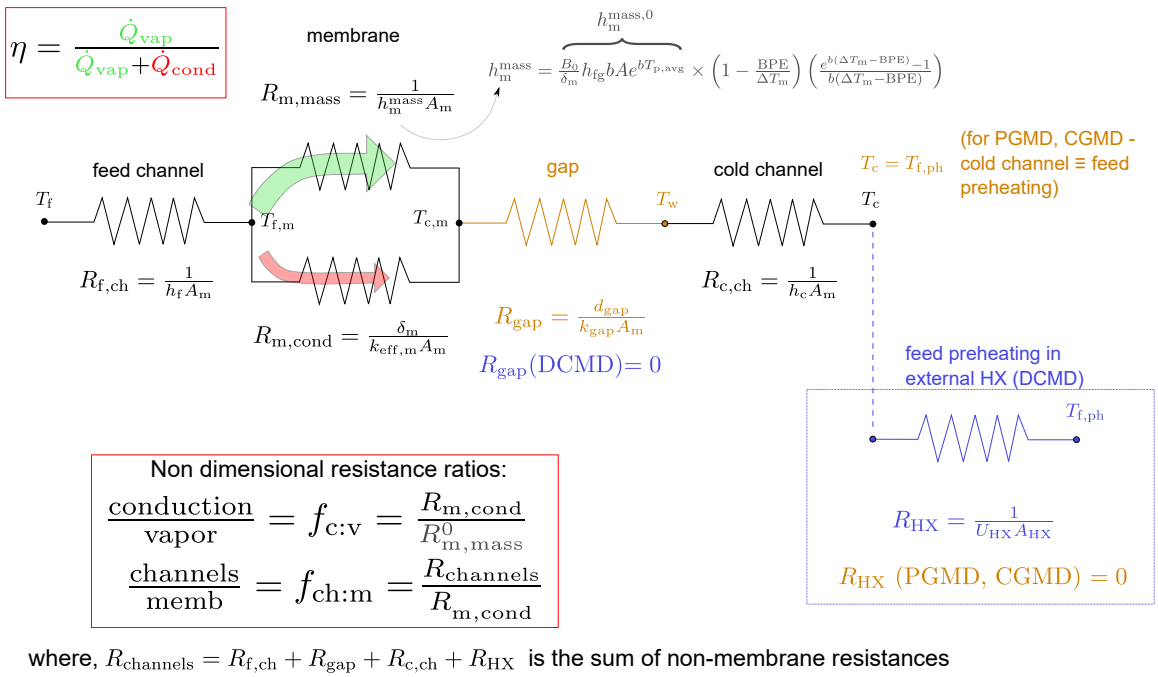

Figure 6-4: The resistance network decribing the HX analogy model of MD, along with two non-dimensional heat transfer resistance or conductance ratios.

of system size. This resistance is a function of the driving temperature difference (ΔT_m) and the boiling point elevation (BPE) of the feed stream. At larger system size, ΔT_m decreases leading to a decrease in h_m^{mass} and increase in $R_{m,mass}$. The non-dimensional resistance ratios will be discussed in detail in Section 6.3.3.

Based on the resistance networks, we can expect that the limiting performance of CGMD (with 0 gap resistance) and DCMD (with 0 external HX resistance) are similar. The energy efficiency of these limiting case designs can be denoted by $GOR^{\infty k}_{CGMD}$ and $GOR^{\infty HX}_{DCMD}$. These limiting systems (at equal area and channel heat transfer coefficients) were compared over a range of system sizes and feed inlet salinity values up to 240 g/kg. Numerically, we confirm $GOR^{\infty HX}_{DCMD} \approx GOR^{\infty k}_{CGMD} \equiv GOR^{limit}$. On average, $GOR^{\infty HX}_{DCMD}$ is marginally (about 1%) greater than $GOR^{\infty k}_{CGMD}$. For the same membrane area, the DCMD system has a lower average flow rate, and hence higher NTU and ε. Along with the difference in balancing [105, 103] of the two exchangers, this can help explain the small difference in performance of the two limiting case designs. Overall, the GOR of these limiting case systems are almost identical. Note

that this $\mathrm{GOR}^{\mathrm{limit}}$ is defined for a specific membrane, feed/cold channel heat transfer coefficient and system size, and does not represent a general upper limit.

For balanced counterflow exchangers that are considered here, the exchanger effectiveness, $\varepsilon = \frac{T_{\mathrm{c,out}} - T_{\mathrm{c,in}}}{T_{\mathrm{h,in}} - T_{\mathrm{c,in}}}$, can be expressed as a function of the number of transfer units, which is a non-dimensional measure of its heat transfer area ($\mathrm{NTU} = UA/\dot{m}_{\mathrm{f}} c_{\mathrm{p}}$, where U is the overall heat transfer coefficient, A is system area and $\dot{m} c_{\mathrm{p}}$ is heat capacity rate):

$$\varepsilon = \frac{\mathrm{NTU}}{1 + \mathrm{NTU}} \tag{6.5}$$

Substituting Eq. 6.5 in Eq. 6.3:

$$\mathrm{GOR} = \eta \times \mathrm{NTU} \tag{6.6}$$

A practical CGMD (and PGMD) or DCMD system would deviate from its limiting case performance due to the limited conductance of the gap or a finite external HX. Therefore, the GOR of a practical CGMD or PGMD system (whose η and U would deviate from the limiting case system) can be written (using Eq. 6.6) as

$$\begin{aligned}
\mathrm{GOR}_{\mathrm{CGMD,PGMD}} &= \mathrm{GOR}^{\mathrm{limit}} \times \frac{\eta}{\eta_{\mathrm{limit}}} \frac{U}{U_{\mathrm{limit}}} \\
&= \mathrm{GOR}^{\mathrm{limit}} \times \frac{\eta}{\eta_{\mathrm{limit}}} \frac{\frac{1}{h_{\mathrm{eff,m}}} + \frac{1}{h_{\mathrm{t,c}}} + \frac{1}{h_{\mathrm{t,f}}}}{\frac{1}{h_{\mathrm{eff,m}}} + \frac{1}{h_{\mathrm{t,c}}} + \frac{1}{h_{\mathrm{t,f}}} + \frac{1}{h_{\mathrm{gap}}}} \\
&= \mathrm{GOR}^{\mathrm{limit}} \times \frac{\eta}{\eta_{\mathrm{limit}}} \frac{U_{\mathrm{limit}}^{-1}}{U_{\mathrm{limit}}^{-1} + h_{\mathrm{gap}}^{-1}} \\
&= \mathrm{GOR}^{\mathrm{limit}} \times \frac{\eta}{\eta_{\mathrm{limit}}} \frac{1}{1 + \frac{U_{\mathrm{limit}}}{h_{\mathrm{gap}}}}
\end{aligned} \tag{6.7}$$

where U_{limit} and η_{limit} are the overall heat transfer coefficient and membrane thermal efficiency for the limiting case system with no gap resistance. PGMD would have a lower h_{gap} than CGMD. When all the other parameters are fixed (irrespective of their actual values), a system with lower h_{gap} always leads to a decline in performance. For relatively high k_{gap}, such as the 10 W/m-K assumed for the CGMD system in [103], $\eta \approx \eta_{\mathrm{limit}}$. Hence,

$$\mathrm{GOR_{CGMD}} \approx \mathrm{GOR^{limit}} \times \frac{1}{1+\frac{U_{\mathrm{limit}}}{h_{\mathrm{gap}}}} \tag{6.8}$$

Similarly, for a realistic DCMD, an equation for GOR can also be developed as a function of the system's heat transfer parameters:

$$\begin{aligned}
\mathrm{GOR_{DCMD}} &\approx \mathrm{GOR^{limit}} \times \frac{\mathrm{TTD_{MD}}}{\mathrm{TTD_{MD}}+\mathrm{TTD_{HX}}} \\
&= \mathrm{GOR^{limit}} \times \frac{1}{1+\frac{\mathrm{TTD_{HX}}}{\mathrm{TTD_{MD}}}} \\
&= \mathrm{GOR^{limit}} \times \frac{1}{1+\left(1-\frac{\mathrm{TTD_{MD}}}{\Delta T_{\mathrm{max}}}\right)\frac{\mathrm{NTU_{limit}}+1}{\mathrm{NTU_{HX}}+1}} \\
&= \mathrm{GOR^{limit}} \times \frac{1}{1+\frac{U_{\mathrm{limit}}A_{\mathrm{m}}}{U_{\mathrm{HX}}A_{\mathrm{HX}}+\dot{m}c_{\mathrm{p}}}}
\end{aligned} \tag{6.9}$$

where the following substitutions are made to obtain the result: $\mathrm{TTD} = \Delta T_{\mathrm{max}}(1-\varepsilon)$, $\Delta T_{\mathrm{max}}^{\mathrm{MD}} = \Delta T_{\mathrm{max}} = T_{\mathrm{f,in}} - T_{\mathrm{c,in}}$, $\Delta T_{\mathrm{max}}^{\mathrm{HX}} = T_{\mathrm{c,out}} - T_{\mathrm{c,in}} = \Delta T_{\mathrm{max}} - \mathrm{TTD_{MD}}$ (cf. Fig. 6-1).

For large $\mathrm{NTU_{HX}} > 1$ (which is necessary for high GOR), an approximate expression for the GOR of a realistic DCMD system can be obtained:

$$\mathrm{GOR_{DCMD}} \approx \mathrm{GOR^{limit}} \times \frac{1}{1+\frac{U_{\mathrm{limit}}A_{\mathrm{m}}}{U_{\mathrm{HX}}A_{\mathrm{HX}}}} \tag{6.10}$$

The two approximate expressions (Eqs. 6.8,6.10), can be used to compare the GOR of DCMD and PGMD/CGMD based on the heat transfer resistances of the heat exchanger in DCMD and the gap in PGMD/CGMD. If $U_{\mathrm{HX}}A_{\mathrm{HX}}$ is lower than $h_{\mathrm{gap}}A_{\mathrm{m}}$, the corresponding DCMD system's GOR will be lower than that of the gap MD system. A similar conclusion can be obtained by inspection from Fig. 6-4. The above result on the relative performance of DCMD and CGMD is validated using the discretized numerical models in 6.5.3.

Figure 6-5 shows the approximate external area requirement in DCMD to achieve the same GOR as a CGMD system, which defined by its gap conductance. The following conditions were considered in Ref. [106]: $h_{\mathrm{gap}} = 10000$ W/m^2·K, and $U_{\mathrm{HX}} = 1300$ W/m^2·K. Numerical modeling of the full systems showed that the DCMD HX had to be about 7 times the size of the membrane to match the GOR of the CGMD

system. DCMD with $A_{HX} = A_m$ was also found to outperform PGMD (with $h_{gap} =$ 600 W/m^2·K). Similar conclusions can be drawn without full modeling from Figure 6-5.

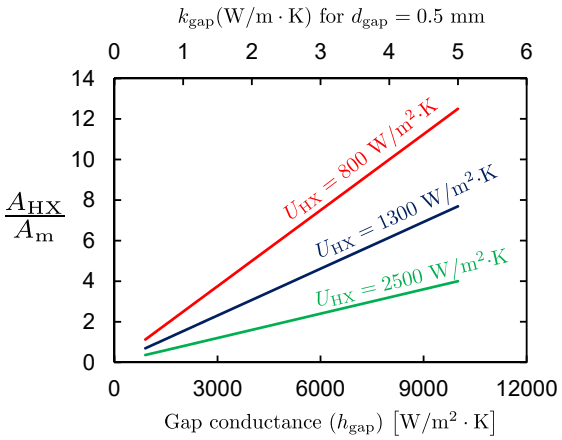

Figure 6-5: The relative size of HX in DCMD to match a CGMD system's GOR.

We have shown that similar performance can be obtained with CGMD or DCMD, based on the choice of gap conductance and external HX size. Designers can consider the cost of implementing these two alternatives (external HX and increasing gap conductance) to obtain similar performance, in order to choose the cheaper option. The additional metal required for implementing CGMD (by lowering gap thickness, adding fins or using a metal spacer in the thin gap) is likely to be much less than the corresponding metal requirement for making the HX larger (about 5 times the membrane area would be needed in DCMD). Note that the use of an external heat exchanger would lead to additional pumping power consumption, which may also influence the choice of best configuration.

The foregoing analysis is silent on the relative performance of AGMD compared to these other systems. In subsequent sections, comparisons will be limited to between AGMD and CGMD with $h_{gap} = 10^4$ W/m^2·K.

6.3.2 Effect of salinity on GOR-flux performance: Systems larger than a critical size must be avoided

For a zero salinity feed stream, the thermodynamic maximum GOR is ∞ [106]. In other words, the thermodynamic least energy required to create pure water from already pure water is 0. With a membrane distillation system, this situation is realized with $A_{\mathrm{MD}} \to \infty$, which correspondingly leads to $J \to 0$. At higher feed salinity, the thermodynamic maximum GOR can be expressed as $\mathrm{GOR}_{\mathrm{max,MD}} = \frac{T_{\mathrm{f,in}} - T_{\mathrm{c,in}}}{\mathrm{BPE}_{\mathrm{f,in}}} - 1$ [106]. This second case (for non-zero salinity) can be achieved in MD only with a perfectly insulating membrane, where even the vapor does not conduct any heat from the feed side to the cold side ($\eta = 1$), and $A_{\mathrm{MD}} \to \infty$, and correspondingly, $J \to 0$ LMH.

For real membranes, $\eta \neq 1$, and η decreases with an increase in system size. In fact, beyond a certain 'critical system size', the rate of decrease of η is faster than the increase in $\frac{\varepsilon}{1-\varepsilon}$, leading to a net decline in GOR $= \eta\varepsilon/(1-\varepsilon)$ (Fig. 6-6). While flux keeps decreasing with an increase in system size, beyond the critical system size, GOR also starts declining rather than improving. As a result, there is no rationale for designing or operating an MD system under this 'counterproductive operating condition'.

Figure 6-6 shows GOR as a function of system size for CGMD and AGMD at multiple feed inlet salinity levels. The system properties are specified in Table 6.2. System size is expressed as a specific area per unit feed flow rate. 2 m^2/(kg/min) here corresponds to a module length of 10 m - and this is close to the critical size for $s_{\mathrm{in}} = 105$ g/kg. The critical system size decreases as inlet salinity increases.

AGMD is more resistant to changes in feed salinity. AGMD also has a critical system size (see Fig. 6-7), but this size is quite large. At smaller sizes, CGMD outperforms AGMD irrespective of feed salinity, but the GOR of AGMD continues to increase even as that for CGMD starts to decline. This indicates that, while at $s_{\mathrm{in}} = 35$ g/kg, CGMD performed two times better than AGMD, this trend does not hold at higher salinity. In fact, the absolute maximum GOR achievable with AGMD is much higher, albeit at the cost of a larger system size.

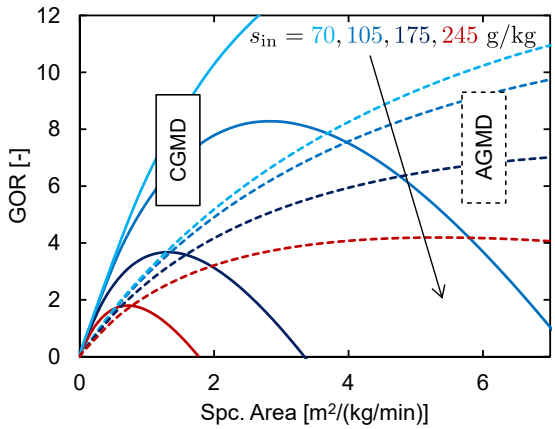

Figure 6-6: GOR starts declining beyond a critical system size, which decreases at higher salinity. Maximum GOR achieved by AGMD (dotted lines) is higher than CGMD (solid lines) at high s, but the system size required is also larger. System parameters: Table 6.2.

The overall performance comparison of AGMD and CGMD needs to consider both GOR and flux. This is presented in Fig. 6-7. At higher feed salinity, AGMD outperforms CGMD at several operating points in terms of both GOR and flux.

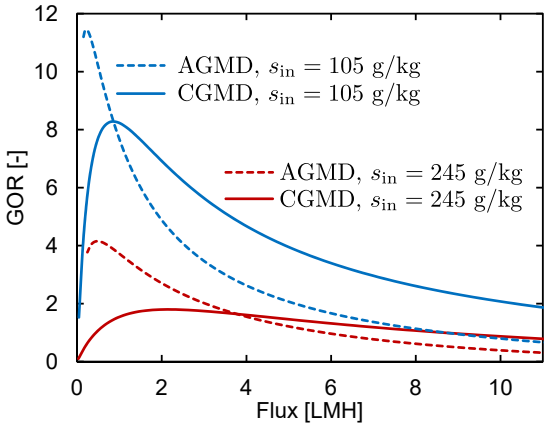

Figure 6-7: GOR vs. flux curves for AGMD and CGMD at high salinity ($s_{in} = 105, 245$ g/kg). The result for low salinity that CGMD outperforms AGMD is no longer valid. At high salinity, AGMD outperforms CGMD at low flux, and achieves a higher max GOR. At s_{in} = 245 g/kg, AGMD performs better energetically even at practically relevant values of flux= 2–4 LMH. System parameters: Table 6.2.

Note that these results and comparisons are for a relatively thick membrane (δ_m = 200 μm). At lower membrane thickness, the maximum GOR and critical system size of CGMD would drop even further. AGMD on the other hand, would not be affected

much by membrane thickness, since the 1 mm thick air-gap dictates the performance rather than the membrane thickness.

6.3.3 Evaluating critical system size as a function of heat transfer resistances

The goal of this section is to derive a generally applicable expression for critical system size, using the simplified HX modeling framework. In order to make this expression generally applicable, we would like to use non-dimensional parameters to describe the system properties. From Eq. 6.6, GOR $= \eta \times$ NTU, where NTU $= UA/\dot{m}c_{\mathrm{p}}$.

U is the overall heat transfer coefficient from the hot stream to the cold (feed preheat) stream. The channel and gap heat transfer coefficients can be assumed to be effectively independent of system size, but $h_{\mathrm{mass,m}}$ (the effective heat transfer coefficient associated with vapor transport across the membrane) is a function of ΔT_{m}. Local ΔT_{m} along the module length is usually lower at the hot end compared to the cold end, since the resistance of the membrane is lower at higher temperature. Variations in ΔT_{m} along length are averaged out in the simplified HX model, and in defining U of the exchanger. Like TTD, average ΔT_{m} also changes significantly with system size, and will decrease at larger exchanger area. Lower ΔT_{m} leads to smaller $h_{\mathrm{mass,m}}$ and correspondingly a decrease in U. Therefore, NTU for an MD system does not vary linearly with size, since U is a function of system size.

Figure 6-8 shows GOR as a function of NTU for various feed salinity levels. The dotted lines are from the simplified HX model of MD. Note that the HX model is able to effectively capture the GOR vs. NTU curves, including the peak GOR and critical system NTU. For pure water, GOR continuously increases with an increase in system size. GOR has no thermodynamic upper limit in this case. This is a result of η remaining relatively unchanged (for pure feed) as the driving temperature difference across the membrane ΔT_{m} decreases. Experimentally, an equivalent result was observed for η as a function of membrane thickness in DCMD. Even at low membrane thickness (corresponding to small ΔT_{m}, η does not decline for a pure feed

[34, 68].

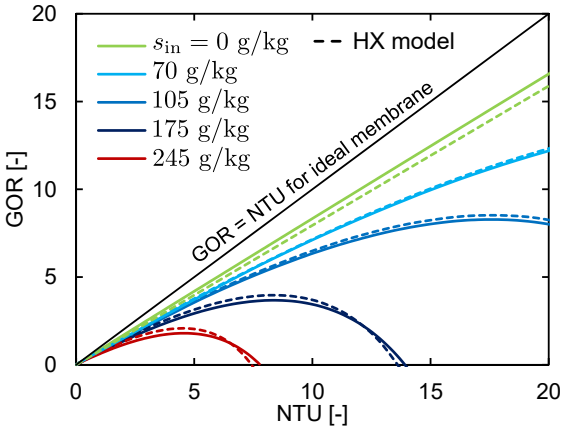

Figure 6-8: GOR is plotted against NTU to show the existence of a critical size (NTU*) beyond which GOR decreases. The operating conditions should always be to the left of this point. Dotted lines show results from the simplified HX model, and indicates that the peak is captured quite well by the simplified HX model as well. System parameters: Table 6.2.

At higher feed salinity on the other hand, while ε increases as system size increases, η decreases due to a decrease in the flux-driving temperature difference. This is modeled in the HX model, based on the approximation $p_{\mathrm{vap}}(T,s) = P_{\mathrm{sat}}(T) \times a_{\mathrm{w}}(T,s) \approx P_{\mathrm{sat}}(T - \mathrm{BPE}(s,T))$, as

$$\eta = \frac{1}{1 + \left[\phi_{\mathrm{c:v}} \left(1 - \frac{\mathrm{BPE}}{\Delta T_{\mathrm{m}}}\right) \left(\frac{e^{b(\Delta T_{\mathrm{m}} - \mathrm{BPE})} - 1}{b(\Delta T_{\mathrm{m}} - \mathrm{BPE})}\right)\right]^{-1}} \tag{6.11}$$

where $\phi_{\mathrm{c:v}}$ is a non-dimensional ratio of the membrane resistance to heat conduction and vapor mass transport:

$$\phi_{\mathrm{c:v}} = \frac{R_{\mathrm{m,cond}}}{R^0_{\mathrm{m,mass}}} = \frac{B_0 h_{\mathrm{fg}} b A e^{\mathrm{bT_{p,avg}}}}{k_{\mathrm{eff,m}}} \tag{6.12}$$

A and b are obtained by fitting $P_{\mathrm{sat}}(T) = \mathrm{A}e^{\mathrm{b}T}$: A = 1054.8 Pa, b = 0.0479 °C^{-1}. Since heat conduction across the membrane constitutes a loss, an ideal membrane would have $\phi_{\mathrm{c:v}} \to \infty$. Note that $\phi_{\mathrm{c:v}}$ is defined to be independent of system size, i.e., independent of ΔT_{m}, by considering $R^0_{\mathrm{m,mass}}$ (See Fig. 6-4) instead of the total resistance to vapor mass transport $R_{\mathrm{m,mass}}$. Also, $\phi_{\mathrm{c:v}}$ is independent of membrane

thickness. A thicker membrane would affect both vapor permeability ($B = B_0/\delta_\mathrm{m}$) and heat conductance ($h_\mathrm{cond,memb} = k_\mathrm{m}/\delta_\mathrm{m}$) similarly, and hence does not impact this ratio. Stated another way, $\phi_\mathrm{c:v}$ is the non-dimensional ratio of membrane's vapor permeability coefficient to its effective thermal conductivity.

NTU can be expressed as a function of $\phi_\mathrm{c:v}$, ΔT_m, salinity (through BPE), and an additional non-dimensional resistance ratio ($\phi_\mathrm{ch:m}$) as:

$$\mathrm{NTU} = \frac{\Delta T_\mathrm{max}}{1 + \phi_\mathrm{ch:m} + \phi_\mathrm{ch:m}\phi_\mathrm{c:v}\left(1 - \frac{\mathrm{BPE}}{\Delta T_\mathrm{m}}\right)\left[\frac{e^{b(\Delta T_\mathrm{m} - \mathrm{BPE})} - 1}{b(\Delta T_\mathrm{m} - \mathrm{BPE})}\right]} - 1 \tag{6.13}$$

where $\phi_\mathrm{ch:m}$ is a ratio of the heat transfer resistance of the rest of module (other than the membrane) to the heat conduction resistance offered by the membrane:

$$\phi_\mathrm{ch:m} = \frac{\left(\frac{1}{h_\mathrm{f}} + \frac{1}{h_\mathrm{c}} + \frac{d_\mathrm{gap}}{k_\mathrm{gap}}\right)}{\frac{\delta_\mathrm{m}}{k_\mathrm{m}}} \tag{6.14}$$

$\phi_\mathrm{ch:m}$ effectively helps compare ΔT_m with TTD or ΔT_b (temperature difference between the hot and cold bulk streams). An ideal MD system would have $\Delta T_\mathrm{m} = \Delta T_\mathrm{b}$ so that the vapor flux driving temperature difference is maximized. This ideal MD system would therefore have zero resistance in other portions of the module (channels, gap, external HX, and condensation surface). The actual resistance of the membrane relative to the overall resistance between the feed and cold bulk streams is

$$\frac{R_\mathrm{membrane}}{R_\mathrm{total}} = \frac{1}{1 + \phi_\mathrm{ch:m}\left[1 + \phi_\mathrm{c:v}\left(1 - \frac{\mathrm{BPE}}{\Delta T_\mathrm{m}}\right)\left(\frac{e^{b(\Delta T_\mathrm{m} - \mathrm{BPE})} - 1}{b(\Delta T_\mathrm{m} - \mathrm{BPE})}\right)\right]} \tag{6.15}$$

This fraction tends to 1 for an ideal system, and this corresponds to $\phi_\mathrm{ch:m} \to 0$. Like $\phi_\mathrm{c:v}$, $\phi_\mathrm{ch:m}$ is also defined to be independent of system size. Note that $\phi_\mathrm{ch:m}$ is a function of membrane thickness. A thicker membrane results in a lower value of $\phi_\mathrm{ch:m}$, but ideally $\phi_\mathrm{ch:m}$ should be reduced by decreasing resistances elsewhere (such as by increasing gap conductance or HX area) rather than by making the membrane thicker. While both strategies may lead to the same value of $\phi_\mathrm{ch:m}$, reducing resistances in the flow channels can help reduce overall system size (by increasing flux), whereas choosing thicker membrane has the opposite effect. The effect of changing $\phi_\mathrm{ch:m}$ by

changing these two resistances is discussed in 6.5.5

Putting Eqs. 6.11 and 6.13 together, GOR can be expressed as a function of $\phi_{\text{ch:m}}$, $\phi_{\text{c:v}}$, BPE, ΔT_{m}, and $\Delta T_{\text{max}} = T_{\text{f,in}} - T_{\text{c,in}}$:

$$\text{GOR} = \frac{\frac{\Delta T_{\text{max}}}{1+\phi_{\text{ch:m}}+\phi_{\text{ch:m}}\phi_{\text{c:v}}\left(1-\frac{\text{BPE}}{\Delta T_{\text{m}}}\right)\left[\frac{e^{b(\Delta T_{\text{m}}-\text{BPE})}-1}{b(\Delta T_{\text{m}}-\text{BPE})}\right]} - 1}{1+\left[\phi_{\text{c:v}}\left(1-\frac{\text{BPE}}{\Delta T_{\text{m}}}\right)\left(\frac{e^{b(\Delta T_{\text{m}}-\text{BPE})}-1}{b(\Delta T_{\text{m}}-\text{BPE})}\right)\right]^{-1}} \tag{6.16}$$

Table 6.1 summarizes the practical significance of the generalized non-dimensional and other parameters.

Now that GOR is expressed as a function of module properties (in non-dimensional form), salinity, and ΔT_{m}. As described previously, ΔT_{m} decreases with an increase in system size, and can be taken as a proxy for system size in the GOR expression. The critical system size (NTU^{crit} or L^{crit}) above which MD systems should not be operated can be evaluated by finding $\Delta T_{\text{m}}^{\text{crit}}$ (below which the system should not be operated). GOR reaches a maximum at this critical system size (see Fig, 6-8). Near the peak GOR, $\Delta T_{\text{m}} \approx \text{BPE}$, and hence $\frac{e^{b(\Delta T_{\text{m}}-\text{BPE})}-1}{b(\Delta T_{\text{m}}-\text{BPE})} \approx 1$, and hence the GOR expression can be simplified to:

$$\text{GOR} \approx \frac{\frac{\Delta T_{\text{max}}}{1+\phi_{\text{ch:m}}+\phi_{\text{ch:m}}\phi_{\text{c:v}}\left(1-\frac{\text{BPE}}{\Delta T_{\text{m}}}\right)} - 1}{1+\left[\phi_{\text{c:v}}\left(1-\frac{\text{BPE}}{\Delta T_{\text{m}}}\right)\right]^{-1}} \tag{6.17}$$

By setting $\frac{\partial \text{GOR}}{\partial \Delta T_{\text{m}}} = 0$, $\Delta T_{\text{m}}^{\text{crit}}$ can be expressed as an explicit function of $\phi_{\text{ch:m}}$, $\phi_{\text{c:v}}$, BPE and ΔT_{max}:

$$\Delta T_{m}^{\text{crit}} = \text{BPE}\cdot\phi_{\text{ch:m}}\times \left[\frac{\Delta T_{\text{max}}+\phi_{\text{c:v}}\left(\Delta T_{\text{max}}+\phi_{\text{ch:m}}\cdot\text{BPE}\right)+\sqrt{\frac{\Delta T_{\text{max}}(1+\phi_{\text{ch:m}})(\Delta T_{\text{max}}+\phi_{\text{c:v}}(\Delta T_{\text{max}}-\text{BPE}))}{1+\phi_{\text{ch:m}}(1+\phi_{\text{c:v}})}}}{\left(\Delta T_{\text{max}}+\phi_{\text{ch:m}}\cdot\text{BPE}\right)\left(1+\phi_{\text{ch:m}}\left(1+\phi_{\text{c:v}}\right)\right)-\Delta T_{\text{max}}}\right] \tag{6.18}$$

The NTU^{crit} at which GOR is maximized can in turn be obtained by plugging $\Delta T_{\text{m}}^{\text{crit}}$ into Eq. 6.13. NTU^{crit} as a function of $\phi_{\text{ch:m}}$, $\phi_{\text{c:v}}$ and salinity is plotted in Fig. 6-9.

NTU is defined as $\frac{UA}{\dot{m}c_p}$. $UA\Delta T_{\text{b}} = \dot{m}c_p\Delta T_{\text{c,axial}}$, where ΔT_{b} is the temperature

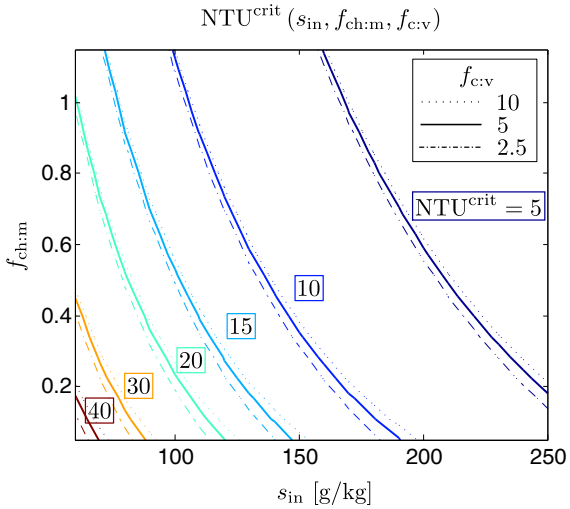

Figure 6-9: Level curves of NTU^{crit} as a function of $\phi_{\text{ch:m}}$ (ratio of channels' resistance to membrane conduction resistance), salinity and $\phi_{\text{c:v}}$ (non-dimensional ratio of membrane vapor permeability to thermal conductivity). Design and operation should ensure $\text{NTU} < \text{NTU}^{\text{crit}}$.

difference between the feed and cold bulk temperatures, and $\Delta T_{\text{c,axial}}$ is the temperature difference along the length of the cold channel. As a result, $\text{NTU} = \frac{\Delta T_{\text{c,axial}}}{\Delta T_{\text{b}}} \approx \frac{T_{\text{c,out}} - T_{\text{c,in}}}{T_{\text{f,in}} - T_{\text{c,out}}}$. These temperatures can be readily measured for an MD module in operation to infer NTU and ensure operation at $\text{NTU} < \text{NTU}^{\text{crit}}$.

NTU^{crit} as a non-dimensional parameter is useful when a system is in operation and inlet and outlet temperatures can be measured. For designing a system, however, the more relevant parameter is the critical length of the module. This critical length can be represented as a function of feed salinity, and non dimensional parameters $\phi_{\text{ch:m}}$ and $\phi_{\text{c:v}}$ as shown in Fig. 6-10. The dimensional critical length also depends on the actual resistance within the module, in addition to the non-dimensional resistance ratios. Figure 6-10 is for $h_{\text{f}} = h_{\text{c}} = 2520$ W/m^2·K, and $h_{\text{gap}} = 10^4$ W/m^2·K, $w = 12$ m, $\dot{m}_{\text{f,in}} = 1$ kg/s.

The maximum length and NTU are strong functions of $\phi_{\text{ch:m}}$ and BPE and are affected less by $\phi_{\text{c:v}}$. The maximum module length is extremely high at low salinities as long as $\phi_{\text{ch:m}}$ is small enough, i.e. the membrane is thick and heat transfer coefficients of non-membrane elements are high. At larger feed salinity, the maximum allowable length decreases (even for a relatively thick membrane). Similarly, as $\phi_{\text{ch:m}}$ increases

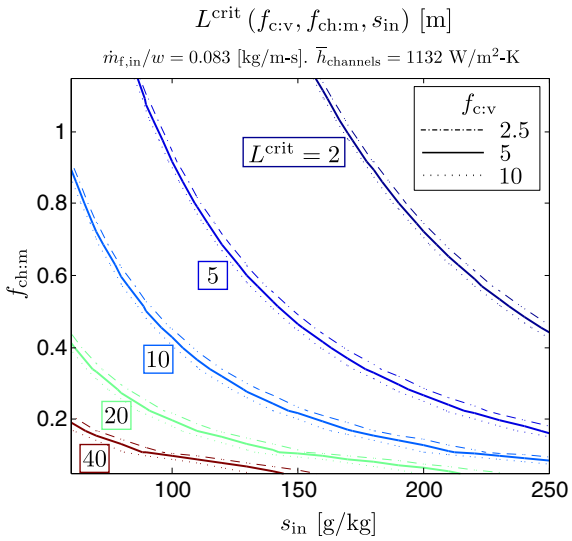

Figure 6-10: Level curves of L^{crit} (in meters) as a function of $\phi_{\text{ch:m}}$, salinity and $\phi_{\text{c:v}}$. This dimensional result is valid for $\overline{h}_{\text{channels}} = 1132$ W/m-K (overall heat transfer coefficient of non-membrane regions), and $\dot{m}_{\text{f,in}}/w = 0.0833$ kg/m-s.

(thinner membrane or higher resistances in other parts of the module other than the membrane), the allowable maximum length decreases. Since GOR = ηNTU (and $\eta^{\text{crit}} \approx 0.4$–$0.6$ at NTU = NTU$^{\text{crit}}$)), in order to achieve high GOR at high feed salinity, it is important to have a low value of $\phi_{\text{ch:m}}$.

The GOR obtained by setting $L = L^{\text{max}}$ is almost identical (within 1%) to the maximum GOR obtained by numerical optimization of the full 1D module over a range of $s_{\text{in}} = 70, 250$ g/kg, $\phi_{\text{ch:m}} = 0.05$–$1.15$, and $\phi_{\text{c:v}} = 3.1, 6.2$.

The above framework for critical system size for a desired feed treatment capacity (at the design stage) can also be applied to finding the critical feed flow rate for a fixed membrane area (e.g., a real system in operation). If channel heat transfer coefficients are independent of flow rate, the critical system size predicted by Fig. 6-10 would have to be matched by increasing feed flow rate instead. As systems should be designed at $L < L^{\text{crit}}$, they should be operated at $\dot{m}_{\text{f}} > \dot{m}_{\text{f}}^{\text{crit}}$. Another way to adjust $\dot{m}_{\text{f}}$ would be to increase the flow rate until NTU is lower than NTU$^{\text{crit}}$ (Fig. 6-9).

Winter et al. [127] noted the existence of a practically relevant value of NTU$^{\text{crit}}$ or $\dot{m}_{\text{f}}^{\text{crit}}$ at high salinity based on experiments with large-scale PGMD modules (Fig. 6-11). Note that the experimental data at $s = 50$ g/kg and 75 g/kg reach a maximum,

with changes in feed flow rate. The numerical model (now including the effect of feed flow on channel heat transfer coefficient) can also predict the existence of a critical flow rate and maximum GOR. If the flow rate is set based on the HX model equation for NTU^{crit}, the GOR obtained is very close to the numerical model's max. GOR.

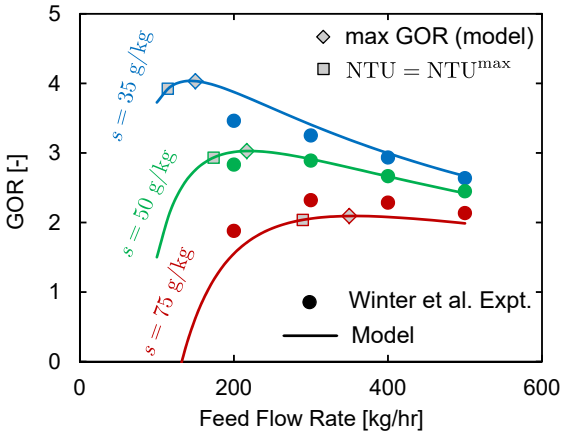

Figure 6-11: Effect of flowrate on NTU^{crit} of a fixed size system at various salinity levels. Data from Winter et al. [127]

The equations developed in this section can therefore be used to design and operate MD systems at high salinity away from counter-productive operating conditions where both GOR and flux are low.

6.3.4 Air Gap: Effectively a thick and insulating membrane

The theoretical development in Section 6.3.1 establishes a general comparison between DCMD, PGMD and CGMD. In view of the non-dimensionalization proposed in the previous section, we revisit the question of comparing AGMD and CGMD to come up with a unified theoretical framework that can be applied to all single stage MD configurations.

Figure 6-12 shows the cross-section of an air gap MD module. In developing the simplified HX model of MD, it was assumed that water exists on either side of the membrane and hence the vapor pressure can be related to the saturation vapor pressure and salt concentration of these streams. In AGMD, the same model can be applicable if the region between the two menisci (salt water meniscus to the left of the

membrane and the condensing film surface) is defined as the effective membrane [106]. In addition to having a thicker 'effective membrane', the overall thermal conductivity ($k_{\mathrm{eff,m}}$) of this 'membrane' in AGMD is also lower (since the membrane material is localized to a small portion of the effective membrane, the remaining being filled with only air). If the porosity of the air gap is high, the permeability coefficient (B_0) of this effective membrane would also be higher than that of the membrane. Therefore $\phi_{\mathrm{c:v}}$ is higher and $\phi_{\mathrm{ch:m}}$ is lower, both of which are especially useful from the perspective of achieving higher $\mathrm{NTU}^{\mathrm{crit}}$ or $\mathrm{GOR}_{\mathrm{max}}$ at high salinity.

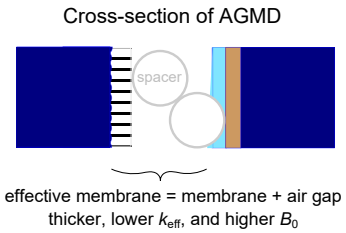

Figure 6-12: Cross section of AGMD. The air gap along with the membrane can be considered as the effective membrane in the case of AGMD.

This framework can be used to understand the region of Fig. 6-6 in which AGMD achieves a higher GOR than CGMD. While having a higher $\phi_{\mathrm{c:v}}$ and lower $\phi_{\mathrm{ch:m}}$ are both desirable from the perspective of achieving high energy efficiency and low η, the fact that the overall resistance in AGMD is higher (since $\phi_{\mathrm{ch:m}}$ is increased by increasing membrane thickness rather than by reducing the resistance in other sections of the module) leads to a lower flux, and larger area requirement in AGMD compared to CGMD, for smaller system size (see Figs. 6-7, 6-19a).

One way to match AGMD's high GOR at low flux with CGMD is to use a thick membrane $\delta_{\mathrm{m}}(\mathrm{CGMD}) = \delta_{\mathrm{m}}(\mathrm{AGMD}) + d_{\mathrm{gap}}(\mathrm{AGMD})$. This prediction is verified by comparing the performance of AGMD against CGMD with a thick membrane in Fig. 6-13. When a CGMD system with a thicker membrane (1.2 mm thick) is considered, its GOR-flux profile starts approaching that of AGMD (green curve).

At $s_{\mathrm{in}} = 175,250$ g/kg, a thick membrane CGMD system performs similar to AGMD (lower GOR compared to thin-CGMD at high flux and higher GOR at low flux), but its peak GOR is around 10–25% lower than that of AGMD. The membrane's

permeability coefficient was set at 60% of the molecular diffusion upper limit permeability, at $B_0 = 1.5 \times 10^{-10}$ s, in order to account for vapor transport inhibition by the membrane, the membrane's porosity, and tortuosity. On the other hand, the air gap spacer was considered to have a higher porosity (see Table 6.2), and as a result the effective permeability coefficient of the air gap was around $B_{0,\mathrm{air-gap}} \approx 2.15 \times 10^{-10}$ s. Similarly, the effective conductivity of the air gap was set at 0.032 W/m·K compared to $k_{\mathrm{eff,m}} = 0.062$ W/m·K. Therefore, $B_0/k_{\mathrm{eff,m}}$ and $\phi_{\mathrm{c:v}}$ were higher for the effective membrane of AGMD, resulting in higher maximum GOR of AGMD compared to CGMD with a thick membrane.

With the development of ultra-porous MD membranes with enhanced vapor permeability and much lower thermal conductivity [58], this disadvantage of thick-CGMD compared to AGMD at high salinity and low flux can be addressed. This is particularly important since AGMD with small gap thickness can get partially flooded, pushing AGMD's performance below that of CGMD towards PGMD (Fig. 6-13). Practical implications of these effects on choice of MD configuration for high salinity are summarized in the following section.

Practical implications for choice of MD configuration

AGMD is particularly promising at high feed salinities. But a thin air-gap (about 1 mm) can get partially or completely flooded during operation (Fig. 6-14). Recent visualizations [50, 76] of the condensation process within the air gap have confirmed that the film is affected by the gap spacer and is quite different from the ideal case depicted Fig. 6-12. In 6.5.4 we show that large scale systems may also be susceptible to gap flooding. This would lead to a shift in AGMD performance towards that of PGMD (red curves in Fig. 6-13) which is particularly bad at high s.

Since CGMD and DCMD system with thick membranes perform similar to AGMD, while eliminating the danger of air gap flooding and PGMD type operation, these may be more robust alternatives to AGMD. This result assumes that high h_{gap} or $(UA)_{\mathrm{HX}}$ can be implemented, since the resistance of the thin film condensate in AGMD is small. Fig. 6-14 shows the overall comparison between various configurations.

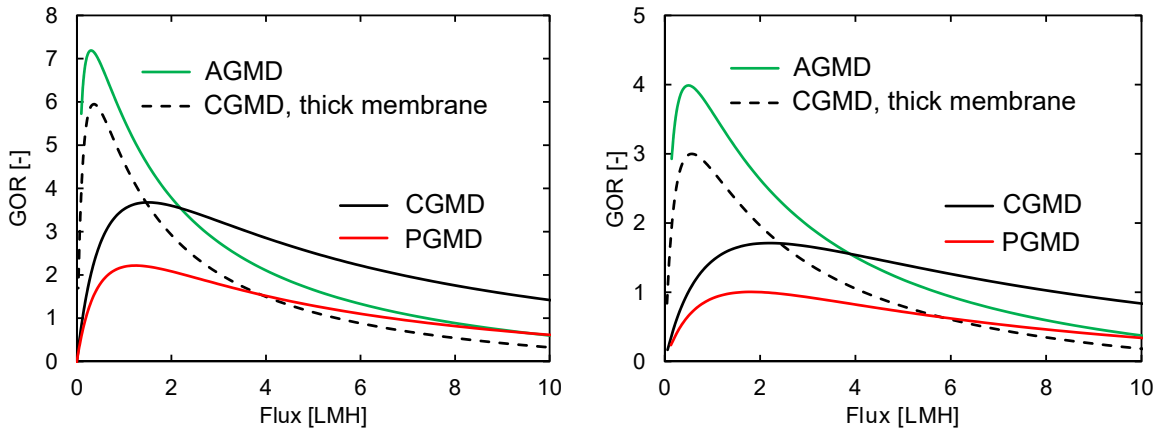

(a) s_{in} = 175 g/kg. δ_m = 1.2 mm for thick CGMD.

(b) s_{in} = 250 g/kg. δ_m = 1.2 mm for thick CGMD.

Figure 6-13: A CGMD with a thicker membrane performs similar to AGMD. When the membrane thickness equals the sum of the membrane and air gap thickness of AGMD, performance of CGMD approaches AGMD. AGMD is still better due to a lower heat loss across the gap with low thermal conductivity. For high salinity, lowering the membrane conductivity makes the CGMD very similar to AGMD. CGMD and PGMD with $\delta_m = 0.2$ mm are also shown for comparison. Other system parameters are provided in Table 6.2.

6.3.5 Choosing MD membrane thickness

Making a more permeable or less thermally conductive membrane (to increase $\phi_{c:v}$) is contingent on developing novel membrane fabrication methods. On the other hand, the thickness of the membrane can be adjusted as an independent parameter during fabrication. We have shown that AGMD is better for low flux and high GOR, whereas CGMD is better at high flux and low GOR. Since AGMD type performance can be obtained by using thicker membranes in CGMD, in this final section, we focus on the choice of optimal membrane thickness for a CGMD system.

The ideal thickness of the membrane depends not only the feed water salinity, but also on the flux at which the system operates. Figure 6-15 shows GOR vs. flux curves for a three representative membrane thicknesses. At high flux, the thicker membranes have a lower GOR compared to thinner membranes, whereas at low flux, the thicker membranes achieve higher GOR. At each flux, there exists an optimum thickness. The overall best-case (upper limit GOR) curve is tangent to a series of

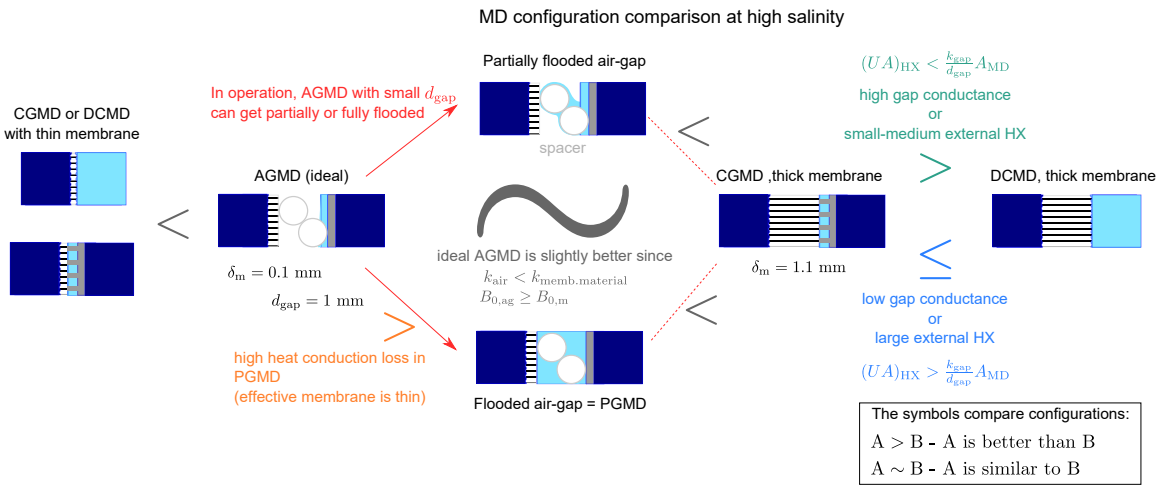

Figure 6-14: Relationship between various MD configuration at high salinity. A < B and A > B are used to indicate that system A is worse or better than system B.

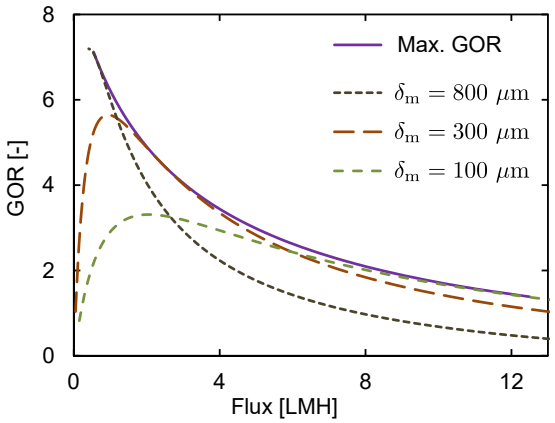

Figure 6-15: GOR vs. flux at various membrane thicknesses for CGMD at $s_{in} = 150$ g/kg. For each flux, GOR is maximized at a specific value of membrane thickness.

GOR-flux curves; at each flux, the upper limit GOR curve is tangent to a GOR-flux curve for particular membrane thickness that maximizes the GOR at that flux value. This resulting curve is shown as a solid line in Fig. 6-15.

Similar upper limit curves can be obtained for each salinity based on the same procedure and are plotted in Fig. 6-16a. Correspondingly, the optimal membrane thickness as a function of flux is shown in Fig. 6-16b. These curves (since they include dimensional flux) are valid for the baseline channel properties listed in Table 6.2.

Figures 6-16a and 6-16b together can be used to pick the optimal membrane thickess for a given application (defined by s_{in}, C_{GOR} and C_{Flux}). First, Fig. 6-

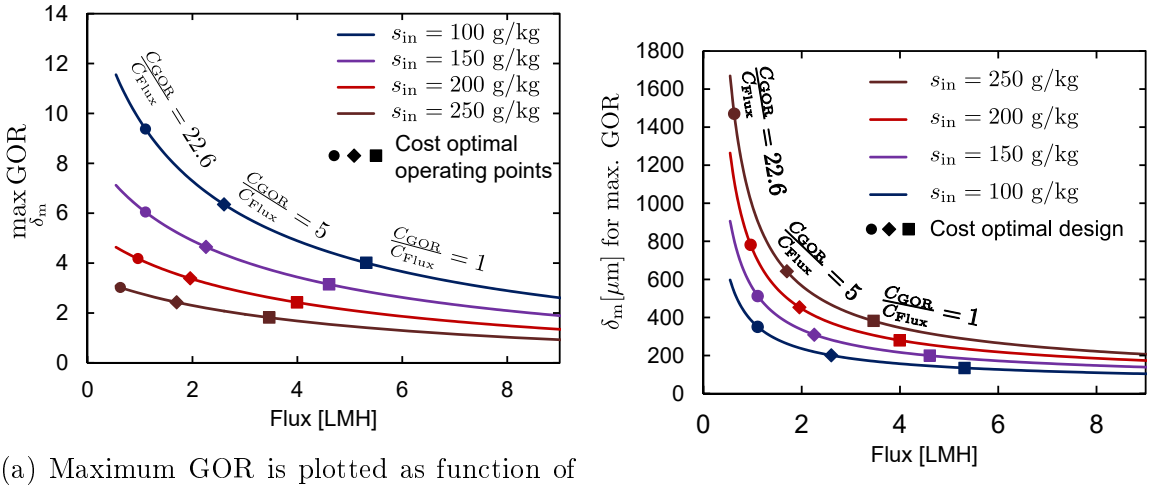

(a) Maximum GOR is plotted as function of flux. At each flux, the system is designed at the membrane thickness that maximizes GOR.

(b) The thickness at which energy efficiency is maximized for CGMD as a function of flux.

Figure 6-16: Choosing membrane thickness and system size: maximum GOR and the thickness at which GOR is maximized are plotted as a function of flux. At the known feed salinity, the point along the max-GOR vs. flux graph is chosen at which cost of water is minimized. Once this operating point is chosen, the corresponding value of membrane thickness can be obtained from Fig. 6-16b. Representative choices of optimal system design are shown for three values of C_{GOR}/C_{flux} [L/m^2-hr].

16a is used to pick an operating point along the max. GOR-flux operating curve to minimize specific cost (Eq. 6.23). The location of the optimum is a function of the relative specific cost of thermal energy and amortized system size (C_{GOR}/C_{flux}). At the baseline condition defined in 6.5.1 using natural gas for thermal energy, this ratio is 22.6. If a cheaper source of thermal energy is available or if the system cost is higher, this ratio would be lower. Once this operating point is identified, the required membrane thickness can be obtained at the same value of flux from Fig. 6-16b. Representative results are shown for three values of the cost ratio.

6.4 Concluding Remarks

In this manuscript, common single stage MD configurations are compared over a range of feed salinities based on their GOR-flux performance characteristics. Increasing the conductance of the gap in PGMD, tending towards CGMD, always leads to better

overall performance. The comparison between CGMD and DCMD is a function of the gap conductance and external HX area and transfer coefficient. The performance of these two configurations is similar when $U_{\mathrm{HX}}A_{\mathrm{HX}} = h_{\mathrm{gap}}A_{\mathrm{MD}}$. Since both CGMD and DCMD can be designed to achieve similar performance, designers can choose to implement the cheaper alternative each scenario.

At high feed salinity, there exists a critical MD system specific size or $\mathrm{NTU}^{\mathrm{crit}}$. Operating at $\mathrm{NTU} > \mathrm{NTU}^{\mathrm{crit}}$ should be avoided since neither flux nor GOR improves in this regime. An analytical expression for $\mathrm{NTU}^{\mathrm{crit}}$ is derived using the simplified HX model of MD, as a function of feed salinity (BPE) and two non-dimensional parameters quantifying the ratio of membrane permeability to vapor transport compared to thermal conductivity, and the relative heat transfer resistance offered by non-membrane portions of the MD module compared to the membrane. This expression can inform the choice of system size at the design stage (for treating a given feed flow rate), or flow rate during operation (for a physical system of fixed size), to avoid the counterproductive operating regime.

Finally, AGMD is also brought into the simplified HX modeling framework by identifying the air gap as a part of the effective membrane separating the evaporation and condensation menisci. If AGMD is used for high salinity desalination, care should be taken to avoid partial or complete flooding of the air-gap. CGMD and DCMD with thicker membranes are also resistant to changes in feed salinity, similar to AGMD, and can reach higher GOR values at high salinity than with thinner membranes. The choice of ideal configuration could therefore be restated as a problem of picking the ideal membrane thickness. A method to simultaneously choose membrane thickness and system size to minimize overall cost of water treatment is presented. An upper limit GOR-flux curve can be evaluated by maximizing GOR at each value of flux over all possible membrane thickness values. The best operating point (and correspondingly optimal membrane thickness) can be inferred from this graph based on the relative specific cost of system CapEx and OpEx.

6.5 Appendices

6.5.1 Economic analysis

The flux-GOR performance curve for a given MD configuration indicates the set of all operating points that are accessible to the technology by varying the specific system size. The purpose of plotting these curves for various configurations is to compare them, being agnostic to actual capital and operating costs that would vary from one desalination plant to another. The overall specific cost of water production from a MD system is influenced by both capital and operating expenditures. The capital cost increases with system size. The operating expense consists of labor, chemicals, membrane and other material replacement, as well as energy. Energy is utilized in an MD system both in the form of heat and electricity. Considering only the cost of capital (assuming capital cost is linearly proportional to membrane area), and energy consumption, the overall cost of water from MD can be written as a function of three terms:

$$c = c_{\text{CapEx}} + c_{\text{thermal}} + c_{\text{electric}} \tag{6.19}$$

c_{CapEx} can be expressed as a function of water flux as:

$$\begin{aligned} c_{\text{CapEx}}[\$/\text{m}^3] &= \frac{C_{\text{system,ammortized}}[\$/\text{hr}]}{\dot{\text{V}}_{\text{p}}[\text{m}^3/\text{hr}]} = \frac{c_{\text{sp,capital}}[\$/\text{m}^2] \times A[\text{m}^2] \times \text{CAF}[\text{hr}^{-1}]}{J[\text{Lm}^{-2}\text{hr}^{-1}] \times A[\text{m}^2] \times 10^{-3}[\text{m}^3/\text{L}]} \\ &= \frac{C_{\text{flux}}}{J} \end{aligned} \tag{6.20}$$

For a 20 year plant life, and annual interest rate of 10%, the capital amortization factor CAF $= 1.35 \times 10^{-5}[\text{hr}^{-1}]$. For a system specific cost of $c_{\text{sp}} = \$100/\text{m}^2$, $C_{\text{flux}} =$ 1.35 [\$-L/m^5-hr] and $c_{\text{CapEx}} = \frac{1.35}{J}$.

The contribution of thermal energy cost to the cost of water produced by MD is directly proportional to the specific cost of thermal energy and the specific thermal energy consumption of the MD process.

$$
\begin{aligned}
c_{\text{thermal}}[\$/\text{m}^3] &= c_{sp,thermal}[\$/\text{kWh}] \times q_{\text{MD}}[\text{kWh}/\text{m}^3] \\
&= c_{sp,thermal}[\$/\text{MMBTU}] \times \frac{h_{\text{fg}}[\text{J/kg}]}{\text{GOR}} \times (0.947 \times 10^{-9})[\text{MMBTU/J}] \times 10^3[\text{kg}/\text{m}^3] \\
&= \frac{C_{\text{GOR}}}{\text{GOR}}
\end{aligned} \tag{6.21}
$$

Considering the cost of energy from natural gas \$13.11/MMBTU and $h_{\text{fg}} = 2.442 \times 10^6$ J/kg, $C_{\text{GOR}} = 30.34[\$/\text{m}^3]$ and $c_{\text{thermal}} = \frac{30.34}{\text{GOR}}$.

If $\dot{W}$ is the electricity consumption in watts, the corresponding contribution to the overall specific cost of water can be written as

$$
\begin{aligned}
c_{\text{electric}} &= c_{\text{sp,electric}}[\$/\text{kWh}] \times w_{sp,electric}[\text{kWh}/\text{m}^3] \\
&= c_{\text{sp,electric}}[\$/\text{kWh}] \times \frac{\dot{W}[\text{W}] \times \cancel{10^{-3}}[\text{kW/W}] \times \cancel{1}\,\text{hr}}{J[\text{Lm}^{-2}\text{hr}^{-1}] \times A[\text{m}^2] \times \cancel{10^{-3}}[\text{m}^3/L] \times \cancel{1}\,\text{hr}} \\
&= \frac{c_{\text{sp,electric}} \left(\frac{\dot{W}}{A}\right)}{J} \\
&= \frac{C'_{\text{pump}}}{J}
\end{aligned} \tag{6.22}
$$

Unlike C_{flux} and C_{GOR}, $C\text{pump}'$ is not independent of system size, as the pumping power increases with an increase in module length. Duong et al. report a low value of around 0.3 kWh/m^3 for the specific electrical energy consumption [29]. Nevertheless, even for a pump power consumption of 1–2 kWh/m^3-product, the relative contribution of pump energy consumption is much lower than that of capital cost and thermal energy. As a result, the total cost of water from MD can be approximated as

$$
c \approx c_{\text{CapEx}} + c_{\text{thermal}} = \frac{C_{\text{flux}}}{J} + \frac{C_{\text{GOR}}}{\text{GOR}} \tag{6.23}
$$

6.5.2 Baseline system parameters

6.5.3 Numerical validation of DCMD and CGMD comparison

The GOR and flux of CGMD are plotted versus h_{gap} in Fig. 6-17 at two combinations of feed inlet salinity and system size. On the same plot, the GOR and flux of DCMD are also plotted versus $U_{\text{HX}} A_{\text{HX}} / A_{\text{m}}$. As predicted, the curves line up almost perfectly.

The maximum deviation is around 1.5% in the case of GOR and 0.75% in flux. DCMD has a slightly higher GOR since it has a higher NTU for the same inlet feed flow rate and area. The average feed flow rate within the module is lower in DCMD, whereas it is equal to the inlet flowrate in the case of CGMD.

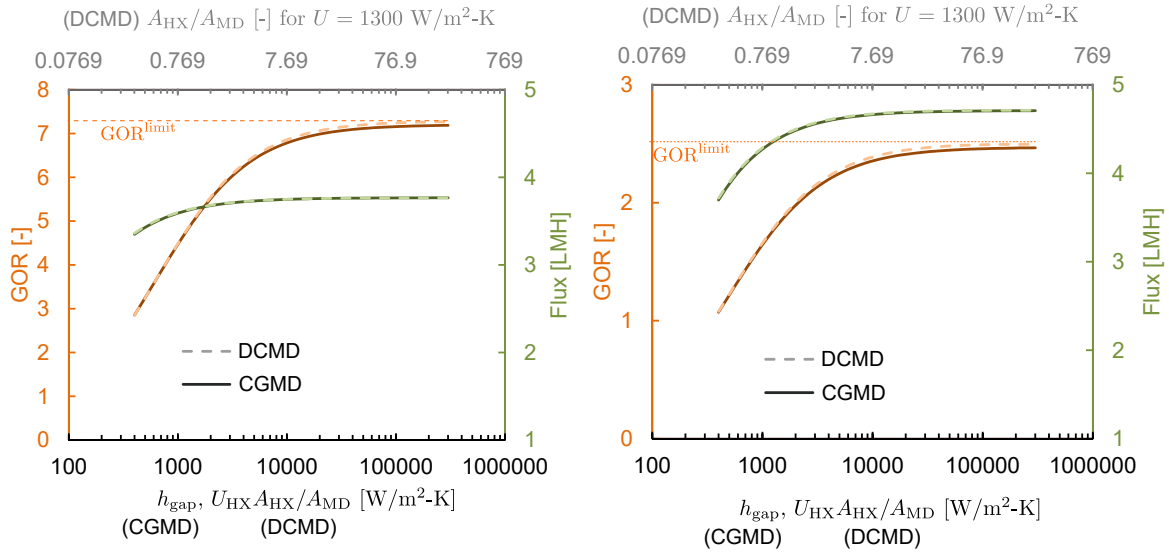

(a) $s_{in} = 70$ g/kg. $L = 5$ m.

(b) $s_{in} = 200$ g/kg. $L = 2.5$ m.

Figure 6-17: The performance of CGMD and DCMD are comparable when the resistance of the gap and the external heat exchanger are matched. $B_0 = 1.8 \times 10^{-10}$ s.

6.5.4 Potential for flooding in AGMD

The present numerical model is compared against results from the Aquastill MD module reported in [29]. The GOR-flux values obtained with changes in feed flow rate (Fig. 6-18a) and top temperature (Fig. 6-18b) at two values of $s_{in} = 0, 35$ g/kg are plotted. The channel geometry, feed flow rate, temperature and salinity in the numerical model are set based on the reported data.

The decline in performance between $s_{in} = 0$ and 35 g/kg cases is more pronounced then what would be expected for an ideal air gap system. The AGMD model prediction shows a small difference in performance between the two salinity levels, whereas the difference predicted by the PGMD model is closer to the observed trend. We can therefore surmise that the large scale experimental module could have had some

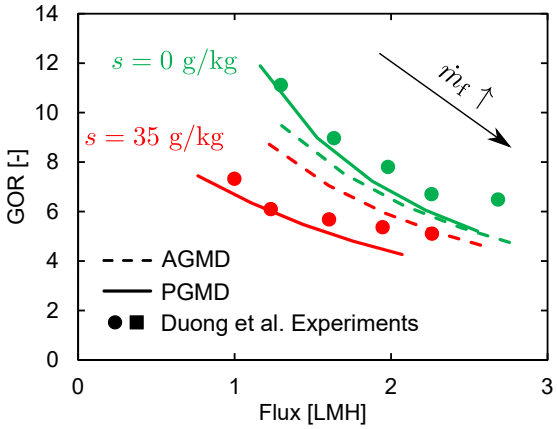

(a) Validation at various feed flow rates.

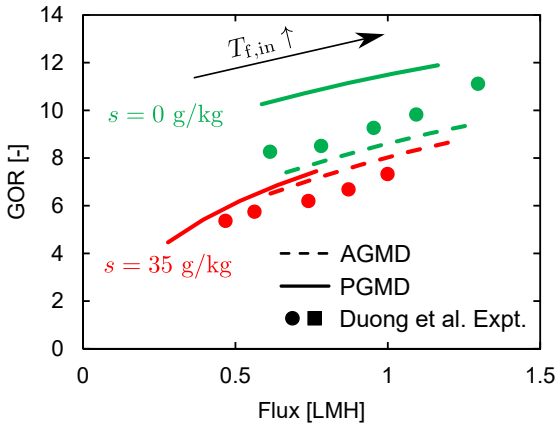

(b) Validation at various feed inlet temperatures

Figure 6-18: Comparison of the full-system model by comparing against published data for flux and energy efficiency. AG (dotted model lines) refers to Air Gap and PG to Permeate Gap (solid model lines). The reported module geometry data was input to the model. Additionally the following parameters were used: $B_0 = 1.5 \times 10^{-10}$ kg/m-s-Pa, $h_{ch} \approx 5000$ W/m^2·K, $h_{gap}^{PGMD} = 500$ W/m^2·K, $d_{gap,eff}^{AGMD} = 0.7$ mm.

water bridging or partial flooding of the gap. On average, experimental results occur between the model predictions for an air-gap system and that of a permeate gap system (where the entire gap is assumed to be filled with produced product water).

Note that in Fig. 6-18a, at larger feed flow rates, the obtained GOR and flux values are higher than predicted by both the AGMD and PGMD models. This could be because a simple laminar correlation is used for the heat transfer coefficient within the flow channels in the model, whereas in reality, with an increase in flow rate, the effective heat transfer coefficient would increase due to increased mixing in the spacer-filled channel. Additionally, the effect of changes in top temperature on B_0 of the membrane have also not been considered in the numerical model.

6.5.5 Effect of non-dimensional parameters on flux

While maximum GOR is only a function of the non-dimensional parameters, flux is not defined only by $\phi_{ch:m}$, $\phi_{c:v}$ and system size, but is also a function of the actual values of the individual resistances.

Figure 6-19a shows the effect of decreasing $\phi_{ch:m}$ in two ways: keeping membrane

thickness constant and increasing h_{ch} or keeping h_{ch} constant and increasing membrane thickness. While the maximum GOR value is the same for these two cases (since $\phi_{ch:m}$ is equal and only the non-dimensional fraction influences GOR), flux behavior is very different.

The flux for the case with higher channel transfer coefficient is about two times higher than the case with a thicker membrane. For a system with lower $\phi_{ch:m} = 0.2$ due to a thicker membrane (larger membrane resistance), the GOR is higher than case with $\phi_{ch:m} = 0.4$ at low flux, but at higher fluxes, the original system with $\phi_{ch:m} = 0.4$ performs better. On the other hand, when $\phi_{ch:m} = 0.2$ is achieved by increasing the channel heat transfer coefficient, performance is better than the system at $\phi_{ch:m} = 0.4$ throughout all flux values.

Similarly, Fig. 6-19b shows the difference in performance based on whether $\phi_{c:v}$ is increased by improving membrane mass transfer or by increasing membrane heat transfer resistance, while keeping $\phi_{ch:m}$ and δ_m constant in both cases.

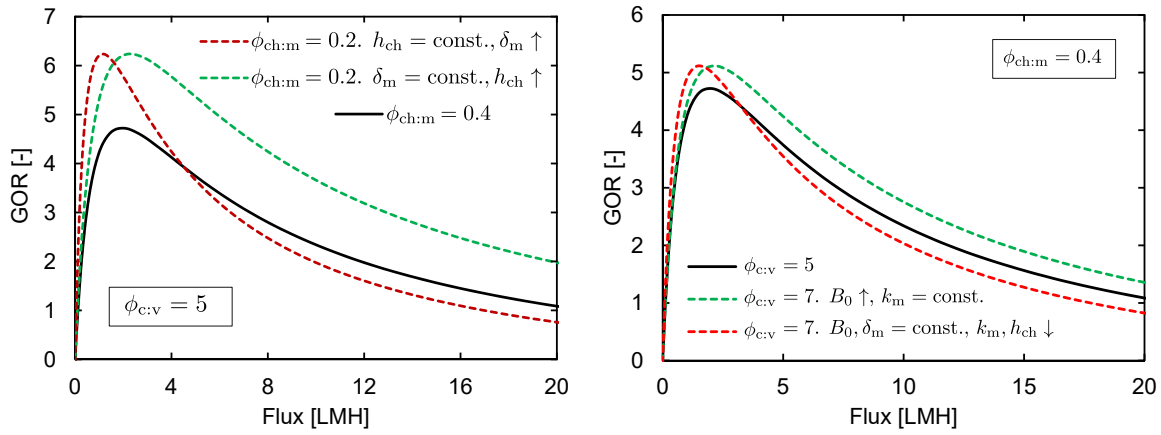

(a) The effect of actual transfer coefficient on flux at the same value of $\phi_{ch:m}$.

(b) The effect of actual transfer coefficient on flux at the same value of $\phi_{c:v}$.

Figure 6-19: Max GOR is only a function of $\phi_{c:v}$ and $\phi_{ch:m}$, but flux depends on the individual resistances rather than just the ratios of resistances. $s_{in=150}$ g/kg.

6.5.6 Equations for generalized HX model of MD

Effects of high salinity

Feed inlet salinity in g/kg-solution or ppt

$$s_{\text{in}} = 60 \ \ [\text{g/kg}] \tag{6.24}$$

This is the average salinity at which BPE is evaluated. The average salinity is taken to be 4% higher than the inlet salinity to account for concentration along the system length and concentration polarization

$$s_{\text{avg}} = 1.04 \cdot s_{\text{in}} \tag{6.25}$$

molality corresponding to avg. salinity

$$\text{molality}_{\text{avg}} = 1000 \cdot \frac{s_{\text{avg}}}{(1000 \cdot \text{MW}_{\text{solute}} - s_{\text{avg}} \cdot \text{MW}_{\text{solute}})} \tag{6.26}$$

NaCl is the solute assumed

$$\text{MW}_{\text{solute}} = 58.44 \ \ [\text{g/mol}] \tag{6.27}$$

The temperature at which BPE is evaluated - average of top and bottom temperatures

$$T_{\text{avg}} = \frac{T_{\text{top}} + T_{\text{bottom}}}{2} \tag{6.28}$$

This BPE (boiling point elevation) is determined for NaCl solution at the average salinity and temperature

$$\text{BPE} = \text{BPE}\left(\text{molality}_{\text{avg}}, \ T_{\text{avg}}\right) \tag{6.29}$$

A fit for the specific heat of NaCl solution as a function of solution salinity at 60 °C

$$c_{\text{p,NaCl}} = 15.566 \cdot \text{molality}_{\text{avg}}^2 - 241.78 \cdot \text{molality}_{\text{avg}} + 4161.9 \tag{6.30}$$

Other system inputs Heat transfer coefficients in the feed channel. Can be determined using a correlation as a function of system properties (such as channel depth and flow velocity) for more general applicability

$$h_{\mathrm{t,f}} = 2522 \ \left[\mathrm{W/m^2 \cdot K}\right] \tag{6.31}$$

Cold channel geometry and flow are assumed to tbe the same as feed channel

$$h_{\mathrm{t,c}} = h_{\mathrm{t,f}} \tag{6.32}$$

Temperature at the heater outlet or feed channel inlet is fixed

$$T_{\mathrm{top}} = 85 \ [^{\circ}\mathrm{C}] \tag{6.33}$$

T_{bottom} corresponds to the incoming cold water temperature. If recirculation is used, the brine is assumed to be cooled to ambient. The simplified model is validated against the more detailed model only for $T_{\mathrm{bottom}} = 25$ C. For other T_{bottom}, $T_{\mathrm{p,avg}}$ below would vary.

$$T_{\mathrm{bottom}} = 25 \ [^{\circ}\mathrm{C}] \tag{6.34}$$

$$\Delta T_{\mathrm{total}} = T_{\mathrm{top}} - T_{\mathrm{bottom}} \tag{6.35}$$

Geometry Flow channel length (dimension along flow direction) - larger length leads to higher GOR, but lower flux

$$L = 4 \ [\mathrm{m}] \tag{6.36}$$

Flow channel width - can be scaled along with $\dot{m}_{\mathrm{f,in}}$ Overall results only depend on $\dot{m}_{\mathrm{f,in}}/w$ - not on either of them independently

$$w = 12 \ [\mathrm{m}] \tag{6.37}$$

Membrane total area

$$A = w \cdot L \tag{6.38}$$

Membrane Characteristics

B_0 is the membrane vapor permeability coefficient

$$B_0 = 1.5 \times 10^{-10} \ \text{[s]} \tag{6.39}$$

δ_m is membrane thickness in microns. For AGMD, δ_m can be set to include the air-gap's effective thickness

$$\delta_\text{m} = 200 \ \text{[}\mu\text{m]} \tag{6.40}$$

Membrane material thermal conductivity - PVDF

$$k_{memb,mat} = 0.2 \ \text{[W/m}\cdot\text{K]} \tag{6.41}$$

$$k_{vapor} = 0.02 \ \text{[W/m}\cdot\text{K]} \tag{6.42}$$

Porosity of the membrane

$$\phi = 0.8 \tag{6.43}$$

Overall thermal conductivity of the membrane (for AGMD, this should also be decreased to account for the effective membrane):

$$k_\text{eff} = \phi \cdot k_\text{vapor} + (1 - \phi) \cdot k_\text{memb,mat} \tag{6.44}$$

Vapor permeability [kg/m^2-s-Pa]

$$B = \frac{B_0}{(\delta_\text{m} \cdot 10^{-6})} \tag{6.45}$$

Thermal conductance of the membrane [W/m^2-K]

$$K_\text{cond} = \frac{k_\text{eff}}{(\delta_\text{m} \cdot 10^{-6})} \tag{6.46}$$

Flow rates Feed inlet mass flow rate

$$\dot{m}_{f,in} = 1 \ \text{[kg/s]} \tag{6.47}$$

Specific heat capacity of the feed solution

$$c_{\text{p,f}} = c_{\text{p,NaCl}} \tag{6.48}$$

For the MD-heat-exchanger, the two heat capacity rates are modeled as equal since the pure water is considered one stream and the feed + pure water is considered the other stream

$$\dot{C}_1 = \dot{m}_{\text{f,in}} \cdot c_{\text{p,f}} \tag{6.49}$$

$$\dot{C}_2 = \dot{C}_1 \tag{6.50}$$

Gap For CGMD k_{gap} =10 W/m-K. For PGMD, k_{gap} would be 0.6 W/m-K. For DCMD, k_{gap} can be set = $U_{\text{HX}} A_{\text{HX}} d_{\text{gap}}/A$. For AGMD air gap, the major resistance will be in the thick effective membrane as defined in the δ_{m} variable above. Hence a high $k_{\text{gap}} = 10$ W/m-K can be used.

$$k_{\text{gap}} = 10 \ \text{[W/m·K]} \tag{6.51}$$

The gap effecitve thickness.

$$d_{\text{gap}} = 0.001 \ \text{[m]} \tag{6.52}$$

Averaging length-wise variations This is a fit obtained for $T_{\text{p,avg}}$ as a function of system top temperature. Bottom temperature was kept constant at 25 °C, but is likely to have a smaller overall effect.

$$T_{\text{p,avg}} = (0.3731 \cdot T_{\text{top}} + 21.834) \tag{6.53}$$

Membrane Transfer Coefficient: Writing the mass transfer across the membrane

in terms of the ΔT_{m} rather than as a function of the vapor pressure difference, using the exponential approximation of $p_{\mathrm{vap}}(T) = 1054.8 \exp 0.0479 * T$, where T is in °C:

$$\mathrm{MT}_{\mathrm{coeff}} = 0.0479 \cdot 1054.8 \cdot \exp\left(0.0479 \cdot T_{\mathrm{p,avg}}\right) \cdot \left(1 - \frac{\mathrm{BPE}}{\Delta T_{\mathrm{m,resistance}}}\right) \tag{6.54}$$

The membrane resistance to heat and mass transfer are considered to be in parallel

$$h_{\mathrm{eff,m}} = \mathrm{MT}_{\mathrm{coeff}} \cdot B \cdot h_{\mathrm{fg}} + K_{\mathrm{cond}} \tag{6.55}$$

Overall Transfer Coefficient

$$U = \frac{1}{1/h_{\mathrm{t,f}} + 1/h_{\mathrm{eff,m}} + 1/h_{\mathrm{t,c}} + d_{\mathrm{gap}}/k_{\mathrm{gap}}} \tag{6.56}$$

ΔT_{m} as a function of overall (terminal temperature difference) TTD - as a function of the relative resistances in various parts of the module

$$\frac{\mathrm{TTD}}{1/U} = \frac{\Delta T_{\mathrm{m,resistance}}}{1/h_{\mathrm{eff,m}}} \tag{6.57}$$

$\mathrm{h_{fg}}(T = 25\,^{\circ}\mathrm{C})$ is used. GOR reported is for

$$h_{\mathrm{fg}} = 2.442 \times 10^{6}\ [\mathrm{J/kg}] \tag{6.58}$$

Using heat exchanger NTU (number of transfer units) - ϵ (exchanger effectiveness) theory

$$\mathrm{NTU} = U \cdot A/\dot{C}_1 \tag{6.59}$$

$$\epsilon = \mathrm{HX}\Big(\text{‘counterflow’ },\ \mathrm{NTU},\ \dot{C}_1,\ \dot{C}_2,\ \text{‘epsilon’ }\Big) \tag{6.60}$$

Final Results

Overall terminal temperature difference

$$\mathrm{TTD} = (1 - \epsilon) \cdot \Delta T_{\mathrm{total}} \tag{6.61}$$

Thermal efficiency - fraction of energy transfer across the membrane through mass transfer, rather than as heat conduction loss

$$\eta = \frac{1}{\left[1 + \left(\frac{K_{\text{cond}}}{B \cdot h_{\text{fg}}}\right) \cdot \left(\frac{1}{\text{MT}_{\text{coeff}}}\right)\right]} \tag{6.62}$$

$$\text{GOR} = \eta \cdot \frac{\epsilon}{(1-\epsilon)} \tag{6.63}$$

Heat input rate - [W]

$$Q_{in} = \dot{C}_1 \cdot \text{TTD} \tag{6.64}$$

Rate of pure water produciton - [kg/s]

$$\dot{m}_{\text{p}} = \text{GOR} \cdot Q_{\text{in}}/h_{\text{fg}} \tag{6.65}$$

Water flux - [L/m^2-hr] or [LMH]

$$J = \dot{m}_{\text{p}} \cdot 3600/A \tag{6.66}$$

Equations to evaluate the critical system size beyond which both GOR and flux start declining

Non-dimensional parameter Y_3 compares membrane mass transfer resistance to resistance in other parts of the system

$$Y_3 = B \cdot h_{\text{fg}} \cdot 0.0479 \cdot 1054.8 \cdot \exp\left(0.0479 \cdot T_{\text{p,avg}}\right) \cdot \left(1/h_{\text{t,f}} + 1/h_{\text{t,c}} + d_{\text{gap}}/k_{\text{gap}}\right) \tag{6.67}$$

Compares membrane conduction resistance to resistance elsewhere in the module - Low value is better. It is called $\phi_{\text{ch:m}}$ in the manuscript.

$$Y_1 = K_{\text{cond}} \cdot \left(1/h_{\text{t,f}} + 1/h_{\text{t,c}} + d_{\text{gap}}/k_{\text{gap}}\right) \tag{6.68}$$

Compares membrane vapor conductance to heat conductance - A high value is

better. It is called $\phi_{\text{c:v}}$ in the manuscript.

$$Y_2 = B \cdot h_{\text{fg}} \cdot 0.0479 \cdot 1054.8 \cdot \frac{\exp\left(0.0479 \cdot T_{\text{p,avg}}\right)}{K_{\text{cond}}} \tag{6.69}$$

Equations for various parameters at the critical system size - They are indicated by the subscript 'crit'

$$\frac{\Delta T_{m,\text{crit}}}{\text{BPE} \cdot Y_1} = \left[\frac{\Delta T_{\text{total}} + Y_2 \left(\Delta T_{\text{total}} + Y_1 \cdot \text{BPE}\right) + \sqrt{\frac{\Delta T_{\text{total}}(1+Y_1)(\Delta T_{\text{total}} + Y_2(\Delta T_{\text{total}} - \text{BPE}))}{1+Y_1(1+Y_2)}}}{\left(\Delta T_{\text{total}} + Y_1 \cdot \text{BPE}\right)\left(1 + Y_1\left(1 + Y_2\right)\right) - \Delta T_{\text{total}}} \right] \tag{6.70}$$

$$\eta_{\text{crit}} = \frac{1}{1 + \left(Y_2^{-1} \cdot 0.0479 \cdot \frac{\Delta T_{\text{m,crit}} - \text{BPE}}{\left(1 - \frac{\text{BPE}}{\Delta T_{\text{m,crit}}}\right) \cdot \left(\exp\left(0.0479 \cdot \left(\Delta T_{\text{m,crit}} - \text{BPE}\right)\right) - 1\right)} \right)} \tag{6.71}$$

$$\text{NTU}_{\text{crit}} = \frac{\Delta T_{\text{total}}}{\left(\Delta T_{\text{m,crit}} \cdot \left(1 + Y_1 + Y_3 \cdot \left(1 - \frac{\text{BPE}}{\Delta T_{\text{m,crit}}} \right) \cdot \frac{\exp\left(0.0479 \cdot \left(\Delta T_{\text{m,crit}} - bpe\right)\right) - 1}{0.0479 \cdot \left(\Delta T_{\text{m,crit}} - \text{BPE}\right)} \right) \right)} - 1 \tag{6.72}$$

$$MT_{\text{coeff,crit}} = 0.0479 \cdot 1054.8 \cdot \exp\left(0.0479 \cdot T_{\text{p,avg}}\right) \cdot \left(1 - \frac{\text{BPE}}{\Delta T_{\text{m,crit}}}\right) \tag{6.73}$$

$$h_{\text{eff,m,crit}} = \text{MT}_{\text{coeff,crit}} \cdot B \cdot h_{\text{fg}} + K_{\text{cond}} \tag{6.74}$$

$$U_{\text{crit}} = \frac{1}{1/h_{\text{t,f}} + 1/h_{\text{eff,m,crit}} + 1/h_{\text{t,c}} + d_{\text{gap}}/k_{\text{gap}}} \tag{6.75}$$

$$A_{\text{crit}} = \text{NTU}_{\text{crit}} \cdot \dot{C}_1 / U_{\text{crit}} \tag{6.76}$$

$$L_{\text{crit}} = A_{\text{crit}} / w \tag{6.77}$$

$$\text{GOR}_{\text{crit}} = \eta_{\text{crit}} \cdot \text{NTU}_{\text{crit}} \tag{6.78}$$

Table 6.1: List of system variables and non-dimensional parameters used to characterize MD system critical size.

System variables	Non-dimensional parameter	Summary
L,$\dot{m}_{\mathrm{f,in}}$	NTU	Defines system size. L is physical length of the module in the flow direction. NTU $= \frac{U\times(Lw)}{\dot{m}c_{\mathrm{p}}}$. NTU is not a linear function of L since $U = f(L)$. Membrane mass transfer coefficient ($h_{\mathrm{mass,m}}$) is a function of ΔT_{m}, which decreases at larger L. Experimentally NTU can be inferred as NTU $= \frac{T_{\mathrm{c,out}}-T_{\mathrm{c,in}}}{\mathrm{TTD_{MD}}}$.
δ_{m}, $h_{\mathrm{f}}, h_{\mathrm{c}}, h_{\mathrm{gap}}$	$\phi_{\mathrm{ch:m}}$	Ratio of combined resistance of non-membrane sections to membrane conduction resistance. $\phi_{\mathrm{ch:m}}$ increases for a thinner membrane or at higher channel heat transfer coefficients.
B_0, $k_{\mathrm{eff,m}}$, $T_{\mathrm{p,avg}}$	$\phi_{\mathrm{c:v}}$	Ratio of the membrane conductance resistance to (size independent part of) membrane mass transfer resistance. A higher value is better. $\phi_{\mathrm{c:v}}$ can be increased by increasing B_0 or reducing $k_{\mathrm{eff,m}}$.
BPE, $s_{\mathrm{f,in}}$	-	The boiling point elevation is a measure of the vapor pressure depression of the saline solution. It is a function feed salinity and average temperature. For NaCl solutions, as feed salinity increases up to saturation at 260 g/kg, BPE increases to around 6 °C.
$\Delta T_{\mathrm{max}} = T_{\mathrm{f,in}} - T_{\mathrm{c,in}}$	-	This is fixed at 60 °C in this study: $T_{\mathrm{f,in}} =$ 85 °C, $T_{\mathrm{f,in}} =$ 25 °C. At lower top temperature, in addition to adjusting ΔT_{max}, the effect of lower temperature on B_0 should also be accounted for.

Table 6.2: Baseline system parameters.

Parameter	Symbol	Value	Units
Membrane permeability coefficient	B_0	1.5×10^{-10}	s
Membrane thickness	δ_{m}	200	μm
Membrane porosity	ϕ	0.8	-
Membrane material conductivity	k_{m}	0.2	W/m-K
Membrane width per unit flow rate	$w/\dot{m}_{\mathrm{f,in}}$	12	m/(kg/s)
Top temperature	$T_{\mathrm{f,in}}$	85	°C
Bottom temperature	$T_{\mathrm{c,in}}$	25	°C
Channel height	d_{ch}	1	mm
Gap thickness	d_{gap}	1	mm
CGMD - gap conductivity	k_{gap}	10	W/m-K
PGMD - gap conductivity	k_{gap}	0.6	W/m-K
AGMD - gap porosity	ϕ_{gap}	0.9	-
AGMD - gap spacer conductivity	$k_{\mathrm{gap,spacer}}$	0.2	W/m-K
DCMD - HX Area ratio	$A_{\mathrm{HX}}/A_{\mathrm{m}}$	1	-
DCMD - HX heat transfer coefficient	U_{HX}	1300	W/m^2-K

Chapter 7

Comparing brine recirculation methods for high recovery

Abstract

Thermal desalination processes such as membrane distillation (MD), humidification dehumidification (HDH), and multi-stage flash (MSF) are restricted to low per-pass pure water recovery ratio. A higher recovery can be achieved through brine recirculation. In this study, we focus on the MD process to understand aspects of process design and compare several recirculation strategies: batch, semibatch, continuous, and multistage. The processes are ranked based on their flux and energy efficiency, which together influence cost. Batch systems outperform semibatch and continuous recirculation. A batch system spends more operating time treating lower salinity water compared to semibatch and continuous recirculation for the same value of overall recovery ratio. Multi-stage recirculation can approach batch-like performance only with a large number of stages. An important operating principle for batch MD systems is to avoid counterproductive conditions characterized by the velocity v being below the critical velocity v^{crit}. Over the course of the cycle-time as the feed becomes more salty, critical feed velocity increases. It is recommended to increase the feed flow rate, if necessary, to maintain $v > v^{\text{crit}}$. An optimal membrane thickness can be identified for batch MD as a function of the relative cost of system area compared to thermal energy, by plotting the GOR-flux performance curves for various values of membrane thickness and choosing the upper limit curve.

7.1 Introduction

Conventional seawater and brackish water reverse osmosis systems are not readily applicable for further concentration of desalination brines, hydraulic fracturing produced water, or industrial effluents towards zero-liquid-discharge. Thermal technologies such as membrane distillation (MD) and humidification dehumidification (HDH) are considered to be promising for such brine concentration applications. However, these applications are characterized by a high recovery ratio requirement. Both HDH and MD (except multi-effect designs which will be considered in the next chapter) are restricted to a low value of per-pass recovery ratio, necessitating brine recirculation.

In this study, we

1. compare various methods of achieving high recovery (batch, semi-batch, continuous recirculation and multi-staging).

2. elucidate the value of additional control system to avoid counter-productive operating conditions over the cycle time of the batch MD process.

3. develop a procedure to identify an ideal membrane thickness for batch MD processes.

7.1.1 Motivation for high product recovery

MD systems without recirculation have low recovery ratio, which is the ratio of pure water to feed water as defined in Eq. 7.1.

$$\mathrm{RR} = \frac{M_{\mathrm{permeate}}}{M_{\mathrm{feed}}} \tag{7.1}$$

where M_{perm} is the final mass of permeate produced and M_{feed} is the initial mass of feed to be treated. Instantaneous recovery ratio or recovery ratio per-pass through the MD system can be defined in terms of the instantaneous pure water production rate ($\dot{m}_{\mathrm{p}}$) and feed inflow rate ($\dot{m}_{\mathrm{f}}$) as $\mathrm{RR}_{\mathrm{m}} = \frac{\dot{m}_{\mathrm{p}}}{\dot{m}_{\mathrm{f}}}$. If the change in temperature along the length of the cold channel is represented by ΔT_{c}, by energy conservation

for the preheated feed stream, $\dot{m}_{\mathrm{f}} c_{\mathrm{p}} \Delta T_{\mathrm{c}} = \dot{m}_{\mathrm{p}} h_{\mathrm{fg}} + \dot{Q}_{\mathrm{m,cond}}$, where $\dot{Q}_{\mathrm{m,cond}}$ is the heat transfered by conduction across the membrane. Since $\dot{Q}_{\mathrm{m,cond}} > 0$,

$$\mathrm{RR}_{\mathrm{m}} < \frac{c_{\mathrm{p}} \Delta T_{\mathrm{c}}}{h_{\mathrm{fg}}} \tag{7.2}$$

and $\Delta T_{\mathrm{c}} < T_{\mathrm{f,in}} - T_{\mathrm{c,in}}$. Both MD and HDH are operated at a top temperature below 100 °C, often in combination with low temperature heat sources. If the ambient temperature is 25 °C, RR < 13%. In practice the limit is lower, around 8% due to a lower top temperature and heat conduction from the feed stream.

In contrast, in order to achieve zero-liquid-discharge, the desalination process would have to concentrate the salt solution up to saturation concentration (260 g/kg for NaCl), at which point, the solution can be passed to a crystallizer. In this study, we will focus on desalinating a 70 g/kg feed solution up to 260 g/kg. The corresponding required recovery ratio is $1 - 70/260 = 72.1\%$, much higher than the limiting value for a single stage system. In order to implement such a high recovery ratio in a hypothetical single pass MD process, the feed stream would have to be heated up to 500 °C, after being pressurized to prevent boiling.

7.1.2 Options for high recovery with MD

The following operation strategies enable high overall pure water recovery employing a low-recovery single stage process:

1. batch recirculation
2. semi-batch recirculation
3. continuous recirculation
4. continuous multi-stage

Figure 7-1 shows a schematic representation of these alternatives. The first two options are discontinuous/unsteady processes. Over each process cycle time (τ_{cycle}) permeate is removed from the feed until a brine stream at the desired high salinity is

produced. At this point, the brine is flushed out and the system volume is refilled with new feed-water and the cycle is repeated. In batch recirculation, higher salinity brine exiting the MD module is added back into the tank. Volume of the tank reduces and solution concentration increases over time, until finally reaching the concentration reaches $s_{\mathrm{b,out}}$ (in our case 260 g/kg). At this point, brine is discharged and the tank is refilled with feed, as indicated by the dotted lines. The rate of permeate production ($\dot{m}_{\mathrm{p}}$) can vary over the cycle time, as the feed to the MD module gets more salty. Duong et al. have implemented MD in batch mode both for small scale systems [28] and pilot scale modules [27] to reduce energy consumption.

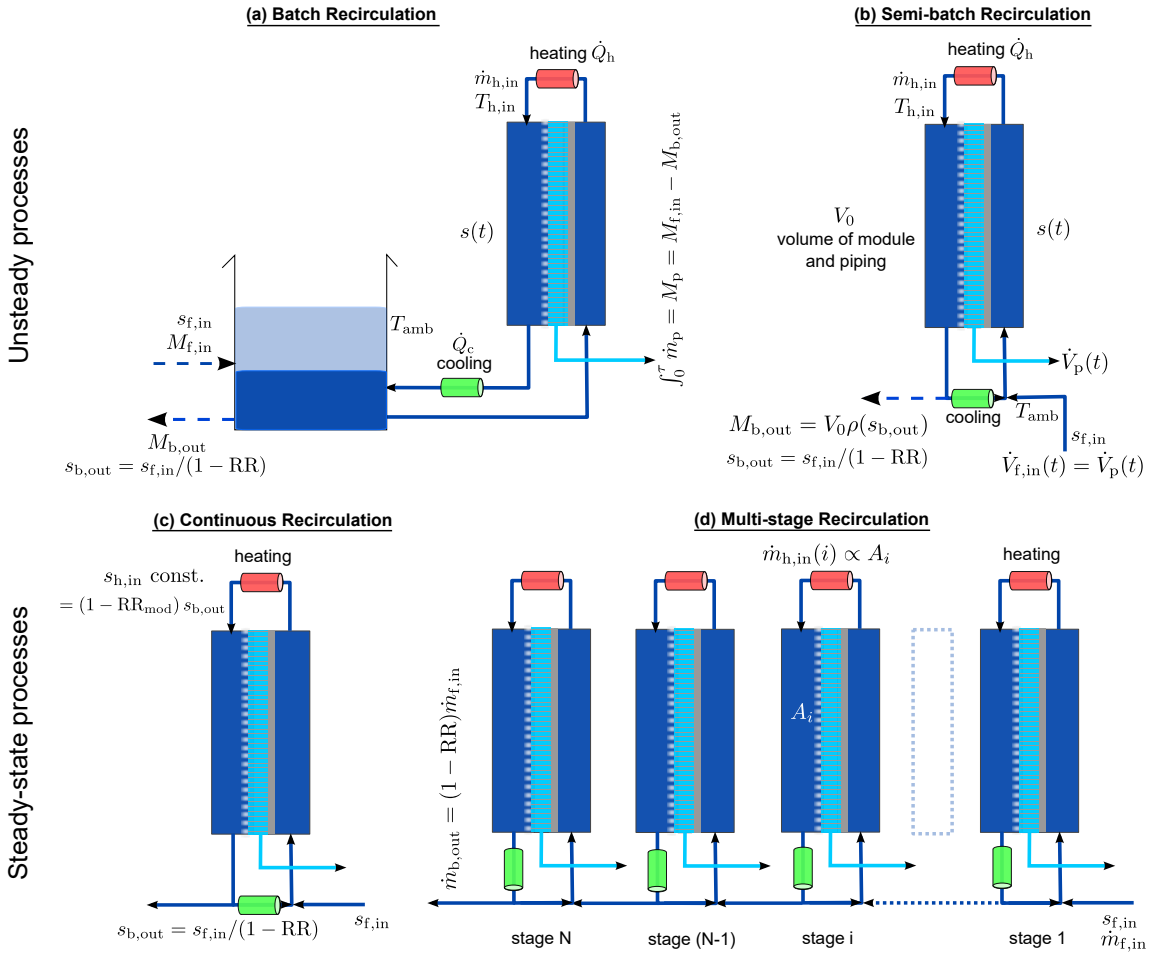

Figure 7-1: Schematic representation of batch, semibatch, continuous and multistage recirculation MD systems. These designs can be used to operate single-stage MD at an overall high recovery.

In the semi-batch process, the feed solution whose salinity increases over time is recirculated in a closed loop. Since the volume of the piping system is constant (V_0), to account for the mass lost into the permeate stream, feed water at $s_{\mathrm{f,in}}$ is added into the loop. Since the rate of permeate production can vary with time, the amount of feed water added into the semi-bath recirculation loop ($\dot{V}_{\mathrm{f,in}}$) is also time varying. Eventually the salinity of water in the system would reach $s_{\mathrm{b,out}}$. At this point, brine is flushed out by opening a valve and replaced by feed water.

A semi-batch recirculation version of RO has been commercially implemented [94]. More recently, “full-batch" or batch recirculation RO has also been proposed as a more energy efficient alternative [123, 125]. Note that unlike MD, a single-pass RO process can reach high recovery ratios by increasing the feed pressure even without recirculation. The batch design has to therefore outperform single stage RO in order to be competitive. On the other hand, here comparisons are made amongst other recirculation options listed in Fig. 7-1.

In the MD literature, continuous recirculation has also been used for achieving high recovery because it is a steady-state process and easier to implement [20, 54]. Continuous recirculation is operates such that the brine leaving the MD module is at the required final brine salinity. In order to maintain this brine salinity, the inlet salinity to the desalination process has to be a little lower: $s_{\mathrm{h,in}} = s_{\mathrm{b,out}} \times (1 - \mathrm{RR_m}) = s_{\mathrm{f,in}} \times \frac{1-\mathrm{RR_m}}{1-\mathrm{RR}}$. The brine stream is mixed with incoming feed make-up water such that the required inlet feed salinity ($s_{\mathrm{h,in}}$) is reached. We will show that the main disadvantage of continuous recirculation is that the desalination system always treats water close to the final brine salinity, even though feed salinity could be much lower for much of the water recovery process.

The multi-stage recirculation process illustrated in Fig. 7-1 combines several single stage recirculation systems in series. The first system would produce water a brine at a low salinity which becomes the make-up feed for the second stage and so on. The system parameters can be adjusted such that the final stage brine concentration is $s_{\mathrm{b,out}}$. A continuous DCMD process for 70% overall recovery is studied by [6]. The system design is similar to the multi-stage recirculation process, except that, a new

permeate cold water stream is employed for each stage.

7.1.3 Economic basis for comparison of high-recovery systems

In this chapter, we compare the various recirculation MD systems on the basis of their average GOR and water flux (J). In the context of brine concentration, the goal is not pure water production, but water volume reduction. In this case too, the same two parameters (GOR and J) would influence the net cost of the process. We have previously shown that the specific cost of water production can be expressed as $c_{\mathrm{w}} = C_{\mathrm{heating}}/\mathrm{GOR} + C_{\mathrm{flux}}/J$. For brine concentration systems at fixed RR, if the cost is expressed per unit of incoming feed water, $c_{\mathrm{f}} = c_{\mathrm{pw}} \times \mathrm{RR}$.

All the recirculation systems include additional cooling of the brine. Since the brine is recirculated into the MD process on the preheating side, without additional cooling, the system temperature would reach a higher value. Also, the flux in the process would continuously decline as the driving temperature difference decreases when warm water is introduced on the preheating side. The cooling load is proportional to the MD system's TTD. In fact, the cooling load is quite close to the heating load since the TTD of a balanced MD system is close at the two ends of the exchanger and c_{p} is not a strong function of temperature. As a result, the additional specific cost of brine concentration can be expressed similar to the thermal energy OpEx term as $C_{\mathrm{cooling}}/\mathrm{GOR}$, where where C_{cooling} is a scaled cost of providing cooling for unit cooling load of the system. Practically the cost of cooling may be related to the pump energy consumption to supply coolant. The overall specific cost of brine concentration with MD can be written as:

$$c_{\mathrm{f}} = \frac{C_{\mathrm{flux}}}{J} + \frac{C_{\mathrm{heating}} + C_{\mathrm{cooling}}}{\mathrm{GOR}} \tag{7.3}$$

7.1.4 Chapter overview

In Section 7.2, the numerical methods used to evaluate the performances of the four recirculation systems is described. Batch, semi-batch and continuous recirculation are

compared in Section 7.3 to show that batch always performs better than semibatch which is in turn better than continuous recirculation. This is because the batch system spends a larger fraction of its cycle time at lower salinity.

Aspects of high salinity MD system design developed in the previous chapter are also particularly important to the design and operation of these recirculation systems. The critical specific feed flow rate (below which both GOR and flux decrease) changes over the cycle time as the MD inlet salinity increases. Active control of flow rate is needed to prevent counterproductive operating regimes where both GOR and flux are diminished (Section 7.4). Just as in single-pass operation, an optimal membrane thickness can be determined for each average flux at which we would like to operate the system. This is described in Section 7.5 along with the development of the upper-limit batch performance curve when allowing membrane thickness to be changed as an additional variable.

In Section 7.6 we compare the multi-stage recirculation system with a batch system to show that their overall performances are similar only when multi-stage employs a large number of stages. In essence, the multi-stage process with many stages treats water over the entire salinity range, in space, whereas the batch recirculation process does the same over time.

Finally in Section 7.7, some specific aspects of unsteady operating conditions such as the reset time (τ_{reset}) are considered.

7.2 Methodology

Since the goal of this chapter is to compare various recirculation methods, we consider only the conductive gap MD configuration (CGMD) throughout. The results developed here will hold independently for air-gap MD or for a thicker more porous membrane used in CGMD mode as well. In all the comparisons, the same membrane, channel heat transfer coefficients, and gap conditions are prescribed.

The overall performance of the unsteady recirculation processes is obtained as a weighted average of the flux and specific thermal energy consumption over the en-

tire range of salinity conditions. Each batch system performance evaluation entails multiple calculations using the single stage MD model at a range of salinity values. Here we use the heat exchanger (HX) analogy model for evaluating single-stage MD performance. The deviation in GOR and flux predicted by the simplified HX model compared to the full discretized model predictions is within 20% over the entire range of salinity considered, and the deviation is higher at high salinity. The average deviation is only about 4% for the conditions considered.

The simplified HX model captures the key aspects of high salinity operation such as the critical feed flow rate, which are important for the design of recirculation system operation. For the batch and semi-batch system comparison, this simplified HX model is used.

7.2.1 Continuous Recirculation

The GOR and flux of continuous recirculation is the easiest to analyze since it operates under steady state. The salinity at the MD module inlet is fixed in time such that $s_{\mathrm{in}}/(1-\mathrm{RR}_{\mathrm{module}}) = s_{\mathrm{b,out}}$. At the steady state condition, the feed salinity at the MD module inlet is close to the brine salinity because of MD's low recovery. For example, concentrating from 70 g/kg to 260 g/kg requires $s_{\mathrm{f,in}} \approx 245$–$250$ g/kg. Effectively, the MD system is operating with feed inlet salinity of $s_{\mathrm{f}} \approx 245$ g/kg even though the actual feed (denoted as makeup) salinity is $s_{\mathrm{mu}} = 70$ g/kg. Another disadvantage of continuous recirculation system from a thermodynamic perspective is the mixing of makeup stream (e.g., 70 g/kg) and recirculated brine stream (e.g., 260 g/kg) to form the feed stream (e.g., 245 g/kg). This irreversible mixing generates entropy, resulting in lowered energy efficiency.

7.2.2 Batch

For batch operation, we consider the case of a large external tank compared to the feed channel volume. As a result, the average salinity of the feed liquid is close to the tank salinity, which is in turn equal to the concentration at the feed channel inlet.

In a batch system, mass and salt mass conservation (with no salt passage through the MD membrane) imply

$$\frac{dM}{dt} = -JA \tag{7.4}$$

$$M(t)s(t) = M_{\mathrm{f}}s_{\mathrm{f}} \tag{7.5}$$

$$\frac{d(Ms)}{dt} = M\frac{ds}{dt} + s\frac{dM}{dt} \tag{7.6}$$

The time required to accomplish a unit change of salinity as a function of salinity can be obtained by rearranging the above equations.

$$dt_{\mathrm{batch}} = \frac{M_{\mathrm{i}}s_{\mathrm{i}}}{s^2 J(s) A_{\mathrm{m}}} ds \tag{7.7}$$

Observe that a greater time is required as the feed salinity increases.

7.2.3 Semibatch

In semibatch MD, the volume of the recirculation loop (V_0) is conserved. As pure permeate is produced, fresh feed water is mixed into the loop to maintain the volume. This mixing of two streams at different salinities results in entropy generation, and this is why semi-batch operation performs worse compared to batch operation.

$$\frac{d(\rho V_0)}{dt} = V_0\frac{d\rho}{dt} = \dot{m}_{\mathrm{f}} - JA \tag{7.8}$$

$$\frac{d(\rho V_0 s)}{dt} = V_0 s\frac{d\rho}{dt} + V_0\rho\frac{ds}{dt} = \dot{m}_{\mathrm{f}}s_{\mathrm{f}} \tag{7.9}$$

Approximating density as a linear function of salinity for NaCl solutions, $\rho(s) = \rho_{\mathrm{pw}} + \alpha s$, where s is in g/kg, $\alpha = 0.7261$ $(\mathrm{kg/m^3})/(\mathrm{g/kg})$, we can rearrange the equations to get

$$dt_{\mathrm{sb}} = \frac{V_0(\rho_{\mathrm{pw}} + 2\alpha s - \alpha s_{\mathrm{f}})}{J(s)As_{\mathrm{f}}} \tag{7.10}$$

7.2.4 Integration over cycle time

Over the cycle time of the batch and semibatch processes, the feed salinity being treated by the system increases from s_{f} to s_{b}. At each instantaneous feed salinity, the

system flux and heat consumption $\dot{Q}_{\mathrm{h}}$ are evaluated using the steady state model.

The average flux and energy consumption over the cycle time can be obtained as:

$$\overline{J} = \frac{\int_0^\tau J(t)\,dt}{\int_0^\tau dt} \tag{7.11}$$

$$\overline{\mathrm{GOR}} = h_{\mathrm{fg}} \frac{\int_0^\tau J(t) A\,dt}{\int_0^\tau \dot{Q}_{\mathrm{h}}(t)\,dt} \tag{7.12}$$

For batch and semibatch modes, the corresponding variable transformations from dt to ds are made using Eqs. 7.7 and 7.10, and the integrals are evaluated numerically.

7.2.5 Continuous multistage recirculation

Multistage recirculation is a an adaption of single stage continuous recirculation MD. Here, many continuous recirculation systems are connected in series.

The overall recovery ratio of continuous recirculation system can be understood by drawing a control volume around the system. To model this configuration, the continuous recirculation model is run at a certain make-up feed flow rate, for the first stage of the multistage recirculation system. The output from this first stage model is used to set the makeup feed flow rate and salinity of the second stage. This process is repeated until the final stage. Based on the final output salinity, the initial makeup feed water flow rate is updated until the outlet brine at the final stage reaches the design value.

7.3 Comparison of batch and semibatch single-stage MD

Just as in single stage MD, recirculation systems can also be designed to operate either at high flux and low energy efficiency or low flux and high energy efficiency. The relative value of these designs and the ideal combination of GOR and flux from among the possible values is a function of the relative cost of system area (CapEx) and heating and cooling OpEx. In order to compare systems, without having to

consider specific values of costs, the performance curves in a GOR vs. flux graph are compared.

Figure 7-2 shows the GOR-flux performance curves of batch and semibatch MD. Batch significantly outperforms semibatch MD over the entire range of system sizes considered. GOR increases, along with a decrease in flux when the system specific area is increased. Here, we represent system size through a specific velocity $= v/L$ (since w and d_{ch} are held constant, and feed velocity could be easier to control in a physical system compared to mass flow rate $\dot{m}$, since feed density changes with salinity). Since fully developed laminar flow is considered in the feed and cold channels, the heat transfer coefficient is independent of velocity. As a result, the same GOR and flux would be obtained with a 12 m module length and 16 cm/s feed inlet velocity as with a 6 m module length and 8 cm/s feed velocity. In reality, a system would be scaled up keeping velocity and length constant and increasing the channel width, so as to not affect channel heat transfer and pressure drop. Here, since we characterize the design space in terms of v and L it is important to note that for laminar flow regime in the channels, the system performance is dictated by v/L rather than by the two values independently.

For a given physical system in operation, L is fixed. The system specific area can be adjusted by changing v. In Fig. 7-2, v/L varies in over the range of 6–20 cm/s-m. At each value of v/L, one of the points on the GOR-flux performance curve is realized as the time-averaged performance evaluated using Eqs. 7.11, 7.12.

Note that just as in single stage MD without recirculation, there exists a critical specific size beyond which both GOR and flux decrease. We will revisit this issue in Section 7.4. For now, we focus on the fact that batch clearly outperforms semi-batch.

7.3.1 Batch spends more time at lower salinities

Figure 7-3 shows the instantaneous flux and heat input rate as a function of feed salinity at the MD module inlet for the batch system. As the inlet salinity increases, the resistance to vapor transport within the MD module rises, and correspondingly, both instantaneous flux and GOR reduce (and $\dot{Q}_{\mathrm{h}}$ increases).

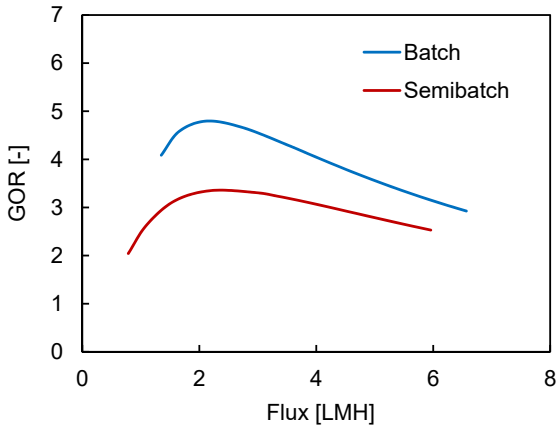

Figure 7-2: Batch performs better than semibatch MD. $\delta_{\mathrm{m}} = 200$ μm, $L = 6$ m, $v = 6$–20 cm/s. Equivalently, $v/L = 1$–3.33 cm/s-m.

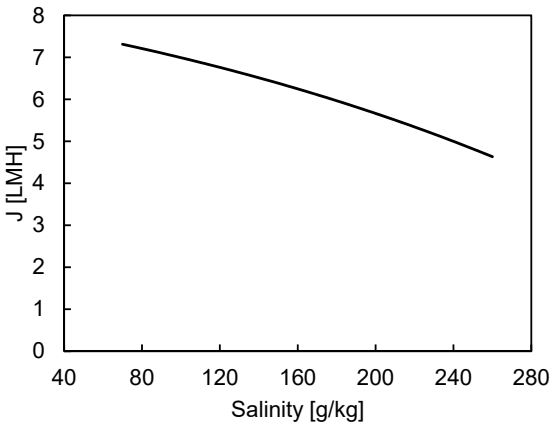

(a) Flux as a function of inlet salinity.

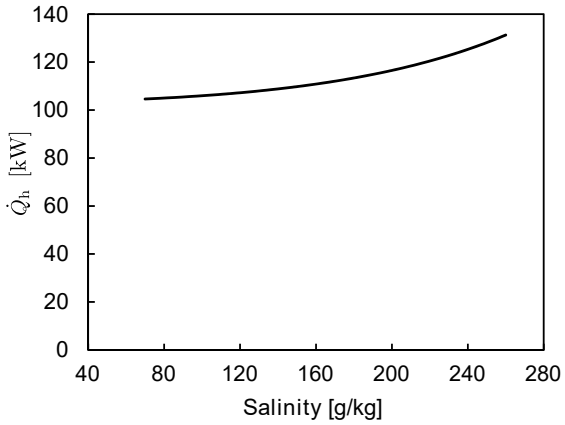

(b) The heater input as a function of inlet salinity.

Figure 7-3: Flux and heat supply as a function of inlet salinity. $v_{\mathrm{in}} = 0.2$ m/s, $L = 6$ m, $\delta_{\mathrm{m}} = 200$ μm, $T_{\mathrm{in}} = 85\,^{\circ}\mathrm{C}$.

While both batch and semibatch MD systems go through same salinity range from 70 g/kg to 260 g/kg, the relative amount of time in each cycle that the two systems spend at various salinities is different. Figure 7-4 shows J and $\dot{Q}_{\mathrm{h}}$ in the batch, semi-batch and continuous recirculation systems over non-dimensional cycle time (t/τ_{cycle}). For continuous recirculation, which is a steady-state process, both J and $\dot{Q}_{\mathrm{h}}$ are constant and close to the value at the end of the cycle time for the batch and semibatch processes. Note that since batch spends relatively larger fraction of time at lower salinity, its time-averaged flux is higher than those of the other configurations and averaged heat input rate is lower.

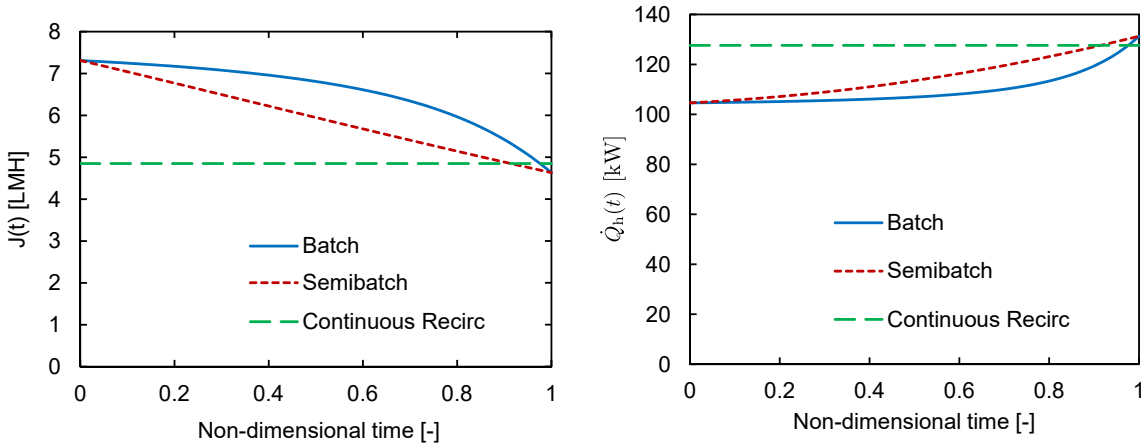

(a) Flux over the process cycle time.

(b) The heater input over the process cycle times.

Figure 7-4: Flux and heat supply over the cycle times of the processes. Continuous recirculation, which is a steady process is also shown for contrast.

7.4 Operational constraint: Avoid operating at feed flow rate less than the critical flow rate

In the previous chapter, a practically relevant critical system size or flow rate was identified for high salinity MD systems. System operation was to be restricted to above the critical feed flow rate in order to avoid operating conditions with both low flux and GOR.

The batch recirculation system has an additional degree of freedom wherein, the feed inlet flow rate into the module can be changed with time by adjusting the feed pump. Since the inlet salinity to the MD module increases with time, the critical feed flow rate or critical feed velocity also rises with time. As a result, it is insufficient to just avoid counterproductive operating regime at the beginning of the process, but in fact throughout the process cycle time it should be ensured that $v > v^{\text{crit}}$. In other words, batch MD should run with a variable speed pump.

Figure 7-5 shows GOR as a function of specific area of the MD system. The critical specific area of the system, beyond which GOR decreases (along with flux which always decreases with an increase in specific area) is indicated by the red dots. Note that the critical specific area decreases significantly as inlet feed salinity increases.

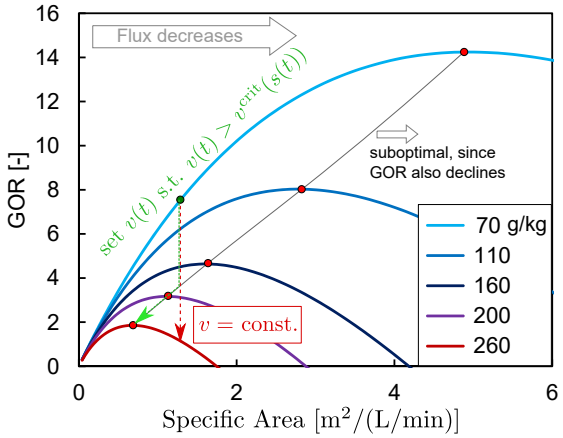

Figure 7-5: Avoid operating at specific area > critical specific area as the system salinity increases. $\delta_{\text{m}} = 200$ μm.

For a fixed area MD system, the inverse of specific area, the feed flow per unit area, is the relevant variable. In this case, MD system operating should ensure that the feed flow per unit area is always higher than the critical feed flow per unit area.

Over the course of the cycle, if the feed velocity is kept constant, it is possible to move from an allowable operating condition (i.e., to the left of the red dots) to the restricted areas (to the right of the red dots) of the GOR-specific area curve, such as in the case of the red arrow shown in Fig. 7-5.

One such operating condition is (for $\delta_m = 200$ μm, $L = 6$ m) v being held constant at 8 cm/s. In this case, the overall GOR is 4.78 and flux is 2.34. The corresponding flux and $\dot{Q}_h$ profiles as a function of time are shown in Fig. 7-6. The operating condition transitions to the counterproductive regime starting at $s = 190$ g/kg.

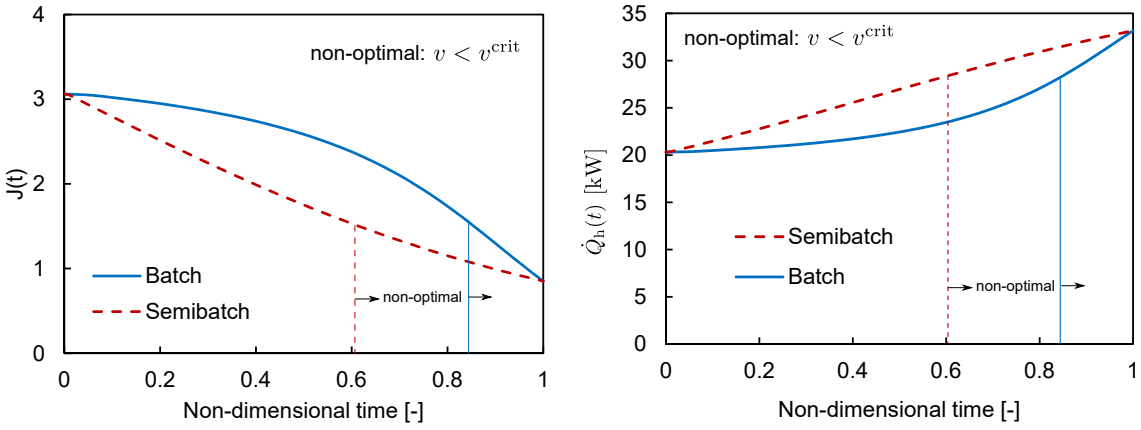

(a) Flux over the process cycle time for batch and semibatch.

(b) The heater input over the process cycle times.

Figure 7-6: Flux and heat supply over the cycle times of the processes: Non optimal condition - $v < v^{crit}$ for $s > 190$ g/kg. $\delta_m = 200$ μm, $v/L = 1.33$ cm/s-m.

Beyond $s = 190$ g/kg, the feed velocity can be increased to match v^{crit} as shown by the green arrow in Fig. 7-5. This would lead to an improvement in both GOR and flux to 4.96 and 2.61 LMH. The corresponding J and $\dot{Q}_h$ profiles over the cycle time are shown in Fig. 7-7. Note the discontinuity in the flux and heat input rate. Even though the heat input rate increases significantly, the flux is also prevented from decreasing to a very low value, and hence the overall specific thermal energy consumption is actually lower in this case, compared to the previous case where a constant velocity was maintained.

The corresponding v profile over the cycle time is shown in Fig. 7-8. During real-time operation, the feed salinity in the tank can be measured. The feed velocity can be controlled by by using a variable frequency drive or valve. The equations presented in the last chapter can be used to calculate v_{crit} as a function of system parameters and the feed instantaneous salinity in the control system. An equivalent method based on NTU would involve measuring the temperatures at the inlets and outlets

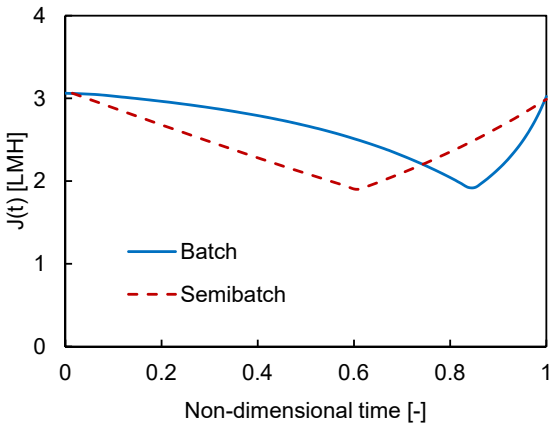

(a) Flux over the process cycle time.

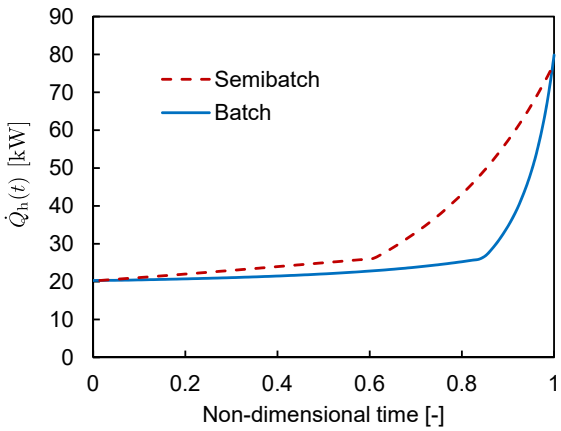

(b) Heat input over the process cycle time.

Figure 7-7: Flux and heat supply over the cycle times of the processes: Non optimal condition is avoided by adjusting v s.t. $v(t) > v^{\text{crit}}(s(t))$.

of the MD module to calculate NTU, compare against NTU^{crit} and adjust flowrate if necessary. Note that the present study assumes constant top temperature. If the top temperature were to change over the cycle time, this too should be considered when calculating v^{crit}.

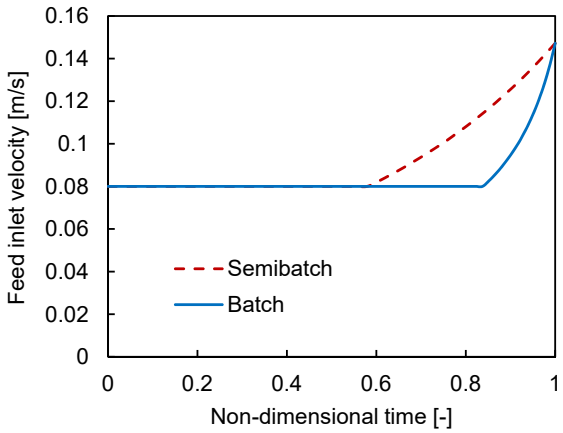

Figure 7-8: Velocity profile over the cycle time to ensure $v > v^{\text{crit}}$.

Figure 7-9 shows the advantage of ensuring instantaneous NTU is always maintained below the critical value of NTU. The dotted lines are reproduced from Fig. 7-2, whereas the solid lines represent the new improved performance. The left-most point of the solid lines is the limiting case where $\text{NTU} = \text{NTU}^{\text{crit}}$ throughout the cycle time. Since GOR is maximized throughout the cycle time, for the given membrane thick-

ness, this is the maximum GOR possible for concentrating 70 g/kg to 260 g/kg. Other points close to this limit have equality of NTU and NTU^{crit} for some time (towards the end of the cycle at high feed salinity), whereas at very high flux, $\text{NTU} < \text{NTU}^{\text{crit}}$ throughout the cycle time.

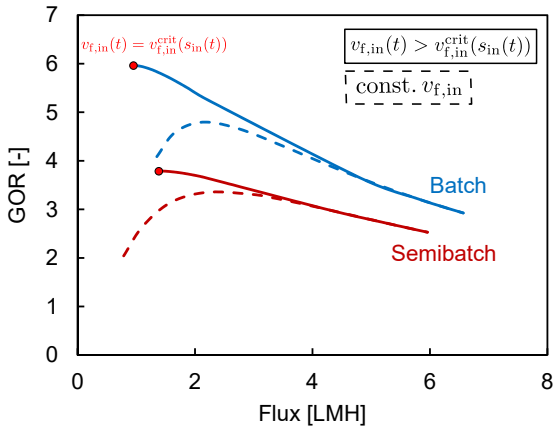

Figure 7-9: Advantage of ensuring $\text{NTU} \leq \text{NTU}^{\text{crit}}$. Significantly higher GOR can be obtained by avoiding counterproductive conditions.

7.5 Optimal membrane thickness and comparison with continuous recirculation

7.5.1 Optimal membrane thickness for batch MD as a function of flux

All the previous analysis was performed at one value of $\delta_{\text{m}} = 200$ μm. Here, we relax this membrane thickness condition. For thicker membranes, since η is higher, GOR is higher, but at the expense of low flux. Overall, the GOR-flux performance curves for all the membrane thicknesses can be plotted together and the upper limit profile can be identified as the best case GOR-flux operating condition for the given membrane $B_0/k_{\text{eff,m}}$ and h_{ch}.

The GOR-flux curves for multiple thicknesses, along with the blue solid line showing an approximate upper limit performance curve of batch (allowing δ_{m} to change as

a design variable) is shown in Fig. 7-10. The specific flow rates used at each thickness are:

Table 7.1: Specific flow rate range in Fig. 7-10 for each membrane thickness

Thickness (δ_m) [μm]	v/L [cm/s-m]
140	2 – 6.66
200	0.33 – 3.75
400	0.2 – 2
600	0.12 – 1.5
1000	0.08 – 1.42

For a thinner membrane, the effective membrane size is small and the effective membrane size increases as the membrane thickness increases.

GOR of batch is 2–3 times higher than that of continuous recirculation system with an optimized membrane thickness (δ_m) at each value of flux.

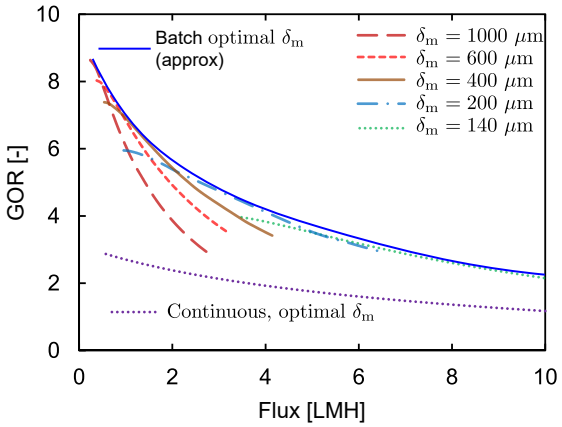

Figure 7-10: Effect of membrane thickness on batch MD performance, and comparison with continuous recirculation system with optimized membrane thickness.

7.5.2 Comparing with AGMD

Based on the discussion in the previous chapter, we understand AGMD performance as corresponding to a thicker, more permeable and less conductive effective membrane A thicker effective membrane is advantageous at high salinity, but disadvantageous at lower salinity. From Fig. 7-10, we can identify the range of flux values at which a 1 mm membrane becomes preferable. If economics drives us to operate under such

conditions (very high GOR and low flow), it would be preferable to use AGMD. Under other conditions as well, AGMD (with its higher $B_0/k_{\mathrm{eff,m}}$) is advantageous, but the required membrane thickness is lower, which may be a challenge to implement in AGMD without flooding. Within CGMD, any membrane with a higher $B_0/k_{\mathrm{eff,m}}$ will also certainly be preferable.

7.6 Multistage recirculation

Figure 7-11 compares the GOR and flux of multistage recirculation with continuous recirculation and batch recirculation. For each N_{stages} the area is split equally among all the stages in this analysis. This is not the ideal design, and for example, for two stages, the ideal area of the first stage is about 66% of the total area. Both GOR and flux of multistage recirculation approaches that of a batch system as the number of stages increases. Multistage recirculation performs in space what a batch system does in time. While it is a steady state process, it is likely that the number of heat-exchangers required would make it unattractive compared to batch recirculation.

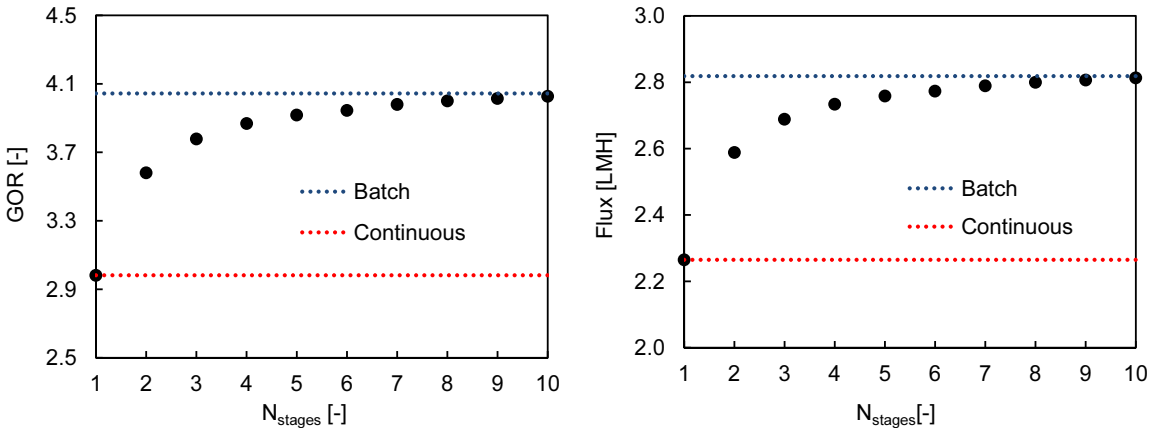

(a) GOR as a function of number of stages. (b) Flux as a function of number of stages.

Figure 7-11: GOR and flux vs. N_{stages} for multi-stage recirculation.

7.7 Additional Operational Considerations

7.7.1 Batch vs. continuous recirculation contrast more pronounced at high salinity

The relative comparison between batch semi-batch and continuous recirculation is a function of the range of feed salinities that are handled by the system. For the same value of overall recovery ratio, the range of salinity treated is much larger when the feed salinity is higher. The performance of each of these systems is a weighted average of the performance over the sanity range. For a 72% recovery process from 5 g/kg – 18 g/kg, the change in GOR and flux over this salinity range is so small that all three designs perform essentially the same. At higher salinity though, the difference is more significant (Fig. 7-12).

Similarly, for AGMD or a thick CGMD membrane system, the change in performance with changes in feed salinity is small. As a result, once again, the difference between batch, semi-batch and continuous recircualtion would be small, and for simplicity, a continuous recirculation system may be preferable.

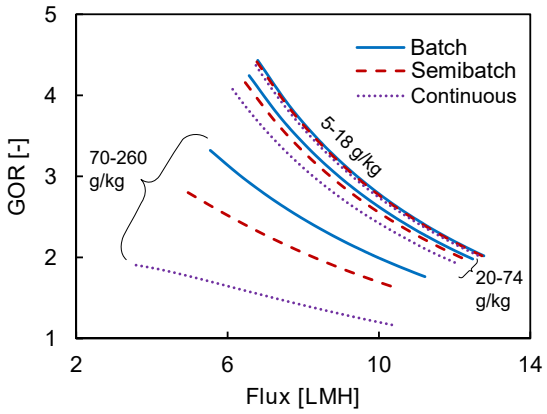

Figure 7-12: At higher absolute salinity, the motivation towards operating in batch is higher. $\delta_m = 200$ μm.

7.7.2 Improve average GOR by operating at constant flux, under some conditions

It is possible to improve overall performance by operating at constant flux over the cycle time of the batch process [51], by allowing feed inlet temperature or feed velocity to change, rather than by operating at constant feed velocity and temperature. The savings in GOR by this approach are small (around 1%), and may not be worth the additional control system required to implement this (Fig. 7-13).

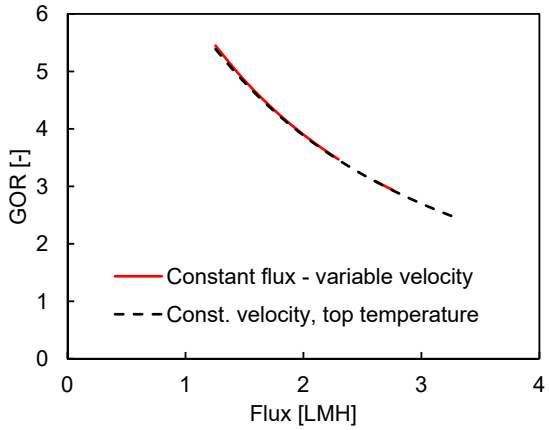

Figure 7-13: Operating at constant flux throughout the cycle time leads to marginal improvement over operating at fixed top temperature or fixed velocity, when the baseline condition is away from the counterproductive conditions.

Cycle reset time

When comparing batch/semibatch unsteady processes with continuous/steady processes, it is important to consider the lower availability factor of the unsteady systems. If the cycle time is τ_{cycle} and the time taken for emptying the final brine and refilling the system with fresh feed for restarting the next cycle is τ_{change}, the fraction of useful (permeate producing time) for the system can be written as $\tau_{\text{frac}} = \frac{\tau_{\text{cycle}}}{\tau_{\text{cycle}}+\tau_{\text{change}}}$.

When designing unsteady processes it is important to maximize τ_{frac} by reducing τ_{change} or by increasing τ_{cycle}. In the design we have considered, τ_{cycle} can be increased by increasing the size of the tank. The reset time can still kept small, if the feed is refilled into the module continuously from the storage tank while the main batch tank

is also being filled (so that the reset time corresponds only to the module filling time, rather than also the large-tank refilling time) as shown in Fig. 7-14. For enabling a fair comparison of the unsteady process with a steady process, the flux of the unsteady process should be scaled by τ_{frac}. We have assumed a high value of τ_{frac} in the foregoing comparisons.

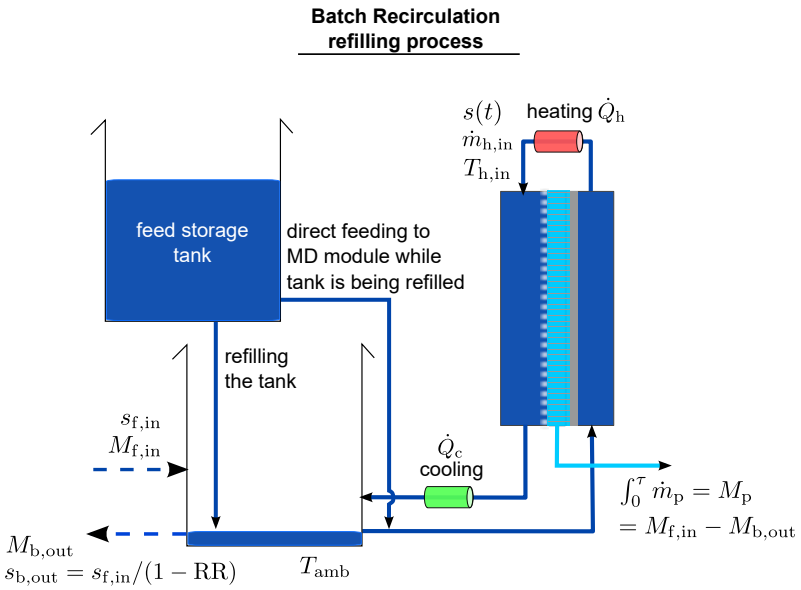

Figure 7-14: Simultaneous feed refilling and feeding to MD module to decrease τ_{change} and increase τ_{frac}.

7.8 Conclusions

1. For recirculation based higher recovery systems, cooling energy is also required in addition to feed heating, and as a result, the relative importance of GOR increases.

2. Batch operation is better than semibatch and continuous recirculation since in batch the system stays at lower feed salinity levels for a larger fraction of the cycle time.

3. It is important to ensure that the system NTU is maintained lower than or equal to the instantaneous critical value of NTU^{crit} which is a function of the

instantaneous inlet feed salinity entering the MD module, as well as module heat transfer properties and system top temperature.

4. As with single stage MD at high salinity, there exists an optimal thickness for batch operation as well, as a function of the relative cost of thermal energy and system area. A thicker membrane is optimal at low flux and high GOR.

5. Overall, batch MD can achieve up to 2–3 times higher GOR, at the same value of flux, compared to a continuous recirculation system.

6. The change-over time should be minimized for unsteady processes, and the flux should ideally be scaled by τ_{frac} before comparing against continuous systems.

Chapter 8

Multi-effect membrane distillation for high recovery

Abstract

Multi-effect membrane distillation (MEMD) is a configuration of MD that is analogous to large scale multi-effect distillation (MED) process. Condensation of the vapor produced in one effect is used to transfer heat into a feed stream at a subsequent effect to further evaporate water from the feed. This is in contrast to the more common single stage MD process, as well as multi-stage vacuum MD, wherein vapor condensation preheats the incoming feed water. As a result, MEMD has a unique advantage of enabling high per-pass pure water recovery. In this chapter, we develop a numerical model of multi-effect membrane distillation (MEMD) to delineate the design parameters that control its energy efficiency, flux, and recovery ratio. The number of effects controls energy efficiency and flux of MEMD, and is analogous to specific area of a single stage device. The specific area of MEMD on the other hand, provides another degree of freedom to control the process recovery ratio. The proposed model enables choice of optimal membrane thickness along with the choice of number of effects to maximize GOR for each desired flux. If heat is recovered from both the brine and permeate streams in the interstage heat exchangers, MEMD can perform better than batch recirculation.

8.1 Introduction

Multi-Effect MD (MEMD) can achieve high recovery ratio per pass because it recovers condensation energy from vapor produced in one effect back into the feed stream in

a subsequent effect, to further evaporate water out of the feed stream. MEMD is analogous to and can be designed based on the MED process, which is commonly used to treat water up to saturation concentrations.

Compared to MED, MEMD could require a lower capital cost and smaller footprint. For example, polymers have been used in MEMD structures and vapor spaces are generally smaller. MEMD can differ from MED in two ways. First, MEMD always has a membrane separating the vapor phase from the feed stream. This way, the feed stream itself is not flashed to a lower vacuum level at each effect, and the feed can remain at ambient pressure throughout. Secondly, a vacuum need not necessarily be applied in MEMD. For example, in this study, we consider multi-effect conductive gap and air-gap MD systems stacked together to form an MEMD system. Vacuum MEMD (V-MEMD) [129, 134] is a popular version of MEMD that can result in higher energy efficiency (due to lack of heat conduction loses through the membrane) and flux. The MEMD designs without vacuum pumps considered in this study would require lower operating expenditure and lesser maintenance costs. A partially evacuated air-gap could also result in improved performance and could be analyzed using the current framework by adjusting the membrane permeability and thermal conductivity appropriately.

The key distinguishing feature of MEMD compared to single stage configurations and multi-stage flash type MS-VMD is that it includes simultaneous evaporation and condensation. Energy from the condensing vapor is recovered within the MD module into the feed stream from which additional water is evaporated. As in multi-effect distillation and mechanical vapor compression, reusing the latent heat from vapor condensation for additional vapor production results in the possibility of high per pass recovery ratio (RR). Other MD configurations where vapor condensation is used to preheat the incoming feed water are restricted to RR $< 110\%$.

Figure 8-1 shows a schematic diagram of a conductive gap MEMD process [108]. The feed enters at a low temperature at the final effect as a coolant. The additional coolant is discharged, and $\dot{m}_{\mathrm{f}}$ portion is passed into a series of interstage heat exchangers where the feed recovers sensible heat energy from the brine and permeate

streams. The preheated feed may additionally be heated up to the top effect's temperature using the external heater ($\dot{Q}_{\text{ext}}$). The hot feed water is then introduces into the first effect.

In the first effect, heat energy ($\dot{Q}_{\text{direct}}$) is added and permeate is collected in the gap. The brine leaving the first effect is cooled down in the interstage HX and introduced into the second effect as feed. Here, the feed stream receives energy from the first effect and additional permeate is produced.

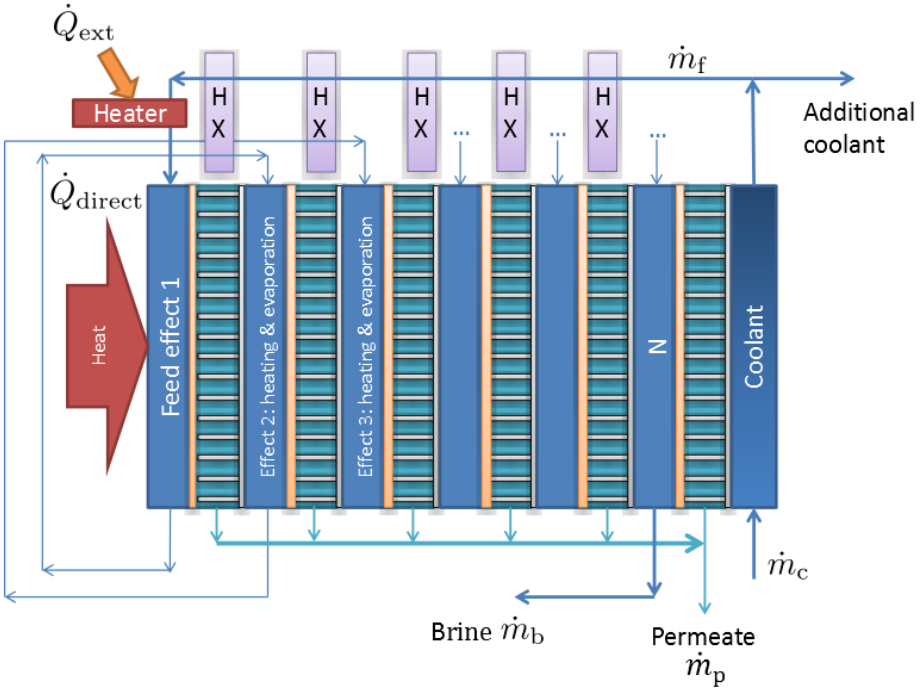

Figure 8-1: Multi-effect conductive gap MD process with brine stream being used for feed preheating. Ideal MEMD will additionally recover energy from the warm permeate leaving each effect to preheat the feed stream.

Another method of obtaining high recovery ratio with MD is through brine recirculation. It has been shown previously that among various recirculation methods (batch, semi-batch, continuous recirculation and multi-stage recirculation), a batch system is the best. A batch process is unsteady, wherein feed starts off at low salinity and as pure water is extracted from the feed stream, its salinity increases. The process continues until the final brine salinity is reached. Since batch is a relatively simple method of operating a single stage MD system at high overall RR, in this

study MEMD performance (GOR and flux) will be compared against that of a batch system.

In this study, we will consider the following research questions:

1. What are the design considerations of an MEMD system - for achieving high GOR, high flux, and high pure water recovery?

2. For the same overall recovery ratio, is MEMD better compared to single-stage batch recirculation in terms of GOR and flux?

8.2 Methodology: Modeling of MEMD performance

In a 'full' numerical model of the MEMD process, the feed channel in each effect is discretized along the length. The mass flow rate, salinity and temperature variations in the feed channel are evaluated based on mass and energy conservation applied to each computational cell. Condensation of vapor from a previous effect, along with heat conduction losses from the previous effect act as heat sources. The energy loss from the feed channel is mediated by evaporation and heat conduction through the membrane.

For a single effect system, it can be shown that the feed stream would reach an equilibrium temperature if the heat flux into the feed channel and the temperature of the condensing wall are held constant. This is because, the rate of vapor transfer out through the membrane is a function of the feed temperature. If the feed enters at low temperature, it would initially get heated up as the flux from the wall exceeds heat transfer through the membrane. As the temperature of the feed increases, the rate of heat transfer through the membrane increases. At very high feed temperature, the rate of heat loss across the membrane may exceed the incoming flux from the wall. The temperature change along the feed flow direction can be written as:

$$\dot{m}_{\mathrm{f}} c_{\mathrm{p}} \frac{dT}{dx} = \dot{q}_{\mathrm{in}} - J\left[h_{\mathrm{vap}}(T_{\mathrm{m}}) - h_{\mathrm{l}}(T, s)\right] - \dot{q}_{\mathrm{m}} \tag{8.1}$$

where J and $\dot{q}_{\mathrm{m}}$ are a function of the feed temperature and increase with feed tem-

perature. There exists a value of feed temperature T such that the right hand side of Eq. 8.1 is zero and hence $dT/dx = 0$.

When modeling the MEMD process, the system top and bottom temperatures are considered to be fixed, based on the heat source and sink temperatures available. In this study, the wall across which $\dot{Q}_{\text{direct}}$ is supplied into the first effect is set at $T_{\text{w}}^{1} = 85\,^{\circ}\text{C}$, and the average temperature of the coolant node is set at $T_{\text{c}} = 25\,^{\circ}\text{C}$. In reality, the coolant may enter at $20\,^{\circ}\text{C}$ and be heated up to $30\,^{\circ}\text{C}$ to result in this average temperature at the coolant node. Based on these set temperatures at the extremities, an equilibrium T can be evaluated within the system as a function of the thermal resistances.

A simpler model of MEMD without length-wise discretization can therefore be implemented where the feed temperature of each effect remains constant along the flow direction. Figure 8-2 shows the equivalent resistance network for this model, along with the key equations connecting the heat fluxes within this system.

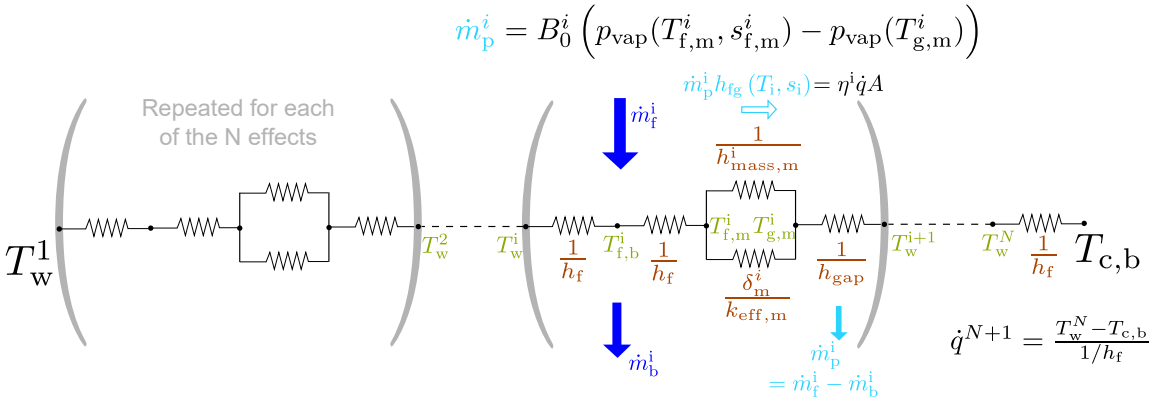

Figure 8-2: Resistance network model of MEMD

By appropriately designing the interstage HX size, the feed at each effect may be introduced close to its equilibrium value. This way, all the heat flux is used for evaporation rather than for sensible heating of the feed and brine is used to preheat

the feed water. If an infinite area HX is used to recover energy from both the brine and permeate stream at each stage, $\dot{Q}_{\text{ext}} \rightarrow 0$. With realistic heat transfer area, a TTD of 3 °C is often used to characterize the feed preheating HXs in this study. Additionally, system performance when no energy is recovered as well as when only the brine stream is used for feed preheating are also considered.

At each effect, the incoming feed is concentrated and a permeate stream at a lower temperature is produced. As a result, $\dot{q}^{i+1}$ can be slightly different from $\dot{q}^{i}$ as shown in Fig. 8-2. At each effect, the average of inlet and outlet salinities is used to determine feed vapor pressure.

The full set of equations that are solved for the equilibrium multi-effect MD model is included in 8.7. The modeling results are presented for the case of concentrating sodium chloride solution from 70 g/kg to 260 g/kg.

8.2.1 Performance metrics

As in the previous chapters, GOR and flux can together be used to characterize the performance of the MEMD system. The specific cost of feed concentration for a given recovery ratio (RR), can be represented as $c_{\text{f}} = C_{\text{flux}}/J + \left(C_{\text{heating}} + C_{\text{cooling}}\right)/\text{GOR}$. Just as in the case of batch-recirculation, a lower GOR results in a higher heating as well as cooling load.

8.3 Results: Major design parameters

8.3.1 Number of effects

GOR is proportional to the number of times the supplied heat energy is reused for evaporation, i.e., the number of effects. The GOR of an ideal MEMD system without losses is therefore $\approx N$ (number of effects), like the GOR of MED. With heat conduction loses through the membrane, even with perfect heat recovery for feed preheating, GOR is reduced to ηN.

The number of effects therefore plays a crucial role in deciding the performance of

MEMD. The equivalent parameter for a single stage system is the membrane area. At larger length in single stage MD enables better heat recovery and higher GOR, but also results in a reduced driving force for pure water production and hence lower flux. Similarly, in MEMD, when the number of effects is raised, the interstage temperature difference (which is the driving force for vapor flux) drops and therefore leads to lower flux.

Figure 8-3 shows the impact of N on the GOR and flux for a fixed value of membrane thickness. The size of each stage is adjusted to achieve the same overall recovery ratio.

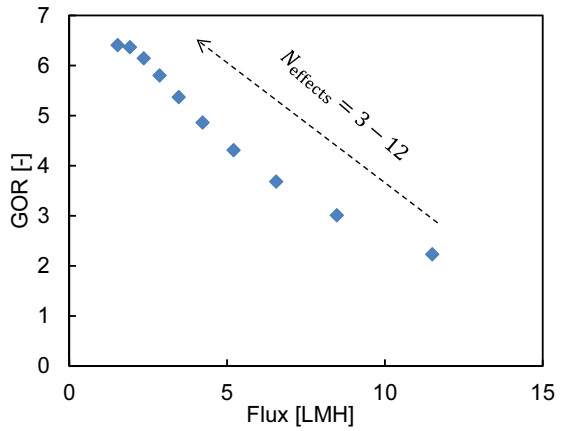

Figure 8-3: GOR-flux values as a function of the number of effects in the MEMD system. $\delta_m = 200$ μm, feed is concentrated from 70 to 260 g/kg.

8.3.2 Per stage area

As described previously, the specific membrane area relative to feed flow rate determines the GOR and flux performance of single stage MD configurations. In MEMD, specific membrane area does not affect GOR or flux directly, as GOR and flux are determined directly by N. The area of each stage is an important second degree of freedom in MEMD that helps tune the overall recovery ratio of the process. Figure 8-4a shows that RR increases with the membrane area. The sub-linear trend is a result of heat condution losses which increase at higher RR (higher salinity). The higher salinity also has a small negative influence on GOR and flux, as shown in Fig. 8-4b.

At fixed TTD_{HX} the GOR initially increases before decreasing, but the trend in the case of perfect heat recovery is similar to that of flux: a continuous small decline, due to the increased salinity of the feed stream at higher RR, which is a result of higher area leading to higher salinity.

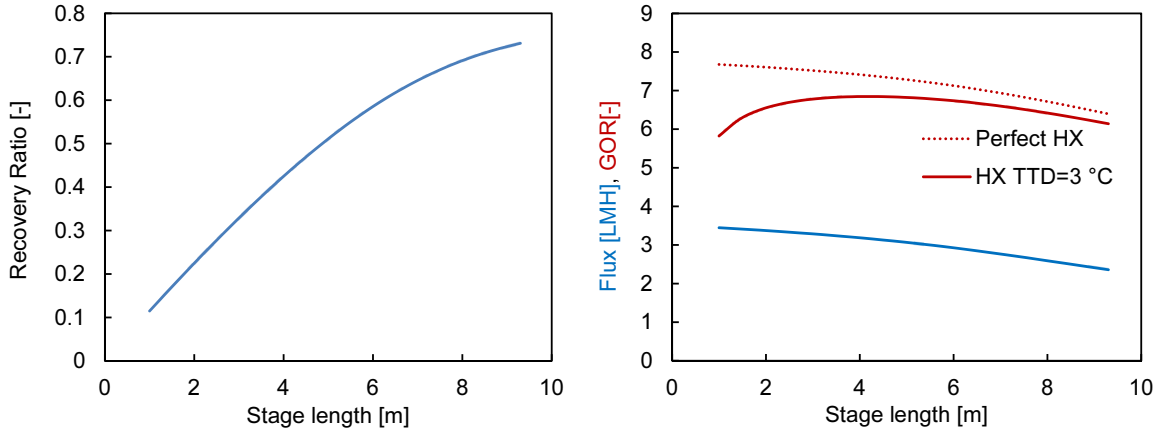

(a) Effect of stage area on recovery ratio. The recovery ratio increases almost linearly with an increase in total membrane area. Width is held constant at 12 m, for $\dot{m}_f = 1$ kg/s.

(b) GOR and flux decrease due to an increase in average salinity of the feed stream, as a result of increased total area, which leads to a larger recovery ratio.

Figure 8-4: Effect of membrane area.

In the numerical model, length is allowed to vary to obtain the required overall pure water recovery ratio.

8.4 Results: Additional design considerations

8.4.1 Coolant flow rate at the final effect

The amount of coolant fluid used in the final stage is an important parameter for MEMD. This parameter will influence the final node's temperature in the resistance network model. The coolant fluid flow rate needs to be large enough such that the condensation of vapor in the final stage doesn't lead to a significant increase in the coolant temperature.

The effect of coolant flow rate on MEMD GOR and flux is evaluated using the length-wise discretized MEMD model and presented in Fig. 8-5. At larger coolant

mass flow rate, the flux is higher since overall temperature difference between the top and bottom temperatures is larger. On the other hand, with a lower coolant flow rate, the extent of preheating of the feed in the coolant channel is higher, leading to a higher GOR.

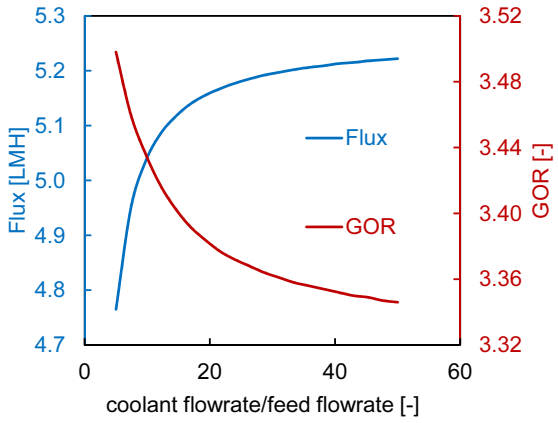

Figure 8-5: Effect of coolant flow rate on GOR and flux.

8.4.2 Feed salinity

Figure 8-6 shows the effect of feed salinity on GOR and flux. Higher feed salinity has a detrimental effect on both GOR and flux, by increasing the mass transfer resistances ($1/h^i_{\text{mass}}$) while leaving the heat transfer resistance of the membrane unchanged.

As in the case of single stage MD configurations, a higher temperature difference across the membrane ΔT_{m} leads to greater resilience to high salinity operation. This can be obtained by reducing the resistance of the non-membrane portions relative to the membranes.

$$f^{\text{ME}}_{\text{ch:m}} = \frac{\frac{2N+1}{h_{\text{f}}} + \frac{2}{h_{\text{gap}}}}{\sum \frac{\delta^i_{\text{m}}}{k_{\text{eff,m}}}} \tag{8.2}$$

A well designed MD system will attempt to reduce the resistances in these flow channels and the gaps as much as possible. Another way to design for high salinity is to increase membrane thickness, and choosing AGMD, or partial vacuum AGMD designs (with higher B_0/k).

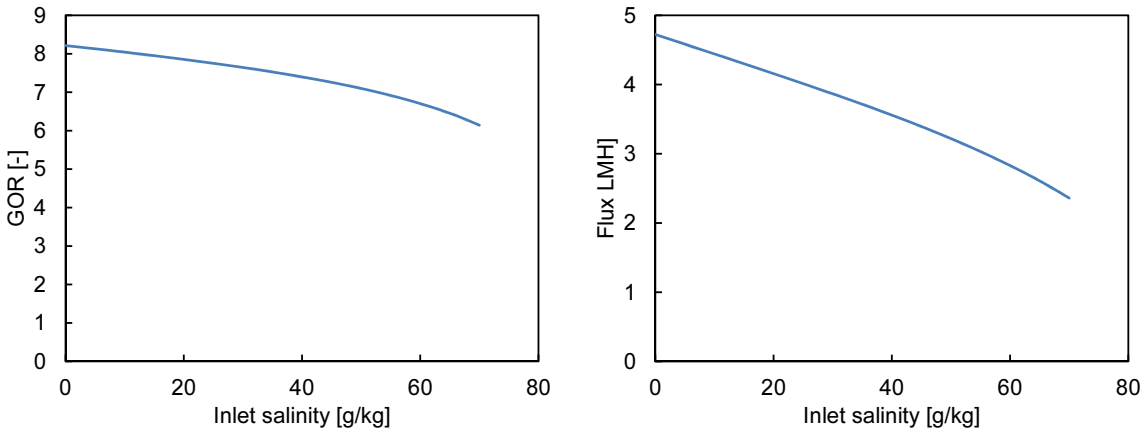

(a) Effect of inlet salinity on GOR at constant RR= 73%, $\delta_m = 200$ μm, and $N_{effects} = 10$.

(b) Effect of inlet salinity on flux constant RR= 73%, $\delta_m = 200$ μm, and $N_{effects} = 10$.

Figure 8-6: Effect of feed inlet salinity on system performance at constant overall recovery ratio.

8.4.3 Membrane thicknesses

Figure 8-7 shows the effect of membrane thickness variation at $N_{effects} = 12$. As the membrane thickness is decreased, flux increases (due to higher $B = B_0/\delta_m$), whereas GO decreases (due to lower η). Beyond a certain membrane thickness, both GOR and flux start to decrease, since the rate of decrease in η dominates.

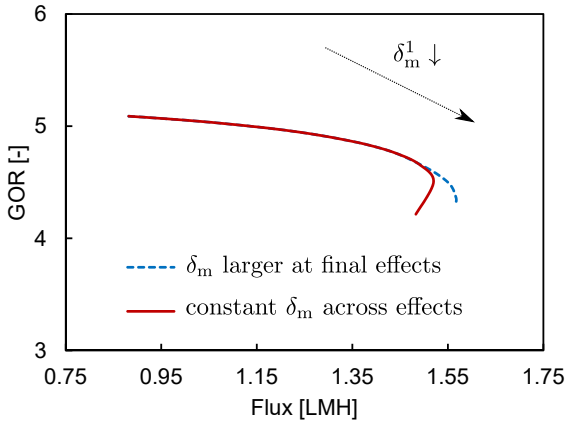

Figure 8-7: Effect of first stage membrane thickness on GOR-flux performance of ME-CGMD. As δ_m^1 decreases, increasing the thickness of final effects helps prevent decline in both GOR and flux.

In MEMD, the thickness of the membrane at each effect can be set independently.

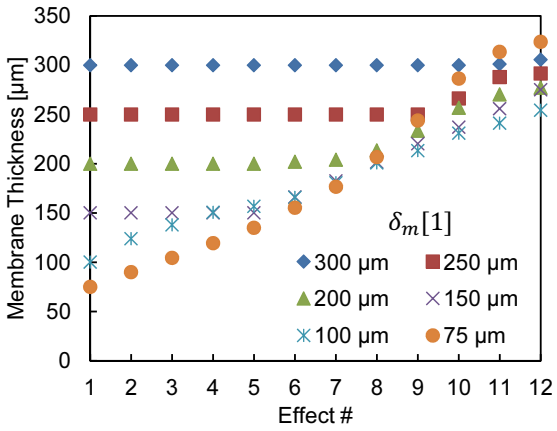

Figure 8-8: A thicker membrane is chosen at the final effects based on numerical optimization. The thickness in a later effect is constrained to be at least as thick as an earlier effect since the salinity at later effects is higher and temperature is lower.

The advantage of choosing thicker membranes is shown in Fig. 8-7. By allowing the membranes to be thicker at the final effects (as shown in Fig. 8-8), a larger value of flux can be achieved at the same GOR.

For each of the N_{effects} considered in Fig. 8-3, the membrane thickness (held constant across all the effects) can be allowed to vary, as an additional degree of freedom in system design. Figure 8-9 shows the set of all accessible points by allowing both number of effects and membrane thickness to vary. The upper limit envelope of this set of curves (that maximizes GOR at a given flux, or maximizes flux for give GOR) can then be extracted as the upper limit performance of MEMD for a given membrane $f_{\text{c:v}} \propto B_0/k_{\text{eff,m}}$ and channel heat transfer coefficents $(h_{\text{f}}, h_{\text{gap}})$.

Note that at larger N, the left hand side portion of the curves constitutes the upper limit, whereas the right hand side portion constitutes the upper limit envelope at lower N. This refers to the fact that at larger N where the goal is to achieve higher GOR, thicker membranes are optimal, whereas at smaller N, where flux is higher, thin membranes are preferred. This is consistent with the observed trend for the optimal membrane thickness for single-stage and batch recirculation systems.

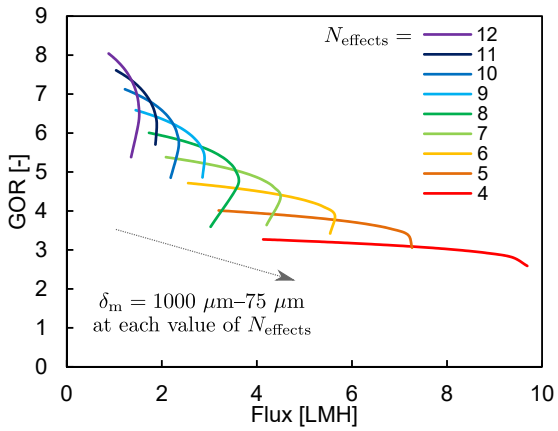

Figure 8-9: Effect of δ_{m} at each N. Membrane thickness provides a second degree of freedom to control GOR-Flux performance of ME-CGMD. Thicker membrane is optimal at larger N.

8.5 Comparing with other MD configurations

8.5.1 Single stage MD

In Figure 8-10, the upper limit performance of ME-CGMD is compared to that of batch CGMD. In both cases, the optimal δ_{m} to maximize GOR at a given flux is used. With heat recovery only from the brine stream, ME-CGMD performs worse than single stage batch recirculation. If the feed preheating in the external HXs uses both the permeate stream and the brine stream from each stage, ME-CGMD reaches higher GOR compared to a single stage batch recirculation system and is therefore better.

The reason for the better energy efficiency of the MEMD system at the same overall pure water production and membrane area is perhaps related to the temperature profiles established within the two processes. In MEMD, temperature at each effect is held constant even as salinity changes, before jumping down to a lower value of temperature at the subsequent effect. The temperature profiles in single stage MD vary more smoothly.

For balanced single stage MD, the ΔT between the hot and cold bulk streams is relatively uniform across the length of the module. The membrane mass transfer resistance is higher at lower absolute temperature and higher feed salinity. As a result,

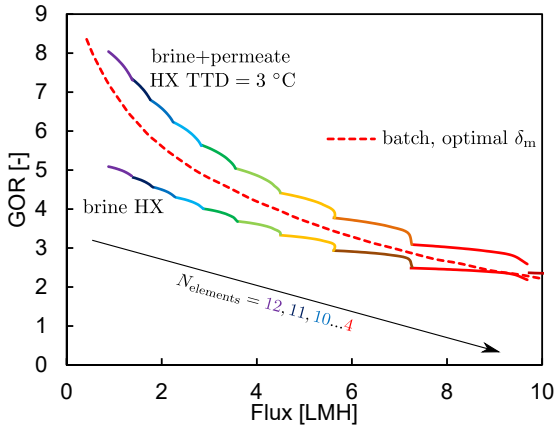

Figure 8-10: Comparison of MECGMD (with brine heat recovery as well as brine and permeate energy recovery for feed preheating) with batch recirculation.

at the lower temperature end of the module the heat flux and pure water flux across the membrane are significantly lower. ΔT_m is higher at this end due to the larger fractional resistance of the membrane.

In the case of MEMD, at the final effects (corresponding to the lower temperature end of single stage system), the total heat flux is still approximately the same as the initial effects. The temperature drop increases at the later effects as a result of their larger resistance. Within each effect since temperature is held relatively constant by simultaneous heating of the feed, the variation in flux along the length at a given effect is only due to changes in feed salinity.

The rate of entropy generation can be decreased by equipartition of flux in space and time for simple systems with uniform resistance [113]. For a heat exchange process with variable resistance, Johannessen et al. [51] showed that while the equipartition of entropy generation is the ideal solution for entropy generation minimization, equipartition of flux is still a good approximation for the solution.

The performance of an upper-limit batch and upper-limit MEMD system are compared. The batch system operates with $\delta_m = 100$ μm, at $v/L = 2.45$ cm/s-m. The GOR and flux of the batch system are 3.32 and 4.54 L/m^2-hr. The optimal MECGMD system operating at approximately the same flux of 4.5 L/m^2-hr consists of 7 effects and has a membrane thickness of 100 μm. The GOR of the MEMD

system is higher at 4.32. The pure water flux in batch MD and MEMD are shown in Fig. 8-11.

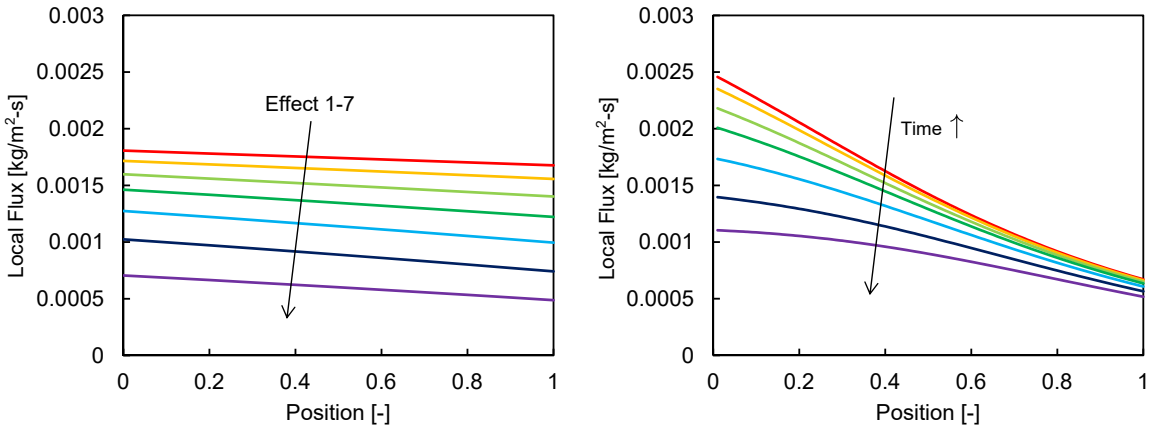

(a) Flux in multi-effect along feed channel length and across several effects.

(b) Flux in single stage batch over time and space.

Figure 8-11: Distribution of pure water flux over the system area (and over time in the case of batch). For the same overall flux, the variability in flux is lower in the MEMD system compared to the batch recirculation system.

Visually we can see that the flux distribution is more uniform in the case of MEMD as a result of its constant temperature difference driving force across the stages. This observation could help explain the numerically predicted improved performance of MEMD compared to batch.

8.5.2 Multi-stage Vacuum MD - MSVMD

MSVMD process [20] is also restricted to a low per-pass recovery similar to single stage MD necessitating the use of recirculation for higher overall recovery ratio. In vacuum MD systems, the heat conduction losses are quite small and hence $\eta = 1$. Under this condition, GOR $= \Delta T_{\text{total}}/\Delta T_{\text{TTD}}$. The terminal temperature difference of the MS-VMD exchanger is a function of the BPE of the feed, number of stages and condenser TTD. As with DCMD systems, the energy efficiency of MS-VMD can be significantly improved only with the use of very large external condensers. The performance of MS-VMD can be analyzed analogous to single stage systems, by setting $f_{\text{c:v}} = \infty$ (corresponding to $\eta = 1$) and evaluating $f_{\text{ch:m}}$ as a function of the

membrane permeability under vacuum and the UA of the external condenser.

8.5.3 Additional considerations

The GOR and flux of MEMD with heat recovery can be better than that of single-stage batch recirculation MD. Here we consider some additional factors for comparing the two systems.

The MEMD process is a steady state process whereas batch recirculation is unsteady. As a result, the flux has to be compared after adjusting for the active fraction of the cycle time of the batch process. This can further decrease J of batch, though we believe that batch MD can be designed with large tanks to ensure high useful fraction of cycle time.

When comparing a MEMD and batch recirculation at the same flux and equal pure water productivity, the cost of membrane and condensing surface area are equal. The difference in cost of cooling is captured by the GOR. A higher GOR results in lower effective cooling energy requirement; in single stage MD this results from lower exchanger TTD and in MEMD, and a lower $\dot{Q}_{\text{direct}}$ that needs to be removed at the final effect. An efficient MEMD requires several interstage HXs to preheat the incoming feed water. This would add an additional CapEx term compared to batch recirculation. The area of external HX required is much smaller than the area of membrane and condenser surface used within MEMD. Nevertheless, system design is more complex as a result of these heat exchangers being required. The size of each HX may also have to be optimized to provide the ideal level of brine cooling before it is introduced into a subsequent effect.

The pumping power requirement may also be different for the MEMD compared to batch recirculation. Since the feed stream acts as the coolant as well, the relative pumping power requirement for MEMD can be lower if the channels correspond to the major pressure drop in these systems.

8.6 Concluding Remarks

Multi-effect membrane distillation (MEMD) is unique among MD configurations in its ability to achieve high pure water recovery in a single pass of feed under steady state operating conditions. For the same overall recovery ratio, the number of effects (N) of MEMD affects both GOR and flux, wheras the specific area at fixed number of stages affects the overall recovery ratio. For each N, the membrane thickness provides another degree of freedom to operate at high-GOR and low flux or vice versa.

The upper limit performance of MEMD is better than that of batch recirculation if both the brine and permeate streams are used to preheat the incoming feed water. As a result of maintaining constant temperature at each effect, and because the temperature drop is larger at the final effects, the overall flux distribution in MEMD is more uniform compared to batch MD and this could help explain the better energetic performance at the same system size and pure wate production rate.

8.7 Chapter Appendix 1: Model equations for MEMD

function $B_{0,\mathrm{MD}}\left(P,\ T_{\mathrm{avg,K}},\ \phi_{\mathrm{m}},\ \tau_{\mathrm{m}}\right)$

$$\mathrm{MW_w} := 0.018\ \ [\mathrm{kg/mol}] \tag{8.3}$$

$$T_{\mathrm{avg}} := \mathrm{ConvertTemp(K,\ ^\circ C,\ } T_{\mathrm{avg,K}}) \tag{8.4}$$

$$R := 8.314 \tag{8.5}$$

$$D_{\mathrm{OMD}} := 1.87 \cdot 10^{-10} \cdot T_{\mathrm{avg,K}}^{2.072} \tag{8.6}$$

$$p_{\mathrm{vap,avg}} := \mathrm{P_{sat}}\left(\mathrm{Steam_{IAPWS}},\ \mathrm{T} = T_{\mathrm{avg}}\right) \tag{8.7}$$

$$p_{\mathrm{air,avg}} := P - p_{\mathrm{vap,avg}} \tag{8.8}$$

$$B_{0,\mathrm{MD}} := \phi_{\mathrm{m}} \cdot P \cdot D_{\mathrm{OMD}} \cdot \frac{\mathrm{MW_w}}{p_{\mathrm{air,avg}} \cdot \tau_{\mathrm{m}} \cdot R \cdot T_{\mathrm{avg,K}}} \tag{8.9}$$

end

function $get_{h,\mathrm{NaCl}}(s,\ T)$

$$\mathrm{MW_s} := 58.44\ \ [\mathrm{g/mol}] \tag{8.10}$$

$$m := \frac{\frac{s}{1-\frac{s}{1000\ \ [\mathrm{g/kg}]}}}{\mathrm{MW_s}} \tag{8.11}$$

$$get_{h,\mathrm{NaCl}} := 1054{-}553.6{\cdot}m{+}4169{\cdot}T{-}292.6{\cdot}m^2{-}249.1{\cdot}m{\cdot}T{-}0.8948{\cdot}m^3{+}16.25{\cdot}m^2{\cdot}T \tag{8.12}$$

end

function $get_{k,\mathrm{NaCl}}(s,\ T)$

$$\mathrm{MW_s} := 58.44\ \ [\mathrm{g/mol}] \tag{8.13}$$

$$m := \frac{\frac{s}{1-\frac{s}{1000\ \ [\mathrm{g/kg}]}}}{\mathrm{MW_s}} \tag{8.14}$$

$$\begin{aligned} get_{k,\mathrm{NaCl}} := {} & 0.5548 - 0.006107 \cdot m + 0.00228 \cdot T + 0.000465 \cdot m^2 - 1.66 \times 10^{-5} \cdot m \cdot T \\ & -1.112 \times 10^{-5} \cdot m^2 - 1.125 \times 10^{-5} \cdot m^2 \cdot T + 4.009 \times 10^{-7} \cdot m \cdot T^2 \\ & +5.934 \times 10^{-22} \cdot T^3 \end{aligned} \tag{8.15}$$

end

function $get_{\rho,\mathrm{NaCl}}(s,\ T)$

$$\mathrm{MW_s} := 58.44\ \ [\mathrm{g/mol}] \tag{8.16}$$

$$m := \frac{\frac{s}{1-\frac{s}{1000\ \ [\mathrm{g/kg}]}}}{\mathrm{MW_s}} \tag{8.17}$$

$$get_{\rho,\mathrm{NaCl}} := 1007{+}39.14{\cdot}m{-}0.2912{\cdot}T{-}1.043{\cdot}m^2{-}0.0166{\cdot}m{\cdot}T{-}0.00184{\cdot}T^2 \tag{8.18}$$

end

function $get_{\gamma}(x_{f,m})$

$$\mathrm{If}(x_{\mathrm{f,m}} \leq 90)\ \ \mathsf{then}\ \ get_{\gamma} := 1 \tag{8.19}$$

$$\text{If}(x_{\text{f,m}} > 90) \;\; \textsf{then} \;\; get_{\gamma} := -2.448 \times 10^{-6} \cdot \left(x_{\text{f,m}}^2\right) + (0.0004262 \cdot x_{\text{f,m}}) + 0.9809 \tag{8.20}$$

end

$$\text{MW}_{\text{NaCl}} = 58.44 \;\; [\text{g/mol}] \tag{8.21}$$

$$\text{MW}_{\text{water}} = 18 \;\; [\text{g/mol}] \tag{8.22}$$

$$\text{TTD}_{\text{HX}} = 3 \;\; [^{\circ}\text{C}] \tag{8.23}$$

$$\dot{m}_{\text{in,1}} = 1 \;\; [\text{kg/s}] \tag{8.24}$$

$$s_{\text{in}} = 70 \;\; [\text{g/kg}] \tag{8.25}$$

$$k_{\text{eff,m}} = 0.056 \;\; [\text{W/m}\cdot\text{K}] \tag{8.26}$$

$$h_{\text{eff,gap}} = 1 \times 10^4 \;\; \left[\text{W/m}^2\cdot\text{K}\right] \tag{8.27}$$

$$P_{\text{f}} = 101325 \;\; [\text{Pa}] \tag{8.28}$$

$$N = 10 \tag{8.29}$$

$$d_{\text{stage1}} = 0.0002 \;\; [\text{m}] \tag{8.30}$$

duplicate $\quad j = 1, \; N - 1$

$$\text{diff}_{d,m,j} = 0 \tag{8.31}$$

end

duplicate $\quad ds = 1, \; N - 1$

$$d_{\text{m},ds+1} - d_{\text{m},ds} = diff_{d,\text{m},ds} \cdot 1 \times 10^{-6} \tag{8.32}$$

end

$$d_{m,1} = d_{\text{stage1}} \tag{8.33}$$

$$w = 12 \ \ [\mathrm{m}] \tag{8.34}$$

$$A_{\mathrm{stage}} = L \cdot w \tag{8.35}$$

$$h_{\mathrm{ch}} = 2450 \ \ \left[\mathrm{W/m^2 \cdot K}\right] \tag{8.36}$$

$$k_{\mathrm{ch}} = 2 \times 10^{-2} \ \ \left[\mathrm{kg/m^2 \cdot s}\right] \tag{8.37}$$

$$T_{w,1} = 85 \ \ [^{\circ}\mathrm{C}] \tag{8.38}$$

$$U_{\mathrm{brineHX}} = 1000 \ \ \left[\mathrm{W/m^2 \cdot \ ^{\circ}C}\right] \tag{8.39}$$

duplicate $\quad i = 1, N$

$$B_{0,i} = 0.6 \cdot B_{0,\mathrm{MD}}\left(P_{\mathrm{f}},\ \mathrm{ConvertTemp}\left(^{\circ}\mathrm{C},\ K,\ \frac{T_{\mathrm{fm,i}} + T_{\mathrm{gm,i}}}{2}\right),\ 1,\ 1\right) \tag{8.40}$$

$$T_{\mathrm{w},i} - T_{\mathrm{f},i} = \frac{\dot{q}_i}{h_{\mathrm{ch}}} \tag{8.41}$$

$$T_{\mathrm{f},i} - T_{\mathrm{fm},i} = \frac{\dot{q}_i}{h_{\mathrm{ch}}} \tag{8.42}$$

$$s_i = \frac{\dot{m}_{\mathrm{in},1} \cdot s_{\mathrm{in}}}{\dot{m}_{\mathrm{in},i}} \tag{8.43}$$

$$s_{\mathrm{avg},i} = \frac{s_i + s_{i+1}}{2} \tag{8.44}$$

$$sm_i = s_{\mathrm{avg},i} \cdot \exp\left(\frac{J_i}{k_{\mathrm{ch}}}\right) \tag{8.45}$$

$$h_{\mathrm{fg},i} = \mathrm{h}\left(\mathrm{Steam_{IAPWS}},\ \mathrm{T} = T_{\mathrm{fm},i},\ \mathrm{x} = 1\right) - get_{h,\mathrm{NaCl}}(s_i,\ T_{\mathrm{fm},i}) \tag{8.46}$$

$$\left(\frac{k_{\mathrm{eff,m}}}{d_{\mathrm{m},i}}\right) \cdot (T_{\mathrm{f}m,i} - T_{\mathrm{gm},i}) = \dot{q}_{\mathrm{cond},i} \tag{8.47}$$

$$m_{\mathrm{fm},i} = \frac{\frac{sm_i}{1 - \frac{sm_i}{1000 \ \ [\mathrm{g/kg}]}}}{\mathrm{MW_{NaCl}}} \tag{8.48}$$

$$\gamma_{\mathrm{w,m},i} = get_{\gamma}\left(sm_i\right) \tag{8.49}$$

$$p_{\text{vap,fm},i} = \text{P}_{\text{sat}}\left(\text{Steam}_{\text{IAPWS}},\ \text{T} = T_{\text{fm},i}\right) \times \left(1 - \left(\frac{2 \cdot \frac{sm_i}{\text{MW}_{\text{NaCl}}}}{\left(2 \cdot \frac{sm_i}{\text{MW}_{\text{NaCl}}}\right) + \left(\frac{1000\ \text{[g/kg]} - sm_i}{\text{MW}_{\text{water}}}\right)}\right)\right) \cdot \left(\gamma_{\text{w,m},i}\right) \tag{8.50}$$

$$p_{\text{vap,gm},i} = \text{P}_{\text{sat}}\left(\text{Steam}_{\text{IAPWS}},\ \text{T} = T_{\text{gm},i}\right) \tag{8.51}$$

$$J_i = \left(\frac{B_{0,i}}{d_{\text{m},i}}\right) \cdot \left(p_{\text{vap,fm},i} - p_{\text{vap,gm},i}\right) \tag{8.52}$$

$$\dot{q}_{\text{mass},i} = J_i \cdot h_{\text{fg},i} \tag{8.53}$$

$$\dot{q}_{\text{mass},i} + \dot{q}_{\text{cond},i} = \dot{q}_i \tag{8.54}$$

$$\eta_i = \frac{\dot{q}_{\text{mass},i}}{\dot{q}_i} \tag{8.55}$$

$$\dot{q}_i = h_{\text{eff,gap}} \cdot \left(T_{\text{gm},i} - T_{\text{w},i+1}\right) \tag{8.56}$$

$$\dot{m}_{\text{pure},i} = J_i \cdot A_{\text{stage}} \tag{8.57}$$

$$\dot{m}_{\text{in},i+1} = \dot{m}_{\text{in},i} - \dot{m}_{\text{pure},i} \tag{8.58}$$

$$\dot{q}_{i+1} = \dot{q}_i + J_i \cdot \left(get_{h,\text{NaCl}}(s_i,\ T_{f,i}) - get_{h,\text{NaCl}}\left(0.001,\ \frac{T_{\text{gm},i} + T_{\text{w},i+1}}{2}\right)\right) + \dot{m}_{\text{in},i+1} \cdot \frac{get_{h,\text{NaCl}}(s_i,\ T_{\text{f},i}) - get_{h,\text{NaCl}}(s_{i+1},\ T_{\text{f},i})}{A_{\text{stage}}} \tag{8.59}$$

$$\dot{Q}_{\text{brine,ph},i} = \dot{m}_{\text{in},i+1} \cdot \left(get_{h,\text{NaCl}}(s_{i+1},\ T_{\text{f},i}) - get_{h,\text{NaCl}}(s_{i+1},\ T_{\text{f},i+1})\right) \tag{8.60}$$

$$get_{h,\text{NaCl}}(s_{\text{in}},\ T_{\text{fph},i}) = get_{h,\text{NaCl}}(s_{\text{in}},\ T_{\text{fph},i+1}) + \frac{\dot{Q}_{\text{brine,ph},i}}{\dot{m}_{\text{in},1}} \tag{8.61}$$

$$\text{LMTD}_{\text{brineHX},i} = \frac{\left(T_{\text{f},i} - T_{\text{fph},i}\right) - \left(T_{\text{f},i+1} - T_{\text{fph},i+1}\right)}{\ln\left(\frac{T_{\text{f},i} - T_{\text{fph},i}}{T_{\text{f},i+1} - T_{\text{fph},i+1}}\right)} \tag{8.62}$$

$$A_{\text{brineHX},i} = \frac{\dot{Q}_{\text{brine,ph},i}}{U_{\text{brineHX}} \cdot \text{LMTD}_{\text{brineHX},i}} \tag{8.63}$$

$$\Delta P_{\text{vap},i} = p_{\text{vap,fm},i} - p_{\text{vap,gm},i} \tag{8.64}$$

end

$$T_{\mathrm{fph},N+1} = T_{\mathrm{c}} \tag{8.65}$$

$$T_{\mathrm{f},N+1} = T_{\mathrm{f},N} - 0.1 \ \ [^{\circ}\mathrm{C}] \tag{8.66}$$

$$s_{N+1} = \dot{m}_{\mathrm{in},1} \cdot \frac{s_{\mathrm{in}}}{\dot{m}_{\mathrm{in},N+1}} \tag{8.67}$$

$$s_{\mathrm{out}} = s_{N+1} \tag{8.68}$$

$$T_{\mathrm{w},N+1} - T_{\mathrm{c}} = \frac{\dot{q}_{N+1}}{h_{\mathrm{ch}}} \tag{8.69}$$

$$T_{\mathrm{c}} = 25 \ \ [^{\circ}\mathrm{C}] \tag{8.70}$$

$$\dot{Q}_{\mathrm{direct}} = \dot{q}_1 \cdot A_{\mathrm{stage}} \tag{8.71}$$

$$\dot{m}_{\mathrm{pure,total}} = \mathrm{Sum}(\dot{m}_{\mathrm{pure}}, 1..N) \tag{8.72}$$

$$\eta_{\mathrm{avg}} = \mathrm{Average}(\eta_{1..N}) \tag{8.73}$$

$$\mathrm{RR} = \frac{\dot{m}_{\mathrm{pure,total}}}{\dot{m}_{\mathrm{in},1}} \tag{8.74}$$

$$h_{\mathrm{fg}} = \mathrm{h}\left(\mathrm{Steam_{IAPWS}},\ \mathrm{T} = 25\ \ [^{\circ}\mathrm{C}],\ \mathrm{x} = 1\right) - \mathrm{h}\left(\mathrm{Steam_{IAPWS}},\ \mathrm{T} = 25\ \ [^{\circ}\mathrm{C}],\ \mathrm{x} = 0\right) \tag{8.75}$$

$$\mathrm{GOR}_{\mathrm{perfectHX}} = \dot{m}_{\mathrm{pure,total}} \cdot h_{\mathrm{fg}} / \dot{Q}_{\mathrm{direct}} \tag{8.76}$$

$$J_{\mathrm{avg}} = \frac{\dot{m}_{\mathrm{pure,total}}}{N \cdot A_{\mathrm{stage}}} \tag{8.77}$$

$$flux_{\mathrm{avg}} = J_{\mathrm{avg}} \cdot 3600 \ \ [\mathrm{s/hr}] \tag{8.78}$$

$$\dot{Q}_{\mathrm{external,brineHX}} = \dot{Q}_{\mathrm{external,noHX}} - \mathrm{Sum}\Big(\dot{Q}_{\mathrm{brine,ph},1..N}\Big) \tag{8.79}$$

$$\mathrm{GOR}_{\mathrm{brineHX}} = \dot{m}_{\mathrm{pure,total}} \cdot \frac{h_{\mathrm{fg}}}{\dot{Q}_{\mathrm{direct}} + \dot{Q}_{\mathrm{external,brineHX}}} \tag{8.80}$$

$$\dot{Q}_{\mathrm{realHX}} = \dot{Q}_{\mathrm{direct}} + \dot{m}_{\mathrm{in},1} \cdot \left(get_{h,\mathrm{NaCl}}(s_{\mathrm{in}},\ T_{\mathrm{f},1}) - get_{h,\mathrm{NaCl}}(s_{\mathrm{in}},\ T_{\mathrm{f},1} - \mathrm{TTD_{HX}})\right) \tag{8.81}$$

$$\mathrm{GOR}_{\mathrm{realHX}} = \dot{m}_{\mathrm{pure,total}} \cdot h_{\mathrm{fg}} / \dot{Q}_{\mathrm{realHX}} \tag{8.82}$$

$$\dot{Q}_{\mathrm{external,noHX}} = \dot{m}_{\mathrm{in},1} \cdot \left(get_{h,\mathrm{NaCl}}(s_{\mathrm{in}},\ T_{\mathrm{f},1}) - get_{h,\mathrm{NaCl}}(s_{\mathrm{in}},\ T_{\mathrm{c}})\right) \tag{8.83}$$

$$\mathrm{GOR}_{\mathrm{noHX}} = \dot{m}_{\mathrm{pure,total}} \cdot \frac{h_{\mathrm{fg}}}{\dot{Q}_{\mathrm{direct}} + \dot{Q}_{\mathrm{external,noHX}}} \tag{8.84}$$

$$sp_{\mathrm{c,w}} = C_{\mathrm{GOR}}/\mathrm{GOR}_{\mathrm{brineHX}} + C_{\mathrm{flux}}/flux_{\mathrm{avg}} \tag{8.85}$$

$$C_{\mathrm{GOR}} = 5 \ \left[\$/\mathrm{m}^3\right] \tag{8.86}$$

$$C_{\mathrm{flux}} = 1 \ \left[\$/\mathrm{m}^3 \cdot \left(\mathrm{kg}/\mathrm{m}^2 \cdot \mathrm{hr}\right)\right] \tag{8.87}$$

Chapter 9

Concluding Remarks

Membrane distillation has been applied for off-grid desalination of seawater or brackish water, producing distilled water for industrial use and brine concentration up to and beyond saturation for waste management. In the literature various configurations of MD have been under development simultaneously. Some of the trade-offs associated with the choice of configuration (air gap, direct contact, permeate gap) and design variables (such as membrane thickness, channel heights, feed flow rate, top temperature, membrane area etc.) as a function of the feed salinity and design objectives (high energy efficiency or high pure water productivity) have been demonstrated. While many of these effects are well-described independently, a clear hierarchy is lacking among the designs which might enable future researchers to focus on the most promising versions. In this thesis, we developed a comprehensive analysis framework to rank various single stage MD designs in terms of overall performance. The complex design space spread across several MD configurations is reduced to three dimensionless variables (two resistance ratios and system size) that affect overall energy efficiency for a given application (defined by feed salinity and top temperature).

The unified framework is based on developing an analogy between MD systems and heat exchangers (HX). As a first step in bringing various configurations together, we considered each separately and optimized its performance through balancing. Balanced counterflow MD exchangers can all be described by a resistance network model using parameters from HX analysis. A general MD design is then understood and

ranked based on a few such parameters.

9.1 Balancing each MD configuration for optimal energy efficiency

MD achieves higher energy efficiency than simple distillation by using the condensation of pure water to preheat the feed stream. Single stage MD configurations differ based on design of the condensation and energy recovery components. The warm evaporating feed stream and the cold preheating feed stream are designed in counterflow orientation to maximize the potential for energy recovery.

The entropy generation rate in a counterflow heat exchanger of fixed area, inlet temperatures and total heat transfer rate is minimized when the heat capacity rates of the two streams are balanced, i.e., $\dot{m}c_p$ of the two streams are equal. Since lowering entropy generation is necessary for lowering specific energy consumption towards the thermodynamic lower limit, we first developed techniques to balance MD exchangers in Chapters 2 and 3.

9.1.1 Gap MD systems

In the case of gap MD systems such as air gap or permeate gap MD (AGMD, PGMD), balancing is related to the flow direction of the pure water in the gap between the membrane and condensing surface, relative to the flow directions of the warm evaporating feed and the cold feed preheating streams. Since the feed-preheating stream mass flow rate remains constant, the feed and the pure water streams can be considered together. To match the constant flow rate of the feed-preheating stream, the pure water stream should be made to flow in the same direction as the hot stream, or counter-current to the cold preheating-feed stream. This is better than having the permeate stream leave perpendicular to the other streams or parallel to the cold preheating feed stream.

Intuitively, this can be understood in terms of the temperature at which the pure

water is extracted from the MD system. By flowing counter-current to the cold preheating feed stream, permeate is removed at the cold end of the module, rather than at warmer temperatures as in the other cases, leading to lower energy discharge to ambient and better energy efficiency.

9.1.2 Direct contact MD

In direct contact MD (DCMD), the inlet flow rate of the cold pure water into the MD module is independent of the inlet flow rate of the feed. Here, the heat capacity rates of the two inlet streams should not be matched since unlike a simple HX, DCMD is primarily a mass exchanger, resulting in a changing mass flow rate along the length. Since all the mass lost by the hot feed is gained by the cold pure water stream, a closer approximation to a balanced system is to match the heat capacity rates of the two streams at one end of the exchanger. This results in nearly balanced heat capacity rates everywhere along the length of the MD module as well as in the external HX, and correspondingly better energy efficiency.

9.2 Overall MD performance: GOR and flux

The overall specific cost of pure water production from MD is a sum the contributions of the capital and operating expenditures. If the capital expenditure is assumed to be proportional to the membrane area, cost of the thermal energy is the main contributor to operating expenditure, the overall specific cost of pure water production can be expressed as:

$$c_{\mathrm{w}} = \frac{C_{\mathrm{GOR}}}{\mathrm{GOR}} + \frac{c_{\mathrm{flux}}}{J} \tag{9.1}$$

where GOR is a dimensionless measure of energy efficiency, defined as the ratio of enthalpy of vaporization to specific thermal energy consumption, and J is the water production per unit time and membrane area, or flux. c_{GOR} and c_{flux} are proportional to the specific cost of thermal energy and amortized specific cost of system area respectively. An improvement in GOR or flux both lead to a lower specific cost of

desalination, and the relative importance of the two is a function of the relative cost of thermal energy to system area: $C_{\mathrm{R}} = \frac{c_{\mathrm{GOR}}}{c_{\mathrm{flux}}}$.

Irrespective of MD configuration, a larger area system at the same feed flow rate can result in a higher GOR at the expense of lower flux. As a result, for each configuration and choice of other parameters, a range of GOR, flux combinations (represented by a line in GOR-flux space) are obtained as a function of changing system area. When comparing different configurations, GOR must be evaluated at the same value of flux, or flux at equal GOR (assuming that c_{GOR} is equal for a given application, based on the source of thermal energy, and c_{flux} is equal across configurations - for example if the membrane constitutes the major capital cost, and system parameters unique to each design are chosen such that their costs are similar). If c_{flux} is different, GOR should be compared at equal c_{flux}/J. In other words, a configuration is better if its performance curve lies to the top-right of the GOR-flux space.

9.3 MD performance metrics: η and ε

Thermal efficiency (η) is a commonly used metric to characterize the extent of heat conduction losses in MD, relative to the heat transfer mediated through evaporation and condensation (pure water production). A high value of η closer to 1 indicates a low fraction of heat conduction losses. While AGMD is known to achieve the highest η, at low salinity, other configurations such as PGMD and DCMD achieve better overall energy efficiency or GOR, at the same flux. Another parameter from HX analysis, the effectiveness (ε) is introduced to understand this trend in GOR among various MD systems. ε is defined as the ratio of actual heat transfer to the maximum possible heat transfer for given inlet temperatures and flow rates of the two streams.

GOR is expressed as $\eta \times \varepsilon/(1-\varepsilon)$. At low salinity, while AGMD has a higher η, the extent of heat recovery (ε) is low due to the large resistance offered by the air gap. As a result, DCMD outperforms AGMD under this condition. At high salinity, η drops significantly for PGMD and DCMD, which overcompensates for any advantage

in terms of ε leading to lower GOR compared to AGMD under this condition.

9.4 Resistance network model of MD

Based on the analogy between balanced counterflow MD designs and balanced counterflow HX, the exchanged effectiveness (ε) can be expressed in terms of the number of transfer units NTU as $\varepsilon = \frac{\text{NTU}}{1+\text{NTU}}$. NTU is a non-dimensional measure of system size, defined as $\text{NTU} = \frac{UA}{\dot{m}c_p}$, where U is the overall heat transfer coefficient between hot evaporating feed stream to the cold preheating feed stream. This means that GOR can rewritten as GOR $= \eta$NTU.To understand this overall heat transfer coefficient, we can represent the various thermal resistances within the MD system as shown in Fig. 9-1.

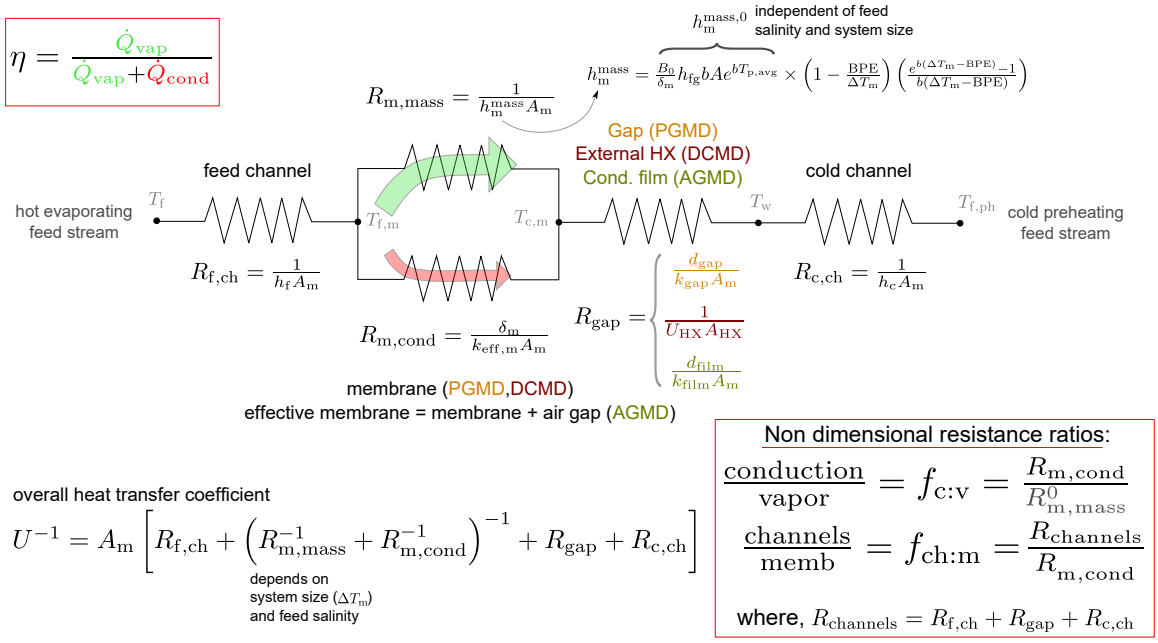

Figure 9-1: Resistance network.

The performance of DCMD is limited by the external HX, whereas that of the PGMD system is limited by the resistance of the gap region. The effective resistance due to using a balanced external HX is simply $1/U_{HX}A_{HX}$. For AGMD, the region between the evaporating and condensing interfaces is defined as the effective membrane, including both the membrane and the air gap region. This means that for the

same membrane and gap width, the effective membrane in AGMD is much thicker. Additionally, the overall effective heat conductivity ($k_{\text{eff,m}}$) and vapor permeability coefficient (B_0) of this effective membrane in AGMD are also redefined as a function of the properties of the physical membrane as well as the air gap. The thin condensate film is an additional resistance, and corresponds to that of the gap and external HX.

Several conclusions can be drawn based on the HX analogy and resistance network representation of single stage MD systems developed above. Since GOR = ηNTU, GOR can be improved by increasing U. η is primarily a function of the membrane properties as well as fluid conditions in contact with the membrane on either side. A change in thermal resistance of a non-membrane region only indirectly affects η. GOR can be increased by decreasing the thermal resistances so as to increase U. It is well known that increasing $h_{\text{f,ch}}$ or $h_{\text{c,ch}}$ leads to an improvement in overall MD performance. These flow channels are therefore designed to be thin to attempt to increase the heat transfer coefficients of the channels while preventing significant pressure drop.

9.4.1 Comparing PGMD vs. DCMD, and introducing conductive gap MD

Decreasing R_{gap} also leads to an improvement in MD performance. The relative performance of PGMD and DCMD can be decided by simply comparing their corresponding R_{gap} values, with the lower value being better. Based on this result, we prose that a high rather than low thermal conductance of the gap region is ideal. We proposed a novel configuration of MD referred to as conductive gap MD (CGMD). The conductance of the gap can be increased by reducing the gap thickness, replacing the plastic spacer with a metal spacer, adding fins to the condensation surface, etc. Since the gap resistance is lower, CGMD outperforms PGMD and DCMD, irrespective of the system top temperature or salinity. CGMD represents the practical upper limit performance of PGMD and DCMD - corresponding to an infinitesimally small gap region in the case of PGMD and a very large external HX in the case of PGMD.

9.4.2 Optimal membrane thickness, comparing AGMD vs. CGMD

Unlike a simple HX, both heat and mass are transferred across the membrane in MD. In addition to a high U, a high η is essential to ensure better energy efficiency. At high feed salinity, and for large system size, the flux-driving temperature difference across the membrane (ΔT_{m}) may be small enough to be comparable to the feed stream's boiling point elevation (BPE). This would lead to a low η and hence low GOR. One way to avoid this outcome is to make the membrane thicker so that a larger fraction of the overall temperature drop occurs across the membrane. For higher feed salinity and larger membrane area, a thicker membrane results in better GOR. This explains why AGMD with a thicker effective membrane outperforms other MD configurations under these conditions.

For every pair of feed salinity and operating flux, an optimal membrane thickness for CGMD at which GOR is maximized can be evaluated. As a result, based on C_{R}, for a given feed salinity, the ideal operating flux-maximum GOR operating point can be chosen along with the corresponding choice of optimal membrane thickness. The optimal membrane becomes thicker for low operating flux (larger membrane area) as well as at high feed salinity. An AGMD system with the same effective membrane thickness would marginally outperform CGMD because of the effective AGMD membrane's larger B_0 and lower $k_{\mathrm{eff,m}}$. Unfortunately, AGMD is sensitive to partial gap flooding when a very small air gap between the membrane and condensing surfaces is maintained by the spacer. With gap flooding, the effective membrane thickness decreases and the resistance of the film increases leading to a major decline in performance. On the other hand, CGMD with a thick membrane eliminates any potential performance decline associated with gap flooding. An ultraporous membrane in CGMD that increases B_0 and reduces $k_{\mathrm{eff,m}}$ also leads to closer performance of CGMD to non-flooded AGMD with a simple film condensation, with optimal effective membrane thickness.

9.5 Dimensional analysis

Based on inspection of the resistance network in Fig. 9-1, the overall performance is not dependent on the individual values of $R_{\mathrm{f,ch}}$, $R_{\mathrm{c,ch}}$ or R_{gap}, but only on the sum of these resistances. Similarly, the fraction of heat transfer across the membrane due to heat conduction losses, quantified as η is a function of the ratio of resistances for the two modes of heat transfer across the membrane. The overall resistance network can be defined in terms of three resistances: membrane vapor transfer resistance, membrane heat conduction resistance and the sum of non-membrane resistances. The non-dimensional energy efficiency of the process is not dependent on these three resistances, but instead only depends on two dimensionless ratios of thermal resistances ($\phi_{\mathrm{c:v}}$, $\phi_{\mathrm{ch:m}}$) as defined in Fig. 9-1.

9.5.1 Optimal system design: decrease $\phi_{\mathrm{ch:m}}$

System design should ensure a low value of $\phi_{\mathrm{ch:m}}$ ideally by reducing the non-membrane resistances such as by implementing conductive gap MD. A less preferred, but sometimes necessary means of increasing $\phi_{\mathrm{ch:m}}$ is to increase the membrane thickness (for fixed non-membrane resistance) required at high salinity and low flux.

9.5.2 Optimal membrane design: increase $\phi_{\mathrm{c:v}}$

Note that attempting to increase the vapor permeability by reducing the membrane thickness results in a corresponding decrease in heat conduction resistance also. $\phi_{\mathrm{c:v}}$ is defined to be independent of membrane thickness and membrane area. It is therefore simply a non-dimensional ratio of membrane vapor permeability coefficient to overall heat transfer coefficient - $B_0/k_{\mathrm{eff,m}}$. An ideal membrane manufacturing process would try to increase this ratio by increasing membrane porosity and pore size, reducing tortuosity, or choosing less conductive materials for membrane fabrication. At the same time, it is crucial to ensure a high liquid entry pressure to prevent membrane wetting.

9.5.3 Critical system size

For a given application, defined by feed salinity or BPE, and system top and bottom temperatures, GOR is a function of the two dimensionless resistance ratios and dimensionless system size or NTU. For fixed values of the two dimensionless thermal resistance ratios, such as for a real MD system in operation, there exists a critical system size relative to feed flow rate (expressed as $\mathrm{NTU}^{\mathrm{crit}}$), beyond which GOR also begins to decrease rather than increase. This operating condition ($\mathrm{NTU} > \mathrm{NTU}^{\mathrm{crit}}$) is referred to as a counterproductive operating condition irrespective of the value of C_{R} since operating at $\mathrm{NTU} = \mathrm{NTU}^{\mathrm{crit}}$ results in both better flux and better GOR.

Using the simplified HX resistance network model, a closed form expression was derived for $\mathrm{NTU}^{\mathrm{crit}}$ $(\phi_{\mathrm{c:v}}, \phi_{\mathrm{ch:m}}, \mathrm{BPE})$. During operation NTU can be inferred by simply measuring the temperatures at the inlets and outlets of the module to then ensure the specific area is less than or equal to the critical specific area by increasing the feed flow rate or feed velocity as required.

9.6 Brine recirculation for high overall pure water recovery

Among brine recirculation designs, full-batch mode results in the best GOR and flux performance. This process is an unsteady process where a tank of solution is slowly concentrated by recirculating only the brine from the MD module back into the tank. The process continues until the tank salinity increases to the required level, at which point the final brine is discharged, the tank is refilled with feed and the process is repeated.

Again, an optimal value of membrane thickness can be identified as a function of the salinity range over which the concentration process operates and the overall flux at which the process is to be operated. For a given membrane thickness, during operation, the feed velocity should be adjusted to avoid counterproductive operating conditions characterized by $\mathrm{NTU} > \mathrm{NTU}^{\mathrm{crit}}$.

9.7 Multi-effect MD: high overall recovery in a steady state, single pass

Another method to achieve high overall recovery is through a multi-effect MD system. Here, a high recovery ratio is achieved in a single pass of the feed stream through the MD module, thereby eliminating the need for brine recirculation. As a result, multi-effect MD is a steady state process, perhaps therefore requiring fewer process control systems. In this study, we analyzed a conductive gap version of MEMD. The number of effects controls the overall flux and GOR of multi-effect MD, along with membrane thickness. The total specific area controls the overall recovery ratio of the MEMD process.

For the same feed and brine salinity levels, and similar membrane (characterized by $\phi_{\text{c:v}}$), it was shown that multi-effect MD achieves a higher GOR at the same value of flux compared to a batch recirculation system. This is a result of the MEMD design which automatically results in a larger driving temperature difference at the later effects, when the resistance of the membrane increases due to lower temperature and higher salinity. As a result, the flux is observed to be better equipartitioned in space, compared to the flux distribution in space and time in the case of the batch recirculation operation of a single stage MD system.

9.8 Overall conclusions

Future research on membrane design should focus on increasing $\phi_{\text{c:v}}$ and system design should ensure balanced operation and focus on implementing conductive gap MD to decrease $\phi_{\text{ch:m}}$. The optimal membrane is thicker for high salinity and low flux. AGMD is a promising configuration for such applications only if gap flooding can be avoided. For brine concentration applications, single stage batch recirculation and multi-effect MD are promising unsteady and steady-state alternatives. A closed form expression for critical system size of MD was derived and a control system is proposed based on this, to prevent counterproductive operation.

Appendix A

Mechanical Vapor Compression – Membrane Distillation Hybrids for Reduced Specific Energy Consumption

Abstract

The energy efficiency of membrane distillation (MD) systems is low when compared to other thermal desalination systems. This leads to high water production costs when conventional fuels such as natural gas are used. In MD, separation of pure product water from feed water is driven by differences in vapor pressure between the streams. Thus, the process can occur at low temperature and ambient pressure. As a result, MD is most frequently paired with waste or renewable sources of low temperature heat energy that can be economically more feasible. MD systems with internal heat regeneration have been compared to and modeled similar to counter-flow heat exchangers. In this study, MD is used to replace the preheater heat exchanger used for thermal energy recovery from the brine stream in Mechanical Vapor Compression (MVC). Using MD in place of the heat exchanger results not only in effectively free thermal energy for MD, but also subsidized cost of capital, since the MD module is replacing expensive heat exchanger equipment. The MVC-MD hybrid system can lead to about 9% decrease in cost of water, compared to a stand-alone MVC system. The savings increase with an increase in MVC operating temperature, a decrease in MVC recovery ratio and with a decrease in MD capital cost. The conductive gap configuration of MD leads to maximum savings, followed by air gap and permeate gap systems, over a range of operating conditions, assuming equal specific cost of

capital for these configurations.

The contents of this chapter are adapted from [109].

A.1 Introduction

A.1.1 Mechanical Vapor Compression

Mechanical vapor compression (MVC) desalination is a work driven desalination process. MVC has been modeled in detail and analyzed by various researchers [13, 31, 33, 74, 119]. Mistry et al. [74] analyzed the entropy generation in various seawater desalination technologies and found that after reverse osmosis (RO), MVC had the highest second law efficiency.

An MVC system primarily consists of preheater heat exchangers, a mechanical vapor compressor and an evaporator/condenser unit. Figure A-1 shows a schematic diagram of a single-effect MVC process where work input to the mechanical compressor causes vapor from the evaporator/condenser unit to be compressed. The compression increases the saturation temperature of the vapor stream and also raises the vapor temperature to a superheated state. The evaporator/condenser unit typically consists of a falling film shell-and-tube heat exchanger where feed seawater is sprayed over the outside of the tubes. Hot compressed vapor from the compressor flows within the tubes while the cooler feed seawater flows outside the tubes. Heat transfer from the vapor to the feed seawater causes vapor to condense inside the tube and form pure water, and also causes some of the feed seawater to evaporate. The vapor is then removed and compressed by the compressor and passed back inside the tubes. Both the pure product water and brine streams exiting the evaporator/condenser unit leave at temperatures much higher than the ambient temperature. The thermal energy in these streams is recovered within the MVC process by using heat exchangers to preheat the incoming feed stream. The incoming feed stream is split into two parts corresponding to the flow rates of the pure water and brine and passed through the heat exchangers. The preheated streams are then mixed together before being

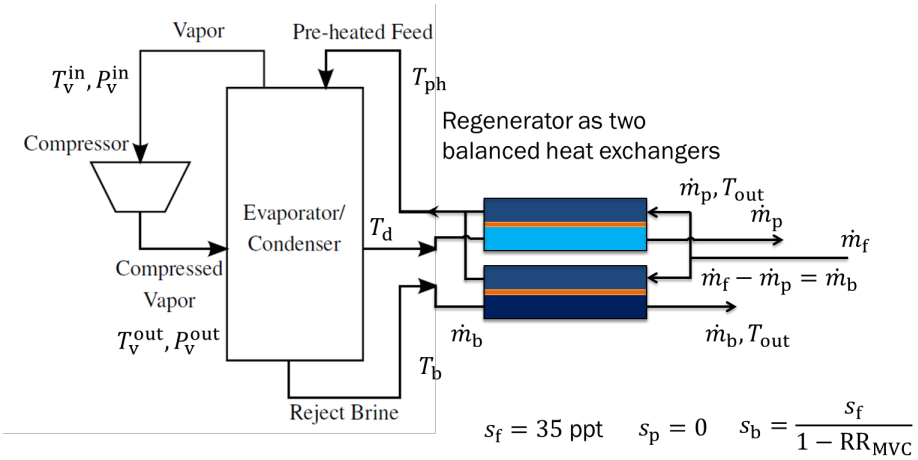

Figure A-1: Schematic diagram of MVC process

introduced into evaporator vessel.

A.1.2 Proposed concept: MVC-MD hybrid

In this paper, we propose the concept of hybridizing MVC with MD for desalination of seawater. Instead of using a conventional heat exchanger for recovering thermal energy from the brine stream and preheating the feed seawater stream, we propose using MD. Figure A-2 shows a schematic diagram of the proposed MVC-MD hybrid system. Only the brine-feed heat exchanger is replaced with the MD module. Since the distillate stream is already pure water, a simple heat exchanger is sufficient to recover energy from this stream. The main motivation for hybridizing MD and MVC is to achieve additional desalination and pure water production, in addition to effecting heat transfer between the two streams. The thermal energy for the MD section of the hybrid system is truly "free". This is in contrast to other "waste-heat" sources for MD, where additional capital cost is associated with introducing heat exchangers to harness this waste heat. In addition to the fact that the thermal energy is free, the cost of capital for the MD system is also offset by the cost of the heat exchanger that the MD module is replacing. If the marginal cost of the additional water produced in the MD section is lower than the specific cost of water from MVC, an overall net cost benefit results from using an MVC-MD hybrid system.

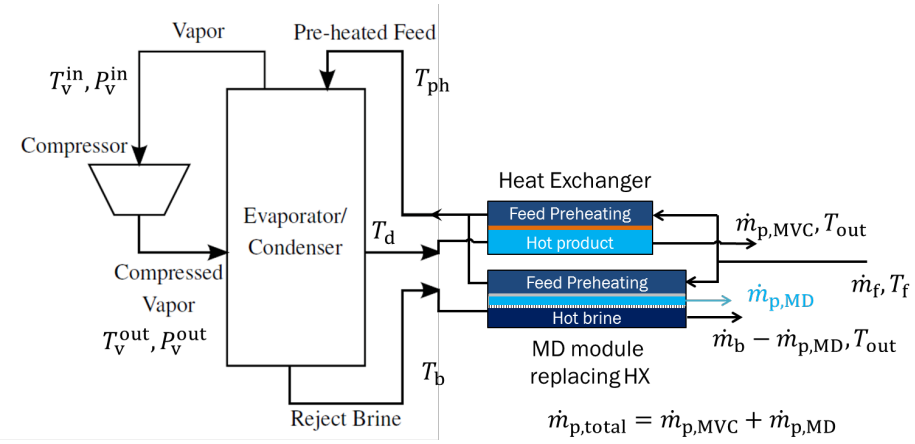

Figure A-2: MVC-MD hybrid system with MD replacing the reject brine regenerator.

A.2 Methodology

A.2.1 Numerical Modeling

The numerical modeling is carried out using a simultaneous equation solver, Engineering Equation Solver [53].

Mechanical Vapor Compression

An analytical model originally developed by El-Dessouky and Ettouney [31] was used for simulating MVC. Key design inputs were also taken from other references [13, 74, 117]. The inputs to the model are given in Table 1.

Table A.1: Summary of inputs to MVC model

Feed salinity	35 ppt
MVC recovery ratio (RR_{MVC})	0.5-0.9
Product salinity	0 ppt
Feed inlet temperature (T_f)	25 °C
Top brine temperature (T_{MVC})	50–90 °C
Evaporator terminal temperature difference (TTD)	3 K
Isentropic compressor efficiency (η_{comp})	0.7

The key assumptions in the model are:

1. Brine and product water exit the pre-heaters into the environment at the same

temperature, T_{out}

2. Rejected brine is assumed to leave at the boiling point of the feed in the evaporator

3. Specific heat capacity of seawater is approximated by that of aqueous sodium chloride.

4. Boiling point elevation (BPE) is calculated using a correlation for sodium chloride solutions as a function of salinity and temperature [114].

5. The mass flow rate of the feed is split between each heat exchanger in the preheater such that each heat exchanger is balanced (i.e. the driving temperature difference is constant along the length of the heat exchanger). The split feed streams recombine after the preheater such that the average temperature is T_{ph}.

6. Complete condensation is assumed in the condenser so that fluid leaving the condenser is a saturated liquid at temperature T_{d}.

7. Vapor entering the compressor is assumed to be saturated.

The recovery ratio of the MVC system relates the mass flow rates of the feed ($\dot{m}_{\text{f}}$) to that of the product water ($\dot{m}_{\text{p}}$) as:

$$\text{RR}_{\text{MVC}} = \frac{\dot{m}_{\text{p}}}{\dot{m}_{\text{f}}} \tag{A.1}$$

The "top brine temperature" (T_{MVC}), as the name suggests, is the highest temperature attained by the brine in the system. This is equivalent to the boiling point of the feed in the evaporator (T_{evap}) and the temperature of the brine leaving the evaporator (T_{b}), and it is an input to the model. The temperature at which vapor from the compressor condenses is given by

$$T_{\text{cond}} = T_{\text{evap}} + \text{TTD} \tag{A.2}$$

where TTD is the terminal temperature difference in the evaporator; TTD is also an input to the model. The corresponding pressures in the evaporator and condenser are given by

$$P_{\text{evap}} = P_{\text{sat,w}}(T_{\text{evap}} - \text{BPE}) \tag{A.3}$$

$$P_{\text{cond}} = P_{\text{sat,w}}(T_{\text{cond}}) \tag{A.4}$$

where $P_{\text{sat,w}}$ is the saturation vapor pressure of pure water.

The energy balance in the evaporator/condenser unit is given by:

$$\dot{Q}_{\text{evap}} = \dot{m}_{\text{f}} c_{p,\text{f}} \left(T_{\text{evap}} - \ T_{\text{ph}}\right) + \dot{m}_d h_{\text{fg, evap}} \tag{A.5}$$

$$\dot{Q}_{\text{cond}} = \dot{m}_{\text{d}}(h_{\text{fg,cond}} + c_{P,v}\Delta T_{\text{suph}}) \tag{A.6}$$

$$\dot{Q}_{\text{evap}} = \dot{Q}_{\text{cond}} \tag{A.7}$$

where $\dot{Q}_{\text{evap}}$ is the rate of heat transfer in the evaporator, $\dot{m}_{\text{f}}$ is the mass flow rate of the feed, $c_{\text{P,f}}$ is the specific heat capacity of the saline feed, T_{ph} is the temperature of the preheated feed coming in to the evaporator, $\dot{m}_{\text{d}}$ is the mass flow rate of the distillate produced in the condenser (from mass conservation, equivalent to the vapor produced in the evaporator and compressed by the compressor), $h_{\text{fg, evap}}$ is the latent heat of vaporization in the evaporator, $\dot{Q}_{\text{cond}}$ is the rate of heat transfer in the condenser, $h_{\text{fg,cond}}$ is the latent heat of vaporization in the condenser, $c_{P,v}$ is the specific heat capacity of water vapor and ΔT_{sup} is the amount to which vapor in the compressor gets superheated. The latter is given by:

$$\Delta T_{\text{sup}} = T_{\text{v}}^{\text{out}} - T_{\text{cond}} \tag{A.8}$$

Solving the foregoing equations gives the temperature of the preheated feed (T_{ph}) before it enters the evaporator. T_v^{out} is calculated from the known values for the compressor's isentropic efficiency and the pressures in the evaporator and condenser.

The energy balance on the preheaters is given by

$$\dot{Q}_{\text{ph}} = \dot{m}_{\text{f}} c_{P,\text{f}} \left(T_{\text{ph}} - \ T_{\text{f}}\right) = \dot{m}_{\text{b}} c_{P,\text{b}} \left(T_{\text{b}} - \ T_{\text{out}}\right) + \dot{m}_{\text{p}} c_{P,\text{w}} \left(T_{\text{d}} - \ T_{\text{out}}\right) \tag{A.9}$$

Where: $\dot{Q}_{\mathrm{ph}}$ is the total heat transfer rate in the preheater; $c_{P,\mathrm{f}}$, $c_{P,\mathrm{b}}$ and $c_{P,\mathrm{w}}$ are the specific heat capacities of the saline feed, brine and that of pure water respectively; $\dot{m}_{\mathrm{f}}$, $\dot{m}_{\mathrm{b}}$ and $\dot{m}_{\mathrm{p}}$ are the mass flow rates of the feed, brine and product water (i.e., distillate); T_{b} and T_{d} are the temperature at which the brine and the product water respectively leave the evaporator/condenser unit while T_{out} is the temperature at which the brine and the product water exits the preheater into the environment. Solving the above energy balance gives the value of T_{out}.

The log mean temperature difference in each of the balanced heat exchangers in the preheater is given by:

$$\mathrm{LMTD}_{\mathrm{ph}} = T_{\mathrm{out}} - T_{\mathrm{f}} \tag{A.10}$$

Equations for the heat transfer coefficient in the evaporator and for the compressor work are given in El-Dessouky and Ettouney [31]. The overall heat transfer coefficient in the preheater (U_{ph}) was assumed to be 1.185 kW/m^2-K. This value was chosen to be consistent with the heat transfer coefficient within the MD module channels. The heat exchanger areas in the evaporator (A_{evap}) and the preheater (A_{ph}) are then obtained by dividing the respective heat transfer rates with the corresponding heat transfer coefficients.

Widely cited correlations from literature were used to calculate equipment costs based on heat exchanger areas and compressor conditions [32, 77]. These are:

$$\mathrm{Cost}_{\mathrm{evap}} = \$430 \times (0.582\ U_{\mathrm{evap}} A_{\mathrm{evap}} {P_t}^{-0.01} {P_s}^{-0.1}) \tag{A.11}$$

$$\mathrm{Cost}_{\mathrm{ph}} = \$1000 \times (12.86 + {A_{\mathrm{ph}}}^{0.8}) \tag{A.12}$$

$$\mathrm{Cost}_{\mathrm{comp}} = \$7364\ \times\ \dot{\mathrm{m}}_d \frac{P_{\mathrm{cond}}}{P_{\mathrm{evap}}} \left(\frac{\eta_{\mathrm{comp}}}{1 - \eta_{\mathrm{comp}}} \right)^{0.7} \tag{A.13}$$

where, $\mathrm{Cost}_{\mathrm{evap}}$, $\mathrm{Cost}_{\mathrm{ph}}$ and $\mathrm{Cost}_{\mathrm{comp}}$ are the costs of the evaporator/condenser, preheater and compressor in units of US dollars, U_{evap} is the overall heat transfer coefficient in the evaporator in units of kW/m^2-K, A_{evap} and A_{ph} are the total areas of the evaporator and the preheat respectively in units of m^2, $\dot{\mathrm{m}}_d$ is the mass flow rate of the vapor in the compressor in kg/s, P_{t} and P_{s} are the pressure drops on the

tube and shell side of the evaporator/condenser in kPa. These correlations are not corrected for inflation or variations in raw material costs and are therefore used to obtain a rough estimate of the cost and understand the trends. The pressure drops are conservatively assumed to be 100 kPa. P_{cond} is the pressure in the condensing tubes while P_{evap} is the pressure in the evaporator and η_{comp} is the isentropic efficiency of the compressor.

A.2.2 Performance Metrics

In order to compare various MVC-MD hybrid systems, the overall cost savings by hybridization compared to using a stand-alone MVC system are evaluated.

The overall cost of water from the MVC-MD hybrid system is given by

$$c_{\text{w}} = \frac{c^{'}_{\text{w,MVC}}\dot{m}_{\text{p,MVC}} + c_{\text{w,MD}}\ \dot{m}_{\text{p,MD}}}{\dot{m}_{\text{p,total}}} \tag{A.14}$$

where $c^{'}_{\text{w,MVC}}$ is the specific cost of water from the stand-alone MVC system per unit pure water production without including the cost of the brine-feed heat exchanger, in \$/m^3.

The overall transfer coefficient of the MD exchanger is lower than that of the heat exchanger due to the existence of the additional membrane resistance and gap thermal resistance. As a result, the area of MD required to achieve the same level of feed preheating is larger than the area of heat exchanger. The cost of water from MD ($c_{w,\text{MD}}$) is therefore defined as the sum of the amortized cost of the exchanger area (A_{MD}), cost of electricity for additional pumping, cost of maintenance (0.5% p.a. of total CapEx) and the cost of membrane replacement at 10% per year. Amortization in both the MVC and MD cost models is based on a 20 year plant-life at 8% rate of interest ($k_i = 1\%$), and the calculations assume a 96% availability factor [87]. The baseline specific capital cost of the MD system (c_{MD}) is taken to be \$40/m^2.

The percentage of extra product produced by the hybrid system is given by $\frac{\dot{m}_{\text{p,MD}}}{\dot{m}_{\text{p,MVC}}} \times 100$. The percentage cost savings using the hybrid system is given by $\frac{c_{\text{w,MVC}} - c_{\text{w}}}{c_{\text{w,MVC}}} \times 100$. $c_{\text{w,MVC}}$ is higher than $c^{'}_{\text{w,MVC}}$ since the cost of the brine-feed heat

exchanger is also included.

The effect of several operating conditions on the cost of water from the hybrid system are then analyzed, including recovery ratio in the MVC stage, membrane permeability (B), MVC brine temperature, and c_{MD}.

A.3 Results and Discussion

A.3.1 Overview of performance of proposed MVC-MD hybrid

The MVC-MD hybrid system proposed in this paper provides better performance than a conventional MVC system whenever the MD part of the system can cost-effectively produce extra product water. For a given MD system, more water can be produced if the vapor flux within the system is increased. Vapor flux in the MD is driven by the vapor pressure difference between the hot and cold streams; the larger the difference, the greater is the flux and the water produced. The vapor pressure difference itself depends on three factors: the mean temperature difference between the two streams (equivalent to $\mathrm{LMTD_{ph}}$), the absolute temperature of the streams and the salinity of the streams. The vapor pressure difference between hot and cold streams in MD:

a. Increases with an increase in $\mathrm{LMTD_{ph}}$,

b. Increases with the absolute temperature of the streams, since vapor pressure is an exponential function of temperature, and,

c. Decreases with an increase in the salinity of the streams, since the vapor pressure of a saline fluid decreases with increasing salinity.

In the MVC-MD hybrid, variation in MD capital costs and the MD membrane permeability directly affect the MD system with little coupling with the MVC system performance. The former affects the cost effectiveness of the water produced directly and the latter allows for a higher water production given the same temperature differences between hot and cold streams. However, there is a strong coupling of the

three factors described previously as well as between the MVC and MD systems, when the MVC parameters such as MVC recovery ratio (RR_{MVC}) and the MVC top brine temperature (T_{MVC}; but $T_{MVC} = T_b = T_{evap}$) are varied. When RR_{MVC} is increased (keeping other inputs constant), by definition, the product water or distillate produced per unit feed increases while the amount of brine produced per unit feed decreases. The reduction in the brine mass flow rates thus reduces the amount of heat transfer possible in the MD component of the MVC-MD hybrid and largely reduces $\dot{m}_{p,MD}$ and the cost benefits of the MVC-MD hybrid. The reduction in the amount of heat transfer possible largely dominates over variations in other MD system parameters such as $LMTD_{ph}$. When T_{MVC} is increased, two competing effects occur: the $LMTD_{ph}$ decreases, whereas the absolute temperature of brine entering the preheater, T_b, increases. The former occurs because a higher T_{MVC} forces an increase in the effectiveness of heat transfer in the preheater, bringing T_{out} closer to the incoming feed temperature, T_f. For the ranges of T_{MVC} considered, the increase in T_b was found to dominate over the decrease in $LMTD_{ph}$ leading to a greater water production in the MD unit, $\dot{m}_{p,MD}$. A more detailed analysis of the effects introduced above is discussed in the sections below.

A.3.2 Effect of MVC recovery ratio

Figure A-3a shows the effect of the recovery ratio of the MVC system on the cost savings for CGMD, PGMD, and AGMD based hybrid systems. Since we are considering the desalination of standard seawater, the recovery ratio in the MVC system would fully determine the salinity of the brine discharged to the MD unit. At a RR_{MVC}=0.5, the cost savings with a CGMD hybrid system is about 8%. For much higher recovery ratios in the MVC section, the savings from the hybrid drop for all the configurations. This is a result of lower relative water production from the MD module compared to the MVC. At very high RR_{MVC}, the AGMD hybrid outperforms the CGMD hybrid, due to its higher η. At larger RR_{MVC}, the salinity of the brine leaving the evaporator is higher. As a result, η is significantly reduced for CGMD and PGMD, whereas, in the case of AGMD, the effect on η is lower.

Figure A-3b shows that the amount of extra product produced in the case of AGMD is higher than in the case of CGMD. This is a direct result of its higher η and lower conduction heat loss. Note that the total heat transfer in all three systems is equal, since the MD system area is allowed to vary to achieve the same extent of preheating that was achieved by the heat exchanger.

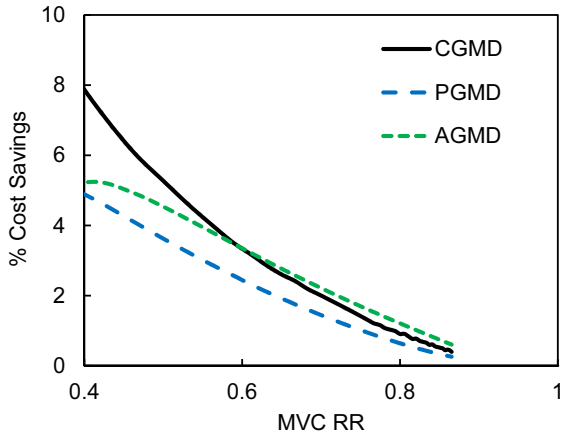

(a) Effect of MVC recovery ratio on cost savings.

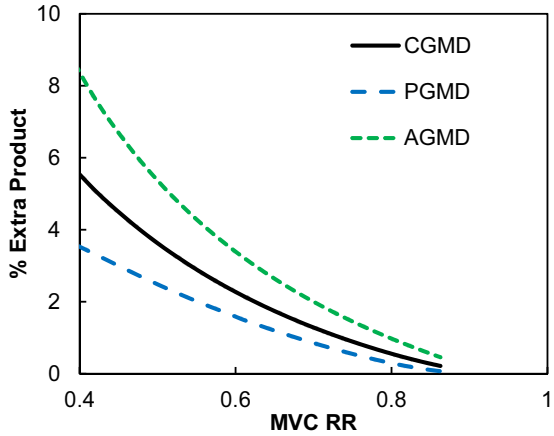

(b) Effect of MVC recovery ratio on the percentage of extra product produced by various systems.

Figure A-3: Effect of MVC recovery ratio on hybrid system performance.

Figure A-4a shows the break-up of the total water cost which is a weighted sum of the cost of water from MVC and MD systems (Eq. 18). The amount of water produced from MD is lower than 10% of the water produced in MVC, and hence the total cost is skewed closer to the specific cost of water for the MVC system. The cost of water from the MD part is a function of the specific membrane area. As $\mathrm{RR_{MVC}}$ increases, the salinity of water flowing into the MD system increases, but the expected temperature of the preheated feed reduces, leading to a larger driving force within the MD system. As a result, the specific MD area required decreases, before increasing due to salinity. Even though $C_{w,\mathrm{MD}}$ is lower at higher $\mathrm{RR_{MVC}}$, the relative savings are higher at lower $\mathrm{RR_{MVC}}$ due to the lower relative productivity of the MD section of the hybrid system at higher $\mathrm{RR_{MVC}}$ (as seen in Fig. A-3b).

Figure A-4b shows a breakdown of the total cost of water for an AGMD hybrid system. The lower cost saving observed at low $\mathrm{RR_{MVC}}$ in the case of AGMD (Fig. A-

3a) is a result of the higher cost of water from MD that results from the higher specific membrane area requirement. This is a result of the lower LMTD_{ph} requirement from the MD system at lower RR_{MVC}.

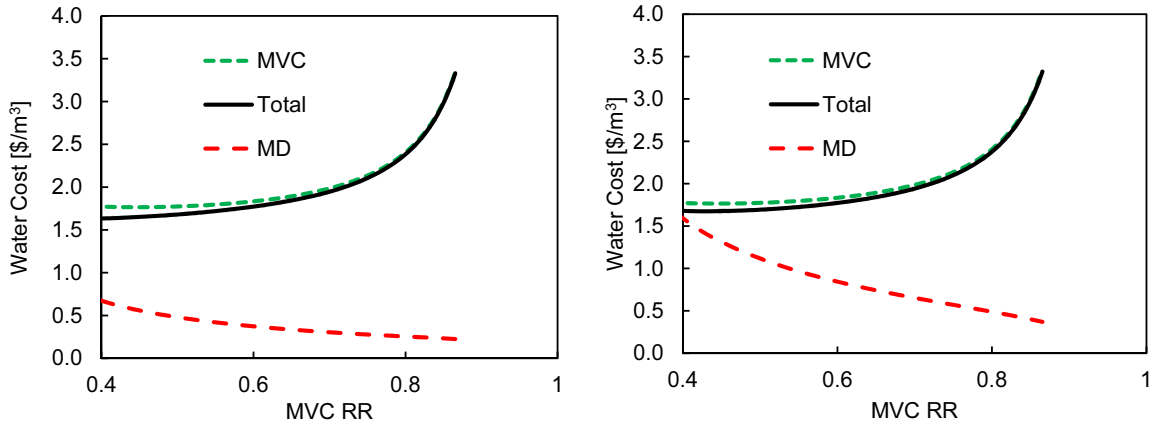

(a) Effect of MVC recovery ratio on the water cost from stand-alone MVC, CGMD section and hybrid system.

(b) Effect of MVC recovery ratio on the water cost from stand-alone MVC, AGMD section and hybrid system.

Figure A-4: Effect of MVC recovery ratio on individual contributions to total specific cost of water.

A.3.3 Effect of MVC top brine temperature

The effect of MVC top brine temperature is shown in Figure A-5a. The savings from the hybrid system reach a maximum value before declining again at very high temperatures. Once again, the CGMD system outperforms other configurations due to its higher overall heat transfer coefficient and hence lower MD area requirement.

Figure A-5b shows the breakdown of the total cost of water for a MVC-CGMD hybrid system. At higher MVC operating temperature, the specific cost of water from MVC decreases. The recovery ratio is held constant (RR_{MVC} =0.5) while the top temperature increases. At higher temperatures, the MVC model leads to a higher value of T_{ph}, with the value of $T_{\text{MVC}} - T_{\text{ph}}$ or LMTD_{ph} decreasing. This results in a larger area requirement. At the same time, pure water production in the MD section increases at higher temperatures, leading to the total cost of water being pulled closer to the cost of MD (Eq. 18). The overall effect of these two effects in the case of

CGMD, over the temperature range considered in this study, is that the percentage savings increases with increase in T_{MVC}, and reaching a maximum at around 7% at $T\mathrm{MVC} = 85\,^{\circ}\mathrm{C}$. In the case of AGMD and PGMD, a maximum is reached at a lower value of $\mathrm{T_{MVC}}$.

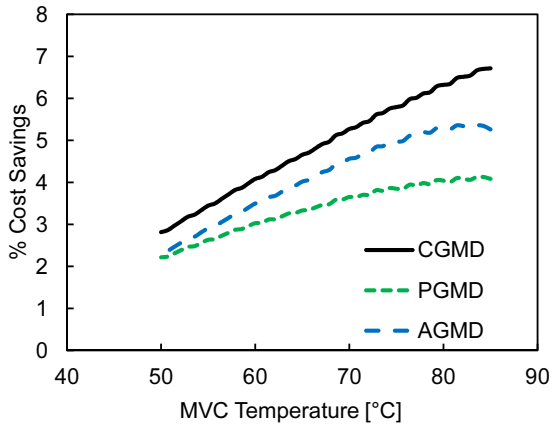

(a) Effect of MVC operating temperature on cost savings.

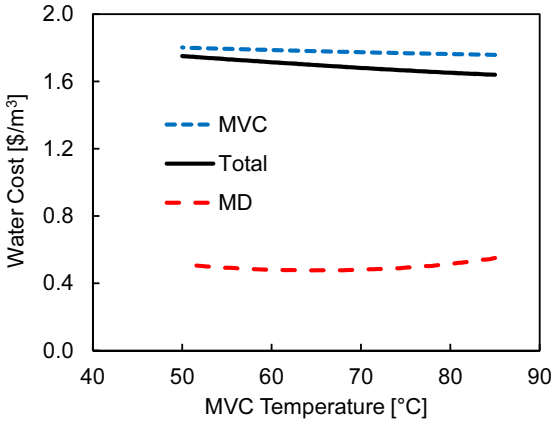

(b) Effect of MVC operating temperature on water cost from stand-alone MVC, CGMD section and hybrid system.

Figure A-5: Effect of MVC temperature.

A.3.4 Effect of MD capital costs

The previous results are reported keeping the specific cost of MD area constant at $\$40/\mathrm{m}^2$, irrespective of MD configuration type. Figure A-6 shows the effect of specific cost of MD system area on savings with a hybrid system. Since AGMD and PGMD require larger membrane area, at larger specific system cost, these systems result in no cost savings. At a very low cost of the MD system, the fact that AGMD needs larger area is offset by the higher water productivity of AGMD compared to CGMD, leading to more savings in the case of AGMD compared to CGMD.

A.4 Conclusions

- Membrane distillation modules can be used in the place of heat exchangers to produce additional pure water while achieving preheating of the feed stream

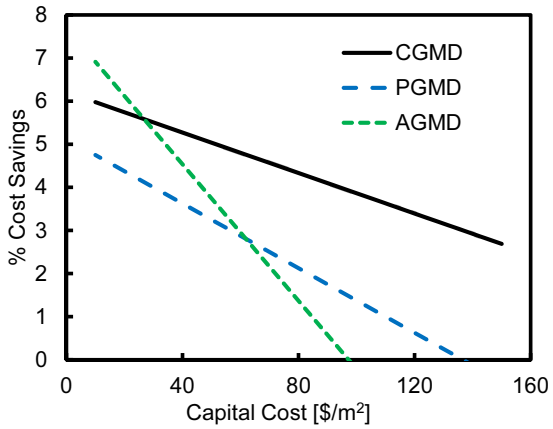

Figure A-6: Effect of MD specific cost on cost savings with various MD configurations.

using the brine.

- Keeping the mechanical vapor compression system operating conditions constant, the cost of water production can be reduced up to 6% by hybridizing MVC and CGMD.

- Conductive gap MD has maximum overall heat transfer coefficient, U, leading to lower area requirements and higher savings than for other systems over a wide range of operating conditions. At very high salinities, or low cost of MD system, air gap MD outperforms CGMD in due to its lower heat loss.

- If the specific cost of the MD system is lower than about US\$40/m^2, a cost savings of about 4-6% can be achieved with either AGMD or CGMD hybridization for a 50% recovery seawater MVC system operating at 70 °C.

Appendix B

Nanofiltration for high permeability textile dyeing effluent desalination

Abstract

Desalination is used in textile dyeing effluent recycling in order to separate a concentrated salt solution, which is reused in the dyebath, from relatively pure water, which is recycled in the other baths. The dyebath solution salinity is maintained at a salt concentration of about 30-100 g/kg, depending on the shade of color, but the overall effluent is diluted by water from the remaining baths to a final TDS of around 7 g/kg. Reverse osmosis (RO) followed by multi-effect evaporation (MEE) is the most common combination for achieving zero liquid discharge of dyeing wastewater in south India. RO is used to concentrate water up to a salinity of about 50 g/kg, corresponding to a recovery ratio of more than 80%. Unlike seawater and brackish ground water, industrial effluents can be designed by choosing appropriate chemicals in the processing steps, such that the energy consumption for desalination and recycling is lower. In textile dyeing, this can be achieved by replacing the NaCl in the dye bath by Na_2SO_4. For the same molality of Na^+ ions in solution, Na_2SO_4 solution has a 50% lower osmotic pressure than NaCl solution. The thermodynamic least work of desalination to concentrate sodium sulfate solution to 120 g/kg is around 40% lower compared to concentrating a sodium chloride solution to 74 g/kg, for reuse in the dyebath. In addition to the thermodynamic advantage of redesigning the effluent composition, a solution without monovalent anions can be desalinated with nanofiltration membranes. The capability of Dow NF90 and NF270 membranes to concentrate sodium sulfate solution to a final concentration of 120 g/kg while operating at feed pressures below 70 bar and achieving >97% salt rejection is experimentally verified. Since the permeability of NF membranes is 2-4 times higher than that of RO membranes, both capital and operating expenditure can be reduced by switching from NaCl to Na_2SO_4 and from RO to NF for the concentration of textile dyeing effluent water.

The contents of this chapter are adapted from [110].

B.1 Introduction

B.1.1 Industrial effluent recycling

Increasing water shortages and environmental impacts of industrial water use are pushing regulators around the world to enforce stricter discharge regulations. In Tamil Nadu in south India for example, textile dyeing is now categorized as a red-category industry by the state pollution control board, and all dyeing units are required to achieve zero-liquid-discharge (ZLD). As industries adapt to these regulatory frameworks, their goal is to recover and reuse as much of the water as possible, along with other components in the water. Primary and secondary treatment involving chemical precipitation, sedimentation and biological treatment are capable of removing microbes and larger organic molecules from the water. Desalination technologies are then necessary to separate any dissolved components.

Reverse osmosis (RO) is used to concentrate the effluent to a salinity of about 40-70 g/kg. Thermal desalination systems such as multiple effect evaporators (MEE) or, occasionally, high-pressure RO systems are used to further concentrate and in some cases eventually crystallize salt out of the concentrated effluent. A solar pond is also typically used to further dry the solid wastes generated.

The cost of water recycling in an industrial setting can be reduced by choosing appropriate chemicals in the processing steps and controlling the effluent composition. Mistry et al. [72] showed that the least energy of desalination is a strong function of the ions present in water, even for the same overall salinity or ionic strength. Unlike naturally occurring seawater or brackish ground water, industrial solutions can be designed such that the energy consumption for desalination of effluents is lower. In addition to the thermodynamic benefit of changing the feed water chemistry, practical advantages such as the use of higher-permeability membranes for desalination, leading to lower energy and capital costs, are also possible.

In this study, we investigate the recovery of pure water from textile effluent for reuse. Replacing sodium chloride with sodium sulfate in the dye bath solution is investigated as a method to reduce the cost of water recycling by replacing reverse osmosis membranes with nanofiltration (NF) membranes that have a higher permeability and which may lessen membrane area or reduce operating pressure and energy consumption.

B.1.2 Textile dyeing process: Water and chemical usage

Industrial textile dyeing of both yarn and woven or knitted fabric is performed in machines that subject the fiber to multiple baths or processing steps. In each of the ten or more baths, about 6-10 L of water per kg of cloth is used.

The dyebath is the most important among these steps. The most commonly used class of dye molecule for cotton dyeing is reactive dye, where the dye molecule is bound to the fabric through a chemical reaction leading to superior color fastness compared to physical adhesion. In addition to the dye chemicals, salt is added to enable dye exhaustion. Since both dye and cloth are negatively charged in water, the cations in the added electrolyte stabilize these charges and enable the dye to approach the cloth for the reaction. The amount of salt required is a function of the shade, with more saturated colors requiring more salt (up to 80-110 g/kg) than lighter shades (about 20-30 g/kg). While plants commonly use sodium chloride for the dye bath solution, some also use sodium sulfate.

Other chemicals added in various baths before and after the dyebath include wetting agents, lubricating agents, sodium carbonate, sodium hydroxide, sodium peroxide, acetic acid, ethelyne glycol, lubricants, fixing agents and detergents. When the dyebath solution is mixed with water from the remaining baths, the final salinity of the effluent is about 7 g/kg. The color of the effluent at this stage is usually black due to the mixing of various dyes.

B.1.3 Conventional effluent treatment and recycling for zero-liquid-discharge

The goal of the effluent treatment plant at a textile dyeing unit is to treat the effluent to meet environmental regulations for disposal. With the introduction of zero liquid discharge (ZLD) regulations, the goal of the recycling system is to produce fresh water for reuse in the various baths as well as a concentrated salt solution for recycling in the dye-bath step. Since multiple shades of color may be dyed on any given day, the typical strategy is to concentrate water to 80-110 g/kg so that it can be used for the darkest shades. For lighter shades, the brine is diluted appropriately before use in the dyebath.

Figure B-1 shows a schematic overview of the effluent treatment processes. The primary and secondary treatment steps reduce color, chemical oxygen demand and biological oxygen demand by a combination of chemical, physical, and microbial methods. The dissolved components such as ions in the stream remain relatively constant through this section of the treatment train. Thereafter, desalination systems such as RO and MEE are used to obtain a concentrated brine stream and pure water for reuse in the dyebath and other baths respectively.

Reverse osmosis (RO) is usually used to concentrate the effluent to a salinity of around 50 g/kg. Although RO is at present the most energy efficient desalination technology [74], conventional RO modules and membranes are limited to a pressure of 70 bar. Following RO, mechanical vapor compression or MEE is used to concentrate water further to about 100-120 g/kg. At this salinity, the brine can be reused in the dyebath solution.

If NaCl is the salt used in the dyebath solution, nanofiltration (NF) may be used to polish the brine solution by separating NaCl from other divalent ions and other compounds. Plants using sodium sulfate cannot use NF to polish the brine before reuse, but may reuse the brine after softening using ion exchange resins.

Excess effluent is concentrated in the forced convection evaporators of the MEE to a supersaturated state. The resulting slurry is then transferred to a centrifuge and

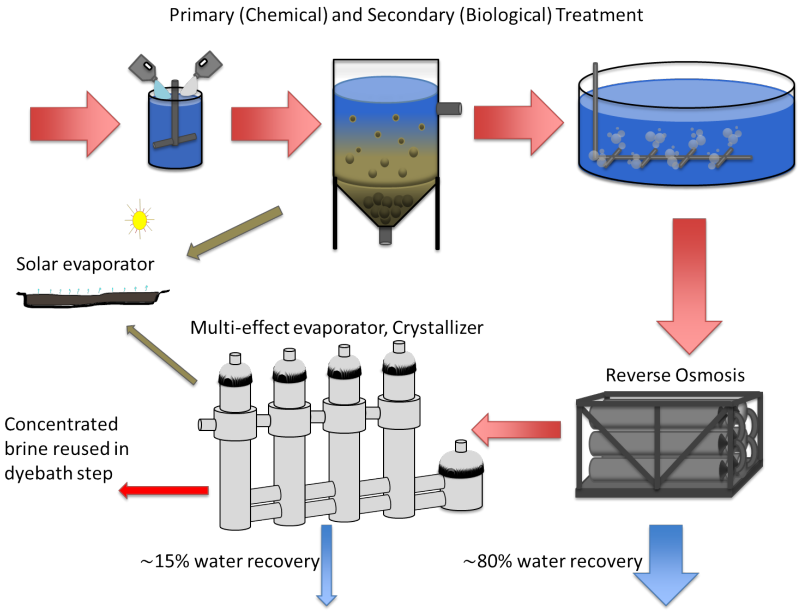

Figure B-1: Typical textile effluent recycling system.

solar evaporation pond to obtain salts and other solid wastes.

RO accounts for over 80% of the total water recovery. Since the thermal systems are less energy-efficient, there is a trend toward increasing the water recovery of the RO stage by designing high pressure RO modules [114]. An improvement in the RO section capital or operating costs can lead to significant cost savings for water recycling.

B.2 Proposed solution

Zero liquid discharge regulations necessitate the use of desalination systems. While desalination is typically viewed as an add-on system, considering the dyeing unit processes along with the desalination system design can result in lower overall cost of the textile dyeing plant. The energy requirement and cost of desalination vary significantly with the solute composition of the effluent. The goal of this work is to identify choices in the dyeing process that enable cheaper desalination, focusing on the choice of salt used in the dyebath solution. The salt used in the dyebath stream constitutes greater than 90% of all the dissolved species in the effluent.

Using sodium sulfate in the dye bath solution can result in lower energy consumption for desalination. Mistry et al. [72] modeled electrolyte solutions using the Pitzer model and found that the least work for desalination of Na_2SO_4 is lower than that of NaCl at constant feed inlet salinity, molality or molal ionic strength. $MgSO_4$ and $ZnSO_4$ solutions have even lower energy of separation than Na_2SO_4. In addition to the thermodynamic advantage, there can be practical advantages such as enabling the use of higher permeability membranes, associated with using particular salts in the dyebath.

Ultrapermeable RO membrane development is an exciting field of research in desalination. However, the performance of a real desalination system is affected by other practical constraints, such as concentration polarization, in addition to membrane permeability. Cohen-Tanugi et al. [22] quantified the cost savings attainable with the availability of more permeable membranes. For low fed salinities (around 3 g/kg), a three times more permeable membrane could lead to a 46% reduction in energy cost at fixed membrane area, or 63% reduction in membrane area at constant energy consumption or a combination of these benefits, for 65% water recovery. These gains drop rapidly with rising feed salinity, to less than 15% energy savings for SWRO; and, further McGovern and Lienhard [69] have recently shown that concentration polarization will produce an asymptotic limit on the achievable flux that is only about 4 times the average flux of today's SWRO membranes. In additional, most ultrapermeable membranes (UPMs) proposed for RO in the literature are manufactured only on a lab scale and are far from being produced at commercially meaningful sizes. On the other hand, membranes with larger pore size and higher permeability - such as nanofiltration (NF), ultrafiltration and microfiltration membranes - are available today. While NF membranes allow smaller solutes such as chloride ions to pass through, they can achieve excellent sodium sulfate rejection of 95-99%, while being 2-4 times more permeable than RO membranes [24, 71].

Conventionally, NF is not used for desalination, but is used as a pretreatment or for targeted removal of the larger solutes since sodium chloride constitutes the major solute in most natural water bodies. Most NF membranes are negatively charged

and achieve high rejection of divalent anions such as sulfate due to a combination of size and charge-based rejection mechanisms. Avoiding the use of monovalent anions (such as chloride) in the processing steps in industry, by using alternate salts such as sulfates, can lead to an effluent stream that can be desalinated using an NF membrane, instead of an RO membrane. As a result, in addition to the thermodynamic advantage, savings are possible in both and capital and operating costs compared to a conventional RO system due to the higher permeability of NF membranes.

B.3 Thermodynamic advantage

The thermodynamic comparison between various solutions involves comparing the least work of desalination for concentration of a feed solution at approximately 7 g/kg inlet salinity up to a brine concentration that can be reused in the dyebath for the darkest shades. In industry, the highest salinity requirement can be as high as 120 g/kg for Na_2SO_4 and as low as 80 g/kg for NaCl. The energy of separation is a function of the osmotic pressure of the solution, with solutions of higher osmotic pressure requiring higher applied pressure and more energy consumption. The following osmotic pressure and least work of separation calculations are performed using a Pitzer electrolyte solution model [47] that has previously been validated against experimental data [112].

Figure B-2 shows the osmotic pressure of pure salt solutions of sodium chloride and sodium sulfate as a function of salinity and solution ionic strength. Since the cation is responsible for ensuring good dye exhaustion, the comparison is performed at constant cation molality rather than salt molality. While other salt solutions such as $ZnSO_4$ and $MgSO_4$ have even lower osmotic pressure, they are not considered in this analysis since they cause water hardness, which would adversely affect the chemical processes in several baths.

The thermodynamic least work of separation can be evaluated by considering the desalination system as a black box, applying the first and second laws of thermodynamics and setting the entropy generation to zero [114]. The least work of desalination

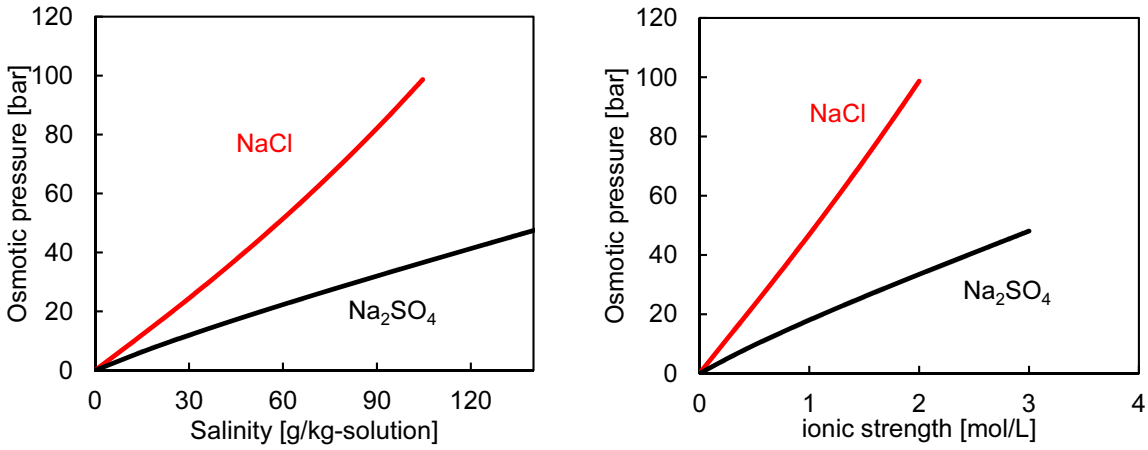

(a) Comparison at equal concentration.

(b) Comparison at equal concentration.

Figure B-2: Osmotic pressure comparison between sodium chloride and sodium sulfate solutions.

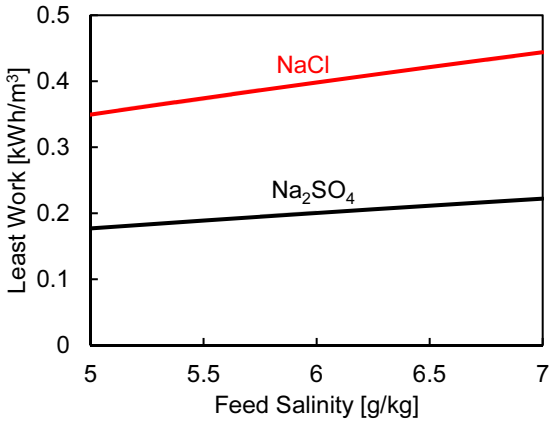

Figure B-3: Least work of desalination of NaCl and Na_2SO_4 solutions as a function of feed salinity. The concentrate salinity is set at 90 g/kg.

is 40% lower for Na_2SO_4 relative to NaCl. For the analysis in Fig. B-3, the feed salinity corresponding to the inlet salinity in the mixed effluent is varied from 5.5-8.5 g/kg. The brine salinity is set at 90 g/kg. The least energy of separation for the sodium sulfate solution is about half than that of the sodium chloride solution at similar inlet feed salinity, across the range of salinity values considered. The permeate stream is considered to be pure in this analysis, and the least work would reduce with an impure product stream.

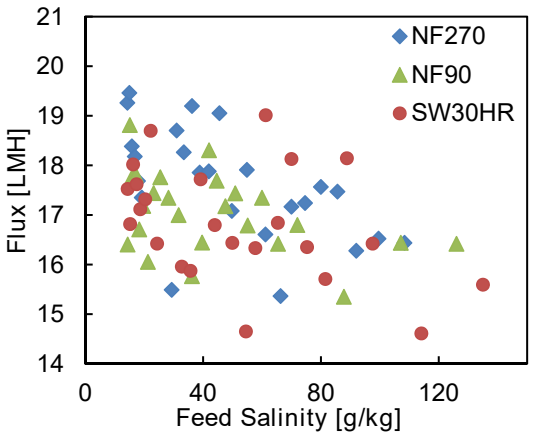

Figure B-4: Flux maintained between 15-20 LMH, comparing the performance of SW30HR, NF90 and NF270.

B.4 Practical Advantage

Dow Filmtec nanofiltration membranes NF90 and NF270 were tested for their ability to desalinate sodium sulfate solution up to a salinity of 110 g/kg or 1.75 mol Na^+/kg-w. The tests were performed using a Sterlitech stirred cell apparatus capable of withstanding pressures up to 172 bar. The stirrer speed was set at approximately 300 RPM and kept constant throughout the various experiments. In order to test the membrane flux and rejection under realistic conditions over a wide range of salinity values, the permeate flux was maintained within a range of 15-20 LMH (as shown in Fig. B-4), by increasing the feed pressure as the feed salinity inside the dead-end apparatus increases with time.

Figure B-5a shows the required pressure to achieve a flux between 15-20 LMH at the feed salinity of interest. The osmotic pressure of Na_2SO_4 is plotted for comparison. Even with low mixing at a stirrer speed of 300 RPM, the solution could be concentrated up to the required final concentration of about 110 g/kg, with a feed pressure of less than 70 bar. In practice, the flux at the end of a spiral-wound module would be lower than the average flux (e.g, 15 LMH), and the driving pressure would be even closer to the brine osmotic pressure. These results demonstrate that, by using Na_2SO_4 in the dyebath and using NF membranes (which exhibited 2- 9 LMH/bar permeability, with a reduction at higher pressure due to compaction, leading to diver-

gence between the required pressure and the osmotic pressure curves in Fig. B-5a), the entire desalination process for generating reusable brine can be achieved using conventional spiral wound membranes and pressure vessels, therefore eliminating the need for high-pressure RO or thermal desalination systems to achieve ZLD textile dyeing effluent reuse.

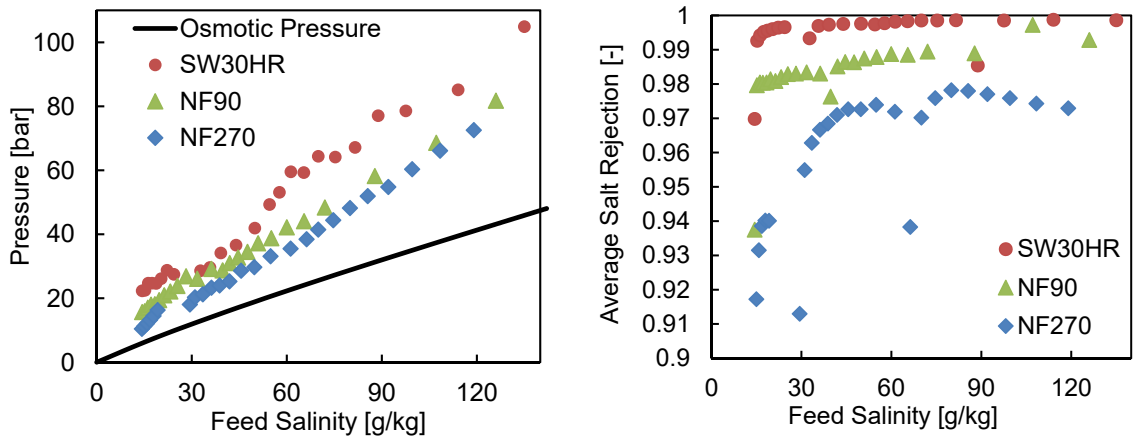

(a) Applied pressure.

(b) Salt rejection.

Figure B-5: Dead-end experimental comparison of membranes for partial desalination of Na_2SO_4 solution up to 110 g/kg.

Figure B-5b shows that over the range of feed salinity tested, the salt rejection, which is a measure of the product quality is found to be greater than 98% for NF90 and around 97% for NF270. The rejection was lower at the beginning of the trial and each time the experiment was restarted, as the membrane took some time to reach a steady state performance. This is consistent with findings in the literature that NF90 has smaller pores, and hence higher rejection, but lower permeability than NF270 [130].

B.5 Discussion

The reusability of NF product water in various baths of the dyeing process needs to be modeled and experimentally verified. The DSPM-DE model [41] can be used to predict NF membrane performance in terms of flux and ion rejection. Roy et al. [85] extended this model to predict the performance of full-scale spiral wound

modules. By fitting appropriate membrane properties from the dead-end apparatus experimental results, this model can be used to infer full-scale membrane performance and is a useful tool for designing systems. In case some chloride exists in the effluent, methods such as ion exchange resins could be used to replace the chloride with sulfate before desalination with NF membranes [89].

B.6 Conclusions

A method to reduce overall cost of water recycling in the textile dyeing industry has been proposed based on existing materials, by substituting sodium sulfate for sodium chloride in the dyebath solution. For the same molality of sodium ions in solution, sodium sulfate has a 50% lower osmotic pressure compared to sodium chloride. As a result, the least work of separation for desalinating a sodium sulfate solution is 40% lower than that of sodium chloride in order to produce a concentrate stream that can be reused in the dyebath for the darkest shades. While previous analysis has shown the potential for energy and capital cost savings with more permeable membranes, the use of nanofiltration membranes enables high-permeability desalination of engineered textile effluent devoid of monovalent anions. Both NF90 and NF270 are found to be capable of concentrating sodium sulfate solution to the target concentration of 110 g/kg while operating below 70 bar pressure, thus showing promise for replacing the standard RO+MEE system with NF alone.

B.7 Acknowledgment

The authors would like to thank Prof. Lallit Anand for permission to use the high pressure Sterlitech stirred cell membrane testing unit.

The authors would like acknowledge Tiffany Tao's contribution in running the dead-end filtration experiments and acknowledge Mallory Whalen for assistance in preparing graphics. The authors thank Dr. Gregory P. Thiel for sharing the Pitzer model for electrolyte solutions.

The authors would like to thank Mr. Saravana Perumal of SP Textile Processors for helping set up a pilot plant to test nanofiltration for textile effluent recycling in Chithode, India, and for the discussions on dyeing process. The authors would also like to thank Mr. Rajesh (Spencer Textile Processors) for the discussions on the effluent treatment and dyeing process.

Appendix C

Effect of practical losses on optimal design of batch RO systems

Abstract

Batch reverse osmosis (BRO) systems may enable a significant reduction in energy consumption for desalination and water reuse. BRO systems operate with variable pressure, by applying only slightly more pressure than is needed to overcome the osmotic pressure and produce reverse water flux. This study explains, quantifies, and optimizes the energy-saving performance of realistic batch designs implemented using pressure exchangers and unpressurized tanks. The effects of additional design parameters such as feed tank volume at the end of the cycle, volume of water in the pipes, per-pass recovery, cycle operating time, and cycle reset time on the performance of BRO are captured. Loss mechanisms including hydraulic pressure drop and concentration polarization as well as friction and mixing in the energy recovery devices are considered. At low cycle-reset time (10% of productive time) and low piping volumes (12% of volume inside membrane elements), about 13% energy savings is possible compared to a continuous system operating at the same overall pure water productivity. Under these conditions, we also show that the ideal per-pass recovery is close to 50%, similar to single-stage RO. This recovery reduces the need for system redesign with additional pressure vessels in parallel, contrary to predictions in the literature. The projected savings in terms of the overall cost of water is around 3%. Additionally, advanced ultra-permeable membranes, such as those based on graphene or graphene oxide, are expected to lead to more significant energy savings in BRO than in single-stage RO.

Emily W. Tow, Richard L. Stover, David M. Warsinger, and John H. Lienhard V contributed to this chapter.

C.1 Introduction

The energy required for seawater desalination has been reduced by a factor of four in the last three decades through advances in energy recovery devices and membrane designs. As the energy required has moved closer to the thermodynamic minimum energy for conventional continuous reverse osmosis (RO) processes, many authors have concluded that further research and development could only yield incremental reductions. However, by changing the process configuration, batch RO systems have demonstrated the potential to provide major additional reductions in energy consumption. Batch RO (BRO) systems operate with variable pressure, applying only enough to overcome the osmotic pressure barrier and maintain water flux. The average applied pressure in BRO weighted by the rate of permeate production over the cycle operating time is lower than that required in conventional continuous single-stage RO systems which operate at constant pressure [120].

BRO can be implemented in one of two ways: using a pressurized feed container or an unpressurized feed container with a pressure exchanger. In this study, we consider BRO implemented with an unpressurized feed tank in combination with a pressure exchanger (PX), as shown in Figure C-1. This design may not be optimal in terms of energy efficiency compared to use of a pressurized feed container, but it is easier to implement since all necessary components are readily available in the market and are widely utilized in the desalination industry.

While the relative advantage of batch RO over conventional single stage systems is likely to be higher for brackish water desalination at high recovery [122], in this study, we focus on seawater RO (SWRO) to understand the potential for energy and cost savings. The goal of this study is to identify practical energy loss mechanisms in batch RO and quantify their effect on the energy consumption. The effects of various design variables that are unique to BRO systems are considered in detail to lay out a framework for the design and evaluation of BRO systems.

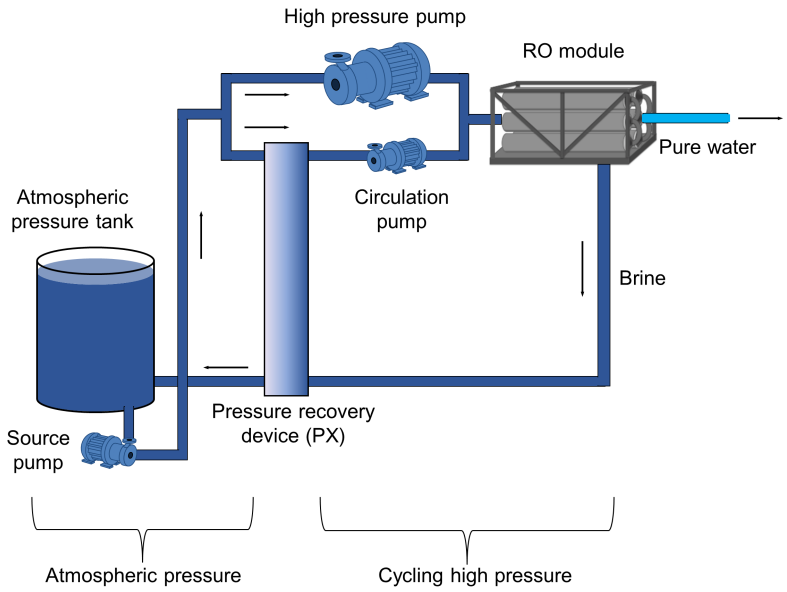

Figure C-1: Batch RO implemented with an atmospheric pressure tank and pressure exchanger.

C.2 Methodology

Energy consumption is evaluated using numerical models for SWRO and SWBRO. The models build on the simpler model for batch systems presented by Warsinger et al. [122] and additionally include membrane physical variables such as water and salt permeability, channel mass transfer coefficients, and friction factors, giving a more realistic accounting of concentration polarization, salt passage, and pressure drop in the channels. The one-dimensional convection equation is solved in the feed channels in space and time. A central difference scheme is used for evaluating derivatives in space, and an explicit method is used to evolve the batch system in time. For batch processes, the inlet boundary condition is linked to the outlet concentration through a well-mixed tank and pipes connecting the inlet and outlet to the tank. The pressure applied at any point in time can be controlled to produce a required average flux from the module. Empirical equations for pump and energy recovery device efficiencies are incorporated.

Werber et al. [125] also present a detailed numerical model of the batch RO process, accounting for physical parameters such as membrane permeability and channel

mass-transfer coefficients. The present model is compared to the results reported in [125] at similar operating conditions and pump and PX efficiencies as a validation exercise in Section C.3.

A large external tank was assumed in Ref. [125]. However, a large external tank is inimical to overall energy consumption as will be shown in Section C.4.2. Warsinger et al. used a collapsing tank whose volume would approach zero at the end of the cycle, which results in the best possible energy efficiency. Figure C-2 shows the BRO system at the end of one cycle of pure water production. In this study, the volume of fluid in the pipes connecting the tank to the RO modules ($V_{\text{piping,in}}$, $V_{\text{piping,out}}$ relative to V_{elements}, which is the volume of the feed channels of the membrane elements) is explicitly considered. A lower limit on piping volume is enforced, and the effect of changing the piping volume and volume of the feed tank at the end of the cycle (V_{tank}) on energy efficiency and process cycle time are evaluated. The volume of fluid remaining outside the membrane elements at the end of each cycle is a key parameter influencing the ideal per-pass recovery, specific energy consumption, and cycle time of the batch process (as shown in Section C.4.2), and motivating detailed modeling including this parameter as is done in the present study.

The present model has several other unique features:

1. A detailed model of PX performance accounts for various internal loss mechanisms

2. Pressure drop along the length of the elements is explicitly considered and taken into account, as are pressure drops in the piping outside of the RO module

3. Salt passage is allowed across the membrane

The osmotic pressure, density, and viscosity of the feed solution are approximated using properties of a pure NaCl solution, and a constant recovery ratio of 50% is considered in all cases.

The modeled batch system operates in cycles. First, the system is filled with feed water. Then the feed is circulated and pressure is applied until 50% of the original feed

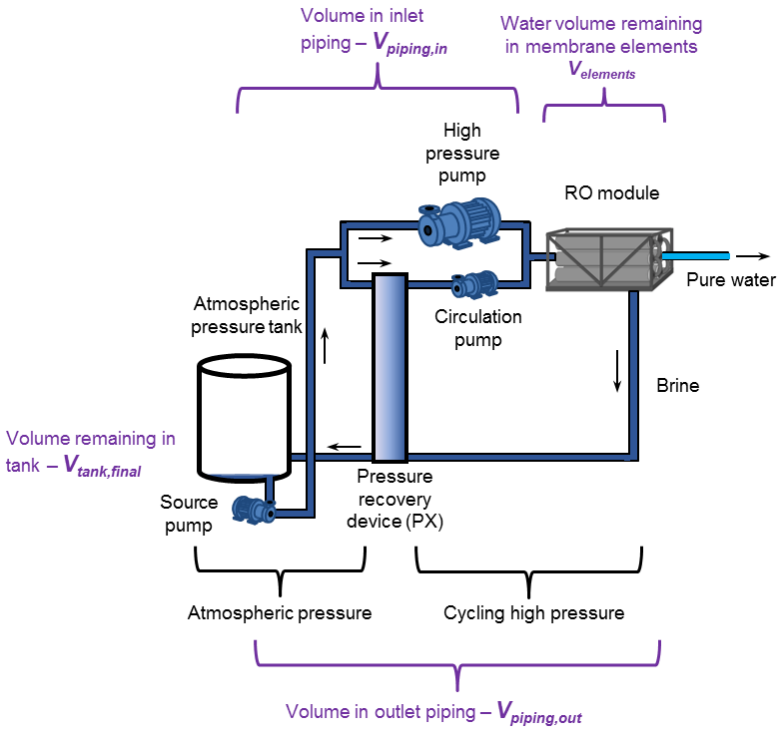

Figure C-2: Distribution of water volume in a BRO system towards the end of its operating cycle (not to scale). The effect of $V_{\text{piping,in}}$, $V_{\text{piping,out}}$ and V_{tank} relative to V_{elements} is investigated in this study.

mass is recovered as pure product. At this point, the remaining brine is discharged as new feed re-enters the system. The model simulation only accounts for the pure-water producing portion of the cycle time. This time is referred to as $t_{\text{productive}}$. The amount of time required to expel high salinity brine and refill the system with the required quantity of feedwater before the high pressure pump resumes operation is referred to as the cycle-reset time (t_{reset}). The overall cycle time of the batch process t_{cycle} is $t_{\text{productive}} + t_{\text{reset}}$.

C.2.1 Baseline system properties

The feed solution salinity is 35 g/kg and recovery ratio is 50%. Overall permeate production of 1633 m^3/day (300 GPM) is considered. Membrane geometry is based on a DOW SW30ULE-440i element [23]. The baseline system properties are listed in Table 1.

C.2.2 Modeling the isobaric energy recovery device (ERD)

The isobaric ERD is modeled by considering three loss mechanisms: [95]

1. Pressure drop from the inlet to the outlet of both the high- and low-pressure streams through the ERD,

2. Leakage reducing the high pressure flow and increasing the low pressure flow exiting the ERD, and

3. Mixing increasing the salinity of the high pressure stream exiting the ERD.

C.3 Validation

The present model was compared with a previous implementation of SWBRO with a PX [10]. The following parameters and assumptions were adapted from [125]: $A_{\text{membrane}} = 3$ kg/m^2-hr-bar, $B_{\text{membrane}} = 0$ kg/m^2-hr, $J = 15$ LMH, $v = 0.2$ m/s, $\eta_{\text{HPP}} = \eta_{\text{CP}} = 0.8$, $\eta_{\text{PX}} = 98\%$, and $\Delta P_{\text{piping}} = 0.1$ bar. The two model predictions

Table C.1: Baseline RO system properties

Parameter	Symbol	Value
Area per element	A_{element}	41 m^2
Length	L_{element}	1.016 m
Channel height	d_{ch}	0.71 mm
Channel porosity	ϕ	0.9 [2]
Inlet bulk velocity	v	0.18 m/s
Average flux	J	14.5 L/m^2-hr (LMH)
Water permeability	A_{membrane}	2 kg/m^2-hr-bar
Salt permeability	B_{membrane}	0.1 kg/m^2-hr
Number of elements in series per pressure vessel	N_{elements}	8
Number of pressure vessels	N_{parallel}	15
Width	$w = N_{\text{parallel}} A_{\text{element}} / 2L$	302.7 m
Volume of feed fluid per element	$V_{\text{element}} \approx \phi A_{\text{element}} d_{\text{ch}}$	13.13 L
Volume of feed fluid inside RO elements	$V_{\text{elements}} = N_{\text{elements}} N_{\text{parallel}} V_{\text{element}}$	1575.5 L
	Pumps, ERD	
Efficiency of pumps at high pressure (high pressure pump, circulation pump)	η_{HP}, η_{CP}	0.75
Efficiency of source pump	η_{SP}	0.8
Mixing in PX		6%
	Properties relevant to batch system	
Inlet piping min. volume	$V_{\text{piping,in,min}}$	33 L
Outlet piping min. volume	$V_{\text{piping,out,min}}$	60 L
Pressure drop in the piping	$\Delta P_{\text{piping,in}}$, $\Delta P_{\text{piping,out}}$	0.1 bar, 0.05 bar
Diffusivity of NaCl	D_{NaCl}	1.5×10^{-9} m^2/s
Tank volume at end of cycle	$V_{\text{tank,final}}$	0 L
Cycle reset time	t_{reset}	10 s

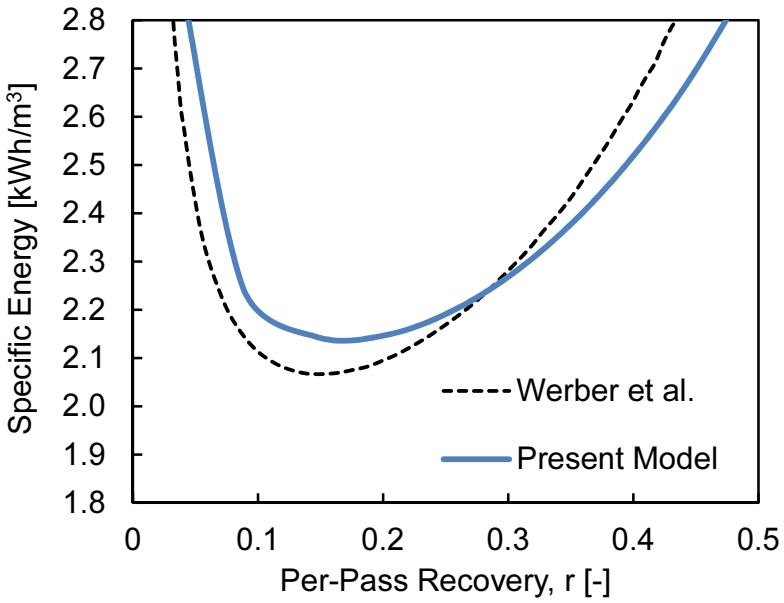

Figure C-3: The ideal per-pass recovery for SWRO is around 18%, close to the result in Werber et al. [10]. $V_{\text{tank,final}} = 12700$ L is about 8 times larger than V_{elements}.

for optimal per-pass recovery ratio as well as specific energy consumption were close. The difference could be a result of different correlations used for osmotic pressure as a function of salinity, channel friction factor and channel mass transfer coefficient.

A large external tank was considered in [125]. As a result, for this comparison, the tank volume at the end of the cycle was taken to be around 8 times larger than the volume of fluid inside the membrane elements. Going forward, such a large external volume will not be assumed, and hence the optimal per-pass recovery ratio obtained in this study is quite different. A detailed discussion on optimal per-pass recovery is included in Section 4.3.

C.4 Results

In this section, several aspects of BRO system design are considered in order to optimize BRO operation before comparing with single-stage continuous SWRO. In Section C.4.1, the performance of continuous SWRO under the baseline conditions is reported. All subsequent results for SWBRO are compared as a function of these metrics. The effect of external volume on specific energy consumption and cycle time

is evaluated in Section C.4.2. An ideal system should have lowest possible values of external volume $V_{\text{external}} = V_{\text{piping}} + V_{\text{tank,final}}$. The ideal per-pass recovery ratio and the resulting ideal number of elements in series are evaluated in Section C.4.3. Unlike previous studies [125], we find that for SWBRO, the ideal per-pass recovery ratio is about 50% (or optimal $N_{\text{elements}} \approx 8$, the same as the baseline continuous RO system). The implications of this result for BRO system design and capital cost are briefly discussed. The effect of the reset time ratio $t_{\text{reset}}/t_{\text{productive}}$ on the comparative performance of BRO to continuous RO is considered in Section C.4.4. Reset time t_{reset} is a very important variable that impacts the predicted savings associated with BRO. In Section C.4.5, the effect on overall cost of water from BRO is estimated in terms of both CapEx and OpEx. Finally, in Section C.4.6, the effect of ultrapermeable membranes on specific energy consumption is compared between SWBRO and SWRO systems. Ultrapermeable membranes result in larger energy savings in the case of BRO compared to continuous RO.

C.4.1 Baseline case: single stage SWRO with isobaric ERD

The batch RO model is used to simulate continuous RO by fixing the tank salinity at 35 g/kg. The overall specific energy consumption of SWRO is 2.32 kWh/m3 in the base case. The average flux over the entire length of the RO elements is 14.5 LMH, and the maximum flux at the lead element (at the entrance) is 52 LMH.

C.4.2 Effect of V_{external} (volume outside the module at the end of the cycle time)

The total external volume at the end of the batch process cycle is represented as V_{external}. Figure C-4 shows the effect of V_{external} on the specific energy consumption and cycle time of the BRO process. A larger external volume at the end of the cycle leads to a higher specific energy consumption.

The total external volume (V_{external}) is the sum of the volume in the piping (V_{piping}) and the final tank volume ($V_{\text{tank,final}}$). For the same final external volume, having the

volume in the piping system is better than having it in the tank. The cycle time is almost identical in these two cases, but the specific energy consumption is higher for the case where $V_{\text{tank,final}}$ increases, compared to when V_{piping} increases. This is because the tank is well mixed, whereas the pipes hold a range of salinity levels. At the end of the cycle, the fluid in the pipe from the module outlet to the tank has a higher salinity than the tank itself, and the tank has a higher salinity than the inlet to the feed tank. On the other hand, when low piping volume and high tank volume are considered, the salinity of the tank tends towards the highest salinity and the module inlet is also exposed to high feed salinity, leading to higher pressures and therefore higher energy requirements. As an extension of this analysis, we can also expect that it is better to design the outlet piping to be longer than the inlet piping so that some of the highest salinity brine remains unmixed with the tank at the end of the cycle. This was numerically verified, although the corresponding savings are low at least for low overall V_{external}. An design ramification of this result would be to locate the tank near the module inlet and have a longer pipe from the module outlet back into the tank.

While $V_{\text{tank,final}} \approx 0$ may be achieved by designing the outlet from the tank and the source pump system appropriately, some volume in the piping is unavoidable. An attempt to decrease the volume of fluid in the piping by reducing the pipe diameters would lead to an increase in frictional pressure drop. A minimum piping volume of 93 L (33 L in the inlet section and 60 L in the outlet) is obtained by considering large enough pipes to reduce pressure drop and estimating lengths for these pipe networks. 93 L corresponds to about 6% of the volume of fluid inside the module elements, and is the lower limit considered in this study (cf. Fig. C-7). Including the volumes in the heads of the pressure vessels and in the pumps, etc., results in an external volume of 186 L (corresponding to about 12% of the element volume).

At $V_{\text{external}} = 0.12 V_{\text{elements}}$ and $V_{\text{tank,final}} = 0$, the specific energy consumption is around 2.01 kWh/m^3. The cycle time of the process is around 96 s. This corresponds to a 13.4% reduction in specific energy consumption compared to the continuous RO system. In the subsequent sections, this analysis is expanded upon to consider the

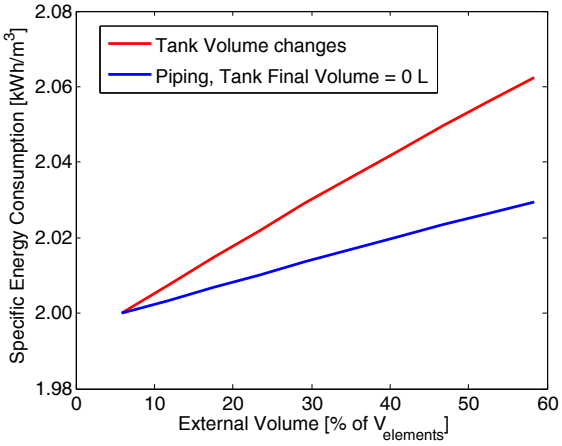

(a) Specific energy consumption as a function of V_{external}.

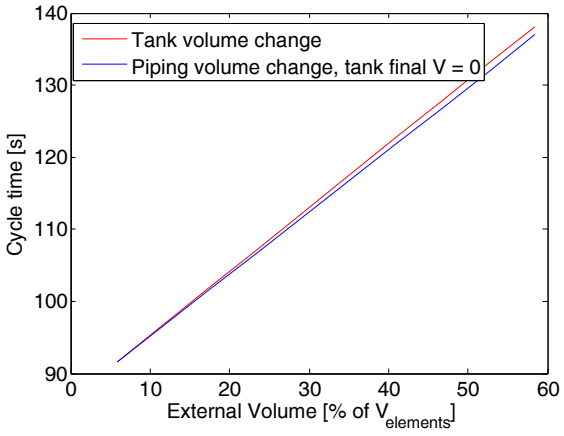

(b) Productive cycle time ($t_{\text{productive}}$) as a function of V_{external}. $N_{\text{elements}} = 8$. $J = 14.5$ LMH. Red lines correspond to increasing the tank volume only; blue lines correspond to increasing the piping volume (beyond 6%) only.

Figure C-4: Effect of brine volume outside the membrane elements at the end of the cycle time.

overall performance of BRO compared to continuous SWRO. The costs of BRO and continuous SWRO are also compared.

A lower final brine volume implies a correspondingly lower volume of initial feed (since recovery ratio is constant). Since flux and membrane area are constant in the present comparisons, cases where the final brine volume is lower have a lower operating cycle time ($t_{\text{productive}}$). This explains the linear relationship between $t_{\text{productive}}$ and final external volume in Fig. C-4b. This has been highlighted as a reason for choosing zero final tank volume by Warsinger et al. [122].

In order to understand the influence of final external volume on specific energy consumption, the salinity profiles within the membrane module are plotted as they evolve with time in Fig. C-5. Figure C-5a shows the salinity profiles for low V_{external} and Fig. C-5b shows the salinity profile evolution with time for high V_{external}.

Note that for the low external volume case, the highest salinity observed within the module is around 70 g/kg, whereas it is around 80 g/kg for the case with higher external volume. In both cases, the average salinity of all the remaining brine in the system at the end of the productive part of the cycle is 70 g/kg. If the mass

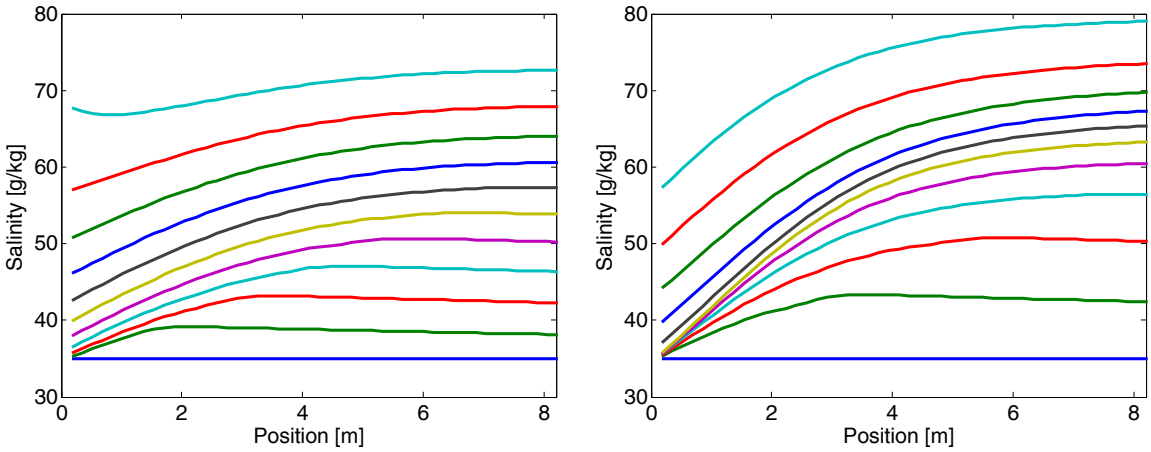

(a) $V_{\text{out}} = 6\%V_{\text{elements}}$ (limiting case). (b) $V_{\text{out}} = 120\%V_{\text{elements}}$.

Figure C-5: Effect of V_{out} on the salinity profiles within the RO module in BRO over the process cycle-time.

outside the elements is negligible, this implies that the average salinity within the RO elements is also around 70 g/kg. If significant brine exists outside the module in the tank, in order to increase the tank salinity close to 70 g/kg, the RO membranes themselves have to concentrate water to an even greater salinity, leading to a higher average pressure and higher energy requirements.

More curves in Fig. C-5a are relatively flat at the beginning of the cycle time compared to in Fig. C-5b. In both cases, equal time is required for the initial low salinity feed water inside the module to be displaced completely by inflow of feed. Since the total cycle time is lower for the low external volume case, the time to displace the flat salinity profile within the system constitutes a larger fraction of the total time in this case compared to the system with large V_{external}. When the external volume is low, the salinity vs. position curves flatten towards the end of the productive part of the cycle time as well, further reducing energy consumption. The local minimum in salinity at the end of a cycle with low external volume occurs due to the rapid return of concentrate exiting the module to the beginning of the module, as discussed in Ref. [122].

C.4.3 Ideal per-pass recovery or number of elements in series per pressure vessel

In Section C.3, we noted that the per-pass recovery is lower than overall recovery of 50% for systems with large external volume. In Section C.4.2, we demonstrated that a large value of V_{external} is counterproductive from an energy efficiency stand-point. As a result, in this section, we evaluate the optimal per-pass recovery for systems with more practically relevant lower external feed volumes at the end of each cycle.

In this study, the module feed inlet velocity is kept constant at 0.18 m/s. Per-pass recovery ratio (RR_{pass}) is defined as the fraction of the incoming mass flow rate that is being recovered as pure permeate at any given time. While feed inlet velocity can be changed, the range of values over which the velocity can be varied is limited considering the maximum and minimum flow rates recommended by membrane manufacturers. On the other hand, by maintaining the feed inlet velocity at 0.18 m/s, the range of velocities within the system can be maintained within the allowable range of values.

While holding the feed inlet velocity constant, RR_{pass} can be adjusted in the design stage by choosing the number of membrane elements in series in each pressure vessel appropriately. Since the overall flux is also fixed along with inlet velocity, RR_{pass} increases linearly with number of elements in series in each pressure vessel. As a result, while the original arrangement of membrane elements may be similar to what is shown in Fig. C-6a, in order to reduce the per-pass recovery ratio to half the original value (in the continuous RO system), N_{elements} would have to be reduced to half its original value, as shown in Fig. C-6b. In order to keep the overall permeate productivity constant, the number of pressure vessels in parallel would have to be increased.

Figure C-7 shows the effect of number of elements in series and correspondingly, the per-pass recovery ratio on the specific energy consumption for various values of V_{external}. At larger V_{external}, such as 500% of the element volume, the ideal value of number of elements and per-pass recovery ratio is about half of what is used in the

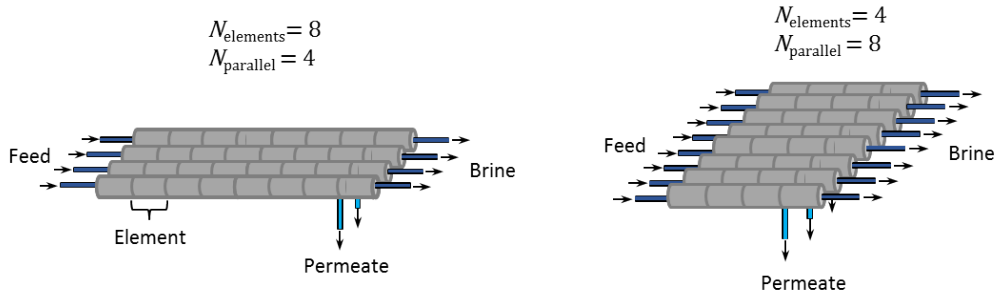

Figure C-6: Example of reverse osmosis modules and elements with different arrangements to implement different RR_{pass}: (a) 8 elements per module and 4 modules in parallel (higher RR_{pass}). (b) 4 elements and 8 parallel modules (lower RR_{pass}).

continuous system (cf. Section 3). On the other hand, at more practically relevant, lower values of $V_{external} = 6 - 12\% V_{elements}$, the ideal number of elements is around 8.

The ideal number of elements is greater than 8 for very low $V_{elements}$, but the difference in performance is small and so $N_{elements} = 8$ is used for all the values of $V_{external}$ considered in this study.

In the absence of any loss mechanisms such as pump and PX inefficiencies or frictional pressure drops, the ideal per-pass recovery ratio is zero, corresponding to an infinitesimally small membrane area. This way, the applied pressure can almost perfectly follow the osmotic pressure evolution of the system without spatial variations in flux, leading to the best energy efficiency possible [113]. At zero system area, the feed has to be recirculated through the system an infinite number of times to achieve desired concentrations, resulting in significant energy loss in the circulation pump and pressure exchanger. As $N_{elements}$ is reduced, the flowrate through the circulation pump and pressure exchanger increases. The number (or capacity) of required circulation pumps and pressure exchangers and the total energy consumption increase correspondingly. With a large number of elements, a large salinity gradient arises within the RO module, resulting in higher pressure requirements than what is dictated by the osmotic pressure of the inlet feed stream. The optimal number of elements represents a balance of these competing mechanisms.

One implication of the ideal number of elements being close to eight for an SWBRO system is that no additional pressure vessels, PXs, or pumps are required compared

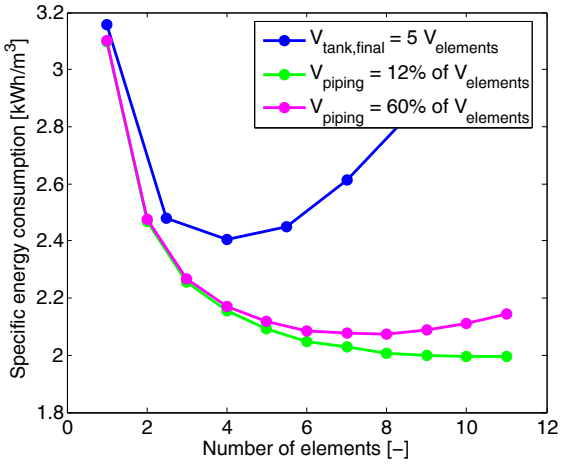

Figure C-7: Identifying the optimal number of elements (and correspondingly per pass recovery) as a function of external volume.

to a continuous SWRO system of the same production capacity. The only additional cost of capital for SWBRO is related to the tank and control system for draining and refilling the BRO system at the end of the cycle. The next section deals with the effect of this reset time on energy consumption.

C.4.4 Cycle-reset time

A BRO process does not produce pure water continuously; it produces pure water during the productive time and not while it is emptying the high salinity brine and refilling feed water into the membrane system and tank. A separate pump system is required for this cycle-reset process. The volumetric flow rate during normal operation at the inlet of the RO module is around 37.8 L/s. In order to refill the entire volume of the RO elements (1575.5 L) at this flow rate, it would take about 41.7 s. Recall that the total productive time of the process (in each cycle) is only around 96 s.

The effective flux in a batch RO process can be represented as:

$$J_{\text{eff}} = J \times \frac{t_{\text{productive}}}{t_{\text{productive}} + t_{\text{reset}}} \tag{C.1}$$

Because of the reset time, a batch system requires a higher flux or more membrane elements to produce the same permeate flow rate as a continuous RO system.

Figure C-8 shows the specific energy consumption and $t_{\text{productive}}$ as a function of operating flux over the process cycle time. As operating flux is increased, the required pressure increases, corresponding to higher energy consumption. Simultaneously, $t_{\text{productive}}$ also decreases with increasing flux since permeate is produced faster. The effect of piping volume on both specific energy consumption and cycle time is similar to what was observed in Section 4.2.

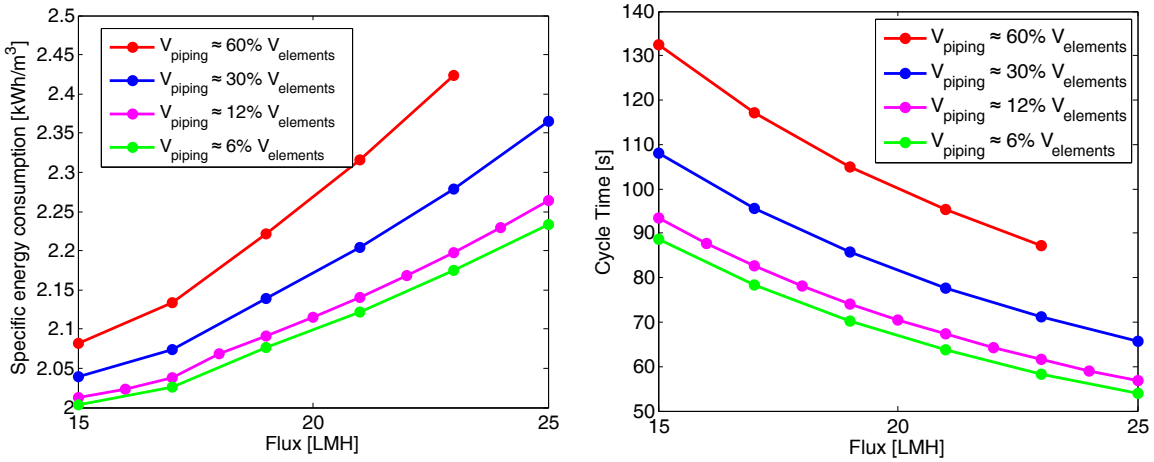

(a) Specific energy consumption

(b) Productive cycle time.

Figure C-8: Specific energy consumption and productive cycle-time as a function of operating flux. At higher operating flux, the specific energy consumption increases, and the process cycle time decreases.

Figure C-9 compares energy consumption to effective flux for two values of t_{reset}. Performance is again calculated for a range of values of external volume. At an effective flux of 14.5 LMH, and $V_{\text{piping}} = 0.12V_{\text{elements}}$, specific energy consumption increases from 2.03 kWh/m^3 for $t_{\text{reset}} = 10$ s to 2.14 kWh/m^3 for $t_{\text{reset}} = 30$ s. Note that in spite of the increase, specific energy consumption of SWBRO is still lower than for continuous SWRO, which was 2.32 kWh/m^3.

Additional concerns associated with operating at higher flux are related to membrane fouling and exceeding maximum flux recommendations. Batch RO systems have exhibited greater fouling and scaling resistance compared to continuous systems due to unsteady operation and the associated decrease in the amount of time that supersaturated salt solutions spend within the RO modules [90]. While specific

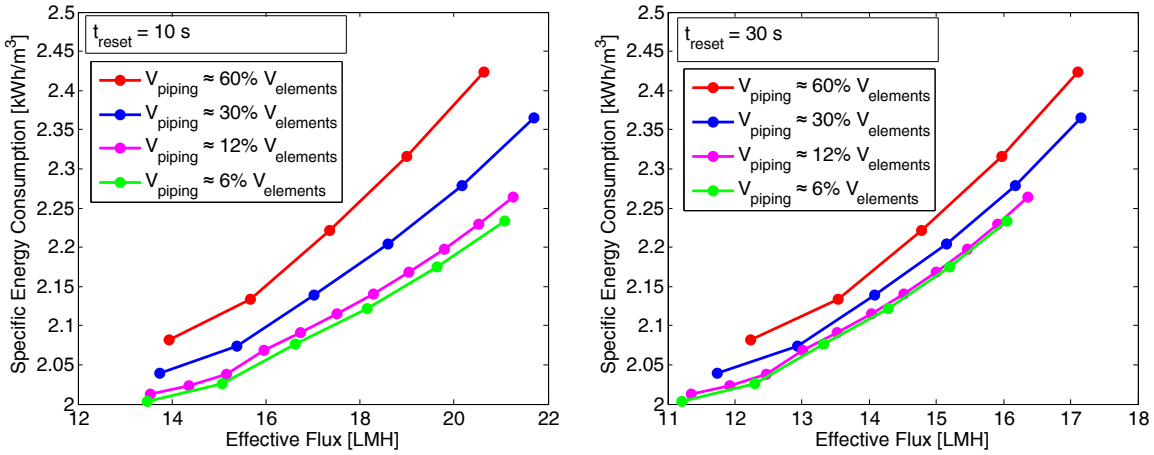

(a) $t_{\text{reset}} = 10$ s (b) $t_{\text{reset}} = 30$ s

Figure C-9: Specific energy consumption of BRO as a function of effective flux for two values of cycle reset time = 10 s and 30 s.

manufacturer recommendations for maximum flux per element are not considered, the maximum flux during the operation of the batch process can be compared with the maximum flux at the inlet of the module observed in the continuous system (52 LMH). When operating at effective flux of 14.5 LMH, the maximum flux in SWBRO is 40 LMH for $t_{\text{reset}} = 10$ s and it increases to 55 LMH for $t_{\text{reset}} = 30$ s.

By comparing the specific energy consumption at equal effective flux, we observe a 12.7% lower energy consumption for SWBRO (if $t_{\text{reset}} = 10$ s), whereas the energy saving is only 7.8% when $t_{\text{reset}} = 30$ s. In addition, there may be practical constraints with respect to operating at higher flux to achieve the same effective flux, especially for the cases with larger fraction of cycle-reset time.

C.4.5 Cost comparison

One way to overcome the limitations highlighted in the previous section with respect to comparing batch and continuous SWRO processes is to keep the same operating flux in batch, but relax the condition of keeping membrane area the same across the two systems. Since the batch system has a lower effective flux, the membrane area in the batch system is increased in order to produce the same overall permeate quantity per unit time. The SWBRO system with $V_{\text{piping}} = 12\%$ of V_{elements}, $N_{\text{elements}} = 8$, $J =$

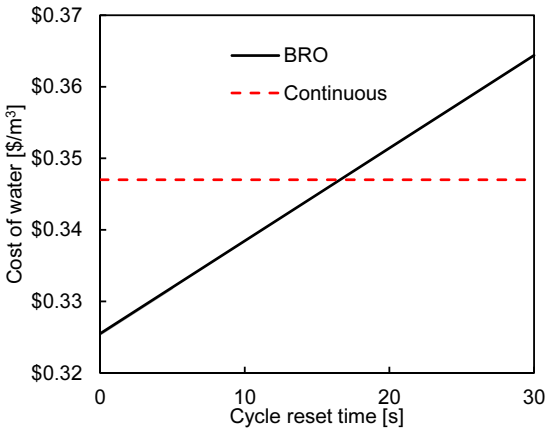

Figure C-10: Specific cost of water production as a function of t_{reset}. This shows that SWBRO is cheaper only if cycle reset time can be much lower than 16 s (for a cycle productive time of 96 s)

14.5 LMH is considered and the corresponding energy consumption and productive time were previously evaluated as 2.01 kWh/m^3 and around 96 s respectively.

The additional membrane area required for the SWBRO system to produce the same amount of permeate water as the continuous system is given by: $A_{\text{continuous}} \times (t_{\text{productive}} + t_{\text{reset}})/t_{\text{productive}}$. The cost of capital can be considered to linearly vary with system size, and hence the cost of capital linearly increases with t_{reset}. Assuming a capital cost of \$608K, plant life of 20 years and interest rate of 8% for a 300 GPM desalination plant, the total amortized cost of capital is 0.12/m^3. The energy cost at 2.32 kWh/m^3 is \$0.23/m^3 assuming an electricity cost of \$0.10/kWh.

For a SWBRO system, the energy cost is reduced to \$0.20/m^3. The baseline capital of SWBRO including the additional tank and pump is \$655K. Depending on t_{reset}, the capital cost is higher than \$0.12/m^3. Based on the linear relationship between CapEx and t_{reset}, Fig. C-10 shows the overall specific cost of water (considering cost of capital and electricity consumption), considering both electricity cost and amortized cost of capital as a function of t_{reset}.

For a system with $t_{\text{reset}} = 10$ s, while the energy saving was predicted to be about 12%, the overall cost saving considering both CapEx and OpEx is about 2.6%. Batch RO systems will need to be designed to rapidly refill the tank and eject brine from the membrane module to minimize the reset time.

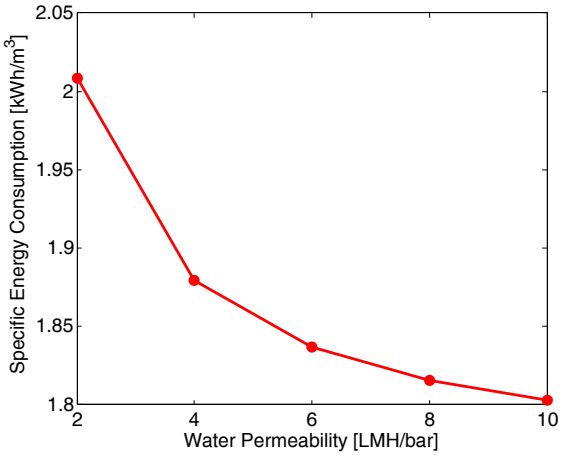

Figure C-11: Effect of water permeability on BRO energy consumption.

C.4.6 Effect of membrane permeability

The impact of ultra-permeable membranes on the energy consumption and performance of continuous RO desalination systems has already been considered by Cohen-Tanugi et al. [22] who showed that some energy savings are possible in brackish water and seawater desalination. McGovern and Lienhard [69] showed the asymptotic flux limits with ultra-permeable membranes due to limitations imposed by concentration polarization. However, the effect of introducing ultra-permeable membranes into batch RO has not been studied.

Figure 11 shows the effect of increasing membrane permeability on the energy consumption of SWBRO. The specific energy consumption drops by about 10% (0.2 kWh/m^3) with an increase in permeability from 2 LMH/bar to 10 LMH/bar. On the other hand, our model shows that the continuous SWRO system energy consumption would decrease only by about 0.11 kWh/m^3. SWBRO is likely to benefit more from the development of novel ultra-permeable membranes such as graphene- and aquaporin-based membranes.

C.5 Conclusion

Batch RO implemented with an atmospheric pressure tank and pressure exchanger has the potential to reduce the energy consumption and overall cost of seawater desalination compared to conventional single-stage RO.

1. The volume of fluid outside the membrane elements at the end of the productive part of the cycle time should be small - less than around 20% of the volume inside the membrane elements. The tank volume should ideally tend towards zero at the end of the cycle.

2. For the component efficiencies used here, the ideal number of elements in SWBRO is close to what is used in continuous SWRO and ideal per-pass recovery ratio is around 50%.

3. The reset time is a key variable controlling overall performance of BRO.

   (a) BRO can be operated at higher flux or with higher area to match the pure water productivity of continuous RO.

   (b) When BRO is operated at higher flux, if the reset time is small (around 10% of the total time), 10% energy savings are possible compared to conventional RO.

4. Compared to conventional RO, the cost of water is around 2.6% lower with BRO (for $t_{\text{reset}} = 10$ s) if BRO is operated at the same flux, but with additional membrane area to maintain same overall productivity. The cost of BRO can be higher than continuous RO if the reset time is larger than about 15% of the total time.

5. Ultrapermeable membranes are likely to yield significantly higher energy savings when coupled with SWBRO than when used in SWRO.

Bibliography

[1] Samer Adham, Altaf Hussain, Joel Minier Matar, Raul Dores, and Arnold Janson. Application of membrane distillation for desalting brines from thermal desalination plants. *Desalination*, 314:101 – 108, 2013.

[2] Sergey P. Agashichev and A.V. Sivakov. Modeling and calculation of temperature-concentration polarisation in the membrane distillation process (MD). *Desalination*, 93(1-3):245–258, 1993.

[3] Faisal Al Marzooqi, Muhamad Roil Bilad, Jaichander Swaminathan, John H Lienhard V, and Hassan Arafat. Flux measurements in novel membrane distillation configurations. In *Submitted to Proceedings of The International Desalination Association World Congress on Desalination and Water Reuse, San Diego, CA, USA*, August 2015.

[4] Sulaiman Al-Obaidani, Efrem Curcio, Francesca Macedonio, Gianluca Di Profio, Hilal Al-Hinai, and Enrico Drioli. Potential of membrane distillation in seawater desalination: Thermal efficiency, sensitivity study and cost estimation. *Journal of Membrane Science*, 323(1):85–98, 2008.

[5] Aamer Ali, C.A. Quist-Jensen, F. Macedonio, and Enrico Drioli. On designing of membrane thickness and thermal conductivity for large scale membrane distillation modules. *Journal of Membrane Science and Research*, 2(4):179–185, 2016.

[6] Aamer Ali, Cejna Anna Quist-Jensen, Francesca Macedonio, and Enrico Drioli. Optimization of module length for continuous direct contact membrane distillation process. *Chemical Engineering and Processing: Process Intensification*, 110:188 – 200, 2016.

[7] Mohamed I. Ali, Edward K. Summers, Hassan A. Arafat, and John H. Lienhard V. Effects of membrane properties on water production cost in small scale membrane distillation systems. *Desalination*, 306:60 – 71, 2012.

[8] Abdullah Alkhudhiri, Naif Darwish, and Nidal Hilal. Membrane distillation: A comprehensive review. *Desalination*, 287:2–18, 2012.

[9] Abdullah Alkhudhiri, Naif Darwish, and Nidal Hilal. Treatment of high salinity solutions: Application of air gap membrane distillation. *Desalination*, 287:55 – 60, 2012.

[10] Abdulaziz M. Alklaibi and Noam Lior. Membrane-distillation desalination: Status and potential. *Desalination*, 171(2):111–131, 2005.

[11] Abdulaziz M. Alklaibi and Noam Lior. Transport analysis of air-gap membrane distillation. *Journal of Membrane Science*, 255(1-2):239–253, June 2005.

[12] Abdulaziz M. Alklaibi and Noam Lior. Comparative Study of Direct Contact and Air Gap Membrane Distillation Processes. *Ind. Eng. Chem. Res*, 2(46):584–590, 2007.

[13] Narmine H. Aly and Adel K. El-Figi. Mechanical vapor compression desalination systems – a case study. *Desalination*, 158(1):143 – 150, 2003.

[14] Leonardo D. Banchik, Mostafa H. Sharqawy, and John H. Lienhard V. Effectiveness–mass transfer units (ε–MTU) model of a reverse osmosis membrane mass exchanger. *Journal of Membrane Science*, 458:189–198, 2014.

[15] Hsuan Chang, Jung-Shing Liau, Chii-Dong Ho, and Wei-Hong Wang. Simulation of membrane distillation modules for desalination by developing user's model on Aspen Plus platform. *Desalination*, 249(1):380–387, 2009.

[16] Karim M. Chehayeb, Farah K. Cheaib, and John H. Lienhard V. A numerical solution algorithm for a heat and mass transfer model of a desalination system based on packed-bed humidification and bubble column dehumidification. In *Proceedings of the 15th International Heat Transfer Conference, IHTC-15, Paper No. IHTC15-8995*, Kyoto, Japan August 2014.

[17] Karim M. Chehayeb and John H. Lienhard V. Effect of feed salinity on the performance of humidification dehumidification desalination. In *The International Desalination Association World Congress on Desalination and Water Reuse, San Diego, USA*, 2015.

[18] Karim M Chehayeb, G Prakash Narayan, Syed M Zubair, and John H Lienhard V. Thermodynamic balancing of a fixed-size two-stage humidification dehumidification desalination system. *Desalination*, 369:125–139, 2015.

[19] Li-Hua Cheng, Ping-Chung Wu, and Junghui Chen. Numerical simulation and optimal design of agmd-based hollow fiber modules for desalination. *Industrial & Engineering Chemistry Research*, 48(10):4948–4959, 2009.

[20] Hyung W. Chung, Jaichander Swaminathan, David M. Warsinger, and John H. Lienhard V. Multistage vacuum membrane distillation (MSVMD) systems for high salinity applications. *Journal of Membrane Science*, 497:128–141, 2016.

[21] Andrea Cipollina, M.G. Di Sparti, Alessandro Tamburini, and Giorgio Micale. Development of a Membrane Distillation module for solar energy seawater desalination. *Chemical Engineering Research and Design*, 90(12):2101–2121, 2012.

[22] David Cohen-Tanugi, Ronan K. McGovern, Shreya H. Dave, John H. Lienhard V, and Jeffrey C. Grossman. Quantifying the potential of ultra-permeable membranes for water desalination. *Energy Environ. Sci.*, 7:1134–1141, 2014.

[23] The DOW Chemical Company. Dow SW30ULE-440i element. http://msdssearch.dow.com/PublishedLiteratureDOWCOM/dh_0988/0901b8038098893c.pdf?filepath=liquidseps/pdfs/noreg/609-03004.pdf&fromPage=GetDoc. Accessed: 2017-03-29.

[24] Efrem Curcio, Xiaosheng Ji, Abdul Matin Quazi, Shahzad Barghi, Gianluca Di Profio, Enrica Fontananova, Trevor Macleod, and Enrico Drioli. Hybrid nanofiltration–membrane crystallization system for the treatment of sulfate wastes. *Journal of Membrane Science*, 360(1):493–498, 2010.

[25] Lourdes Martínez Díez and M. Isabel Vásquez-González. Temperature and concentration polarization in membrane distillation of aqueous salt solutions. *Journal of Membrane Science*, 156(2):265 – 273, 1999.

[26] Ludovic F. Dumée, Simon Smart, Mikel C. Duke, and Steve R. Gray. *Next generation membranes for membrane distillation and future prospects*. Woodhead Publishing, 2015.

[27] Hung C. Duong, Allan R. Chivas, Bart Nelemans, Mikel Duke, Stephen Gray, Tzahi Y. Cath, and Long D. Nghiem. Treatment of RO brine from CSG produced water by spiral-wound air gap membrane distillation - a pilot study. *Desalination*, 366:121 – 129, 2015. Energy and Desalination.

[28] Hung C. Duong, Paul Cooper, Bart Nelemans, Tzahi Y. Cath, and Long D. Nghiem. Optimising thermal efficiency of direct contact membrane distillation by brine recycling for small-scale seawater desalination. *Desalination*, 374:1 – 9, 2015.

[29] Hung C. Duong, Paul Cooper, Bart Nelemans, Tzahi Y. Cath, and Long D. Nghiem. Evaluating energy consumption of air gap membrane distillation for seawater desalination at pilot scale level. *Separation and Purification Technology*, 166:55 – 62, 2016.

[30] Felinia Edwie and Tai-Shung Chung. Development of simultaneous membrane distillation-crystallization (SMDC) technology for treatment of saturated brine. *Chemical Engineering Science*, 98:160 – 172, 2013.

[31] Hisham T. El-Dessouky and Hisham M. Ettouney. *Fundamentals of Salt Water Desalination*. Elsevier, Amsterdam, The Netherlands, 2002.

[32] Yehia M. El-Sayed. Designing desalination systems for higher productivity. *Desalination*, 134(1):129–158, 2001.

[33] Hisham Ettouney. Design of single-effect mechanical vapor compression. *Desalination*, 190(1):1 – 15, 2006.

[34] Lies Eykens, I Hitsov, Kristien De Sitter, Chris T.E. Dotremont, Luc J.J. Pinoy, Ingmar Nopens, and Bart Van der Bruggen. Influence Of Membrane Thickness And Process Conditions On Direct Contact Membrane Distillation At Different Salinities. *Journal of Membrane Science*, 498:353–364, January 2015.

[35] Lies Eykens, T. Reyns, Kristien De Sitter, Chris T.E. Dotremont, Luc J.J. Pinoy, and Bart Van der Bruggen. How to select a membrane distillation configuration? Process conditions and membrane influence unraveled. *Desalination*, 399:105 – 115, 2016.

[36] Anthony G. Fane, RW Schofield, and Christopher Jospeh D Fell. The efficient use of energy in membrane distillation. *Desalination*, 64:231–243, 1987.

[37] Lijo Francis, Noreddine Ghaffour, Ahmad A. Alsaadi, and Gary L. Amy. Material gap membrane distillation: A new design for water vapor flux enhancement. *Journal of Membrane Science*, 448:240–247, 2013.

[38] Amy E. Childress Francisco Suárez, Scott W. Tyler. A theoretical study of a direct contact membrane distillation system coupled to a salt-gradient solar pond for terminal lakes reclamation. *Water Research*, 44(12):4601–4615, 2010.

[39] Clemens Fritzmann, Jonas Löwenberg, Thomas Wintgens, and Thomas Melin. State-of-the-art of reverse osmosis desalination. *Desalination*, 216(1–3):1–76, 2007.

[40] Hongxin Geng, Haoyun Wu, Pingli Li, and Qingfeng He. Study on a new air-gap membrane distillation module for desalination. *Desalination*, 334(1):29–38, 2014.

[41] Vítor Geraldes and Ana Maria Brites Alves. Computer program for simulation of mass transport in nanofiltration membranes. *Journal of Membrane Science*, 321(2):172 – 182, 2008.

[42] Noreddine Ghaffour, Sabine Lattemann, Thomas Missimer, Kim Choon Ng, Shahnawaz Sinha, and Gary Amy. Renewable energy-driven innovative energy-efficient desalination technologies. *Applied Energy*, 136:1155–1165, 2014.

[43] Jack Gilron, Liming Song, and Kamalesh K. Sirkar. Design for cascade of cross-flow direct contact membrane distillation. *Industrial & Engineering Chemistry Research*, 46(8):2324–2334, 2007.

[44] Global Water Intelligence. Global water intelligence and water desalination report 2014. *http://desaldata.com/*, 2014.

[45] Guoqiang Guan, Xing Yang, Rong Wang, and Anthony G. Fane. Evaluation of heat utilization in membrane distillation desalination system integrated with heat recovery. *Desalination*, 366:80–93, 2015.

[46] Yunshan Guan, Jianfeng Li, Fangqin Cheng, Jing Zhao, and Xuming Wang. Influence of salt concentration on DCMD performance for treatment of highly concentrated NaCl, KCl, $MgCl_2$ and $MgSO_4$ solutions. *Desalination*, 355:110–117, 2015.

[47] Charles E Harvie, Nancy Møller, and John H Weare. The prediction of mineral solubilities in natural waters: The Na-K-Mg-Ca-H-Cl-SO_4-OH-HCO_3-CO_3-CO_2-H_2O system to high ionic strengths at 25 řc. *Geochimica et Cosmochimica Acta*, 48(4):723 – 751, 1984.

[48] Mohamed I. Hassan, Ayoola T. Brimmo, Jaichander Swaminathan, John H. Lienhard V, and Hassan A. Arafat. A new vacuum membrane distillation system using an aspirator: Concept modelling and optimization. *Desalination and Water Treatment*, 57:12915—12928, June 2016.

[49] Qingfeng He, Pingli Li, Hongxin Geng, Chunyao Zhang, Juan Wang, and Heying Chang. Modeling and optimization of air gap membrane distillation system for desalination. *Desalination*, 354:68–75, 2014.

[50] I. Hitsov, Kristien De Sitter, Chris T.E. Dotremont, Peter Cauwenberg, and Ingmar Nopens. Full-scale validated air gap membrane distillation (AGMD) model without calibration parameters. *Journal of Membrane Science*, 533:309 – 320, 2017.

[51] Eivind Johannessen, Lars Nummedal, and Signe Kjelstrup. Minimizing the entropy production in heat exchange. *International Journal of Heat and Mass Transfer*, 45(13):2649 – 2654, 2002.

[52] Mohamed Khayet and Takeshi Matsuura. *Membrane Distillation Principles and Applications*. Elsevier, 2011.

[53] Sanford A. Klein. Engineering Equation Solver.

[54] Nienke Elisabeth Koeman-Stein, Raymond J.M. Creusen, Martin Zijlstra, Cornelis K. Groot, and Wilbert B.P. van den Broek. Membrane distillation of industrial cooling tower blowdown water. *Water Resources and Industry*, 14:11 – 17, 2016.

[55] Joachim Koschikowski, Marcel Wieghaus, and Matthias Rommel. Solar thermal-driven desalination plants based on membrane distillation. *Desalination*, 156(1-3):295–304, 2003.

[56] Kevin W. Lawson and Douglas R. Lloyd. Membrane distillation. *Journal of Membrane Science*, 124(1):1–25, 1997.

[57] Hanyong Lee, Fei He, Liming Song, Jack Gilron, and Kamalesh K Sirkar. Desalination with a cascade of cross-flow hollow fiber membrane distillation devices integrated with a heat exchanger. *AlChE Journal*, 57(7):1780–1795, 2011.

[58] Megan E. Leitch, Chenkai Li, Olli Ikkala, Meagan S. Mauter, and Gregory V. Lowry. Bacterial nanocellulose aerogel membranes: Novel high-porosity materials for membrane distillation. *Environmental Science & Technology Letters*, 3(3):85–91, 2016.

[59] Megan E. Leitch, Gregory V. Lowry, and Meagan S. Mauter. Characterizing convective heat transfer coefficients in membrane distillation cassettes. *Journal of Membrane Science*, 538:108 – 121, 2017.

[60] Baoan Li and Kamalesh K Sirkar. Novel membrane and device for vacuum membrane distillation-based desalination process. *Journal of Membrane Science*, 257:60–75, 2005.

[61] Chen Li and GP Peterson. The effective thermal conductivity of wire screen. *International Journal of Heat and Mass Transfer*, 49(21):4095–4105, 2006.

[62] Zhehao Li, Yuelian Peng, Yajun Dong, Hongwei Fan, Ping Chen, Lin Qiu, and Qi Jiang. Effects of thermal efficiency in DCMD and the preparation of membranes with low thermal conductivity. *Applied Surface Science*, 317:338–349, October 2014.

[63] John H. Lienhard V and John H. Lienhard IV. *A Heat Transfer Textbook, Fourth Edition*. Dover Publications, Inc, 2011.

[64] Shihong Lin, Ngai Yin Yip, and Menachem Elimelech. Direct contact membrane distillation with heat recovery: Thermodynamic insights from module scale modeling. *Journal of Membrane Science*, 453:498–515, 2014.

[65] Zidu Ma, Timothy D Davis, James R Irish, and Gary D Winch. Membrane distillation system and method, January 27 2010. US Patent App. 12/694,757.

[66] C. Riziero Martinetti, Amy E. Childress, and Tzahi Y. Cath. High recovery of concentrated RO brines using forward osmosis and membrane distillation. *Journal of Membrane Science*, 331(1–2):31 – 39, 2009.

[67] Leopoldo Martínez and Jose M. Rodríguez-Maroto. On transport resistances in direct contact membrane distillation. *Journal of Membrane Science*, 295(1-2):28–39, 2007.

[68] Leopoldo Martinez and Jose Miguel Rodriguez-Maroto. Membrane thickness reduction effects on direct contact membrane distillation performance. *Journal of Membrane Science*, 312(1-2):143 – 156, 2008.

[69] Ronan K. McGovern and John H. Lienhard V. On the asymptotic flux of ultrapermeable seawater reverse osmosis membranes due to concentration polarisation. *Journal of Membrane Science*, 520:560 – 565, 2016.

[70] Ronan K. McGovern, Gregory P. Thiel, G. Prakash Narayan, Syed M. Zubair, and John H. Lienhard V. Performance limits of zero and single extraction humidification-dehumidification desalination systems. *Applied Energy*, 102(0):1081 – 1090, 2013.

[71] Liu Meihong, Yu Sanchuan, Zhou Yong, and Gao Congjie. Study on the thin-film composite nanofiltration membrane for the removal of sulfate from concentrated salt aqueous: Preparation and performance. *Journal of Membrane Science*, 310(1):289–295, 2008.

[72] Karan H. Mistry, Harrison A. Hunter, and John H. Lienhard V. Effect of composition and nonideal solution behavior on desalination calculations for mixed electrolyte solutions with comparison to seawater. *Desalination*, 318(0):34–47, 2013.

[73] Karan H. Mistry and John H. Lienhard V. Generalized Least Energy of Separation for Desalination and Other Chemical Separation Processes. *Entropy*, 15(6):2046–2080, 2013.

[74] Karan H. Mistry, Ronan K. McGovern, Gregory P. Thiel, Edward K. Summers, Syed M. Zubair, and John H. Lienhard V. Entropy Generation Analysis of Desalination Technologies. *Entropy*, 13(10):1829–1864, 2011.

[75] Karan H. Mistry, Alexander Mitsos, and John H. Lienhard V. Optimal operating conditions and configurations for humidification–dehumidification desalination cycles. *International Journal of Thermal Sciences*, 50(5):779–789, 2011.

[76] Lucien L. Morales. Visualization and measurement of filmwise and dropwise air gap membrane distillation at varied module inclination angle and gap spacer orientation. S.B. thesis, Massachusetts Institute of Technology, 2016.

[77] Ahmed Safwat Nafey, Hassan Elbanna S. Fath, and Abdulnasser A. Mabrouk. Thermoeconomic design of a multi-effect evaporation mechanical vapor compression (MEE-MVC) desalination process. *Desalination*, 230(1-3):1–15, 2008.

[78] G. Prakash Narayan, Maximus G. St. John, Syed M. Zubair, and John H. Lienhard V. Thermal design of the humidification dehumidification desalination system: An experimental investigation. *International Journal of Heat and Mass Transfer*, 58(1):740–748, 2013.

[79] Kishor G. Nayar, Mostafa H. Sharqawy, Leonardo D. Banchik, and John H. Lienhard V. Thermophysical properties of seawater: A review and new correlations that include pressure dependence. *Desalination*, 390:1–24, 2016.

[80] Jirachote Phattaranawik, Ratana Jiraratananon, and Anthony G. Fane. Heat transport and membrane distillation coefficients in direct contact membrane distillation. *Journal of Membrane Science*, 212(1-2):177–193, 2003.

[81] Kenneth S. Pitzer, J. Christopher Peiper, and R. H. Busey. Thermodynamic Properties of Aqueous Sodium Chloride Solutions. *Journal of Physical and Chemical Reference Data*, 13(1):1–102, January 1984.

[82] Mohammed R. Qtaishat, Takeshi Matsuura, Boguslaw Kruczek, and Mohamed Khayet. Heat and mass transfer analysis in direct contact membrane distillation. *Desalination*, 219(1-3):272–292, 2008.

[83] Cejna Anna Quist-Jensen, Aamer Ali, Suchintan Mondal, Francesca Macedonio, and Enrico Drioli. A study of membrane distillation and crystallization for lithium recovery from high-concentrated aqueous solutions. *Journal of Membrane Science*, 505:167 – 173, 2016.

[84] Lord Rayleigh. On the influence of obstacles arranged in rectangular order upon the properties of a medium. *The London, Edinburgh, and Dublin Philosophical Magazine and Journal of Science*, 34(211):481–502, 1892.

[85] Yagnaseni Roy, Mostafa H. Sharqawy, and John H. Lienhard V. Modeling of flat-sheet and spiral-wound nanofiltration configurations and its application in seawater nanofiltration. *Journal of Membrane Science*, 493:360–372, 2015.

[86] Mohammadali Safavi and Toraj Mohammadi. High-salinity water desalination using VMD. *Chemical Engineering Journal*, 149(1–3):191 – 195, 2009.

[87] Rasha B. Saffarini, Edward K. Summers, Hassan A. Arafat, and John H. Lienhard V. Economic evaluation of stand-alone solar powered membrane distillation systems. *Desalination*, 299:55–62, 2012.

[88] Rosalam Sarbatly and Chel-Ken Chiam. Evaluation of geothermal energy in desalination by vacuum membrane distillation. *Applied Energy*, 112:737–746, 2013.

[89] Sudipta Sarkar and Arup K SenGupta. A new hybrid ion exchange-nanofiltration (HIX-NF) separation process for energy-efficient desalination: process concept and laboratory evaluation. *Journal of Membrane Science*, 324(1):76–84, 2008.

[90] S. Sen, A. Lau, Eileen Idica, and Shane Trussell. Maximizing product water through brine minimization. In *Proceedings of the WateReuse Forum, Tampa, FL, Sept.*, 2016.

[91] Mostafa H. Sharqawy, Leonardo D. Banchik, and John H. Lienhard V. Effectiveness–mass transfer units (ε–MTU) model of an ideal pressure retarded osmosis membrane mass exchanger. *Journal of Membrane Science*, 445:211–219, 2013.

[92] Mostafa H. Sharqawy, John H. Lienhard V, and Syed M. Zubair. Thermophysical properties of seawater: A review of existing correlations and data. *Desalination and Water Treatment*, 16:354–380, April 2010.

[93] Dhananjay Singh and Kamalesh K. Sirkar. Desalination by air gap membrane distillation using a two hollow-fiber-set membrane module. *Journal of Membrane Science*, 421–422:172 – 179, 2012.

[94] Richard L. Stover. Industrial and brackish water treatment with closed circuit reverse osmosis. *Desalination and Water Treatment*, 51(4-6):1124–1130, 2013.

[95] Richard L. Stover and William Andrews. Isobaric energy recovery devices - past, present and future. In *Proceedings of The International Desalination Association World Congress on Desalination and Water Reuse, Perth, Australia*, 2011.

[96] Francisco Suarez, Jeffrey A. Ruskowitz, Scott W. Tyler, and Amy E. Childress. Renewable water: Direct contact membrane distillation coupled with solar ponds. *Applied Energy*, 158:532–539, 2015.

[97] Edward K. Summers. *Development of Energy Efficient Membrane Distillation Systems*. PhD thesis, Massachusetts Institute of Technology, Cambridge, Massachusetts, U.S.A., 2013.

[98] Edward K. Summers, Hassan A. Arafat, and John H. Lienhard V. Energy efficiency comparison of single-stage membrane distillation (MD) desalination cycles in different configurations. *Desalination*, 290:54–66, 2012.

[99] Edward K. Summers and John H. Lienhard V. Cycle performance of multistage vacuum membrane distillation (MS-VMD) systems. In *Proceedings of the 2013 IDA World Congress on Desalination and Water Reuse, Tianjin, China*, Oct 2013.

[100] Edward K. Summers and John H. Lienhard V. Experimental study of thermal performance in air gap membrane distillation systems including direct solar heating of membranes. *Desalination*, 330:100–111, 2013.

[101] Edward K. Summers and John H. Lienhard V. Experimental study of thermal performance in air gap membrane distillation systems, including the direct solar heating of membranes. *Desalination*, 330:100–111, dec 2013.

[102] Jaichander Swaminathan. Numerical and experimental investigation of membrane distillation flux and energy efficiency. Master's thesis, Massachusetts Institute of Technology, 2014.

[103] Jaichander Swaminathan, Hyung Won Chung, David Warsinger, Faisal Al-Marzooqi, Hassan A. Arafat, and John H. Lienhard V. Energy efficiency of permeate gap and novel conductive gap membrane distillation. *Journal of Membrane Science*, 502:171–178, 2016.

[104] Jaichander Swaminathan, Hyung Won Chung, David Warsinger, and John H. Lienhard V. Experimental investigation of high efficiency single-stage membrane distillation configurations. *Proceedings of the International Desalination Association World Congress, San Diego*, August 2015.

[105] Jaichander Swaminathan, Hyung Won Chung, David M. Warsinger, and John H. Lienhard V. Simple method for balancing direct contact membrane distillation. *Desalination*, 383:53 – 59, 2016.

[106] Jaichander Swaminathan, Hyung Won Chung, David M. Warsinger, and John H. Lienhard V. Membrane distillation model based on heat exchanger theory and configuration comparison. *Applied Energy*, 184:491 – 505, 2016.

[107] Jaichander Swaminathan and John H. Lienhard V. Energy efficiency of sweeping gas membrane distillation desalination cycles. In *Proceedings of the 22nd National and 11th International ISHMT-ASME Heat and Mass Transfer Conference, IIT Kharagpur, India*, Dec 2013.

[108] Jaichander Swaminathan, Ronan K. McGovern, Hyung-Won Chung, David Elan-Martin Warsinger, and John H Lienhard V. Multi-effect membrane distillation, July 15 2016. US Patent App. 15/211,424.

[109] Jaichander Swaminathan, Kishor G. Nayar, and John H. Lienhard V. Mechanical vapor compression-membrane distillation hybrids for reduced specific energy consumption. *Desalination and Water Treatment*, 57(55):26507–26517, 2016.

[110] Jaichander Swaminathan, Emily W. Tow, Yagnaseni Roy, and John H. Lienhard V. Nanofiltration for high permeability textile dyeing effluent desalination. In *The International Desalination Association World Conference on Water Reuse and Recycling – Nice, France*, 2016.

[111] P. Termpiyakul, Ratana Jiraratananon, and Surapit Srisurichan. Heat and mass transfer characteristics of a direct contact membrane distillation process for desalination. *Desalination*, 177(1-3):133–141, 2005.

[112] Gregory P. Thiel and John H. Lienhard V. Treating produced water from hydraulic fracturing: Composition effects on scale formation and desalination system selection. *Desalination*, 346:54 – 69, 2014.

[113] Gregory P. Thiel, Ronan K. McGovern, Syed M. Zubair, and John H. Lienhard V. Thermodynamic equipartition for increased second law efficiency. *Applied Energy*, 118:292–299, 2014.

[114] Gregory P. Thiel, Emily W. Tow, Leonardo D. Banchik, Hyung Won Chung, and John H. Lienhard V. Energy consumption in desalinating produced water from shale oil and gas extraction. *Desalination*, 366:94–112, 2015. Energy and Desalination.

[115] R. Tian, H. Gao, X.H. Yang, S.Y. Yan, and S. Li. A new enhancement technique on air gap membrane distillation. *Desalination*, 332(1):52–59, 2014.

[116] Tiezheng Tong and Menachem Elimelech. The global rise of zero liquid discharge for wastewater management: Drivers, technologies, and future directions. *Environmental Science & Technology*, 50(13):6846–6855, 2016.

[117] José M. Veza. Mechanical vapour compression desalination plants – a case study. *Desalination*, 101(1):1–10, 1995.

[118] David E. M. Warsinger, Jaichander Swaminathan, and John H. Lienhard V. Effect of module inclination angle on air gap membrane distillation. In *Proceedings of the 15th International Heat Transfer Conference, IHTC-15, Paper No. IHTC15-9351*, Kyoto, Japan August 2014.

[119] David M. Warsinger, Karan H. Mistry, Hyung Won Chung, Kishor G. Nayar, and John H. Lienhard V. Entropy generation of desalination powered by variable temperature waste heat. *Entropy*, 17:7530–7566, 2015.

[120] David M. Warsinger, Kishor G. Nayar, Emily W. Tow, and John H. Lienhard V. Efficiency and fouling of closed circuit reverse osmosis and a novel variant: Pushing the limits on desalination efficiency. In *Oral Presentation, New England Graduate Student Water Symposium (NEGSWS), Amherst, MA, USA*, September 2015.

[121] David M. Warsinger, Jaichander Swaminathan, Laith Maswadeh, and John H. Lienhard V. Superhydrophobic condenser surfaces for air gap membrane distillation. *Journal of Membrane Science*, 492:578–587, 2015.

[122] David M. Warsinger, Emily W. Tow, Kishor Nayar, Laith A. Masawadeh, and John H. Lienhard V. Energy efficiency of batch and semi-batch (CCRO) reverse osmosis desalination. *Water Research*, 106:272–282, 2016.

[123] David M. Warsinger, Emily W. Tow, Kishor G. Nayar, Laith A. Maswadeh, and John H. Lienhard V. Energy efficiency of batch and semi-batch (CCRO) reverse osmosis desalination. *Water Research*, 106:272 – 282, 2016.

[124] David M. Warsinger, Emily W. Tow, Jaichander Swaminathan, and John H. Lienhard V. Theoretical framework for predicting inorganic fouling in membrane distillation and experimental validation with calcium sulfate. *Journal of Membrane Science*, 528:381 – 390, 2017.

[125] Jay R. Werber, Akshay Deshmukh, and Menachem Elimelech. Can batch or semi-batch processes save energy in reverse-osmosis desalination? *Desalination*, 402:109 – 122, 2017.

[126] Daniel Winter. *Membrane Distillation: A Thermodynamic, Technological and Economic Analysis*. PhD thesis, University of Kaiserslautern, Germany, 2015.

[127] Daniel Winter, Joachim Koschikowski, and Marcel Wieghaus. Desalination using membrane distillation: Experimental studies on full scale spiral wound modules. *Journal of Membrane Science*, 375(1-2):104–112, June 2011.

[128] Ho Yan Wu, Mason Tay, and Robert W. Field. Novel method for the design and assessment of direct contact membrane distillation modules. *Journal of Membrane Science*, 513:260–269, 2016.

[129] Yu-lei Xing, Chun-hua Qi, Hou-jun Feng, Qing-chun Lv, Guo-rong Xu, Hong-qing Lv, and Xin Wang. Performance study of a pilot-scale multi-effect vacuum membrane distillation desalination plant. *Desalination*, 403:199 – 207, 2017.

[130] Suna Yüksel, Nalan Kabay, and Mithat Yüksel. Removal of bisphenol A (BPA) from water by various nanofiltration (NF) and reverse osmosis (RO) membranes. *Journal of Hazardous Materials*, 263, Part 2:307 – 310, 2013.

[131] Hui Yu, Xing Yang, Rong Wang, and Anthony G. Fane. Numerical simulation of heat and mass transfer in direct membrane distillation in a hollow fiber module with laminar flow. *Journal of Membrane Science*, 384(1-2):107–116, November 2011.

[132] Yanbin Yun, Runyu Ma, Wenzhen Zhang, AG Fane, and Jiding Li. Direct contact membrane distillation mechanism for high concentration NaCl solutions. *Desalination*, 188(February 2005):251–262, 2006.

[133] Guillermo Zaragoza, Alba Ruiz-Aguirre, and Elena Guillén-Burrieza. Efficiency in the use of solar thermal energy of small membrane desalination systems for decentralized water production. *Applied Energy*, 130:491–499, October 2014.

[134] Kui Zhao, Wolfgang Heinzl, Marco T. Wenzel, Sebastian Büttner, F. Bollen, Götz Lange, Susanne Heinzl, and N. Sarda. Experimental study of the Memsys vacuum-multi-effect-membrane-distillation (V-MEMD) module. *Desalination*, 323:150–160, 2013.

[135] Guangzhi Zuo, Rong Wang, Robert Field, and Anthony G. Fane. Energy efficiency evaluation and economic analyses of direct contact membrane distillation system using Aspen Plus. *Desalination*, 283:237–244, 2011.